TECHNISCHE UNIVERSITÄT DARMSTADT

Enhancing the Light Absorption of Solar Cells with Carbon Nanotubes

Darmstadt März 2023

zur Erlangung des akademischen Grades

Doktors der Naturwissenschaften (Dr. rer. nat.)

genehmigte Dissertation im Fachbereich Material- und Geowissenschaften

von M.Sc. Chem. Laura Wieland aus Baden-Baden

Berichter:	Prof. Dr. Ralph Krupke
Mitberichter:	Prof. Dr. Jan Philipp Hofmann
Prüfer 1:	Prof. Dr. Peer Kirsch
Prüfer 2:	Prof. Dr. Alexander Colsmann

The Potential of Carbon Nanotubes to Extend the IR-Absorption of Solar Cells

submitted doctoral thesis by Laura Wieland

Date of submission: 21. March 2023

Date of thesis defense: 16. June 2023

Declaration/ Erklärung zur Dissertation

Hiermit versichere ich, die vorliegende Dissertation ohne Hilfe Dritter nur mit den angegebenen Quellen und Hilfsmitteln angefertigt zu haben. Alle Stellen, die aus Quellen entnommen wurden, sind als solche kenntlich gemacht. Diese Arbeit hat in gleicher oder ähnlicher Form noch keiner Prüfungsbehörde vorgelegen und ich habe zu einem vorherigen Zeitpunkt noch keine Promotion versucht.

Ich versichere hiermit, dass die elektronische Version meiner Dissertation mit der schriftlichen Version übereinstimmt.

Darmstadt, den 21. März 2023

_____

(Laura Wieland)

‘Wer immer tut, was er schon kann, bleibt immer das, was er schon ist.‘
- Henry Ford

Zusammenfassung

Der Energiebedarf der Welt wächst schnell, daher ist es eine der größten wissenschaftlichen Herausforderungen, Energiequellen oder -techniken zu entwickeln, um diesen zukünftigen Bedarf zu decken. Solarzellen haben Aufmerksamkeit als saubere Energiequelle erregt, da sie einerseits die Fähigkeit besitzen Licht in Strom umzuwandeln und andererseits einfach zu installieren sind. Die anorganischen Silizium-Solarzellen dominieren nach wie vor den Markt, da Silizium in der Halbleiterindustrie im Überfluss vorhanden ist, sie eine hohe Effizienz sowie eine hohe Stabilität aufweisen, was zu einem hervorragenden Preis-Leistungs-Verhältnis führt. Rasche Fortschritte haben zu hohen Wirkungsgraden von Solarzellen der dritten Generation wie Perowskit-Zellen geführt, die nun mit Siliziumsolarzellen vergleichbar sind. Auch die organische Photovoltaik holt in Bezug auf den Wirkungsgrad auf. In den letzten 5 Jahren hat sich dieser aufgrund neuer organischer Halbleitermaterialien von 12 % auf über 18 % entwickelt. Diese Leistungssteigerung der letzten Jahre kann auf die Entwicklung von Nicht-Fulleren-Akzeptoren (NFA) zurückgeführt werden, die in der Regel aus einem gekoppelten Ringsystem bestehen. Die breite spektrale Absorption der NFA ist vorteilhaft im Vergleich zu den sonst üblichen Fulleren-Akzeptoren, ebenso wie der höhere Extinktionskoeffizient und die Anpassbarkeit der Energieniveaus für maßgeschneiderte Donor/Akzeptor-Paare. Einfachere und umweltfreundliche Synthesewege, die geringere Kosten verursachen, sind daher noch nötig für einen Durchbruch organischer Solarzellen.

Kohlenstoff-Nanoröhren (CNTs) sind ein vielseitiges Material mit zahlreichen potenziellen Funktionen in organischen Photovoltaikzellen. Im Prinzip können alle Elemente einer Solarzelle, von der lichtempfindlichen Komponente bis hin zu selektiven Kontakten für bestimmte Ladungsträger, Passivierungsschichten und den transparenten Elektroden, durch Kohlenstoffnanoröhren ersetzt werden. Die Hindernisse für ihre Anwendung in der Industrie schwinden schnell z.B. durch die fortgeschrittenen Dispergier- und Sortierungstechniken, die die Ausbeute und Reinheit einzelner chiraler Spezies drastisch erhöhen. Derzeit ist die Polymersortierung in Toluol ein einfaches Verfahren, mit dem eine hohe Reinheit erreicht wird, aber die Ausbeute ist gering. Die wässrige Sortierung hingegen ermöglicht den Zugang zu viel mehr chiralen Spezies und höheren Ausbeuten.

Die schmalen Absorptionsbanden und die anpassbaren elektronischen Eigenschaften von CNTs sind für transparente Elektroden und Schichten zum Transport von Löchern nützlich.

Insbesondere CNTs als Passivierungsschicht und als loch-selektiver Kontakt in der Siliziumsolarzelle haben sich bereits als wettbewerbsfähig erwiesen im Vergleich zu aktuellen industriellen Zellen. Für CNTs in der aktiven Schicht von organischen Solarzellen bestehen jedoch noch viele Herausforderungen, die es zu bewältigen gilt. Diese stehen vor allem im Zusammenhang mit der Verbesserung der Lichtabsorption der Solarzellen und dem damit verbundenen geringen Wirkungsgrad. In der Dissertation wurden verschiedene Arten von SWCNTs getestet, um zu zeigen, dass es möglich ist, das gesamte Spektrum halbleitender Kohlenstoff-Nanoröhren (kleiner und großer Durchmesser) zu verwenden, und dass Strategien zur Verringerung der Exzitonenfallen in Mischungen mehrerer Arten erforderlich sind. Die interessanten Fragen für CNT-basierte Solarzellen sind, welche Art von Nanoröhren sind in der Photovoltaik vorteilhaft und wie können diese in ein Zelle integriert werden.

Die Verbesserung der Lichtabsorption von CNT/C_{60}-Solarzellen ist sehr gefragt und kann durch den Austausch etablierter Materialien wie z.B. Fulleren-Akzeptoren erreicht werden oder durch die Zugabe von Materialien wie Farbstoffen, die Photonen in anderen Spektralbereichen absorbieren. In diesem Zusammenhang können CNTs als Hohlraum für Farbstoffe verwendet werden, die wiederum ihre absorbierte Energie auf das Nanoröhrchen übertragen müssen, um höhere Wirkungsgrade zu erzielen. Der Ersatz von Fulleren-Akzeptoren durch Nicht-Fulleren-Akzeptoren dient dem Zweck einer breiteren Lichtabsorption und kann gleichzeitig eine Lösung für das Problem bieten, Kohlenstoff-Nanoröhren mit größerem Durchmesser zugänglicher zu machen.

Dennoch ist die Dicke der CNT-Schicht durch die kurze Diffusionslänge der Exzitonen begrenzt. In Anbetracht dieser Einschränkung ist es wichtig, die Forschung an gemischten Systemen fortzusetzen, um die Morphologie zu optimieren und die Rekombination zu unterdrücken. Die Lichtabsorption solcher Bulk-Heterojunctions kann durch den Wechsel zu breitbandigen Komponenten oder die Zugabe eines dritten Materials vervollständigt werden, das im Idealfall eine Kaskade für den Elektronentransfer ermöglicht. Diese Strategie hat eine viel höhere Wahrscheinlichkeit, wettbewerbsfähige Effizienzen zu erreichen, da diese ternären Systeme auf etablierten Materialkombinationen aufbauen. Alternativ können CNT-basierte Solarzellen mit etablierten Photovoltaikzellen zu einem Tandem kombiniert werden, um deren Absorption in den Infrarotbereich zu erweitern.

Abstract

The energy demand of the world is growing fast, it is therefore one of the greatest scientific challenges to develop energy sources or techniques to satisfy those future demands. Solar cells have aroused attention as clean energy source due to their light harvesting ability while being easy to install everywhere. The inorganic silicon solar cells still dominate the market due to the silicon's abundance in semiconductor industry, their high efficiency and high-stability which results in a great performance-to-cost ratio. Rapid advances in emerging fields have led to high efficiencies of third generation solar cells like perovskite devices that are already comparable to silicon solar cells. Organic photovoltaics are also catching up with regard to efficiency, in the last 5 years they have developed from 12 % to over 18 % based on new organic semiconductor materials. This performance increase of the last years can be attributed to the development of non-fullerene acceptors (NFA), which typically consists of a fused ring system. Their broad spectral absorption is advantageous compared to standard fullerene acceptors, as well as the higher extinction coefficient and tunability of energy levels for tailored donor/acceptor pairs. Simpler and environmentally friendly synthesis routes and thus lower costs are required for the breakthrough of organic solar cells.

Carbon nanotubes (CNTs) are a versatile material with multiple potential functions for organic photovoltaics. In principle, all elements of a solar cell, from the light sensitive component to carrier selective contacts, layers for passivation and transparent conducting films can be replaced by carbon nanotubes and their composites. The barriers to their application in industry are diminishing rapidly like the advanced dispersion and separation techniques with dramatically increase in yield and purity of single chiral species. Currently, polymer-sorting in toluene is a simple procedure which achieves high purity, but yields are low. On the other hand, aqueous sorting provides access to many more chiral species and higher yields.

The narrow absorption bands and the tailorable electronic property of CNTs are useful for transparent electrodes and hole transport layers. Especially, CNTs as a passivation layer and hole selective contact in silicon photovoltaics have already been demonstrated to be competitive with current industrial cells. However, CNTs in the active layer of organic solar cells still face many challenges that need to be addressed. Primarily these are associated with improvements in the light absorption of the solar cells and the correspondingly low efficiency. In the thesis, different species of SWCNTs were tested to show that is possible to use the entire range of semiconducting

CNTs (small and large diameter) and strategies to reduce excitonic trapping in mixtures of several species are required. The interesting questions for CNT based solar cells are what kind of nanotubes are favourable in PV and how can those be integrated into a device.

Improving the light absorption of CNT/C_{60} cells is highly desired and can be accomplished by exchanging established materials like fullerene acceptors or adding materials such as dyes which absorb photons in other spectral regions. In this regard, CNTs can be used as cavity for dyes which have to transfer their absorbed energy to the nanotube to gain higher efficiencies. The replacement of fullerene acceptors with non-fullerene acceptors serves the purpose of broader light absorption and can simultaneously provide a solution to the accessibility issue of larger diameter CNTs.

Nevertheless, the CNT film thickness will still be limited by the short exciton diffusion length. Considering this limitation, it is important to continue research on blended systems to optimize morphology and suppress recombination. The light absorption of such bulk heterojunctions can be completed by changing to broadband components or the addition of a third material that ideally facilitates a cascade for electron transfer. This strategy has a much higher probability of reaching competitive efficiencies because these ternary systems are built on established materials combinations. Alternatively, CNT based solar cells can be combined with established photovoltaic devices to a tandem stack for absorption extension into the infrared.

Acknowledgement

I would like to thank Prof. Dr. Krupke for evaluating this thesis as referee, being my supervisor over this dissertation time and for supporting me in my extra courses I attended at TU Darmstadt. Moreover, I would like to express my gratitude towards Dr. Benjamin S. Flavel for being my supervisor and for the on-going support, advice and critical questions about experimental methods. Without his passion and patience these results wouldn't have been possible.

This work presents results that could not have been achieved without Dr. Jianhui Chen from Hebei University during his time in our group and beyond. His practical advice and broad view on the solar cell field, lead us to the idea of silicon tandem cells where he provided the bifacial silicon device. In the polymer cell project, he and Dr. Xuning Zhang helped me to optimize the fabrication process of the PM6:Y6 layer.

I'm grateful to Chris, my best office and lab mate in the last years. Thanks to your dead-end filtration setup I was able to produce aqueous sorted nanotube films for the solar cells. Besides, you have always cheered me up with your optimism or sarcastic comments.
I would also like to thank Dr. Han Li for communicating with China and being a great lab mate, you have produced large volumes of aqueous sorted CNTs as comparison to my polymer-wrapped nanotubes. Your sorting ability led to the collaboration with Prof. Sophie Cambré and Salomé Forel from University of Antwerp on squarylium filled CNTs.
Dr. Daniel Tune was the one introducing me to the solar cell project with all the procedures, thank you for the design of layer stack, the evaporation patterns and your patience.

I'm thankful to all members of the Krupke group for the open and helping working atmosphere and all the other people at Institute of Nanotechnology who have supported me like Rui Kang by providing the HINA dye. At the Institute of Microstructure Technology (IMT), Dr. Ian Howard and Marius Jakoby have measured the transient absorption of (6,5) nanotubes for me, thank you for pushing your setup to the limit.

Finally, I am also very grateful to my family for their support and motivation during my PhD time and of course my fiancé Christophe, for his patience and endorsement that helped me to complete this work successfully.

Content

List of Abbreviations

a_{c-c}	Carbon Bond Length
ADC	Ammonium Deoxycholate
AFM	Atomic Force Microscopy
Al-BSF	Aluminium Back Surface Field
ATPE	Aqueous Two -Phase Extraction
a.u.	Arbitrary Unit
BCP	Bathocuproine
BHJ	Bulk Heterojunction
C_{60}	Fullerene with 60 Carbon Atoms
CdTe	Cadmium Telluride
CIGS	Copper Indium Gallium Selenide
CNT	Carbon Nanotube
CoMoCAT®	Carbon Monoxide Disproportionation on a Cobalt-Molybdenum Catalyst (CNT Raw Material)
CVD	Chemical Vapor Deposition
d	Diameter
DANS	Dimethylaminonitrostilbene
DGU	Density Gradient Ultracentrifugation
DOC	Sodium Deoxycholate
DOS	Density of States
DWCNT	Double Walled Carbon Nanotube
E_b	Exciton Binding Energy
E_g	Bandgap
EPS	Exciton Phonon Sideband
EQE	External Quantum Efficiency
ETL	Electron Transport Layer
FF	Fill Factor
△G	Thermodynamic Driving Energy
GPC	Gel Permeation Chromatography
HINA	3-Hydroxyisonicotinealdehyde
HiPco	High Pressure Carbon Monoxide (CNT Raw Material)
HOMO	Highest Occupied Molecular Orbital
HTL	Hole Transport Layer
IBC	Interdigitated Back Contact
IQE	Internal Quantum Efficiency
ITIC-2F or ITIC-4F	3,9-bis(2-methylene-((3-(1,1-dicyanomethylene)-6,7-difluoro)-indanone))-5,5,11,11-tetrakis(4-hexylphenyl)-dithieno[2,3-d:2',3'-d']-s-indaceno[1,2-b:5,6-b']dithiophene
ITO	Indium Tin Oxide
J_{SC}	Short Circuit Current
J-V	Current Voltage
LUMO	Lowest Unoccupied Molecular Orbital
MWCNT	Multi Walled Carbon Nanotube
Nafion	Tetrafluoroethylene-perfluoro-3,6-dioxa-4-methyl-7-octenesulfonic acid copolymer
NFA	Non-Fullerene Acceptor

OD	Optical Density
OPV	Organic Photovoltaics
OSC	Organic Solar Cells
P2	CNT Raw Material Synthesized by Electric Arc
P3HT	poly(3-hexylthiophene2,5-diyl)
PCBM or $PC_{61}BM$	[6,6]-Phenyl-C61-Butyric Acid Methyl Ester
$PC_{71}BM$	[6,6]-Phenyl-C71-Butyric Acid Methyl Ester
PCE	Power Conversion Efficiency
PEDOT:PSS	Poly(3,4-ethylenedioxythiophene) Polystyrene Sulfonate
PEG	Polyethylene Glycol
PERC	Passivated Emitter and Rear Cell
PF12	Poly(9,9-di-ndodecylfluorenyl-2,7-diyl)
PFO	Poly(9,9-dioctylfluorenyl-2,7diyl)
PFO-BPy	Poly[(9,9-dioctylfluorenyl-2,7-diyl)-alt-(6,6'-(2,2'-bipyridine))]
PL	Photoluminescence
PM6	Poly[(2,6-(4,8-bis(5-(2-ethylhexyl-3-fluoro)thiophen-2-yl)-benzo[1,2-b:4,5-b′]dithiophene))-alt-(5,5-(1′,3′-di-2-thienyl-5′,7′-bis(2-ethylhexyl)benzo[1′,2′-c:4′,5′-c′]dithiophene-4,8-dione))]
PMMA	Poly(methyl methacrylate)
PolyTPD or PTPD	Poly[N,N' -bis(4-butylphenyl)-N,N' -bis(phenyl)-benzidine]
PTCDI-C8	N,N'-Dioctyl-3,4,9,10-perylene dicarboximide
RBM	Radial Breathing Mode
RMS	Root Mean Square
S_{xx} (x = 1, 2, …)	First/ Second/ … Transition of Semiconducting Nanotubes
SC	Sodium Cholate
SDS	Sodium Dodecyl Sulphate
SFM	Shear-force Mixing
SHJ	Silicon Heterojunction
Spiro-MeTAD	2,2',7,7'-Tetrakis[N,N-di(4-methoxyphenyl)amino]-9,9'-spirobifluorene
SQ	Squarylium Dye
SSC	Silicon Solar Cells
SWCNT	Single Walled Carbon Nanotube
TA	Transient Absorbance
TC	Transparent Conductor
TUBALL	Larger diameter CNT raw material
VHS	Van Hove Singularities
V_{OC}	Open Circuit Voltage
wt	Percentage by Mass (Weight)
Y6	2,2'-((2Z,2'Z)-((12,13-bis(2-ethylhexyl)-3,9-diundecyl-12,13-dihydro-[1,2,5]thiadiazolo[3,4-e]thieno[2",3'':4',5']thieno [2',3':4,5]pyrrolo[3,2-g]thieno[2',3':4,5]thieno[3,2-b]indole-2,10-diyl)bis(methanylylidene)) bis(5,6-difluoro-3-oxo-2,3-dihydro-1H-indene-2,1-diylidene))dimalononitrile

- this page left intentionally blank -

List of Publications

The following contains a list of the original publications arising from the author's Ph.D. studies.

(1) **L. Wieland**, H. Li, C. Rust, J. Chen, B. S. Flavel, *Carbon Nanotubes for Photovoltaics: From Lab to Industry*, Adv Energy Mater 2020, 11,2002880

(2) **L. Wieland**, C. Rust, H. Li, M. Jakoby, I. Howard, F. Li, J. Chen, B. S. Flavel, *The Potential of SWCNTs to Extend the IR-Absorption of Silicon Solar Cells*, Carbon 2021, 184, 828

(3) S. Forel, H. Li, S. Van Bezouw, J. Campo, **L. Wieland**, W. Wenseleers, B. S. Flavel, S. Cambré, *Diameter-dependent single- and double-file stacking of squaraine dye molecules inside chirality-sorted single-wall carbon nanotubes*, Nanoscale 2022, 14, 8385

(4) **L. Wieland**, H. Li, X. Zhang, J. Chen, B.S. Flavel, *Ternary PM6:Y6 Solar Cells with Single Wall Carbon Nanotubes*, Small Science 2022, 3, 2200079

Partial content (text and figures) of this work have been previously published in the listed publications shown above. The permission for reproduction was granted by Wiley-VCH GmbH and Elsevier under the creative commons agreement, which allows for reproduction by adequate citation of the contents.

Publication (2) forms the basis of chapter 3 and 5.

Publication (4) is reproduced in chapter 6.

Finally, content of (1) will be found in the introduction and conclusion, mainly: 1.1.3, 1.1.5, 1.2.1, 1.2.4. and complete 1.3, as well as in chapter 7.

Additionally, figures of other authors are reproduced under the license of the respective publisher.

- this page left intentionally blank -

1 Introduction

1.1 Carbon Nanotubes

Carbon nanotubes (CNTs) are rods made only of carbon atoms and they can either be single walled (SWCNT), double walled (DWCNT) or multi walled (MWCNT). Discovered in 1991[1], CNTs, their growth mechanism, separation and electronic properties are still an ongoing research topic as well as their integration in electronic devices. For an introduction into the field of carbon nanotubes, first the structure and nomenclature are elucidated, followed by the basic electronic and optical properties and their characterization. The main synthesis processes are outlined and the need of separation methods are emphasized to yield high purity of single species out of the multispecies raw material. While separation is based on the non-covalent functionalization of the CNT surface, the inner cavity of a carbon nanotube can also be modified by filling the void with different molecules leading to shifts in the optical properties. For the integration of CNTs into applications, it is necessary to prepare CNT networks or films from the sorted or functionalized nanotube dispersions that are compatible with the other fabrication steps.

1.1.1 Structure and Nomenclature

Carbon nanotubes can be envisioned as a rolled-up graphene sheet and as such there are countless ways to achieve the cylindrical shape. Each direction of roll-up results in unique diameters and electronic and optical properties. The honeycomb lattice of graphene and the unit vectors a_1 and a_2, are shown in Figure 1.1.1A and are the basis for describing each individual nanotube. To represent the different circumferences of the SWCNTs the graphene lattice vector

$$C = n \cdot a_1 + \ m \cdot a_2 \tag{1}$$

is formed of the rolled-up vectors n and m. These are also called chiral indices (n, m), which enable diameter calculation:[2]

$$d = \sqrt{(n^2 + n \cdot m + m^2)} \cdot a_{c-c} \cdot \frac{\sqrt{3}}{\pi} \tag{2}$$

where a_{c-c} is the carbon bond length of 0.142 nm.[2] The angle Θ between c and the unit vector a_1 can only assume values between 0° and 30° due to the hexagonal lattice structure of graphene.[3]

$$cos\theta \ = \frac{C \cdot a_1}{|C| \cdot |a_1|} = \frac{2n + m}{2\sqrt{n^2 + nm + m^2}} \tag{3}$$

There are three different SWCNT types (chiral, armchair or zig-zag) depending on how the rolled-up vectors are chosen: $(n, 0)$ is named zig-zag, (n, n) armchair and all other CNTs are chiral. Figure 1.1.1A highlights these types in the honeycomb lattice of graphene and in Figure 1.1.1B the shape of the three CNT species is displayed.[4]

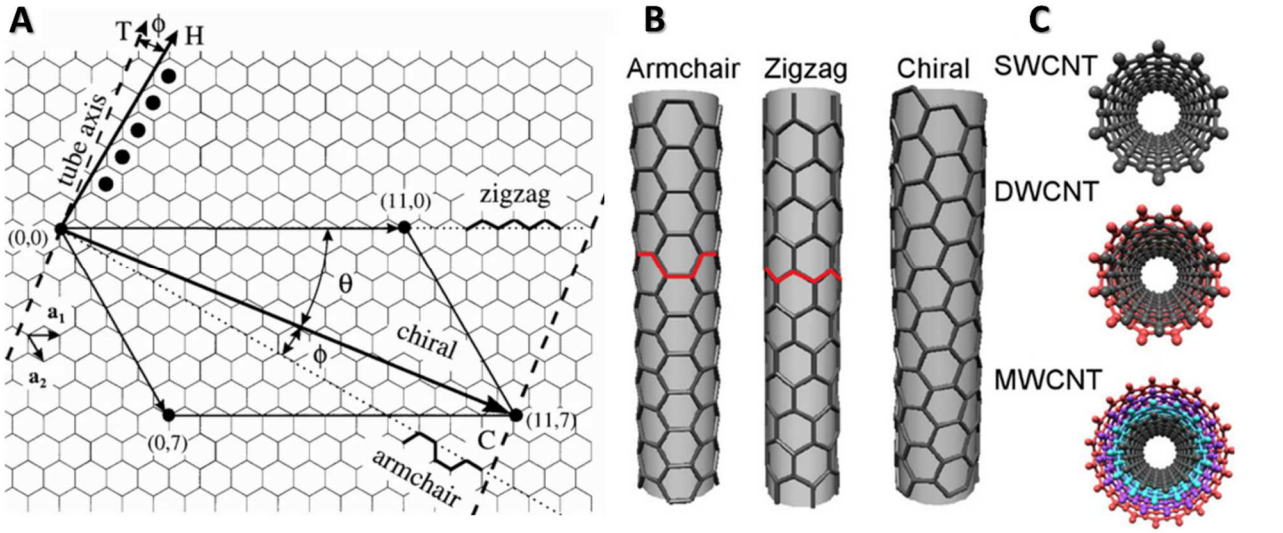

Figure 1.1.1: (A) The graphene lattice vector C results from the multiple n and m of the unit vectors a_1 and a_2. The addition of these vectors, e.g. $11a_1$ and $7a_2$ gives the so-called chirality (11,7) of the carbon nanotube.[4] (B) Carbon nanotubes are all chiral except zig-zag (n,0) and armchair (n,n).[5] (C) They can be either single, double or multi walled. *[(A) 'Electronic Structure of Atomically Resolved Carbon Nanotubes', Wilder et al., Nature, 391, 1998, reproduced with permission from SNCSC. (B,C) Reprinted with permission from Yu et al. 'Recent Development of Carbon Nanotube Transparent Conductive Films' Chem. Rev. 2016, 116, 22, 13413 Copyright 2016 American Chemical Society.]*

Carbon nanotubes are considered as 1D material due to their high aspect ratio with nanometer diameter and micrometres length. This particular shape restricts the electrons in their movement which creates unique material properties, like individual absorption bands and electronic characteristics either semiconducting or metallic. The electronic type of carbon nanotubes can be determined by use of the chiral indices. If $n - m$ is zero or a multiple of 3 then the SWCNT is metallic. Otherwise they are semiconducting with an energy gap in the order of ~0.5 eV.[4] These electrical and optical properties can be derived from the zero-gap semiconductor material graphene.[3]

1.1.2 Electrical Properties

The electronic properties can be deduced from the Brillouin zone of graphene and its folded band structure. Whereas the nanotube nomenclature was derived from the hexagonal lattice in real space (Figure 1.1.2A), the basis for the construction of the Brillouin zone is a hexagonal reciprocal lattice. First, the nearest neighbours are connected to the starting point and perpendicular

bisectors of these sides are drawn. The area which these lines enclose is called the Brillouin zone (blue area in Figure 1.1.2B) and the high symmetry points are labelled Γ, K and M, as shown in Figure 1.1.2B. The electronic band structure of graphene with an occupied π-band and an unoccupied π^*-band is unique because the bands only cross at the K-points of the Brillouin zone, where the Fermi energy lies. Therefore graphene is a semiconductor with zero bandgap as illustrated in Figure 1.1.3A.[6]

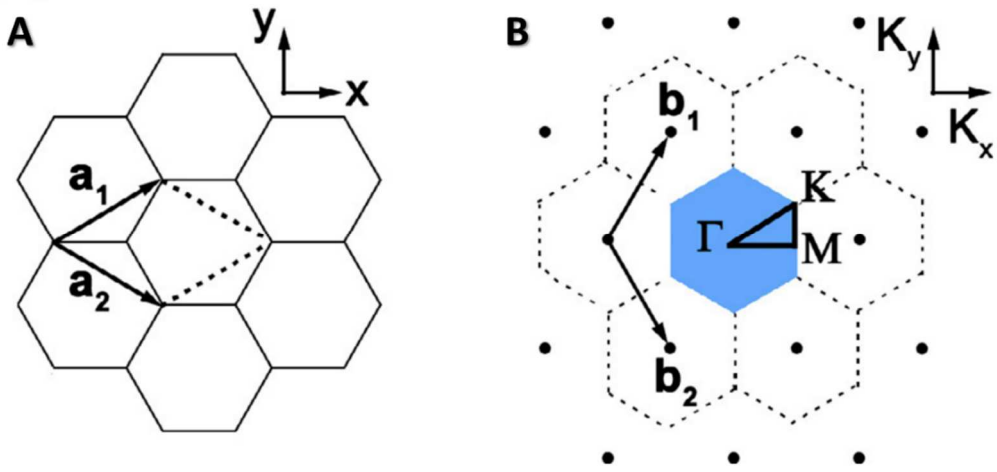

Figure 1.1.2: (A) The unit cell (dotted rhombus, containing two carbon atoms) of hexagonal graphene lattice defined by the basis vectors a_1 and a_2 in real space. (B) The reciprocal lattice of graphene (dashed hexagons) with the basis vectors b_1 and b_2 and the first Brillouin zone of graphene (blue hexagon) with three high symmetry points Γ, K and M (connected by the black triangle). Bold dots correspond to Γ points. [3] *[Reprinted from Progress in Materials Science, Vol 77, Kharlamova, 'Advances in tailoring the electronic properties of single-walled carbon nanotubes', 125-211, Copyright 2016, with permission from Elsevier]*

The 1D band structure of carbon nanotubes can be obtained by zone folding of the 2D graphene into a one-dimensional Brillouin zone of the CNTs. This Brillouin zone of carbon nanotubes corresponds to the unit cell of the specific nanotube due to their chirality. To obtain the nanotube structure the unit cell is repeated along the entire tube axis, therefore the wave vector $k_{\parallel}$ of an electron or phonon is supposed to be continuous. In contrast, the wave vector along the circumference is quantized $k_{\perp} = 2\frac{\pi}{\lambda}$.[7] Hence, the wave function of the electron (or phonon) must have a phase shift of an integer multiple of 2π, otherwise the waves won't interfere constructive.[8] The allowed states of $k_{\perp}$ can be plotted in the Brillouin zone of graphene as parallel lines. In the case of armchair nanotubes, these lines are parallel to the tube axis. Whenever one line crosses the K point, the corresponding SWCNTs are metallic. (represented in Figure 1.1.3B) One third of nanotubes have lines passing through the K point due to the honeycomb geometry, every time when $(n - m)$ is a multiple of 3. The metallic character is based on the contact of valence and conduction band at the Fermi energy level E_F at these points. A CNT is semiconducting and shows a band gap around E_F, if the K and K' points are not part of the allowed states, as illustrated in

Figure 1.1.3B. If the cutting line of the first valence and conduction bands is located on the left side of the K point, it is called semi-type I and for the right-side semi-type II.[9]

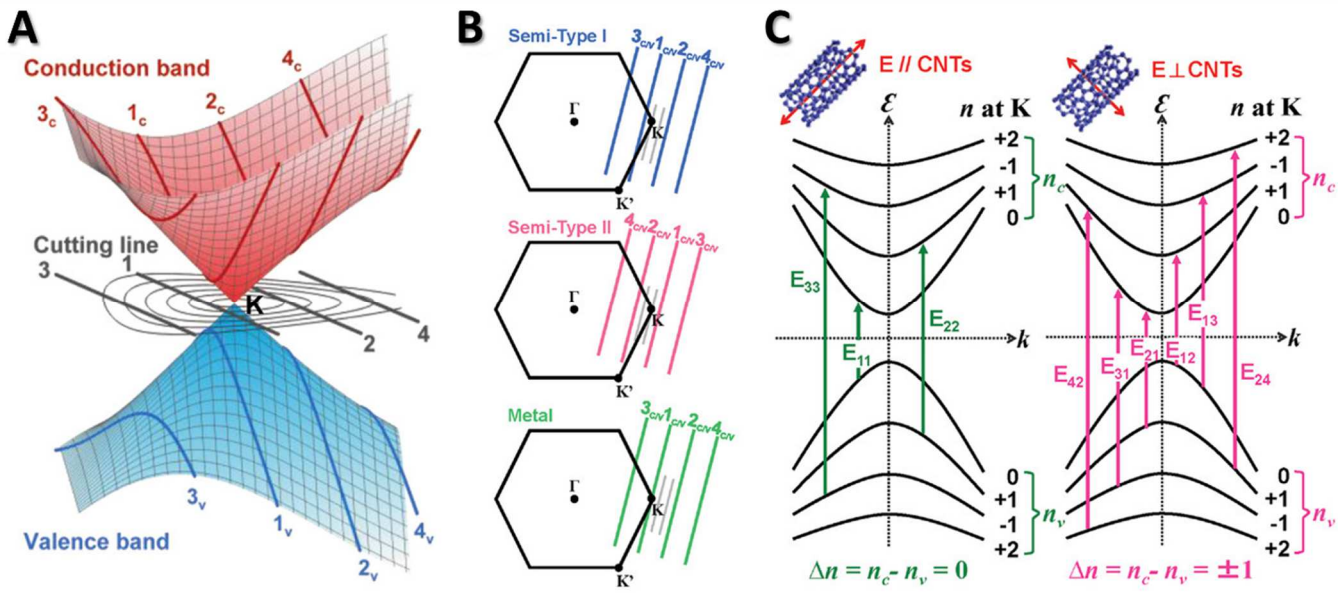

Figure 1.1.3: (A) Schematic diagram of the conduction and valence band of single-layer graphene around the K point and cutting lines in the reciprocal space of SWCNTs. (B) Reciprocal space of the graphene and cutting lines corresponding to metallic or semiconducting type I and type II SWCNTs. (C) Energy bands and allowed optical transitions of a semiconducting SWCNT depending on the light polarization.[9] *[Reproduced from Advanced Science, Wei et al. 'Recent Advances in Structure Separation of Single-Wall Carbon Nanotubes and Their Application in Optics, Electronics, and Optoelectronics' 9, 14, 2022, under Creative Commons license agreement from Wiley-VCH GmbH.]*

The allowed optical transitions of semiconducting SWCNTs in Figure 1.1.3C depend on the polarization of the incoming light. If the electric field polarization is parallel to the axis, E_{ii} transitions are allowed meaning from the valence band in the conduction band with the same band indices at the K-point. Polarization perpendicular to the SWCNT only enables E_{ij} transitions which are damped compared to the well-defined spectral peaks of parallel polarized light.[10]

Electrical properties of individual carbon nanotubes can be measured for example by implementing them into simple electronic devices like transistors. If only a single nanotube is placed between the two electrodes, semiconducting and metallic behaviour can be distinguished. A linear current-voltage (IV) dependence is characteristic for metallic CNTs with a nearly constant source-drain current I_{SD} for various gate voltages. Semiconducting CNTs have non-linear IV behaviour due to a Schottky barrier at the electrode-nanotube contact. Source-drain current is strongly depending on the gate voltage with high on/off ratios. Individual SWCNT field-effect transistors have already shown high current carrying capacity in the quantum ballistic regime, high carrier mobility in the diffusive regime and low leakage current.[11]

The electronic as well as the optical properties of SWCNTs can be approximately described by the 1D model of the density of states (DOS). This concept relies on the number of available states at each energy level.[7] In the DOS-diagram sharp peaks appear because of the one-dimensionality and the quantized energy values around the circumference of a nanotube. These spikes close to the band edges are called Van Hove singularities (VHS)[12] which are arranged symmetrically to the Fermi level. An energy minimum or maximum of each subband near the K point corresponds to a VHS highlighted in Figure 1.1.4. They originate from the energy dispersion along the parallel lines near the K points of graphene's first Brillouin zone. If the lines cross the K point, the metallic nanotubes show no bandgap, meaning their density of states has a constant value at the Fermi level given by[3]

$$D(E_F) = \frac{\sqrt{3}a_{c-c}}{2\pi^2\gamma_0 d} \tag{4}$$

a_{c-c} is the carbon bond length, γ_0 is here the nearest-neighbour carbon–carbon interaction energy and d the diameter.

For semiconducting CNTs the density of states is zero between the first VHS which corresponds to the forbidden energy states leading to the band gap at the Fermi level. Figure 1.1.4 represents the electronic energy dispersion and the differences in the density of states of (A) metallic and (B) semiconducting SWCNTs.[13]

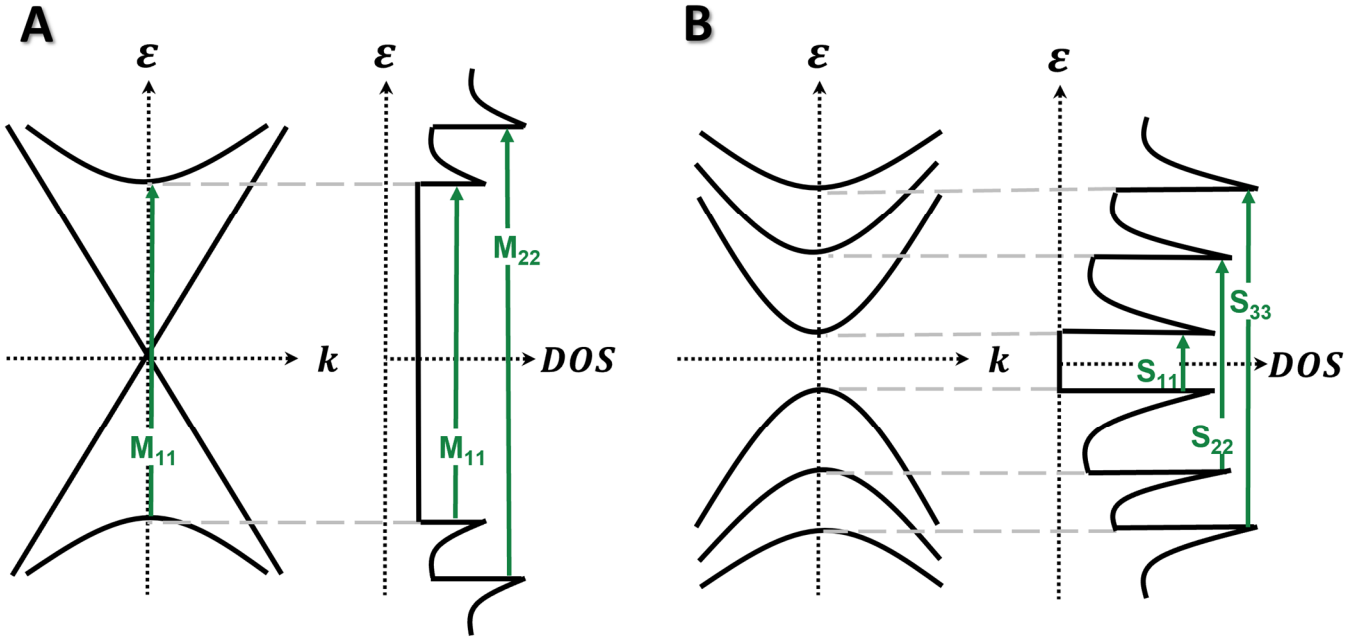

Figure 1.1.4: Schematic electronic energy-dispersion relations and densities of states of (A) metallic (n = m) and (B) semiconducting (n-m = ±1) single walled carbon nanotubes.[13] Green arrows highlight the first few transitions of each type.

1.1.3 Optical Properties

The optical properties of the carbon nanotubes can be explained with respect to the transition energies between the valence and conduction band. If the transition energy is equal to the energy of the incoming photon, the probability for the absorption of this photon is high and the states in the conduction band become occupied. The relaxation process can either be thermally through the continuous DOS of the metallic nanotubes or radiative through fluorescence for the semiconducting CNTs. The transition energy is labelled S_{XX} for the semiconducting and M_{XX} for the metallic SWCNTs referring to transition from VHS x in the valence band to the VHS x in the conduction band, start counting from the Fermi level. The green arrows in Figure 1.1.4 illustrate the first few transitions for each kind of SWCNTs.[13] These dominant parallel polarized transitions can only occur between symmetrical x-VHS in the valence and conducting band due to selection rules.[3] The correlation of a specific transition energy $E(S_{11})$, $E(S_{22})$, $E(M_{11})$ etc. and the diameter of the carbon nanotubes is given by[14]

$$E(S_{11}) = \frac{2}{d} \cdot a_{c-c} \cdot \gamma \quad E(S_{22}) = \frac{4}{d} \cdot a_{c-c} \cdot \gamma \quad \dots \tag{5}$$

$$E(M_{11}) = \frac{6}{d} \cdot a_{c-c} \cdot \gamma \quad \dots \tag{6}$$

where d denotes the diameter, a_{c-c} the carbon bond length and γ an empirical value which considers curvature effects.[14, 15] For semiconducting CNTs the predicted VHS pattern is 1, 2, 4, 5… relative to E_F (spacing also $1\beta, 2\beta, 4\beta, 5\beta, \dots$) and for metallic nanotubes 1, 2, 3… however with a spacing of $3\beta, 6\beta, 9\beta$ etc. The spacing factor is $\beta = \frac{2\pi}{3} C$ [7] with C the graphene lattice vector.

The optical transition energy can be utilized to calculate the excitation energy by the single particle model.[8] However this approximation doesn't sufficiently determine the optical transition energy and leads to the well know 'ratio problem' where the ratio between the second and first transition is found by photoluminescence measurements to be 1.8 [16] instead of 2 following equation (5).[17] One factor for this deviation is the binding energy (E_b) of the strongly bound exciton states[18], whereas higher transitions are affected by unbound electron-hole pairs or delocalized exciton states.[19] Therefore an excitonic model instead of a single particle approach should be considered, which includes the electron-electron repulsion and the electron-hole attraction.[18] However, many properties like a diameter dependence can still be predicted based on less accurate tight binding models. For example, the Kataura plot in Figure 1.1.5A showing the transitions energy as a function of diameter and chirality, undergoes a distortion of the energy axis but the trend

remains the same. The plot covers the first optical transitions of metallic and semiconducting (type I and II) SWCNTs, represented as stars, open and filled circles, respectively.[20]

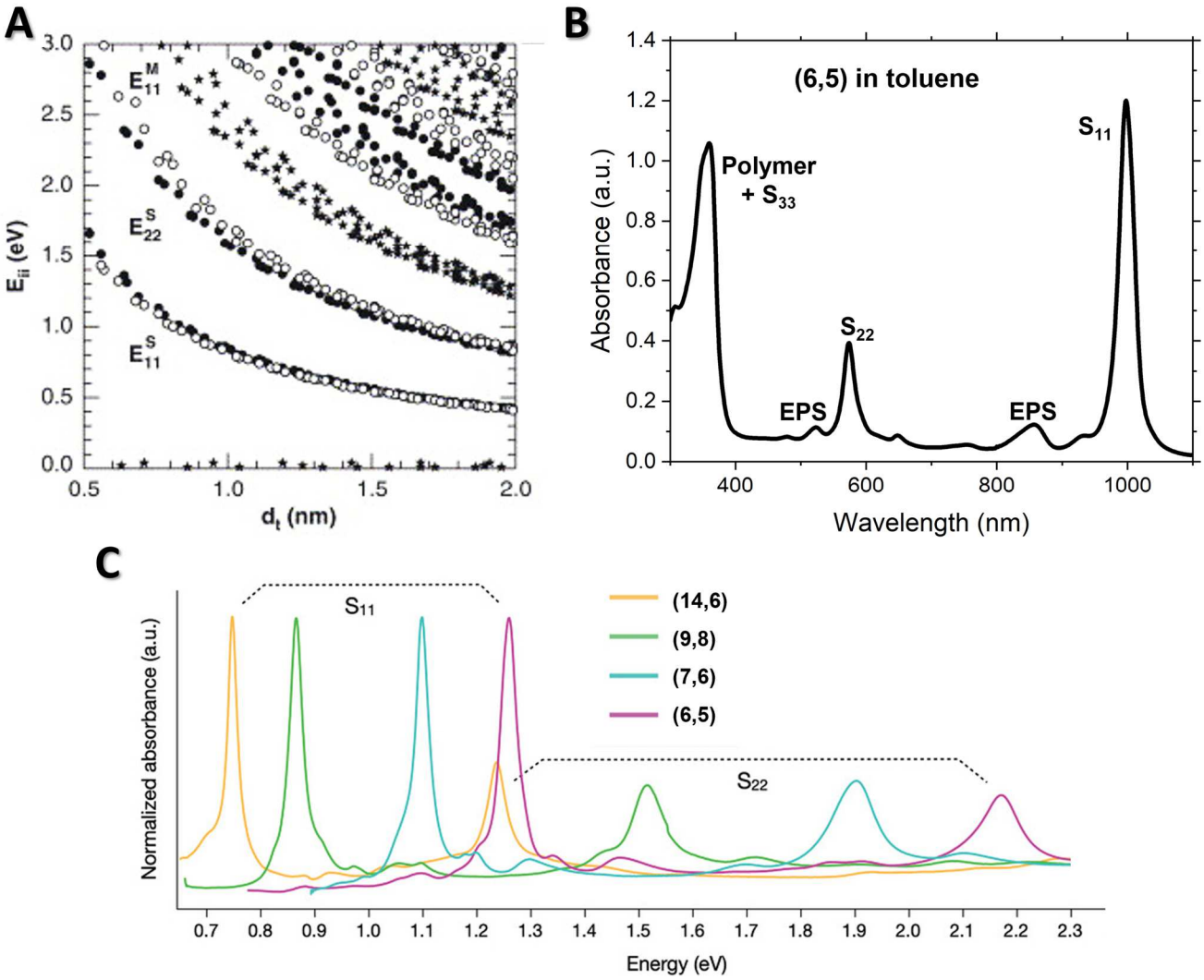

Figure 1.1.5: (A) Kataura plot: The electronic transition energies vs. nanotube diameter for SWCNTs calculated by the first-neighbour tight binding method. Stars, filled and open circles stand for metallic and semiconducting (type I and II) SWCNTs, respectively.[20] (B) Absorbance spectrum of (6,5) SWCNTs sorted by shear-force mixing and polymer wrapping. (C) Representative absorbance spectra show the variability of the first (S_{11}) and second (S_{22}) optical transitions for CNTs of various diameter.[21] *[(A) Reprinted from Physics Reports, Vol 409, Dresselhaus et al., 'Raman spectroscopy of carbon nanotubes', 47-99, Copyright 2005, with permission from Elsevier (C) Reproduced from Advanced Energy Materials, Wieland et al. 'Carbon Nanotubes for Photovoltaics: From Lab to Industry' 11, 3, 2021, under Creative Commons license agreement from Wiley-VCH GmbH.]*

A widely used optical characterization tool for SWCNTs is absorption spectroscopy in the range of UV up to infrared (IR). The spectroscopically accessible window of carbon nanotubes in aqueous solution is 200 to ~1850 nm due to the IR-absorption of water, however in D_2O the detection range extends up to 2500 nm and in organic solvents also up to approximately 2500 nm depending on the specific solvent. By analysing absorbance spectra, the shape of the background has to be considered and is often attributed to carbonaceous impurities, catalytic particles or the metallic nanotubes.[22]

As an example, Figure 1.1.5B shows the absorbance of a nearly monochiral (6,5) SWCNT in toluene dispersion, separated by polymer wrapping. Here the S_{11} and S_{22} are sharp signals at 998 nm and 574 nm while the third transition S_{33} of the SWCNT overlaps with the polymer absorption. The observed broader signals located on the right side of each main optical transition are assigned to a resonance of a bound exciton phonon state, the so-called exciton phonon sidebands (EPS).[23] The intensity transferred from S_{11} absorption to the sideband scales inversely with the diameter of the nanotubes.[18] This phenomenon reinforces that optical transitions in CNTs are exitonic.

With the aid of the Kataura plot, the individual optical properties of SWCNTs can be assigned to specific (n, m) chiralities determining the composition of CNT dispersions. Figure 1.1.5C displays four different absorption spectra for chiralities with increasing diameter from (6,5), (7,6), (9,8) to (14,6) resulting in lower transition energies according to equations (5). Larger diameter CNTs therefore absorb at higher wavelengths due to the inverse relation of wavelength and energy $E = \frac{hc}{\lambda}$. The overlay of only 4 absorption spectra in Figure 1.1.5C already highlights the difficulty of spectral analysis for multi-chiral samples. The overlap of individual optical transition peaks into a broad absorption band makes it difficult to distinguish between chiralities especially those in lower concentration. The phonon sideband can as well overlap with other CNT chiralities. In the region over 2 eV (or below 620 nm) lots of possible S_{33}, M_{11} or higher transitions can occur, here only fitting the complete spectra including S_{11} and S_{22} regions allows for concrete assignment of SWCNTs.[24] The chirality specific peaks also shift due to the dielectric environment so only comparisons in the same solvent are reasonable.[25]

The photoluminescence (PL) of semiconducting nanotubes is also chirality specific and can be analysed to determine the composition of CNT solutions. Light is absorbed by the CNTs causing the material to rearrange in a higher electronic state. This exited state relaxes to a lower energy level or ground state by emitting a photon. Mainly fluorescence is observed in SWCNTs where the excited state undergoes rapid thermal energy loss through vibrations and the photon is emitted from the lowest singlet excited state (S_{11}). Metallic nanotubes don't show PL because of their overlapping valence and conduction band leading to non-radiative relaxation.

Figure 1.1.6A and B show the absorbance (solid line) and PL spectrum (dotted) of monochiral (6,5) or (7,5) samples for an excitation energy E_{22} associated with the S_{22} transition (570 nm or

650 nm). The photoluminescence excitation (PLE) maps in Figure 1.1.6C and D reveal only one emission wavelength corresponding to the fluorescence from the first optical transitions S_{11} (1000 nm and 1050 nm).

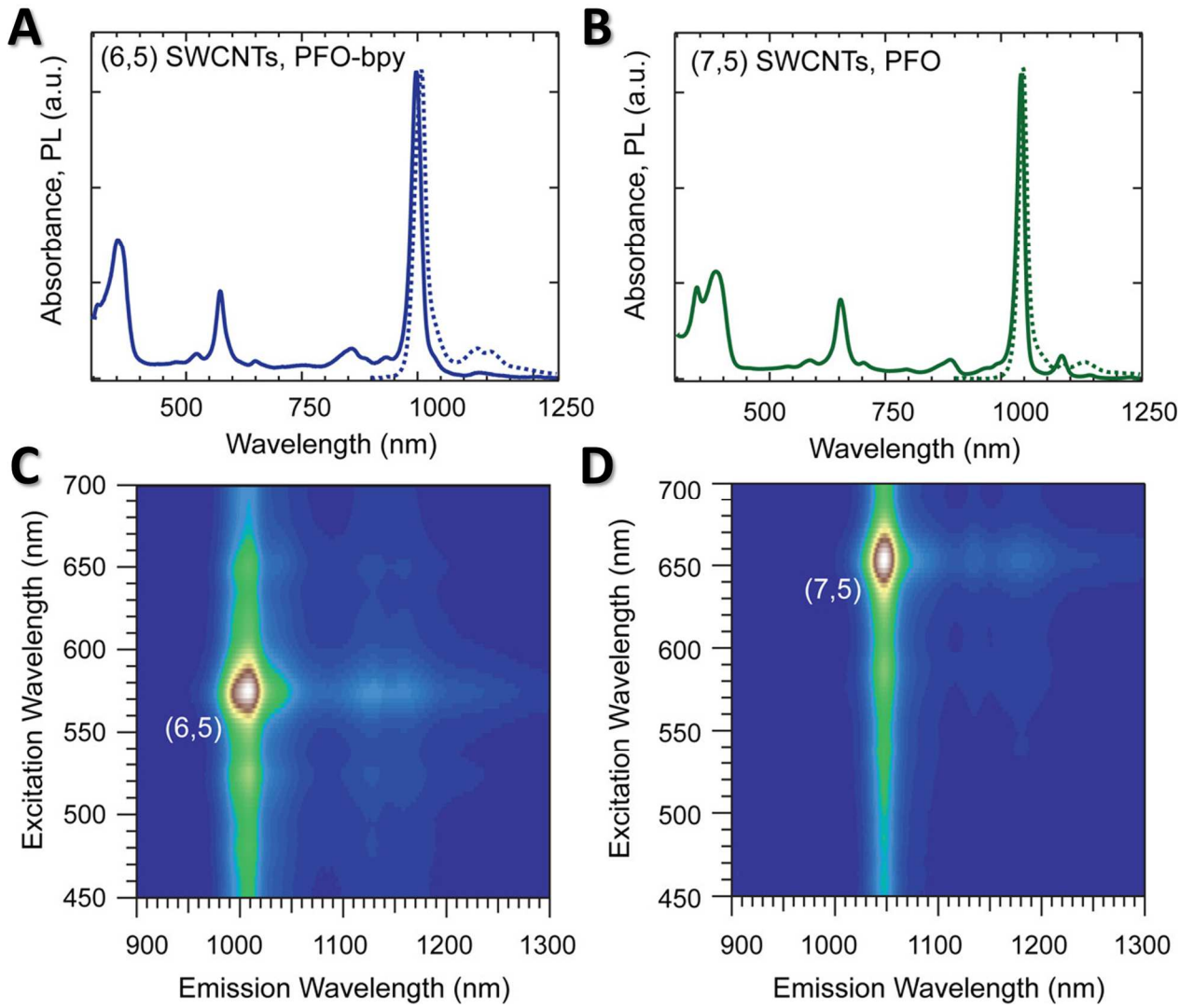

Figure 1.1.6: (A) Absorbance of (6,5)/PFO-BPy sample, with PL spectrum (dotted trace) obtained for E_{22} excitation at 570 nm. (B) Absorbance of (7,5)/PFO sample, with PL spectrum (dotted trace) obtained for E_{22} excitation at 650 nm. (C) PLE map of (6,5)/PFO-BPy and (D) of (7,5)/PFO sample.[26] *[Reprinted with permission from Hartmann et al. 'Photoluminescence Imaging of Polyfluorene Surface Structures on Semiconducting Carbon Nanotubes: Implications for Thin Film Exciton Transport', ACS Nano 2016, 10, 12, 11449, Copyright 2016 American Chemical Society.]*

1.1.4 Synthesis

There are basically three different processes to grow carbon nanotubes: arc discharge, laser ablation and chemical vapor deposition.[27] All techniques require the use of high temperatures, a carbon source and metallic catalysts which initialize the growth of the carbon nanotubes and control the purity, diameter or electronic type of the nanotubes.

The arc discharge process generates mainly multi walled CNTs by applying a DC voltage between two graphite rods. This creates an arc discharge between the rods and the anode is evaporated in the process at temperatures of 1000 – 2000°C. A plasma is formed between the electrodes, in which the particles are partially ionized.[28] MWCNTs remain on the cathode. If the anode contains catalysts such as nickel, iron or cobalt, single walled nanotubes with a diameter range of 1.2 - 1.7 nm are formed. Tuning parameters are the temperature as well as the size and composition of the catalysts. Nickel produces more crystalline nanotubes especially by adding a second transition metal, whereas iron is often combined with sulphur. The drawback of an Fe catalyst is the relatively easy oxidation and if these iron oxides once formed they are not catalytically active anymore.[29] A method for smaller nanotubes invented and developed by Smalley's group[30] is the evaporation of a graphite target by laser ablation in an inert atmosphere at a certain temperature. On the surface of the graphite a plasma is created and the evaporated carbon clusters or atoms are carried with argon flow to a cooling finger where they adsorb.[28] Thess et al.[31] managed to form SWCNTs with a narrow diameter distribution around 1.4 nm by using the laser ablation technique and a nickel-cobalt catalyst at a fixed temperature.

One drawback of these first two synthesis techniques is that they are not a high throughput process. When the graphite is depleted, the process must stop, and the rod or target source has to be renewed. In industry a continuous process such as chemical vapor deposition (CVD) is preferred. The small carbon nanotubes can be achieved by use of CVD where the carbon source is a carbon feed gas instead of graphite. The hydrocarbon feed gas, like acetylene or ethylene, contains either the required catalytic particles or the stream is passed above a substrate with a layer of catalyst. The hydrocarbons decompose at lower temperatures than their decomposition temperature because of the catalytic reaction.[32] The growth is induced by supersaturation followed by precipitation of carbon with metallic catalyst and during this process the catalytic particles either stay at the bottom (e.g. iron) or move up as a tip of the nanotube (e.g. nickel). Whether the grown carbon nanotubes are multi or single walled depends on the particle size and the temperature. Below 850°C the formation energy of MWCNTs is higher than for SWCNTs. In the case of single walled nanotubes their diameter is directly related to the particle size,[32] thus CVD is the most controllable and scalable method for industry.

The widely known HiPco material is produced by a modified CVD process using high pressure carbon monoxide (30-50 atm) and iron carbon monoxide $Fe(CO)_5$ as catalyst. Additional iron in

the carbon monoxide flow leads to decomposition of $Fe(CO)_5$ and formation of iron clusters which are the actual catalyst of the reaction. This method produces a large amount of defect free SWCNTs in a diameter range of 0.6 - 1.3 nm.[33]

The raw material CoMoCAT® contains mainly small CNTs with a mean diameter of 0.78 nm enriched in (6,5) or (7,5). The CoMoCAT® process is based on the catalytic chemical vapour deposition and is performed in a fluidized bed reactor. This enables in situ formation of the catalytic sites with high precision, which allows superior purity and control of structure such as 95% semiconducting CNTs with approximately 40% of those nanotubes being (6,5) chirality.[34]

All these methods are facing one problem, the growth of mixtures containing metallic and semiconducting nanotubes typically in a ratio of 1:2. Chiral specific growth is an ongoing research topic with new designs of bimetallic solid alloy catalysts [35, 36] or approaches in nanotube cloning of single chirality seeds.[37] Bottom up synthesis is using carbonaceous precursors formed as end-cap to create a limited number of chiral species.[38] However, the only opportunity to achieve high purified single chirality SWCNTs is the sorting of commonly prepared nanotubes.

1.1.5 Separation

To separate individual SWCNTs first a suspension of the black nanotube powder in either organic or aqueous solvents is necessary. This requires a modification of the outer walls, which can be covalent [39] or non-covalent, e.g. polymers or surfactants.[40-42] In this work, only non-covalent modifications of CNTs will be discussed because they don't affect the nanotube properties.

Sorting and dispersing nanotubes in organic solvents can be achieved by mixing the raw CNT powder with a polymer like poly(9,9-dioctylfluorenyl-2,7-diyl) (PFO), poly[(9,9-dioctylfluorenyl-2,7-diyl)-alt-(6,6'-(2,2'-bipyridine))] (PFO-BPy, see Figure 1.1.7A) or poly(9,9-di-n-dodecylfluorenyl-2,7-diyl) (PF12) in an organic solvent such as toluene. The mixture is exposed to ultrasound or shear-force (Figure 1.1.7B) followed by centrifugation to remove bundles and non-dispersed nanotubes.[40, 43, 44] The combination of commercially available polymers such as PFO-BPy with SWCNTs of a specific diameter range like CoMoCAT® allows (n,m) selective separation.[44] Moreover PF12 was found to disperse even large diameter nanotubes in comparison to PFO with its shorter side chains, on the other hand the rigid back bone complicates wrapping the smallest SWCNTs.[45]

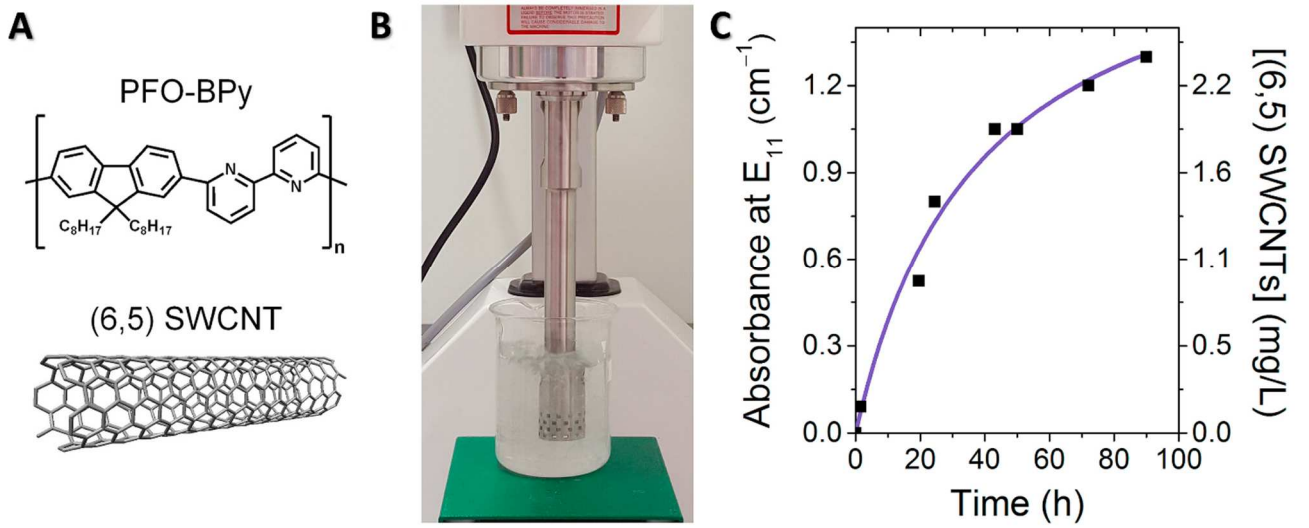

Figure 1.1.7: (A) Molecular structure of the copolymer PFO-BPy and a (6,5) SWCNT. (B) Labscale shear-force mixer used for dispersing SWCNTs in toluene by polymer wrapping. (C) Time dependence of the absorbance at E_{11} and corresponding carbon concentration for (6,5) SWCNTs during SFM.[44] *[Reproduced from Carbon, Graf et al. 'Large scale, selective dispersion of long single-walled carbon nanotubes with high photoluminescence quantum yield by shear-force mixing' 105, 593-599, 2016, under Creative Commons license agreement from Elsevier.]*

The advantage of polymer wrapping is to selectively sort semiconducting carbon nanotubes from their metallic counterparts and to adapt polymers to wrap near-monochiral or monochiral SWCNTs like (6,5) or (7,5).[44, 46] Despite the high selectivity for these two species, the method is limited to special enriched raw soot and the yield of separation is often low, while PFO and its derivates are expensive.[21] Though the conjugated polymers are essential for dispersion and sorting, it is highly desirable to remove them as they limit the electronic properties of the device. The so-called metal-chelation-assisted polymer removal process is based on a Rhenium salt dispersed in the toluene sample which enables complexation of the polymer. At temperatures above 100°C, selective thermal degradation of the polymer into oligomers facilitates the metal complexation reaction.[47, 48]

Polymer sorting can afford long SWCNTs up to 2 µm with low defect density[44] and the extraordinary high semiconducting content (> 99.99 %)[49, 50] especially by the gentle shear-force mixing. In applications the lower exciton quenching facilitates longer lifetimes and higher quantum yields. The SFM technique can yield quite high concentrations of those SWCNTs, however the process is time consuming with durations of several days as shown in Figure 1.1.7C. In addition, the tailorable optical and electronic properties of SWCNTS cannot be provided by polymer extraction. Over the last decade, researchers only identified a handful polymer/nanotube pairs to separate specific (n,m) chiralities[40, 50-52] which are highlighted in Figure 1.1.8 as pink shaded honeycomb.

Aqueous based methods yield more different single chirality semiconducting carbon nanotubes in larger amounts without tailoring special polymers. Figure 1.1.8 shows all (n,m) species currently accessible by aqueous sorting with yellow and cyan surrounding. Additionally, aqueous techniques can separate metallic SWCNTs[42, 53] as well as enantiomers.[54-56] Besides lower semiconducting content and comparatively shorter nanotubes[44], this method is more complex than polymer sorting.

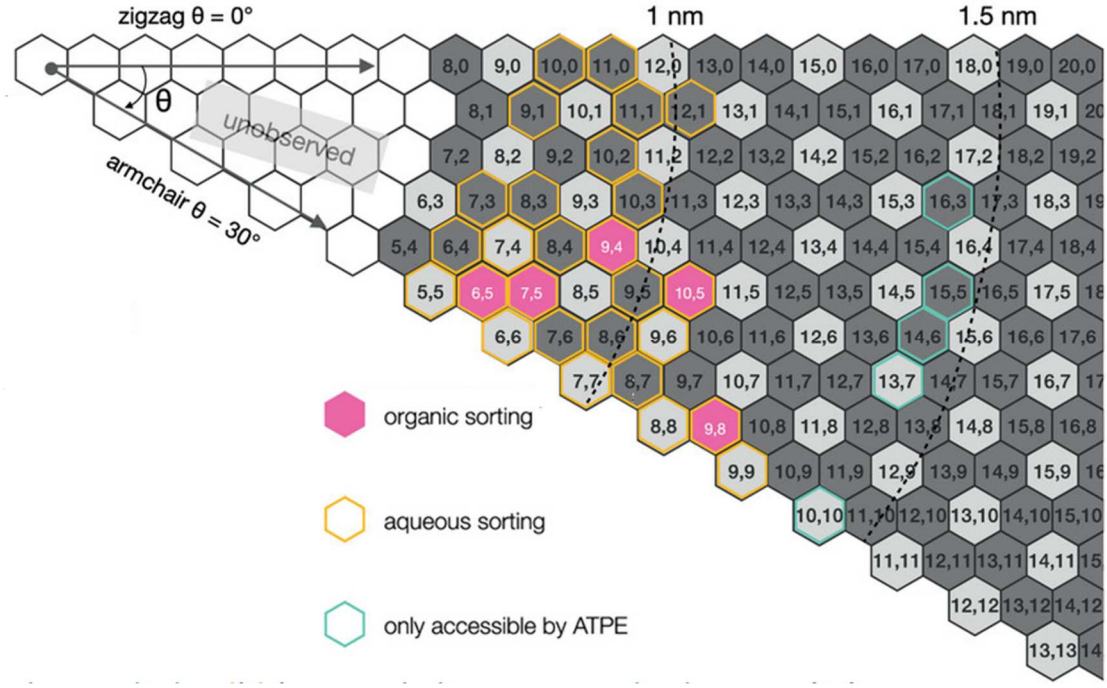

Figure 1.1.8: Theoretically possible (n,m) species in the diameter range 0.6–1.5 nm separated by organic (pink shade) and aqueous (yellow and cyan surrounding) sorting techniques.[21] *[Reproduced from Advanced Energy Materials, Wieland et al. 'Carbon Nanotubes for Photovoltaics: From Lab to Industry' 11, 3, 2021, under Creative Commons license agreement from Wiley-VCH GmbH.]*

The complexity arises from the non-specific surfactants like sodium cholate (SC), sodium deoxycholate (DOC) or sodium dodecyl sulfate (SDS) that disperse all chiralities of the raw material. [57-59] The separation of single chiralities have to be performed in solution, where the wrapping with surfactant molecules is influenced by their concentration, the nanotube diameter[60], the electronic type of the CNTs[61], temperature and pH.[62] The non-specific surfactants display small structural differences in their coating around the nanotubes tuning the interaction with the separation medium.[63]

SDS in low concentrations is known to lay with its hydrophobic tail parallel to the axis of small diameter nanotubes and leave larger uncoated regions which are exposed to the solution. Increasing the SDS concentration gives rise to the formation of disordered rings of adsorbed surfactant at the already coated parts of the SWCNT, while the other uncoated regions are

preserved. The larger diameter SWCNTs are generally more covered than the smaller nanotubes due to their lower energetic penalty for off-axis wrapping .[64] The disordered coverage and the orientation of the hydrophobic tail along the tube axis leads to a hydrophobic structure of the coated CNT.[65] DOC and SC instead are predicted to point their hydrophilic side into solution and the hydrophobic face on the CNT.[59] DOC selectively interacts with small diameter SWCNTs and thus reveals a higher coating[66], whereas SC preferentially covers the large diameter ones.[67] Moreover, SC has been found to be selective to large-chiral-angles[66] which is not observed for DOC. In surfactant mixtures it has been shown that DOC can displace SC which is capable of displacing SDS.[61] These differences in the surfactant shell adjust the interaction of the nanotubes with the separation medium[63] and determines the dielectric environment that strongly influences the optical properties of CNTs. The removal of surfactants is desirable for applications, however the standard high temperature annealing still leaves residues and can oxidize small diameter CNTs. A cleanly removable surfactant is ammonium deoxycholate (ADC), it disperses as good as DOC and decomposes already at 70°C by sublimation in Argon.[68]

Several methods for isolating chirality specific SWCNTs in aqueous solution have been developed such as gel permeation chromatography (GPC)[69], density gradient ultracentrifugation (DGU)[57, 70] or aqueous two-phase extraction (ATPE).[65] GPC is known to be highly sensitive to different surfactant coating of the CNTs and can separate electronic type[69], as well as enrich CNTs with specific chirality.[41, 71] However, the inhomogeneous gel packaging, non-specific adsorption, loss of CNT material in the column and other issues as well as the slightly differences of coverage around CNTs often result in an overlap of chiralities upon elution.[72] The DGU separation is based on the centripetal force in a fluid medium with varying density and during the ultracentrifugation the nanotubes enrich in layers due to their buoyant densities.[57] This process is also sensitive to the surfactant wrapping of the SWCNTs which can be used for isolation of specific chiralities.[70] A drawback of DGU is the limited yield depending on the centrifuge and centrifuge tubes, also the method is time intensive and expensive.

Aqueous two-phase extraction (ATPE) is currently the fastest and thereby most scalable technique to sort different kind of nanotubes with high sensitivity.[65] In principle the CNTs are exposed in two immiscible phases that separate spontaneously. Aqueous solutions of polyethylene glycol (PEG) and dextran are commonly used as shown in Figure 1.1.9A. The separation is based on the different solvation energy of the hydrophobic, PEG enriched, top phase and the hydrophilic,

dextran rich bottom phase for CNTs [59] due to their surfactant coverage.[73] A completely SDS-covered SWCNT will be for example in the PEG, whereas DOC or SC coated nanotubes are in dextran-phase, as illustrated in Figure 1.1.9B.

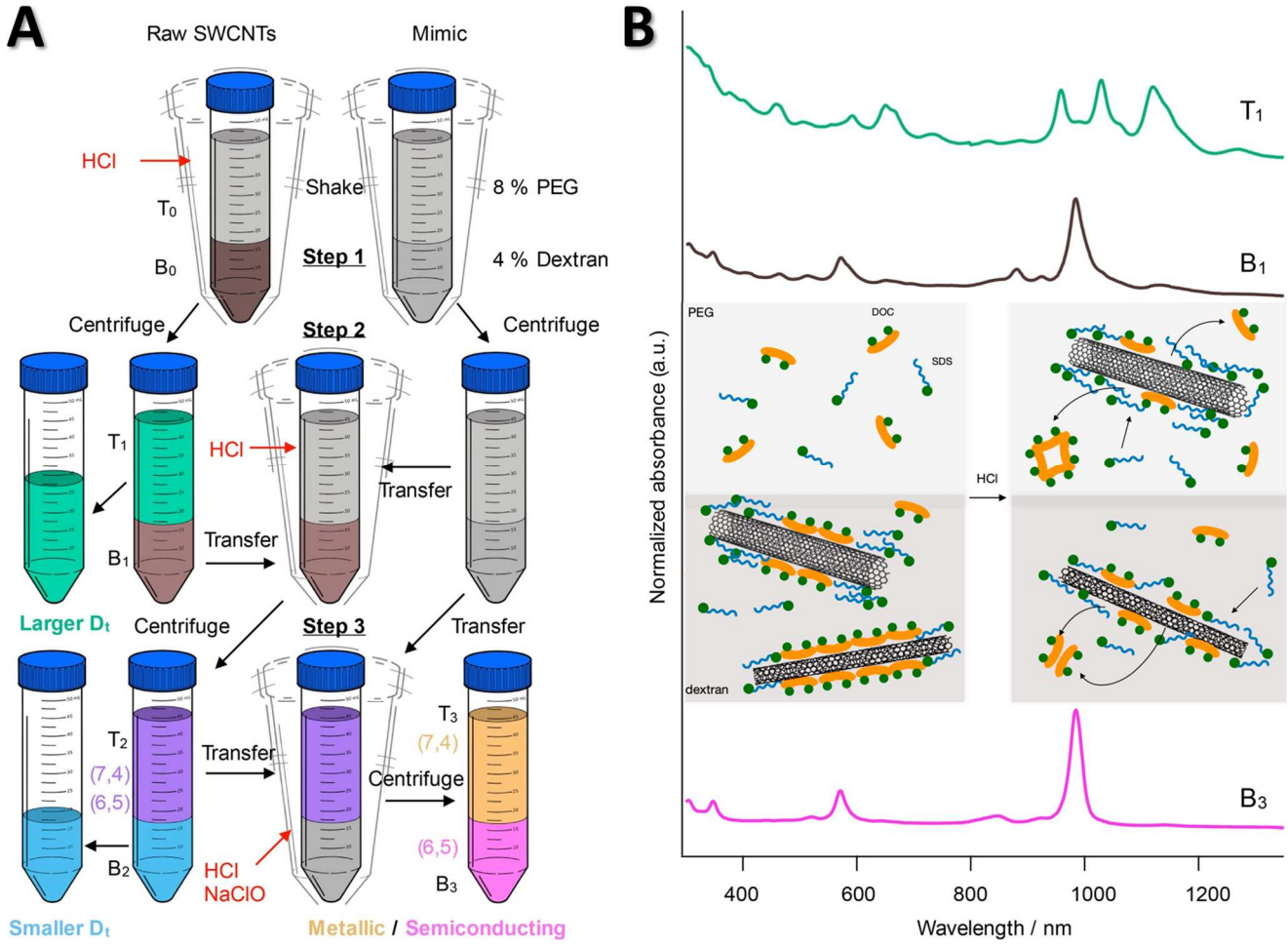

Figure 1.1.9: (A) Experimental ATPE of (6,5) and (7,4) from CoMoCAT® raw material. (B) Absorption spectra of the first and last separation steps with B_3 the pure fraction of (6,5). Inset: Proposed mechanism for pH-driven ATPE showing small and large diameter CNTs wrapped in SDS/DOC before and after the addition of HCl. While DOC becomes aggregated, it is replaced by SDS pushing the nanotubes into the top PEG phase.[42] *[Reprinted with permission from Li et al. 'Separation of Small-Diameter Single-Walled Carbon Nanotubes in One to Three Steps with Aqueous Two-Phase Extraction', ACS Nano 2019, 13, 2, 2567, Copyright 2019 American Chemical Society.]*

Basically, ATPE are multiple steps of removal and addition of a top or bottom phase that contains CNTs to a new opposing clean phase, for example, Figure 1.1.9A gives the detailed experimental steps necessary for (6,5) separation (pink line Figure 1.1.9B). The adaption of the surfactant coating for an optimized ratio of SDS/DOC/SC enables the separation of small [42] and larger diameter nanotubes.[54, 60] Adding strong oxidants or reductants[74], salts[73, 75] or changing the temperature or pH[42, 76] can influence the CNT distribution in the phases. Figure 1.1.9B displays small and large diameter CNTs wrapped in SDS/DOC before and after the addition of HCl which protonates the carboxylic acid on DOC leading to a dramatic increase in its aggregation.

Consequently, DOC is replaced by SDS that preferably wraps larger diameter SWCNTs driving them first into the hydrophobic top PEG phase.

There is no sharp distinction of phases and the concentration of PEG, dextran and surfactants in each phase is uneven distributed.[60] Trapping at the interface of the two phases occurs for high nanotube loads[73, 76] which hinders the industrial upscaling. For industry the multiple experimental steps must be automated, here counter current chromatography could be a solution.[77, 78] Currently, the separation purity is quite low with this automated CCC setup[77] due to problems with high viscosity components and low retention of the stationary phase.

In summary, separation of the CNT raw soot is necessary for many SWCNT applications.[9] Research efforts in carbon nanotube purification achieved sorting abilities according to the diameter,[57] length,[79] wall-number,[80] electronic property,[70] chirality,[42, 54] and even enantiomeric type. [54-56]

1.1.6 Filling Inner Volume of CNTs

A side effect of CNT dispersion as required by the aforementioned purification methods is the removal of the CNT endcaps, and this allows for spontaneous filling of their inner volume. In aqueous surfactant suspensions, water enters the nanotube cavity and affects the vibrational and electronic properties which depend on the diameter and chirality of the CNTs. Raman measurements can probe these changes in vibrational modes of CNTs which are unique for each chirality. Particularly metallic CNTs can be assigned by Raman due to the lack of PL measurements. The radial breathing mode (RBM) causes bond stretching meaning all carbon atoms move in the radial direction[20]. The Raman shift of this vibrational RBM mode is inversely correlated to the diameter and chirality specific.[81] Raman peak shifts can also be used to differentiate between open and closed carbon nanotubes because the open CNTs tend to be filled which hardens the radial breathing mode.

A study of quantitatively nanotube opening was published by Wenseleers et al.[82], which revealed that water-filled and empty nanotubes can be well resolved because the filling caused an upshift of the RBM even by measuring surfactant solubilized nanotubes. Figure 1.1.10 displays the details in the 2D Raman maps of (A) as-received raw SWCNTs and (C) air oxidized plus acid treated

SWCNTs that were recorded over the range of 755 to 835 nm in D_2O and DOC. Four main types of SWCNTs were identified in the samples where each type shows a pair of Raman peaks that are shifted in vibrational as well as electronic frequency. For (9,7) with frequencies around 218 cm^{-1} and (10,5) with 228 cm^{-1} distinct differences with and without treatment are observed.

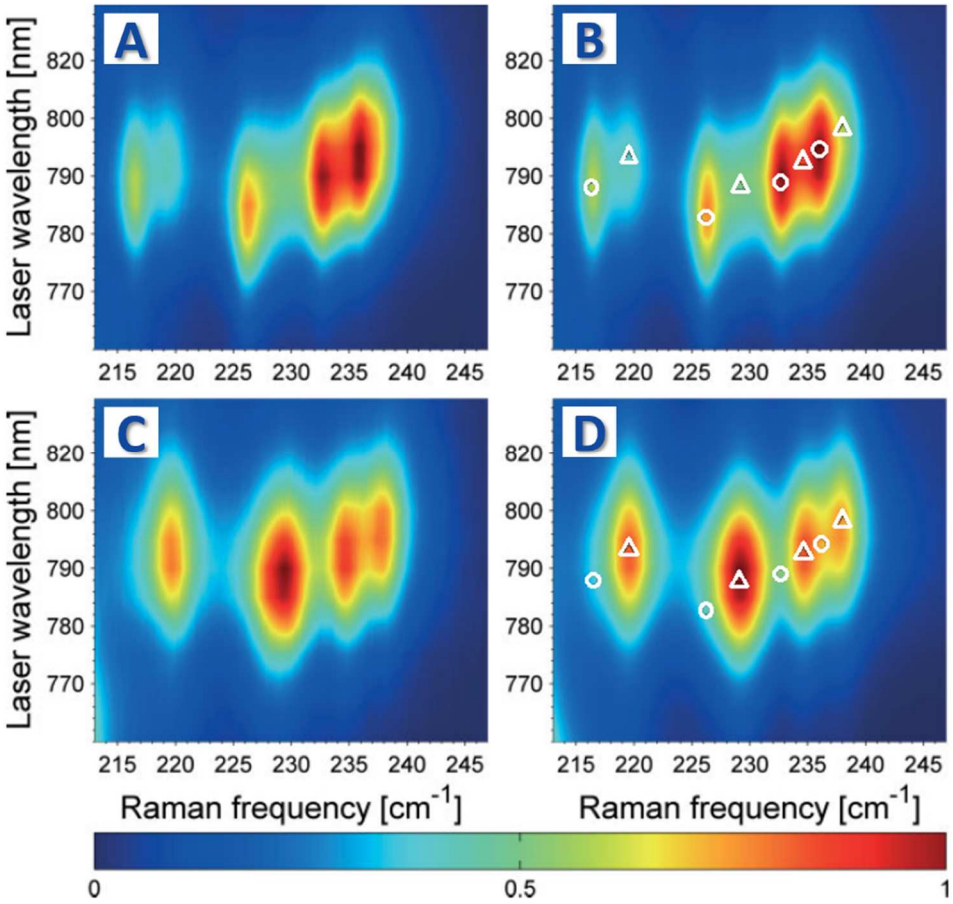

Figure 1.1.10: 2D Raman map of (A) raw or (C) air oxidized and acid treated SWCNTs with the corresponding fitted data (B,D) for (9,7), (10,5), (11,3) and (12,1) either empty (○) or D_2O filled (△) nanotubes.[82] *[Reprinted from Advanced Materials, Wenseleers et al., 'Effect of Water Filling on the Electronic and Vibrational Resonances of Carbon Nanotubes: Characterizing Tube Opening by Raman Spectroscopy', 19, 17, 2274, Copyright 2007, with permission from John Wiley and Sons]*

For the raw SWCNT sample, Figure 1.1.10B, the peaks at lower wavenumbers (○), which correspond to the empty CNTs, exhibit higher intensities than the peaks for water-filled nanotubes (△). The treated material in Figure 1.1.10D displays only the right upper peak of the pairs. These results confirm that in the raw material a large fraction of CNTs is closed and empty, while the treated SWCNTs are almost all open and thereby water filled. The external environment is for both samples identical, so this cannot be the cause of different Raman peak positions.[82] Briefly, air oxidation and acid treatment were found to be the most effective ways to obtain open CNTs, besides the ultrasonic treatment which achieves only partial opening depending on the exposure time. On the other hand high temperature vacuum annealing closes the nanotubes.[82]

The separation of the empty and water-filled fractions was examined by DGU[83, 84] and revealed that each chirality concentrates at two different densities which corresponds to empty and water-filled carbon nanotubes. The buoyant density of empty CNTs decreases with increasing diameter which allows the enhancement of larger nanotubes in the top bands as illustrated in Figure 1.1.11A.

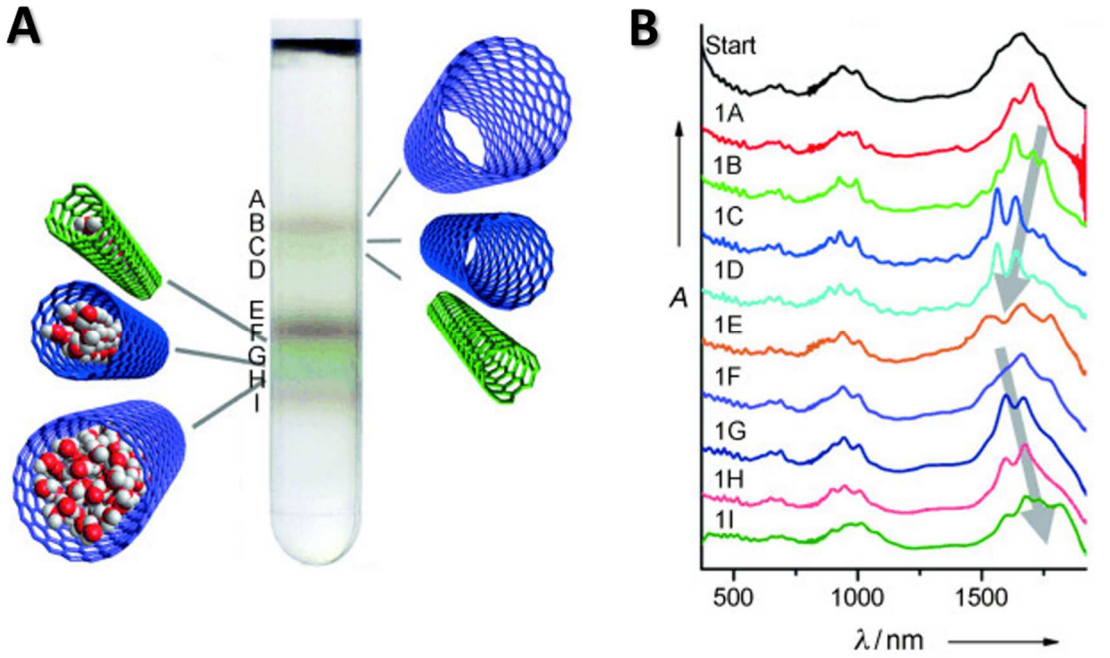

Figure 1.1.11: (A) Centrifuge tube containing empty and water-filled arc SWCNTs sorted by density gradient ultracentrifugation. (B) Absorption spectra of the original solution (black) and the sorted fractions.[83] *[Reprinted from Angewandte Chemie International, Cambré et al., 'Separation and Diameter-Sorting of Empty (End-Capped) and Water-Filled (Open) Carbon Nanotubes by Density Gradient Ultracentrifugation', 50, 12, 2764, Copyright 2011, with permission from John Wiley and Sons]*

Accordingly, the absorption peaks in Figure 1.1.11B display a blue-shift for bands with higher buoyant density. Water-filled SWCNTs show the opposite behaviour and therefore larger diameters are enriched in the bottom bands, though the density of water-filled nanotubes becomes essentially constant at large diameters. The red shift arises from the water with its high internal dielectric constant. Moreover, the electronic and vibrational transitions of the SWCNTs that are already sharp due to their regular, unperturbing bile salt micellar coating[85], became even more narrow for empty nanotubes and much broader for water-filled CNTs.[82, 86]

Solvent filling was established by Campo et al.[25]. The so called liquid-phase filling is based on the immersion of CNTs in solvents leading to specified filling. The filled SWCNTs can be used as parent material for typical aqueous or non-aqueous dispersion and separation processes.[87] The separation yield is depending on the filling for polymer extraction, partially filled SWCNTs achieve higher yields than completely filled ones and the best yield was obtained for empty SWCNTs. One

explanation for low (6,5) yield from CoMoCAT® is simply that it contains only few empty and completely closed carbon nanotubes in the raw material.[87] The simplicity and generality of the liquid-phase filling enables precise and controlled material modification for improved optical or modified properties. Water is known to fill even extremely thin diameter CNTs (d = 0.548 nm),[86] whereas larger molecules exhibit a size dependent threshold.[25]

Encapsulation of linear and cycloalkanes was achieved through the liquid-phase technique[25], followed by rinsing with a good solvent to remove the excess filling molecules. The absorption spectra of alkane-filled SWCNTs are represented in Figure 1.1.12A with the optical transitions related to S_{11} (1400-2000 nm), S_{22} (850-1200 nm), M_{11} (600-800 nm) and S_{33} (450-550 nm). The peak position of the alkane filled CNTs falls between the empty and the water-filled signals. (Figure 1.1.12B)

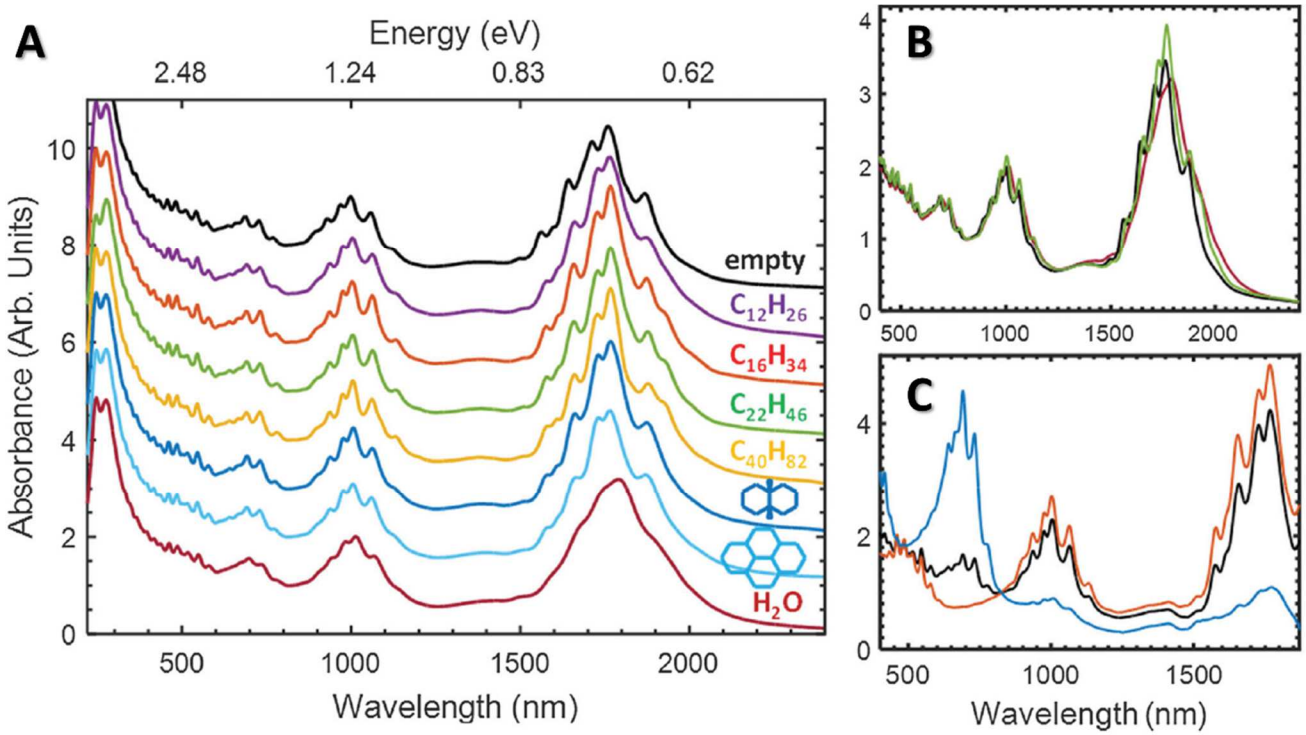

Figure 1.1.12: Absorbance spectra of SWCNTs with different endohedral filling: (A) empty, dodecane, hexadecane, docosane, tetracontane, cis-decalin, perhydropyrene and water. (B) Alkane-filled nanotubes exhibit similar optical transition peaks that are intermediate in position and breadth to empty and water-filled CNTs. (C) Absorbance spectra of aqueous two-phase extraction isolated metallic (blue) and semiconducting (red) SWCNT populations of octadecane-filled SWCNTs (black).[25] *[Reproduced from Progress in Nanoscale Horizons, Vol 1, Campo et al., 'Enhancing single-wall carbon nanotube properties through controlled endohedral filling'317-324, Copyright 2016, with permission from the Royal Society of Chemistry]*

The measurements were performed in the same external environment so the peak shifts can be assigned to the molecules inside the SWCNTs. In general, the sharpness of the alkane-filled peak features improves with increasing chain length due to their differences in molecular packing.[25]

The encapsulation of cis-decalin in smaller diameter CNTs and the corresponding shift in absorption is only observed for chiralities larger than (8,6) as confirmed by Raman and fluorescence measurements. Alkane-filling was found to be robust to separation procedures like ATPE and DGU, as illustrated in Figure 1.1.12C, the metallic and semiconducting species of octadecane-filled CNTs can be isolated by aqueous two-phase extraction.

The filling of linear alkanes into the endohedral volume of small-diameter SWCNTs at the threshold is found to apply expansive radial strain on the nanotube's hexagonal lattice.[88] SWCNTs with the same diameter but different chiral structure, like (6,5) and (9,1), were used to demonstrate the alkane filling when the size of the molecule approximates the size of the inner pore of the nanotube. In the absorption spectra in Figure 1.1.13 both blue and red-shifted peaks are observed, as well as peak sharpening for the alkane-filled sample.

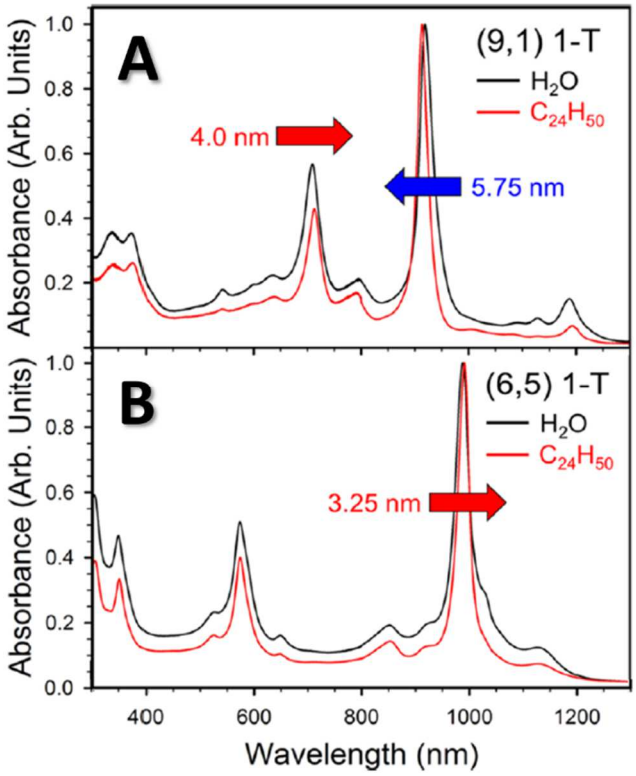

Figure 1.1.13: Absorbance spectra of identically processed single chirality (6,5) and (9,1) SWCNT dispersions filled with water (black line) or tetracosane (red line). For the S_{11}, (6,5) exhibits a red and (9,1) a blue shift, arrows indicate the direction of the peak shift from water- to alkane-filling.[88] *[Reprinted with permission from Streit et al. 'Alkane Encapsulation Induces Strain in Small-Diameter Single-Wall Carbon Nanotubes', J. Phys. Chem. C 2018, 122, 21, 11577, Copyright 2018 American Chemical Society.]*

Hypotheses for the different shifts include (1) the breakdown of the continuum (bulk) dielectric effect for highly confined molecules, (2) non-bulk arrangement of the filler molecules within the SWCNTs leading to an effective dielectric environment very different from the bulk value, and (3) application of strain to the nanotube lattice. The first two effects are likely to be primarily

dependent on the degree of confinement, so it should be the same for two SWCNTs of the same diameter. Effective dielectric effects would cause all peak features to shift in the same direction. The application of strain should also depend on confinement but will additionally be affected by SWCNT's electronic band structure, and thus would apply different effects to two SWCNTs of the same diameter but a different chiral structure.[88] This applies to SWCNTs of semi-type I or type II, for which optical transitions are predicted to shift in opposite directions.[89]

Figure 1.1.13 shows the absorption spectra of (6,5) and (9,1) filled with water or the alkane tetracosane, $C_{24}H_{50}$, in contrast to the results of Campo et al.[25] each SWCNT chirality is pure. Streit et al.[88] exhibit that the direction of the peak shift is correlated with semi-type of the nanotube. Whereas (6,5) with semi-type I displays a red shift in S_{11}, the (9,1) as semi-type II SWCNT displays a blue shift. S_{22} peaks are observed to shift in the opposite direction of the S_{11} or just slightly. The results are in accordance with effects caused by strain on a nanotube[89] and could not be explained by a diameter-dependent mechanisms.

The strain effect is dominant for CNTs near the sieving diameter, in contrast, the dielectric effect is dominant for larger diameter CNTs. By encapsulating any molecule into a carbon nanotube strain should be considered as an important factor especially by molecules close to the sieving size of the SWCNT cavity.

1.1.7 Film Preparation

Separated and optionally filled single walled carbon nanotubes can only be incorporated into applications e.g., solar cells, if films or layers are prepared from the CNT dispersions. The different dispersants enable film formation for either aqueous or organic solutions but in all solvents SWCNT concentration is a key parameter. The challenge is to find a technique that is controllable and reproducible in morphology and thickness.

The use of organic solvents simplifies film formation because dispersions can be deposited directly on the device with dip-coating[90], doctor blading,[46] spin-coating,[91, 92] or ultrasonic spraying.[93] Among the simplest and oldest methods of CNT film formation is dip coating (Figure 1.1.14A), here the substrate is immersed in a reservoir containing a CNT dispersion followed by withdrawal and drying. To reduce the dead processing time between the dips, mainly

highly volatile solvents are used, such as chlorinated hydrocarbons or low-molecular-weight alcohols. The key drawback of dip coating is the lack of uniformity in the CNT film due to gravity the film is thicker at the end that was injected deeper into the CNT reservoir.[94] To alleviate this problem, doctor blading can be employed. Here the dispersion is in between the substrate and the blade which is moved with constant speed to spread the solution. The distance of the blade to the substrate and the speed allows to control the film thickness.[46] However, thin films are quite challenging especially uniform areas larger than 0.04 cm^2. A high concentrated SWCNT dispersion is fundamental for the doctor-blading. The same applies to spin coating (Figure 1.1.14B) which relies on controlling the rotation speed and duration of casting.[92] Unfortunately, the excess material is often wasted to reach homogeneity.

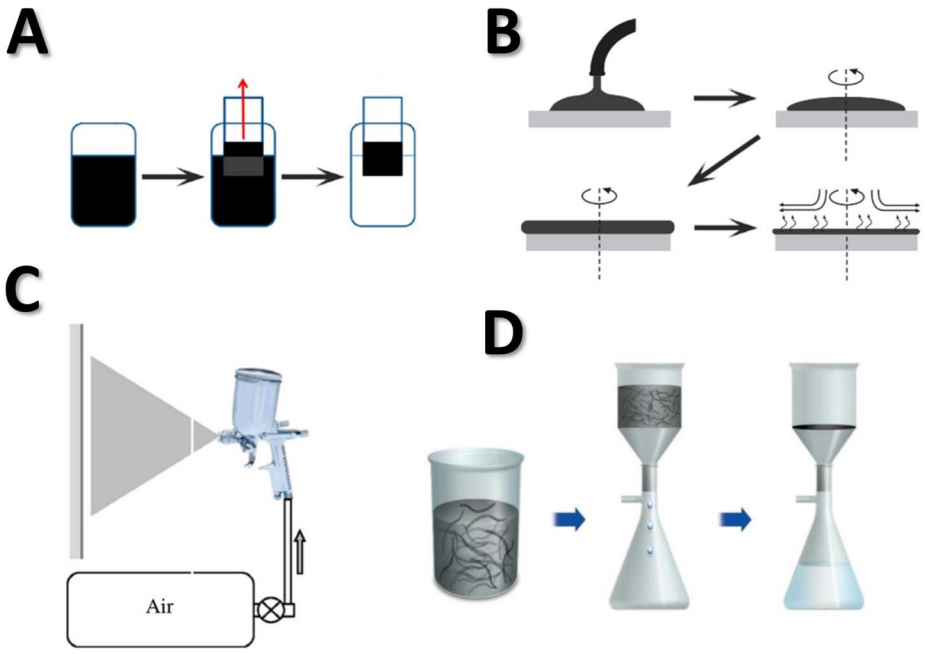

Figure 1.1.14: Overview of techniques to produce carbon nanotube films: (A) dip coating (B) spin coating (C) spray coating (D) filtration.[94] *[Reproduced from Energies, Rdest et al. 'Carbon Nanotube Films for Energy Applications' 14, 7, 2021, under Creative Commons license agreement from MDPI.]*

Spray coating (Figure 1.1.14C) is able to produce homogeneous larger area films with less waste but with a relatively low density compared to the other methods.[93] The CNT dispersion is hereby pushed through a small needle with compressed gas creating a fine mist of CNTs that readily deposit onto the substrate.[94] The advantage of organic SWCNT dispersions is the direct incorporation of the films into the layer stack of the electronic devices, nevertheless the solvent sequence is important to prevent dissolution.

The use of aqueous-surfactant CNT dispersions has been considerably more difficult. Material incompatibilities usually prohibit that films from aqueous dispersions can be incorporated

directly, only spray coating was demonstrated to work for direct application.[95]. Films are normally prepared separately by filtration (Figure 1.1.14D) and laminated onto the device by either dissolving a membrane[96, 97] or through wet-transfer processes.[98] Typically, a CNT dispersion is passed through a membrane with appropriate porosity. The liquid medium permeates across the membrane, whereas the filter captures the CNT filter cake. The process is commonly facilitated by employing pressure on the funnel or vacuum in the receiving flask. One of the disadvantages of filtration is the deceleration of the process with increasing film thickness.[94] To separate the nanotube film from the membrane, a filter type to which CNTs have low adhesion (e.g. PTFE) is preferred. Alternatively, a dissolvable membrane made of polycarbonate, mixed cellulose esters or alumina can be used, which upon contact with an organic solvent or NaOH, readily disintegrates. Dissolving alumina membranes with NaOH base in aqueous solution allows to dilute and replace the base with water afterwards, ending up with a clean floating CNT film due to the water surface tension.[96] It is difficult to transfer the floating film onto the device in the correct position without any wrinkles. In the case of mixed cellulose ester[99] or polycarbonate[97], the membrane is placed upside down on the substrate for direct contact to the CNT film before dissolution takes place. Arrangement of the film is therefore easier, but solvent or membrane residues can contaminate the layer stack.

In general, the type of residual species left on the device, or the nanotube sidewall are very different for aqueous and organic dispersions and these play an important role in energy transfer, exciton lifetime. For aqueous dispersions, the surfactants, especially the metallic cations, can usually be washed away with water and pristine films of CNTs are obtained, albeit the complete removal of the cations and residues of the membrane is often difficult to ensure. For organic dispersions a minimum polymer content is required to disperse the CNTs that ends up in the assembled device. Joo et al.[47] developed an unwrapping method by selective chelation of BPy to remove the PFO-BPy as post treatment process. Despite initial concerns that residual polymer content might be detrimental, it turns out to enhance the exitonic lifetime by shielding the nanotube from the surrounding environment.[26, 100, 101] Thus polymer-wrapped SWCNTs reveal exciton lifetimes of ≈ 1 ps, while ATPE sorted SWCNTs achieve only ≈ 300 fs.[102, 103]

The anisotropy of SWCNTs results in another research topic for thin film preparation: the in-plane alignment of SWCNTs. Methods range from dry shear of vertically grown forests or mis-aligned films to Langmuir–Blodgett deposition, evaporation induced self-assembly, the use of magnetic

and electric fields, the stretching of SWCNT-polymer matrices, or the confined shear of nanotube dispersions. Drawbacks of these techniques are either the limited control of chirality by direct growth methods or only small area coverage and the need to remove dopants.[104, 105] Alignment was shown for organic polymer wrapped SWCNTs[106], however most techniques rely on aqueous sorted nanotubes because variability of single chirality samples exists. Vacuum filtration became the most attractive method due to the achievements by He et al. with wafer-scale films of high nematic order and with high density.[107] With this dead-end filtration technique, our group demonstrated global alignment with surfactant coated SWCNTs for accurately controlled flow rate conditions.[104] Despite parameter optimization, the alignment depends on the length and diameter of the nanotubes and their zeta potential.[105]

- this page left intentionally blank -

- this page left intentionally blank -

1.2 Solar Cells

The energy demand of the world is growing fast, it is therefore one of the greatest scientific challenges to develop energy sources or techniques to satisfy those future demands. Carbon-free or carbon-neutral energy sources such as nuclear, geothermal, biomass, wind or solar radiation will contribute together to the future energy mix to meet climate goals. Using sunlight to produce electrical energy has been demonstrated to be one of the most promising solutions to the world's energy crisis because the sun is a source of abundant energy. Only a small portion of the large amount of solar energy is utilized today, in principle all the sunlight reaching the earth could be capable of fulfilling even the complete increasing energy demand on its own.

Solar cells have aroused attention as clean energy source due to their light harvesting ability while being easy to install everywhere. Silicon solar cells are best known because they are installed on rooftops all over the world. These inorganic solar cells still dominate the market due to the silicon's abundance in semiconductor industry and the high stability of the cells. Rapid advances in emerging fields have led to high efficiencies of third generation solar cells like perovskite devices that are already comparable to silicon solar cells. Organic photovoltaics are also catching up with regard to efficiency, in the last 5 years they have developed from 12 % to over 18 % based on new organic semiconductor materials. The organic solar cells rely on type-II heterojunctions while the silicon devices are working on another principle called pn-junction. Thus, the designs are different for organic and inorganic devices.

1.2.1 Inorganic Solar Cells

Inorganic solar cells consist of one or more semiconductors with covalent bounds in a repeating crystal structure, forming valence and conduction band. The working principle is based on the photovoltaic effect at the electron (n) or hole doped (p) semiconductor interface, called pn-junction.[108] The photovoltaic effect includes three essential steps, first the absorption of photons in the semiconductor crystal generating significant numbers of free charge carriers. If the photon energy is higher than the bandgap E_g of the doped semiconducting material, this energy can excite an electron from the valence to the conduction band. A void (hole) emerges at the valence band. The excess energy larger than the band gap of the semiconductor is given as additional kinetic energy to the electron and hole or dissipated as heat. Secondly, photo-generated charges have to be separated. The holes flow through the p-region and the electrons across the n-region to the

metal contacts in an external circuit as illustrated in Figure 1.2.1A. Finally, the electrons generate a current flow in an electric circuit, then move back to the positive contact and recombine with the holes. In general, the n-type region is designed thinner than the p-type, to facilitate the electron transport through the circuit before they can recombine with holes. Besides, an anti-reflective coating is applied over the n-layer to reduce surface reflection and enhance the transmission of the light to the semiconductor material.[109]

In principle a solar cell is a semiconductor diode made of a single crystal semiconducting material like the widely used silicon. In a solid crystal, each silicon atom shares each of its four valence electrons with another nearest silicon atom, hence creating covalent bonds. Light absorption of this silicon crystal can excite electrons of covalent bonds generating free electrons; however, doping is necessary to create a potential barrier and supress recombination. Silicon that is doped with phosphorous forms a n-type region due to its 5 valence electrons one more than silicon. The fifth phosphorous electron is loosely bound and can be donated even at room temperature, leading to excess negative charges. Whereas the p-type side is doped with boron a trivalent molecule, creating unpaired valence electrons in the silicon or vacancies. This doping process creates additional mobile carriers called majority carriers in the respective region.

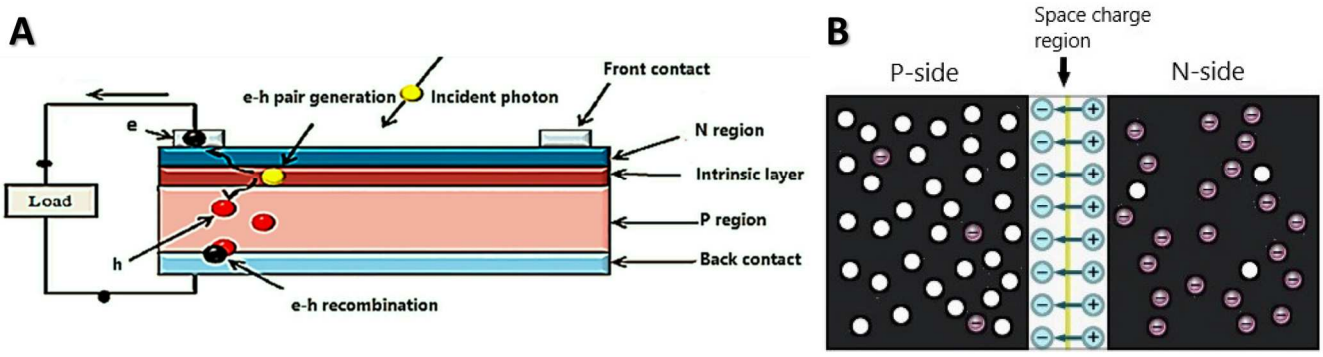

Figure 1.2.1: (A) Schematic of an inorganic pn-junction solar cell with electron (n) and hole (p) doped regions creating a space charge region or intrinsic layer in between. (B) Instant formation of the space charge region by direct contact of p- and n-doped semiconductors generating an electric field. [109] *[Reproduced from Applied System Innovation, Al-Ezzi et al. 'Photovoltaic Solar Cells: A Review' 5, 4, 67, 2022, under Creative Commons license agreement from MDPI.]*

When n- and p-region semiconductors are brought into contact, the free electrons will diffuse from the n-section into the p-section leaving a region of positively charged donor atoms at the p-n interface near the n-zone. The opposite is true for the diffusion of holes resulting in negatively charged acceptor atoms near the p-zone, as shown in Figure 1.2.1B. This creates a diffusion current and a depleted region of charge carriers also called space charge region. In other words, negative charge layer in the p-type side and positive charge layer in n-type side together form a barrier which opposes migration of charge carriers. If an external voltage is applied the depletion

region shrinks or the barrier potential is reached and electrons can flow again. Under illumination, the photons are absorbed by the n-type semiconductor on top of the pn-junction solar cell which generates electron-hole pairs, as already described. The electrons migrate to the front contact because of the repulsion of an electric field across depletion layer. Simultaneously, the holes cross the depletion region due to the attractive electric field and recombine with the electrons in the space charge region. The lack of electrons is compensated by valence electrons of the p-type material shifting the holes in the p-doped region where they are trapped by the repulsion of the potential barrier.[109]

Silicon solar cells (SSC) are basically designed around the substrate material, single or multi crystalline silicon, with thicknesses >200 µm. Although silicon has slightly to low band gap for optimum solar cells and is also an indirect semiconductor, the SSC dominate the market. The formation of a pn-junction requires to dope the base material and the front surface with opposing charges, in the early designs shown in Figure 1.2.2A p-type silicon is doped with phosphorous (n-region) by high temperature diffusion or ion implant. Besides the optimum thickness of the emitter layer and the correct dose of doping, the front surface is typically textured to increase light absorption while dielectric passivation with SiN_X prevents recombination. A metal grid on top is necessary to conduct all the generated charges because silicon's resistivity is so high. There is always a trade-off between the resistance of the metal grid and the shading area underneath.[108]

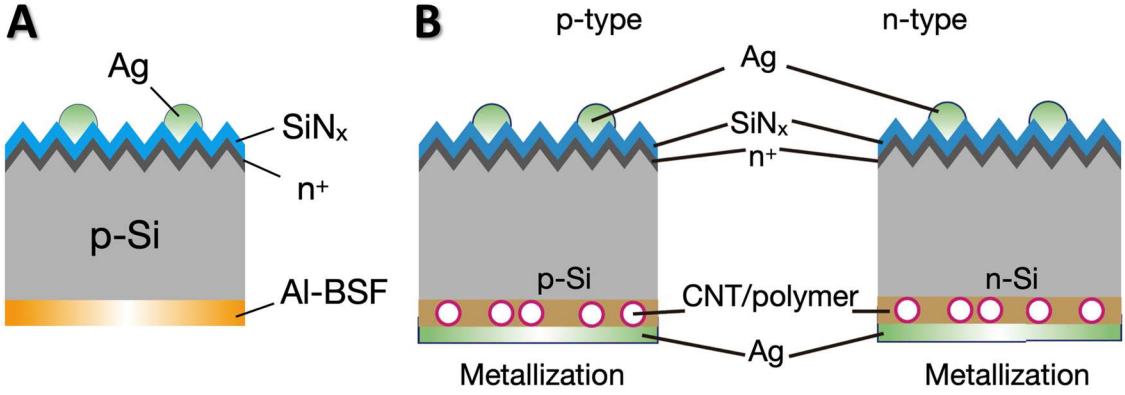

Figure 1.2.2: (A) Early silicon photovoltaic technology, so called Al-BSF cells and (B) design of silicon solar cells with CNT passivation contact for p or n-type substrates.[21] *[Reproduced from Advanced Energy Materials, Wieland et al. 'Carbon Nanotubes for Photovoltaics: From Lab to Industry' 11, 3, 2021, under Creative Commons license agreement from Wiley-VCH GmbH.]*

Power conversion efficiencies of up to 26.7 % are achieved due to several developments in passivation and interdigitated back contacts.[110, 111] Dopant free hetero contacts can replace the doped silicon layer, for example PEDOT,[112, 113] MoO_x[114, 115] or even CNTs.[116, 117] A hole selective contact to p- or n-type silicon is formed in the case of carbon nanotubes (Figure 1.2.2B).[21]

1.2.2 Organic Solar Cells

Approaching similar levels of efficiency as silicon solar cells, organic photovoltaic (OPV) gain acceptance through their more practical fabrication process, lower costs, flexibility etc. In contrast to silicon devices , organic solar cells rely on molecules that only show semiconducting properties if delocalized valence electrons are present. The valence and conduction band can have a band gap of maximum 4 eV afterwards it becomes insulating.[118] Before the organic solar cell architecture is explained in detail, the working principle is described based on the photovoltaic effect and charge separation with the aid of electrostatic potential energy.

The working principle of donor acceptor OPV is shown in Figure 1.2.3 and consists of four steps.

(1) Photon absorption and exciton generation: Sunlight enters the organic semiconductors and photons are injected resulting in excitation of an electron from the highest occupied molecular orbital (HOMO) to the lowest unoccupied molecular orbital (LUMO) of the donor material. The confinement of the electron and hole leads to the generation of a strongly bound exciton.

(2) Diffusion of excitons: Excitons diffuse from the donor material to the interface with the acceptor driven by the concentration difference.[119]

(3) Dissociation of excitons: Separation of the charges can only occur if the large exciton binding energy (E_b) can be overcome. The necessary dissociation energy is depending on the thermodynamic driving energy ΔG [120, 121]

$$\Delta G = (HOMO_D - LUMO_A) - (E_g - E_b) \quad (7)$$

with the indices D and A for the donor and acceptor molecular orbitals and E_g the electronic bandgap of the donor minus the exciton binding energy (E_b). If $\Delta G > 0$ charges can be separated. A simplified model focuses on the energetic offset between the lowest unoccupied molecular orbitals of the donor and acceptor as dissociation energy.[98]

(4) Transfer and collection of carriers: After charge separation at the interface, the electron is conducted through the acceptor to the cathode and the hole migrates through the donor layer to the anode. Finally, the charges are collected at the corresponding electrodes driven by the electric field which is determined by the work function difference of the anode and cathode materials.[119]

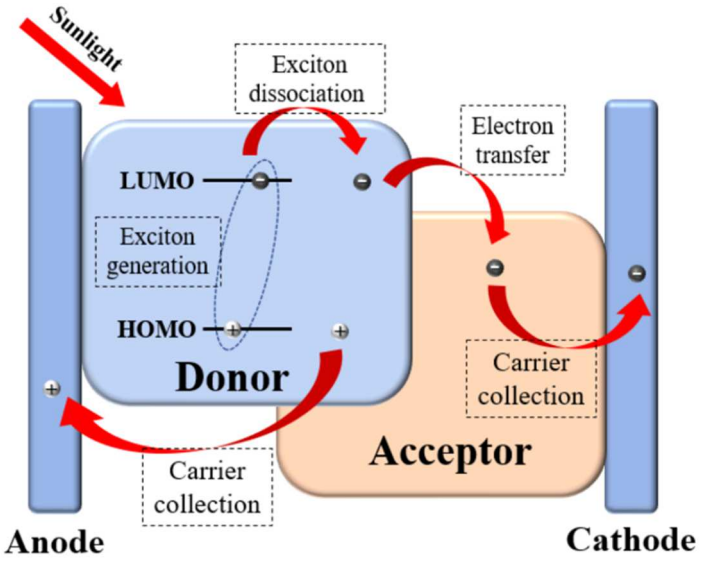

Figure 1.2.3: Working principle of donor-acceptor organic solar cells[119] *[Reprinted from Chemistry Asian Journal, Sun et al., 'Organic Solar Cells: Physical Principle and Recent Advances', 18, 5, Copyright 2023, with permission from John Wiley and Sons]*

The way of an exciton from generation to charge collection comprise many possible energy losses or recombination paths reducing the efficiency of the solar cell. Directly after exciton creation the bound electron-hole-pair can recombine. An appropriate driving force or LUMO offset for the dissociation is essential to minimize this geminate recombination of the charge carriers. Recombination of the charge carriers can also occur after separation. On one hand, a direct radiative recombination of an electron and hole involves the emission of a photon, which is the reverse process of the exciton generation. On the other hand, non-radiative energy loss is either an Auger recombination or indirect recombination. The Auger process requires a free electron and an exciton that transfers its energy and momentum on the negative charged particle before recombination. The excited electron thermalizes afterwards. Indirect recombination is a two-step process and occurs if first a free electron is trapped in a lower energy trap site for example dislocations, impurities, or surfaces, and secondly the electron relaxes into the HOMO. Measuring the open circuit voltage (V_{OC}) with various light intensities is one method to distinguish radiative and non-radiative recombination.[118]

Another intrinsic energy loss is reorganization. An excited molecule loses energy by its rearrangement due to vibrational or structural relaxation resulting in heat dissipation.[118] A kinetic model for electron transfer to/ from such excited electronic states is the Marcus theory[122], which describes the rate k_{ET} of an electron that pass over from one excited molecule (electron donor) to another (electron acceptor). On the molecular level, electron transfer involves (a) inner-sphere reorganization of bonds and atoms in the donor and acceptor and (b) outer-

sphere reorganization of the surrounding solvent molecules. Marcus stated that the inner- and outer-sphere motions happen synchronously leading to lower activation energy for the reaction. The electron transfer rate k_{ET} is depending on the reaction free energy (ΔG^0_{ET}). Figure 1.2.4A shows the potential energy surfaces of reactants $f_r(Q)$ and products $f_p(Q)$. In the normal region, ΔG^0_{ET} is smaller than the reorganization energy λ associated with the adjustment of the solvent after electron transfer.[123] If the driving force ΔG is increasing, k_{ET} is also increasing as illustrated in Figure 1.2.4B.

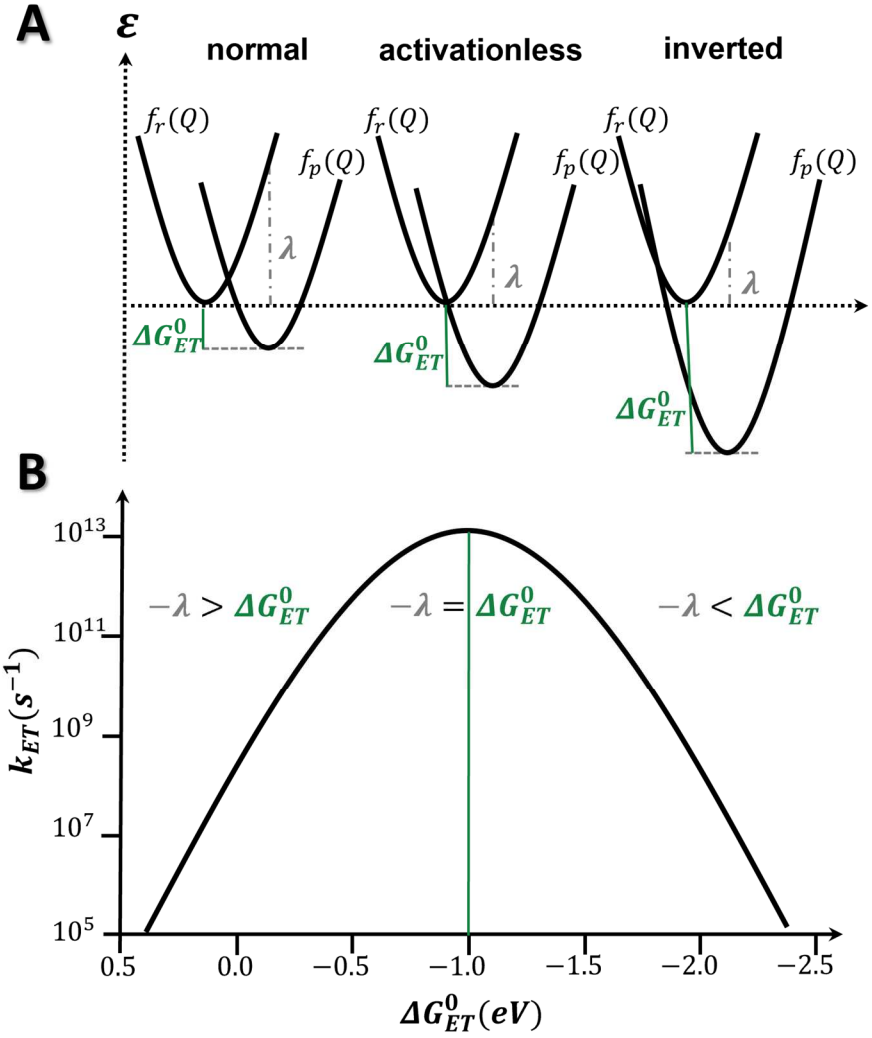

Figure 1.2.4: (A) Reactant ($f_r(Q)$) and product potential energy surfaces ($f_p(Q)$) for electron transfer in three different regimes; (B) dependence of electron transfer rates (k_{ET}) on reaction free energy (ΔG^0_{ET}). A reorganization energy (λ) of 1.0 eV was arbitrarily chosen.

The k_{ET} maximum is reached for $\Delta G^0_{ET} = -\lambda$ when the activation barrier is zero due to the intersection of $f_r(Q)$ and $f_p(Q)$ in the equilibrium position of $f_r(Q)$. If the driving force is further increased becoming larger than the absolute value of the reorganization energy, $\Delta G^0_{ET} > -\lambda$, an activation barrier reappears resulting in a decrease of k_{ET}. This counter intuitive trend is called

inverted driving force effect or Marcus inverted region.[123] Photoinduced electron transfer profits from this effect because the recombination or back electron transfer to ground states is so thermodynamically favourable that this reaction is prohibitively slowed down.

The basic designs for fabrication of organic solar cells can be split into two basic architectures focussing on the active layer: First is the bulk heterojunction (BHJ), here the donor and acceptor material are mixed to maximize the contact area, and the second option is a planar or bilayer device architecture. For both kinds of active layer design, the electrode on the front needs to be transparent for most wavelengths, such as indium tin oxide (ITO). While the backside electrode is usually reflective to scatter the light back into the solar cell and increase the light path. Between the electrodes and the active layer, normally hole or electron transport layers are prepared to prevent recombination, aid charge separation, and support the respective carrier transport. Typically, the transparent electrode is the anode, and the hole transport layer facilitates the corresponding charge transport. (Figure 1.2.5A) The inverted configuration in Figure 1.2.5B has a transparent cathode with an electron transport layer on top and the anode is a high work function metal.[124]

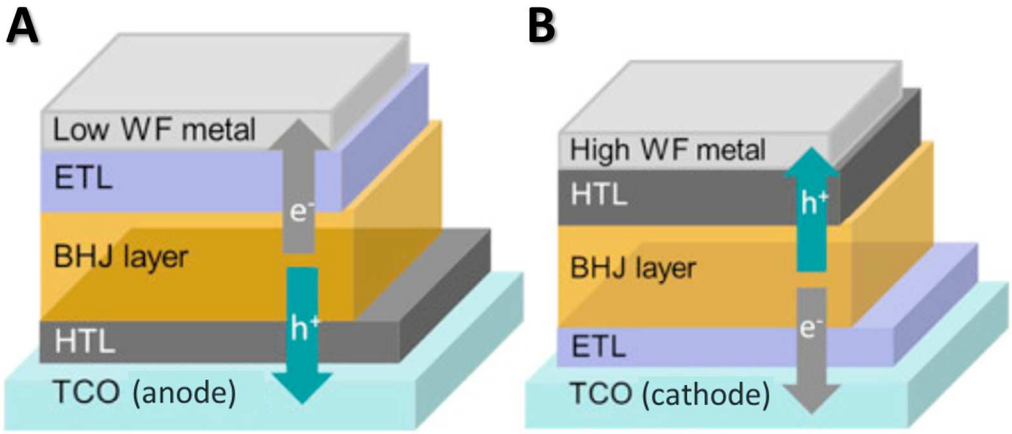

Figure 1.2.5: Schematic of conventional (A) and inverted (B) OPV device structure. Electron transporting layer (ETL) and hole extracting layer (HTL) are adopted to form ohmic contact and extract charges at cathode and anode respectively.[124] *[Reprinted from Materials Today, Vol 16, Lai et al., 'Properties of interlayer for organic photovoltaics', 424-432, Copyright 2013, with permission from Elsevier]*

1.2.3 Solar Cell Characterization

Solar cells are tested under '1 sun illumination' of a solar simulator, this light represents the AM1.5G spectrum of the sun including an incidence angle of 48° to the earth surface, absorbance losses due to water etc. and scattering or reflective processes.[118] The incident power shining on the solar cells is therefore set to 100 mW/cm^2.

The standard characterization of solar cells is sweeping a voltage while measuring the generated current all under 1 sun illumination, the so called current-voltage curves. (black line Figure 1.2.6) These JV-curves show representative parameters used to evaluate solar cell performance: The short circuit current density (J_{SC}) is the operating current of a solar cell at zero output voltage. The point at zero output current is called open circuit voltage (V_{OC}). The fill factor is a parameter for the loss due to resistance during a period. It can be calculated as the ratio of maximum output power (P_M) of the cell and the maximum power possible, defined by $J_{SC} \cdot V_{OC}$. Figure 1.2.6 visualizes this relation: Blue rectangular shows the maximum actual power output in relation to the red rectangular as maximum power possible.[119]

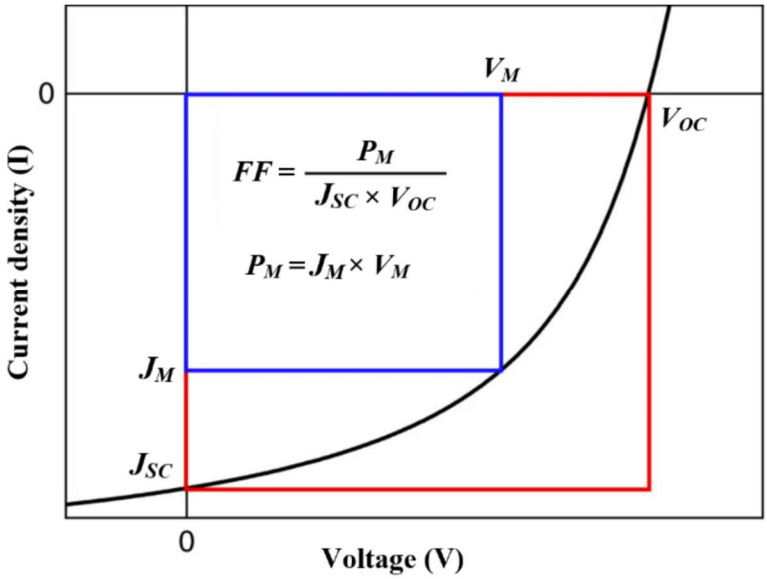

Figure 1.2.6: Output characteristic current density-voltage curve with representative parameters such as J_{SC}, V_{OC} and the calculation of the fill factor (FF). Blue rectangular shows the maximum actual power output in relation to the red rectangular as maximum power possible.[119] *[Reprinted from Chemistry Asian Journal, Sun et al., 'Organic Solar Cells: Physical Principle and Recent Advances', 18, 5, Copyright 2023, with permission from John Wiley and Sons]*

The power conversion efficiency (PCE) is the most common solar cell parameter and given as the ratio of the maximum output power (P_M) and the incident light energy (P_{in}).[119]

$$PCE = \frac{P_M}{P_{in}} = \frac{J_{SC} \cdot V_{OC} \cdot FF}{P_{in}} \tag{8}$$

The competition in the research field of solar cells is to gain the highest PCE. A higher energy production under the same light condition also results in better cost-benefit analysis.

Besides those characteristics of the JV-curve, the external quantum efficiency (EQE) is an important parameter to analyse which photon energies contribute to the photocurrent generation. Typical EQE measurements vary the wavelength (or energy) and record the corresponding

photocurrent. The definition of EQE is the ratio of the number of electrons that can be extracted by a photocurrent to the number of photons injected:[119]

$$EQE = \frac{N_{electron}}{N_{photon}} \, 100\% \tag{9}$$

where the photon flux is determined by a reference diode. The area under the curve of an EQE spectrum should be equal to the short circuit current density J_{SC} and is given by:[97]

$$J_{SC}^{EQE}(\lambda) = \frac{e}{hc} \int_{\lambda_1}^{\lambda_2} \lambda \cdot EQE(\lambda) \cdot AM1.5(\lambda) \, d\lambda = \int_{\lambda_1}^{\lambda_2} \frac{\lambda \cdot EQE(\lambda) \cdot AM1.5(\lambda)}{1.24} d\lambda \tag{10}$$

The conversion of electron volt into wavelengths is set by the elementary charge e, Planck's constant h and the speed of light c.

To account for differences in material absorption, the internal quantum efficiency (IQE) is defined as the ratio of the number of charge carriers generated to the number of photons absorbed, within the active layer of the device. It can be calculated from the EQE and the transmittance τ and reflectance ρ of the layers.

$$IQE\ (\%) = \frac{EQE\ (\%)}{1 - \tau(\lambda) - \rho(\lambda)} = \frac{EQE\ (\%)}{1 - 10^{-Abs(\lambda)} - \rho(\lambda)} \tag{11}$$

With the focus on one wavelength, even an EQE intensity of 10 % by a film absorbance of 30 % results in an IQE of one third. Donor material should have high IQE values besides material compatibility with the acceptor and processability.

J-V curves can be measured with varying light intensity to check what recombination effects are present in the solar cell. At the V_{OC} point all generated excitons or charge carriers have to recombine because no current is flowing.[118] Radiative recombination , also called bimolecular, can be determined by drawing the logarithm of light intensity against V_{OC} .[125] If the slope is about 1 $k_B T/e$ bimolecular recombination is prevailing in the solar cells which is typical for bulk heterojunctions. While silicon solar cells show normally trap states and therefore non-radiative recombination the plot has a slope of 2 $k_B T/e$ or larger, where k_B is the Boltzmann constant, T is room temperature and e is the elementary charge.

Fill factor reduction is observed for increasing series resistance (R_S) and voltage loss occurs for decreasing shunt (parallel) resistance (R_{SH} or R_P). R_S is a macroscopic phenomenon that can be explained by contact resistances of metal and semiconductor or by the current flow through the active layer, while shunt resistance arises from alternative current paths that cause internal

shorts. Both can be derived from JV-curves (Figure 1.2.7B) by assuming the following equivalent circuit for a solar cell.[118]

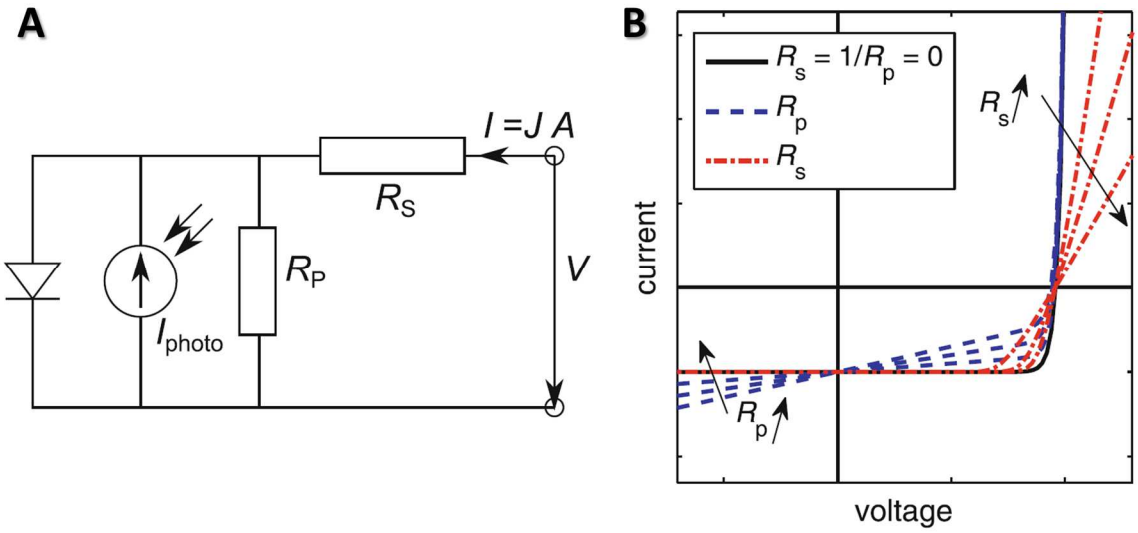

Figure 1.2.7: (A) Simple equivalent circuit of a real solar cell. It contains a diode, a photocurrent source, and parallel and series resistances. (B) Influence of series resistance R_S and parallel or shunt resistance R_P on the current-voltage curve. The resistances mainly reduce the fill factor.[118] *[Reprinted from W. Tress, 'Organic Solar Cells: Theory, Experiment and Device Simulation', Springer International Publishing, page 138 Figure 3.37, Cham, 2014, with permission from Springer Nature.]*

The cell output current J in the equivalent circuit (Figure 1.2.7A) is composed of the light generated current J_{photo}, the current through the diode and through the parallel resistance:

$$J = J_L - J_0 \exp\left(\frac{e(V + JR_S)}{nk_BT}\right) - \frac{V + JR_S}{R_{SH}} \qquad (12)$$

The diode current is characterized by the exponential function of elementary charge e, adjusted voltage, diode ideality factor n, Boltzmann's constant k_B and (room) temperature T. The dark saturation current density J_0 is the measured residual current flowing in dark mode and $V = 0$, which should be negligible small. The ideality factor n is 1 for ideal solar cells, for higher values non-radiative recombination via trap sites becomes dominant.

1.2.4 Development of Highly Efficient Solar Cells

Since the last three decades, silicon solar cells dominate the photovoltaic market due to silicon's abundance in semiconductor industry. Their high PCE, high-stability, long-lifetime, and a scalability of the fabrication steps have led to continuous development of solar cells with a great performance-to-cost ratio. Despite rapid efficiency advances in emerging fields or so-called third generation solar cells (perovskites, organics, and CIGS solar cells), silicon is still the leading photovoltaic technology due to process optimization and new designs. Figure 1.2.8 illustrates a

series of high-efficiency designs from the early aluminium back surface field (Al-BSF) cell to the recently industrialized passivated emitter and rear cell (PERC) and in the future to the scaled silicon heterojunction (SHJ) and interdigitated back contact (IBC or HJ-IBC) cells.[21] Key drivers for the development are high-quality surface passivation and carrier selective contacts resulting in power conversion efficiencies of 26.7%.[110]

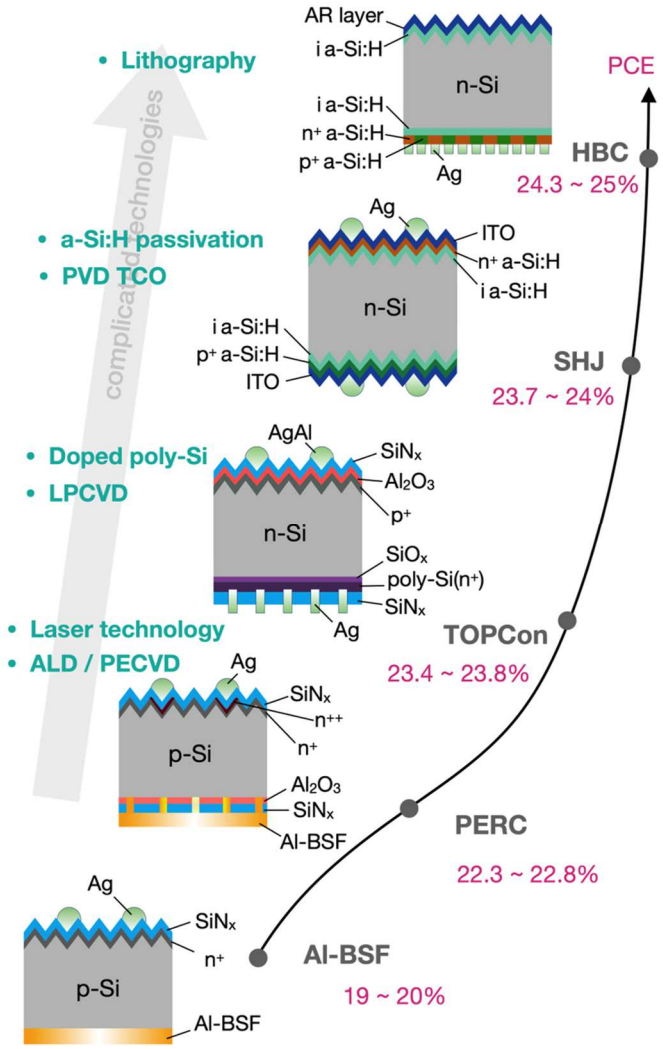

Figure 1.2.8: The advancement of silicon photovoltaic technology to achieve high PCEs from early Al-BSF cells to current market mainstream PERC cells, transitional TOPCon cells to next-generation SHJ and HBC cells. The efficiency values shown are typical for industry at the present stage.[21] *[Reproduced from Advanced Energy Materials, Wieland et al. 'Carbon Nanotubes for Photovoltaics: From Lab to Industry' 11, 3, 2021, under Creative Commons license agreement from Wiley-VCH GmbH.]*

These improvements in architecture design bring the PCE closer to the theoretical maximum of 29.4 %[126] but come along with complexity in fabrication and high costs which limits the industrialization. Thus, the commercially available solar cells are still based on the Al-BSF design while PERC solar cells slowly enter the market. In research labs, tandem perovskite/silicon cells have already exceeded the theoretical limit[127] and recently outbid former records reaching 32.5 %.[128] Perovskite solar cells on their one already achieved 25.7 % which is the highest value

of third generation photovoltaic cells including organic, quantum dot or dye-sensitized solar cells, as well. Besides the emerging field, the classic thin film solar cells made of copper indium gallium selenide (CIGS), cadmium telluride (CdTe) or amorphous silicon obtain PCE values of 23 %, 22 % and 14 %, respectively.[128]

Organic photovoltaics can already compete with their maximum efficiency of 18.2 %[111] and are promising candidates for the future considering their quite fast development from 12 % to 18 % in the last 5 years.[128] Mainly these OPV are thin film polymer solar cells based on a combination of polymer donors with fullerene or non-fullerene acceptors (NFA), which typically consists of a fused ring system. The performance increase of the last years can be attributed to the development of NFA. Their broad spectral absorption is advantageous compared to standard fullerene acceptors, as well as the higher extinction coefficient and tunability of energy levels for tailored donor/acceptor pairs.[129-131] Thus the best performing OPVs (with two active layer components) are all fabricated with a polymer donor and a non-fullerene acceptor; for example, D18:Y6[132] or PM6:L8-BO.[133] Further development of organic solar cells include optimization of the morphology, recombination suppression and broadening light absorption of the components or by addition of a third material.[134] The third component in the active layer ideally facilitates a cascade for electron transfer across the materials. A double cascading charge transport in the stack of PM6:PM7:Y6:PC_1BM has enabled an PCE of 18 %.[135] Despite the achievements of ternary or quaternary devices, the morphology becomes even more complex in these systems. Vertical controlled distribution in films could be a compromise between BHJ and bilayer device architecture. The film preparation can be performed by preaggregation,[136] with additives like 1-Chloronaphthalene[137] or by solvent vapor annealing as post-treatment.[138]

- this page left intentionally blank -

- this page left intentionally blank -

1.3 SWCNTs in Solar Cells

The utility of single walled carbon nanotubes in solar energy harvesting is given due to their tailorable optical and electrical properties that cover a wide range in the semiconductor field. SWCNTs have defined chirality and molecule-like absorption, with extremely narrow excitonic and vibronic resonances. Their gigantic aspect ratio with a regular periodic lattice is a property much more in line with inorganic semiconductors or nanowires. Therefore, semiconducting SWCNT films function as active or charge-transporting materials in solar cells. In this chapter, first SWCNTs as a transparent conductive layer are discussed in several applications such as silicon, organic and perovskite solar cells. Besides this fast-growing research area, CNTs are used as back electrode, where transparency is irrelevant, or as charge transport layer. Finally, the focus is on SWCNTs as light harvester in the photoactive layer and challenges in the field, like film thickness or polychiral devices.

1.3.1 SWCNT as Transparent Conductive Electrode or Charge Transport Layer

Narrow absorption bands and the tailorable electronic property of SWCNTs are advantageous for the use as transparent conductive electrodes or hole transport layers.[121] The two most important roles of a transparent conductor (TC) in a solar cell are to transmit as many photons to the active layer as possible and to efficiently collect one type of charge carrier (electron or hole). SWCNT TCs are an intertwined network of individual SWCNTs, therefore individual SWCNT properties and collective properties in the film must be considered by light transmission and charge transport. The photon absorption and transmission are controlled through the individual excitonic optical transitions that are quite narrow for semiconducting and metallic SWCNTs. The conductivity of the SWCNT TC is determined by the mobility and density of charge carriers which is based on the characteristic density of states. Metallic SWCNTs have a finite DOS at all energies and free carriers at the Fermi level. In contrast, semiconducting SWCNTs have a true band gap and should be electronically insulating.[139] However, s-SWCNTs can be made conductive by adsorption of molecular charge transfer dopants that lower or raise the Fermi level. The adsorption of acidic molecules (HNO_3, $SOCl_2$, etc.) leads to an electron withdrawal from the SWCNT π-network and lowers the Fermi level, creating a p-type s-SWCNT.[140] Basic molecules (hydrazine, ethylenediamine, etc.) donate electron density to the π-network, creating an n-type SWCNT.[141] Importantly, molecular charge transfer doping is achieved solely by physisorption which preserves the associated delocalized π-electron network.[139]

The mobility of the charge carriers is high for individual SWCNTs, however each nanotube junction in a SWCNT film is a barrier for charge transport and limits the carrier mobility in SWCNT TC.[95, 140, 142] Conductivity is primarily controlled by thermally assisted tunnelling through inter-tube barriers. Employing charge transfer doping decreases the barrier magnitude and increases SWCNT TC conductivity.[142] A drawback of charge transfer doping is the instability of the thermally labile dopants resulting in irreversible loss in conductivity for higher temperatures. Alternatively, an increase in carrier mobility is achieved by minimal processing attributed to longer SWCNTs and a reduction of nanotube junctions.[95]

SWCNTs have been studied for nearly two decades as passive charge extraction layer in PV to efficiently collect charges (most often holes) from the photoexcited active layer. The SWCNT network can be utilized as an interfacial layer in between the active layer and a metallic electrode, or can serve as the (transparent) electrode itself.[120] Examples for SWCNTs as transparent conductive electrodes or hole transport layers can already be found for perovskite,[143-145] copper indium gallium selenide (CIGS),[146] CdTe,[147, 148] and organic solar cells.[149-152] In organic solar cells, P3HT-dispersed SWCNTs are used as a HTL with comparable results to the standard PEDOT:PSS layer.[152] In CIGS solar cells, the CNTs replace the ZnO transparent oxide and in CdTe solar cells they serve as semi-transparent back contact.[146, 147] Improved hole extraction has also been demonstrated for perovskite solar cells by introducing an SWCNT interlayer between the perovskite and the hole transport layer spiro-MeTAD.[143] An aerosol-synthesized SWCNT film as transparent electrode infiltrated by spiro-MeTAD approached a PCE of 16 %. Undoped SWCNT HTL coupled with PMMA or spiro-MeTAD have enabled stable 17.4 % or 20 % PCE perovskite solar cells.[144] Additionally, triflic acid doped CNTs as transparent electrodes have outperformed the metal counterpart in a perovskite solar cell with 18.8 % and 18.4% PCE.[145]

In silicon solar cells, SWCNTs can act as hole selective contact where chiral species with optical transitions outside the spectral range of silicon (350 – 1100 nm) are preferred and in addition, these larger diameter nanotubes show increased conductivity.[153, 154] However, raw soot is already sufficient as hole selective contact and in general aqueous sorted species are better suited due to their pristine surface maximizing contact area.[21] Until a few years ago, CNT:Si solar cells are fabricated in the design of a window like geometry defined in the middle of a silicon wafer. In this geometry shown in Figure 1.3.1, a SiO_2/ Si wafer is etched to reveal a small silicon opening in the SiO_2 usually 0.008–2 cm^2 and the surrounding SiO_2 is coated with Au, etc. [21] While the CNT

film was processed separately and transferred to the window, where it remained the top layer on the front side to test various chemical dopants.

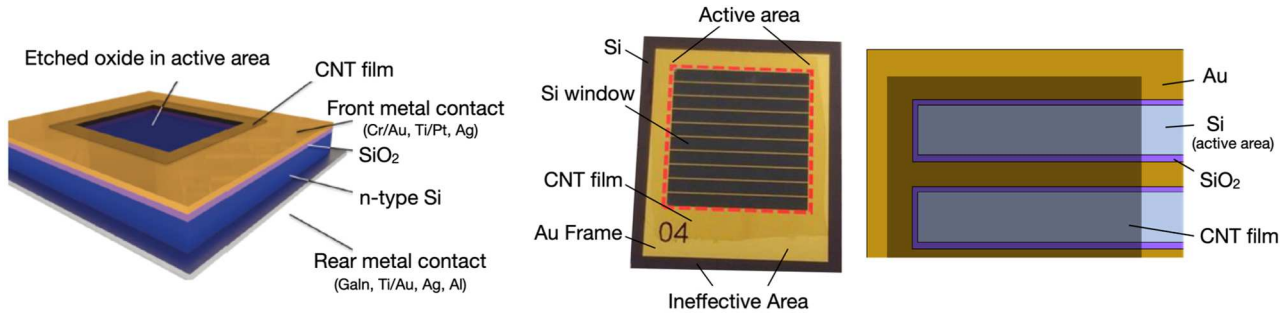

Figure 1.3.1: CNT:Si solar cells with window like geometry defined in the middle of a silicon wafer. Typically, a SiO_2/Si wafer is etched to reveal a small silicon opening in the SiO_2 usually 0.008–2 cm^2 and the surrounding SiO_2 is coated with Au. The CNT film is finally transferred onto the device stack and remains as top layer.[21] *[Reproduced from Advanced Energy Materials, Wieland et al. 'Carbon Nanotubes for Photovoltaics: From Lab to Industry' 11, 3, 2021, under Creative Commons license agreement from Wiley-VCH GmbH.]*

This window design facilitated the use of porous CNT films and avoided metal penetration because the carrier selective contact is placed above the metal top contact. Nevertheless, the CNTs have two contradictory functions in this architecture, first as hole selective layer and secondly as transparent conductive layer. Most of the improvements in the field were achieved by doping the CNTs with HNO_3, superacid, AuCl, $SOCl_2$, $CuCl_2/Cu(OH)_2$, and Nafion.[21] This development led to CNT films that function as a transparent conductive layer and less as a hole selective contact.

1.3.2 SWCNT as Back Electrode

The PCE of CNT:Si solar cells remained below 17 % mainly due to the unusual window design, until the last couple of years when a new passivation scheme was revealed with polymers containing a sulfonic functional group. This technique allows to use CNTs on the front as well as on the back side of a junction. The new passivation technique is relying upon spin-coating polymers with a sulfonic functional group ($-SO_3H$) and the ability of these to spontaneously form suboxides (Si-O-R) at the silicon surface.[155] PSS, poly(2-acrylamido-2-methylpropanesulfonic acid)'; PS-b-PERB, polystyrene-block-poly(ethylene-ran-butylene)-blockpolystyrene-sulfonated-cross-linkable and Nafion have been used for this technique but on their own, these polymers are insulating.[21] By spin casting onto a porous film they additionally fill the void space between the CNTs and the silicon surface enabling metal contacts directly on top of the CNT/Nafion film. In 2020, Chen et al.[116] demonstrated that spin-coated Nafion onto CNT:Si solar cells resulted in the formation of a passivated charge selective contact. On one hand, the CNTs contact the silicon facilitating exciton dissociation and hole transport. On the other hand, Nafion is acting as

passivation layer and simultaneously as an antireflective coating and nanotube dopant.[156, 157] The Nafion film thickness was tailored to ensure that the uppermost CNTs could still be electrically contacted, but effectively avoid metal penetration during electrode evaporation by the void filling. This new technique allows to use CNTs on the front as well as on the back side of a standard silicon cell geometry on areas up to 16 cm^2 and PCEs approaching 19 %.[116] The process was simplified by combining CNTs and Nafion into a single ink[156] that could be spin-coated in one step, as shown in Figure 1.3.2A. This concentrated CNT/Nafion ink was used to replace the doped back junction of an industrial architecture consisting of phosphorous-doped silicon with SiN_x antireflection layer and silver grids on the front.(Figure 1.3.2B)[156, 158]

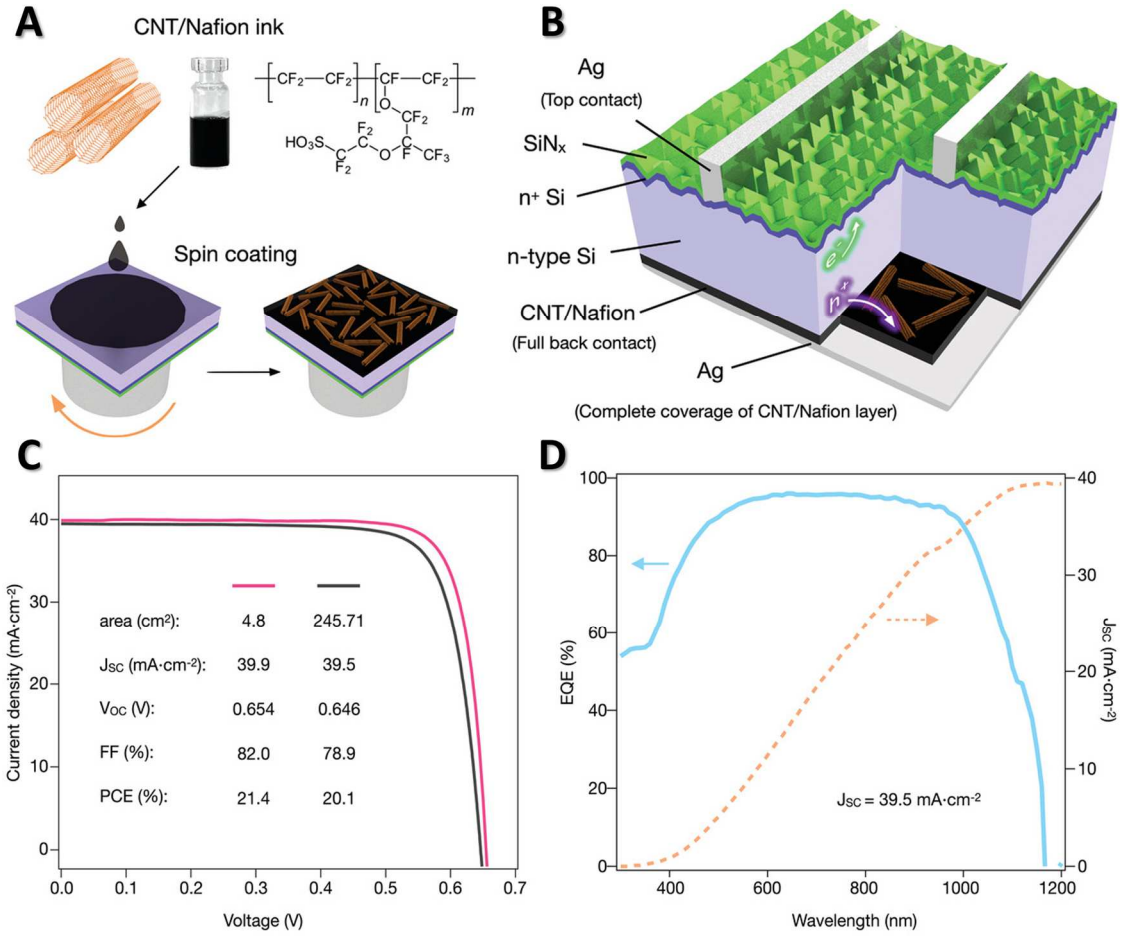

Figure 1.3.2: (A) CNTs and Nafion are shear-force mixed to form an ink that can be spin coated onto the back of an (B) industrial n-type silicon solar cell. (C) J–V data for champion solar cells with device areas of 4.8 and 245.71 cm^2.(D) EQE and integrated Jsc data.[156] *[Reproduced from Advanced Funtional Materials, Chen et al. 'A Polymer/Carbon-Nanotube Ink as a Boron-Dopant/Inorganic-Passivation Free Carrier Selective Contact for Silicon Solar Cells with over 21% Efficiency' 30,38,2004476, 2020, under Creative Commons license agreement from Wiley-VCH GmbH.]*

On the rear of the device, CNTs function solely as a hole transport layer and factors like film morphology and alignment are less important. So, a high power conversion efficiency of 21.4 % (4.8 cm^2) was obtained with an FF of 82 % (Figure 1.3.2C) surpassing all previous CNT/Si heterojunction devices and establishing the record for dopant-free contact architectures including

other hole-selective silicon solar cells.[115] Even on industrial sized wafers (>245 cm^2) over 20 % efficiency could be achieved, IV and EQE curves are displayed in Figure 1.3.2C and D. The work function difference between p-type CNTs and n-type silicon creates a built-in potential and dopants only further enhance the work function of the CNTs. For example, Nafion doping altered the work function of the CNT film from 4.6 eV (undoped) to 5.1 eV corresponding to an enhancement of the built-in potential from 0.41 to 0.7 V.[116] Recently, a commercially available chirality enriched SWCNT raw soot mixed with Nafion achieved a record efficiency of 23.03 % acting as back contact and passivation layer in conventional passivated emitter and rear cell (PERC) solar cells.[117] In this case the ink forms a passivated charge selective contact on a p-type silicon solar cell.

The replacement of the standard back junction by a CNT/ Nafion layer is simple, scalable and completely eliminates the metal-semiconductor contact known to cause high interfacial recombination. It doesn't require high temperatures or vacuum equipment which makes it overall comparably cost effective by achieving high PCE. In the future, the back-junction design is one of the most promising ways to utilize CNT in silicon solar cells. The new strategy is the combination of low-dimensional materials with an organic passivation, here CNTs with their tunable band structure may lead to further improvements in built-in potential, especially at the CNT:Si interface.[21]

1.3.3 SWCNTs in the Active Layer of Organic Solar Cells

Organic SWCNT based solar cells have almost exclusively been fabricated in conventional bilayer stacks between an indium tin oxide (ITO) substrate and metals like silver or aluminium.[21, 46, 91, 159] The carbon nanotubes are integrated in the photoactive layer typically as the electron donor combined with acceptors like fullerene C_{60} or its derivates forming a type II heterojunction.[21] Common hole transport materials are poly(3,4-ethylenedioxythiophene) polystyrene sulfonate (PEDOT:PSS)[91, 160] or molybdenum oxide (MoO_x),[159, 161] for aqueous CNTs poly[N,N' -bis(4-butylphenyl)-N,N' -bis(phenyl)-benzidine] (PTPD) was tested.[97] Characteristic electron transport layers are made off bathocuproine (BCP)[46, 92, 97, 162] or zinc oxide (ZnO).[159] A typical bilayer stack is illustrated in Figure 1.3.3A. The same materials can be used in bulk heterojunctions, the challenge of this architecture is the relatively small amount of SWCNTs that can be mixed with an acceptor like [6,6]-Phenyl-C_{61}-butyric acid methyl ester ($PC_{61}BM$).[159] The

nanotube content is on those mixtures often below 10 wt%, so SWCNTs are rather acting as hole collector and morphology additive instead of a donor that absorbs significant amount of light. Rarely, SWCNTs are used as electron acceptor together with polymers such as poly(3-hexylthiophene2,5-diyl) (P3HT) or poly(3-octylthiophene) (P3OT) as corresponding donors.[163-165]

In 2010, Bindl et al. were able to fabricate the first planar SWCNT:fullerene solar cells and shortly after a bulk heterojunction each with polymer sorted carbon nanotubes.[46, 163, 166] The first polymer-free solar cell with aqueous sorted SWCNTs and fullerene C_{60} as acceptor were demonstrated by Jain et al. in 2012.[96] The record efficiency for SWCNT solar cells of 3.2 % is held by a BHJ with inverted structure containing P3HT wrapped SWCNTs and $PC_{71}BM$ as acceptor.[159, 161] This is just one example, where SWCNTs are added into an existing organic photovoltaic material combination (P3HT/$PC_{71}BM$) to push their efficiency due to extended light absorption in the infrared.[21]

One main difference between the BHJ and the planar architecture is the lower contribution of SWCNTs to the current due to lower concentrations in BHJ.[159, 167] EQE in Figure 1.3.3B clearly shows the incident photons are mainly absorbed in the visible by P3HT and $PC_{71}BM$ reaching an EQE of 50 % whereas the SWCNTs in the IR region only contribute with about 3 % to the current generation.[159] Similar approaches are found in the SWCNT/fullerene bilayer devices where the classical C_{60} fullerene[46, 101, 167, 168] is replaced by $PC_{71}BM$[91, 169] to gain from its broader light absorption. While $PC_{71}BM$ devices show EQE response from 350 – 700 nm[159], C_{60} only contributes up to maximum 600 nm as illustrated in Figure 1.3.3B and C. Unsurprisingly, the best PCE of layered device architectures is 2.9 % achieved by (6,5)/$PC_{71}BM$[91] which is slightly lower than the 3.2% of the BHJ. The EQE of the SWCNTs in the IR region was determined to be 26 % for (6,5)/$PC_{71}BM$, 10 times higher compared to the BHJ. However, the highest published EQE is 49 % in a bilayer SWCNT cell made of shear-force mixed (6,5)/C_{60}.[167] (blue line, Figure 1.3.3D) All these SWCNT solar cells are quite small area devices with approximately 1 - 2 mm^2, although (6,5)/$PC_{71}BM$ bilayer was upscaled to 10.4 mm^2 with a PCE of 2.7 %.[91]

High semiconducting SWCNT content is essential for the SWCNT solar cells, as well as low defect density and long nanotubes which minimize exciton quenching.[167] Polymer wrapped SWCNTs especially shear-force mixed (SFM) ones fulfil this requirement[44, 167, 170] and working in organic

solvents simplifies direct film formation on the device. Semiconducting SWCNT films showed a 20 % more efficient energy transfer if they are prepared by SFM compared to sonicated samples.[170] The probability of an exciton transfer onto a neighbour SWCNT is here higher than becoming trapped on a defect site. These long, weakly defected nanotubes therefore improve the interfiber hopping and exciton diffusion to the interface.[21] Solar cells made of dispersions with PFO-BPy wrapped (6,5) exposed to either shear-force mixing, brief or extended ultrasonication show increased FF and V_{OC} for less harsh dispersion methods like SFM. The EQE spectra are shown in Figure 1.3.3D, where the SFM device also achieved the best value of 49 % (4.2 ps) compared to 38 % (3.0 ps) and 28 % (2.1 ps) for the brief or extended sonication samples due to less defect sites and extended exciton lifetime.[167]

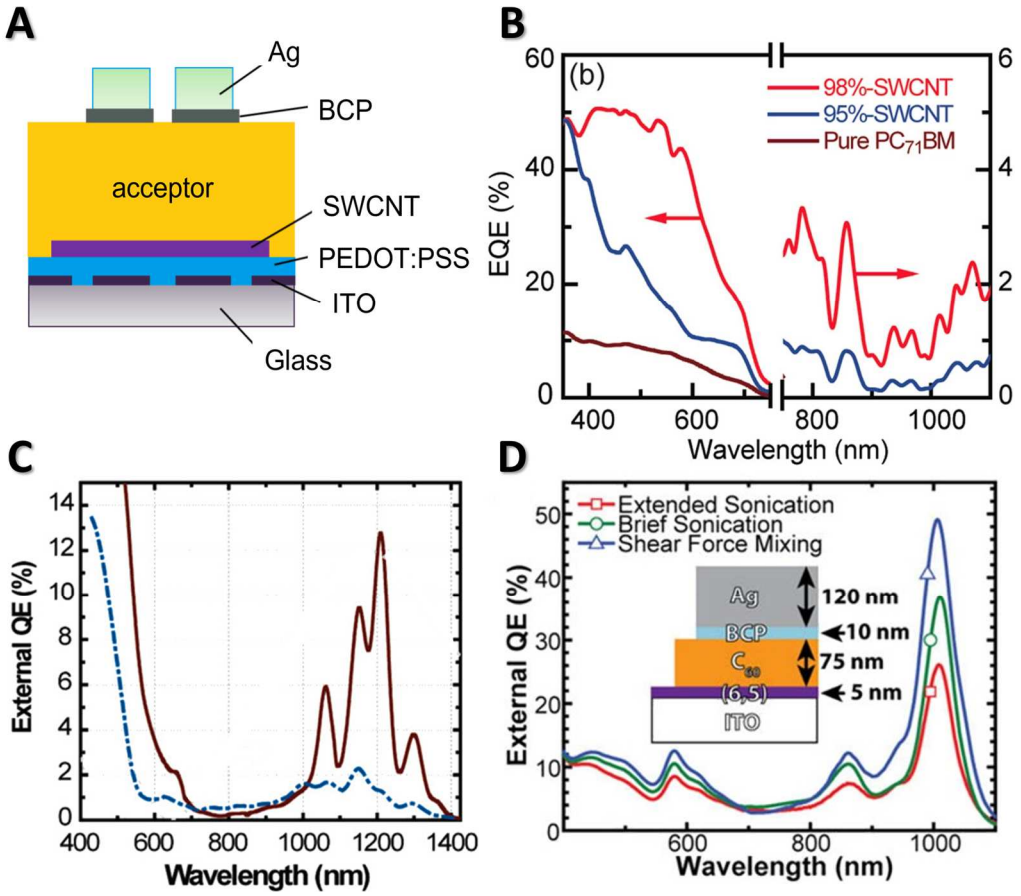

Figure 1.3.3: (A) Schematic of a bilayer SWCNT solar cell. (B) SWCNT/$PC_{71}BM$ device: Effects of SWCNT semiconducting purity on EQE in the visible and NIR regions.[159] (C) SWCNT/C_{60} device: Comparison of spectrally resolved short-circuit external QE between mixed-SWCNT (dot-dash, blue) and pure semi-SWCNT (solid, red) devices.[46] (D) (6,5) SWCNT/C_{60} device: Variation of EQE with the nanotube dispersion technique achieving maximum EQE of 49 % with SFM nanotubes.[167] *[(A) Reprinted from Carbon, Vol 184, Wieland et al., 'The potential of SWCNTs to extend the IR-absorption of silicon solar cells', 828-835, Copyright 2021, with permission from Elsevier (B) Reprinted with permission from Gong et al. 'Polychiral Semiconducting Carbon Nanotube–Fullerene Solar Cells', Nano Lett. 2014, 14, 9, 5308, Copyright 2014 American Chemical Society. (C) Reprinted with permission from Bindl et al. 'Efficiently Harvesting Excitons from Electronic Type-Controlled Semiconducting Carbon Nanotube Films', Nano Lett. 2011, 11, 2, 455, Copyright 2011 American Chemical Society. (D) Reproduced from APL Materials, Shea et al. 'Less severe processing improves carbon nanotube photovoltaic performance' 6, 056104, 2018, under Creative Commons license agreement from AIP Publishing.]*

Functionalized PFO-wrapped (7,5) SWCNTs showed even for moderate levels of covalent sp^3-defects a 5fold reduction in EQE for (7,5)/C_{60} bilayer devices.[171] Such exciton traps with similar depth are also found for oxygen-related sp^3-defects. In general, all common dispersion techniques are performed under ambient conditions implying a minimum of oxygen-related defects in every dispersion.[120] Simulations of defect density in semiconducting SWCNTs suggest that even for one defect per micron the excitons can diffuse less than 10 nm for SWCNTs of 1 µm or shorter. Creating long s-SWCNTs (>2 µm) with reduced defect density of 0.1/µm could increase the exciton harvesting depth 10-20 times to roughly 100 nm.[171]

Polymer-free solar cells with nearly single chirality (6,5) from aqueous solutions have only accomplished efficiencies of approximately 0.1 % in combination with C_{60}.[96, 98, 160] If the SWCNTs are pristine, they are strongly coupled to each other leading to rapid downhill energy transfer to the smallest bandgap chirality. In contrast, for SWCNTs with polymer shell exciton lifetime is enhanced due to the shielding of the nanotube from the surrounding environment.[26, 100, 101] Longer migration is enabled by extended exciton lifetime resulting in more excitons reaching the donor-acceptor interface and more efficient solar cells.[102, 103, 139]
The majority of SWCNT solar cells are therefore fabricated with single chiral films of (6,5) and (7,5) mainly polymer-sorted because these are also the easiest to separate.

1.3.4 Challenges

The interesting questions for SWCNT based solar cells are what kind of nanotubes are favourable in PV and how can those be integrated into a device. The main challenges are the narrow absorption of single chirality SWCNTs and the limited film thickness in bilayer architectures. Improving the light absorption is therefore highly desired and can be accomplished by exchanging established materials like fullerene acceptors or adding materials such as dyes which absorb photons in other spectral regions. In this regard, SWCNTs can be used in ternary bulk heterojunctions or tandem architectures to complement the absorption of standard devices into the IR region.

1.3.4.1 Film thickness

Solar cells, especially bilayer architectures, suffer from the considerable distance every created exciton must travel to reach the interface. Rationally, thicker films should absorb more light and

create more excitons resulting in higher efficiencies for SWCNT solar cells. However, most of these excitons will never reach the interface and be separated into charge carriers.[21] The optimum CNT film thickness is given by the exciton diffusion length which is defined as the average distance that an excited carrier will travel before recombining. In SWCNT bilayer cells the exciton diffusion length has been determined by ultrafast spectroscopy[102, 172] or photocurrent measurements to be 5-10 nm.[46, 102, 173] Consequently, the SWCNT/C_{60} cells, already discussed in Figure 1.3.3D with different processing techniques, exhibit increasing EQE with SWCNT film thickness until 5-10 nm and then fall abrupt, as shown in Figure 1.3.4.[97, 167, 168, 173]

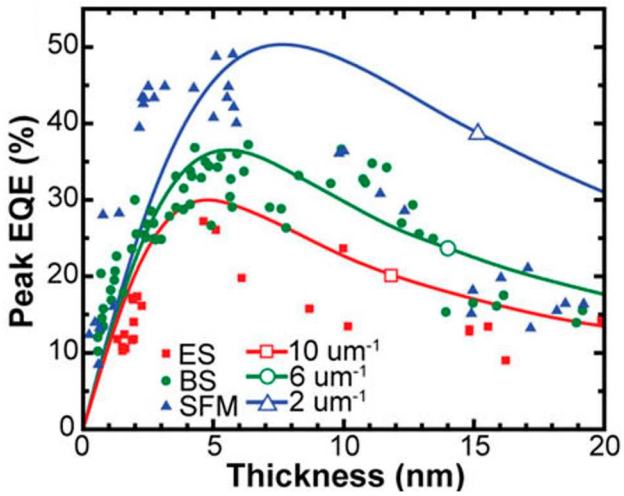

Figure 1.3.4: SWCNT/C_{60} device: Peak EQE at 1000 nm as a function of thickness measured for representative devices fabricated from solutions undergoing shear-force mixing (blue), brief or extended sonication (green and red). The maximum EQE occurs near 5 nm for all samples but decreases as processing intensity increases.[167] *[Reproduced from APL Materials, Shea et al. 'Less severe processing improves carbon nanotube photovoltaic performance' 6, 056104, 2018, under Creative Commons license agreement from AIP Publishing.]*

The graph shows higher EQE intensities for shear-force mixed CNTs and a small increase in maximum film thickness before the EQE signal drops.[167] All high efficient SWCNT solar cells therefore contain only few nanometer thick CNT films.[91, 168] A comparable thick acceptor layer of 30-120 nm is typically prepared to smooth probable inhomogeneities in the CNT network. Transfer matrix calculations can be used to tune the thicknesses for optimal electric field intensity that match with the physical position of the SWCNTs in a device.[21, 93, 98, 171]

Despite the optimized thickness, in all thin films the SWCNTs tend to orient predominantly within the plane of the film, however, out-of-plane exciton transport is desired. Whereas the intra-nanotube exciton diffusion length can be hundreds of nanometers, the corresponding inter-nanotube value in the cross-plane direction is the short exciton diffusion length of 5-10 nm discussed above. This can amplify the deleterious effect of exciton or charge trapping, even for extremely small defect densities. One potential solution to make use of the longer intra-nanotube

diffusion length are aligned SWCNTs perpendicular to the underlying transparent conducting substrate. These so called 'forests' of carbon nanotubes would not need to be very tall but dense and aligned to avoid nanotube junctions. Many examples already proofed the growing of aligned carbon nanotube forests mainly by CVD[174], unfortunately, none has demonstrated specific growth of highly pure semiconducting SWCNT.

New architectures are necessary to address the short exciton diffusion length, so bulk heterojunctions were developed. However, the (6,5)/$PC_{71}BM$ BHJ has shown reduced J_{SC} and FF (1.91 mA cm^{-2} and 33 %) compared to the corresponding bilayer structure. (6.76 mA cm^{-2} and 49 %)[91] In SWCNT/fullerene BHJ the morphology is hard to control because of the rigidity of the carbon nanotubes and their high aspect ratio.[139] Furthermore, solvent systems capable of simultaneously dispersing SWCNTs and C_{60} in high concentration are rare.[166] Inefficient intermixing especially forming of large domains can hinder exciton dissociation, therefore morphology control in the active layer is key.

1.3.4.2 Polychiral CNT films

The high absorbance coefficients of carbon nanotubes are advantageous for light capture, in contrast to the narrow excitonic absorption peaks. These tailorable chirality dependent optical properties of SWCNTs led researchers to predictions of possible broadband light absorption for polychiral films. Arnold et al.[139] predicted that a 150 nm thick film of 10 small diameter semiconducting SWCNTs (0.8-1.4 nm) would be capable to collect up to 86 % of the solar spectrum until 1200 nm. Likewise, Tune and Shapter[175] simulated the light harvesting ability of mono- and polychiral films and found that (7,5) s-SWCNTs could attain an efficiency of ~7 %. Whereas a mixture of (6,4), (9,1), (7,3), and (7,5) can collect up to 28 % of the AM1.5 solar spectrum, as illustrated in Figure 1.3.5A. The combination of four larger diameter species yielded 19 % (Figure 1.3.5B) but here the goal was to maximize the infrared absorption whilst minimizing it in the visible region. This could be useful for transparent photovoltaic applications in windows.

However, the practical use of polychiral SWCNT samples or thicker films is limited due to energy transfer within the film and trapping in smaller band gap species [100, 102, 103], along with a significant fraction of the generated excitons ending up in dark nonradiative states.[170] Exciton hopping between parallel bare nanotubes occur with a rate ~60 fs, as illustrated in Figure 1.3.5C from the larger band gap (7,5) nanotube (green) to a (7,6) or (8,4) species (red). Transfer between

non-parallel nanotubes happens on a time scale of <500 fs, and diffusion of excitons to quenching sites (represented with an asterisk) and subsequent exciton decay on a time scale of ~400 fs.

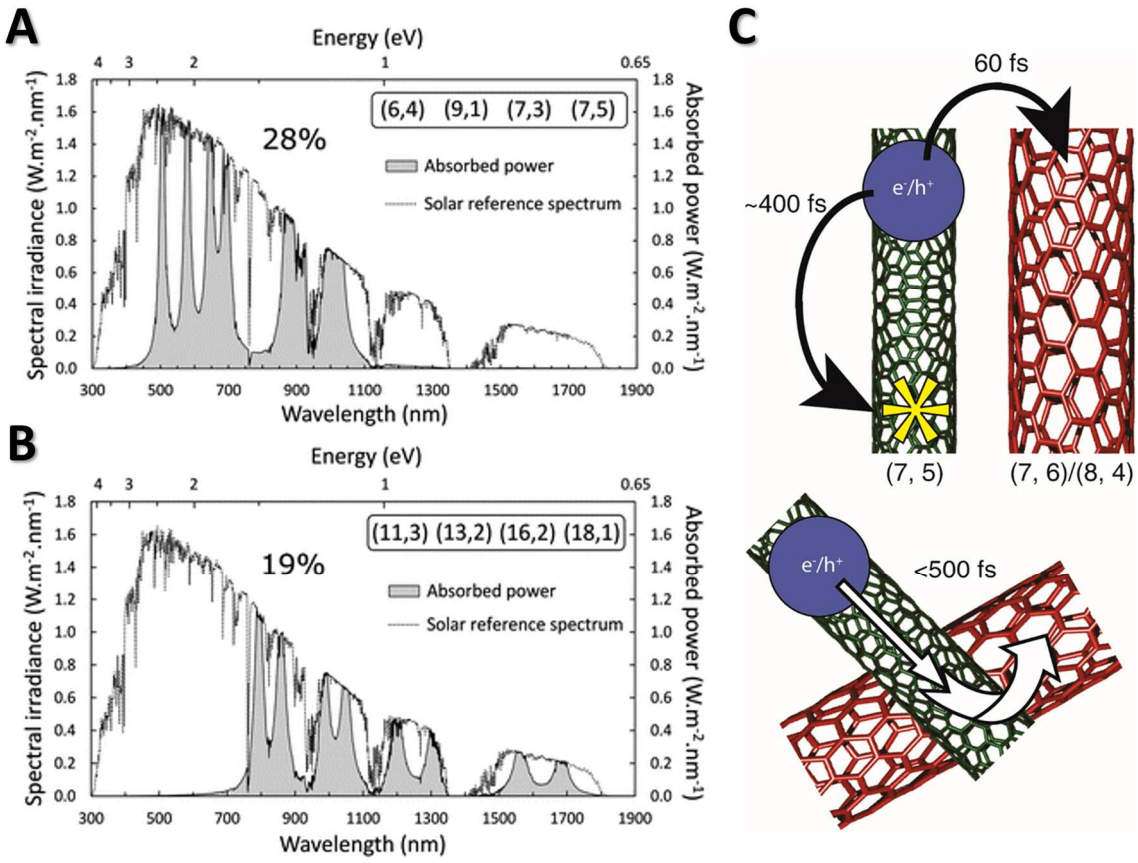

Figure 1.3.5: Simulation of (A) a multilayer solar cell consisting of four individual (n,m) species to provide maximum power absorption, yielding a calculated sunlight harvesting efficiency of 28.3%. (B) A similar multilayer solar cell to maximise absorption in the infrared, yielding 19.0% efficiency, whilst minimising absorption of visible light (S_{33} is not considered).[175] (C) Processes in the bare (7,5)/(7,6)/(8,4) nanotube thin films with the associated time scales.[102] *[(A,B) Reproduced from Energy and Environmental Science, Vol 6, Tune et al., 'The potential sunlight harvesting efficiency of carbon nanotube solar cells' 2572-2577, Copyright 2013, with permission from the Royal Society of Chemistry (C) Reprinted with permission from Mehlenbacher et al. 'Ultrafast Exciton Hopping Observed in Bare Semiconducting Carbon Nanotube Thin Films with Two-Dimensional White-Light Spectroscopy', J. Phys. Chem Lett.. 2016, 7, 11, 2024, Copyright 2016 American Chemical Society.]*

These energy transfer rates always compete with the lifetime of the SWCNTs. The results in Figure 1.3.5C are based on aqueous dispersed CNTs after ATPE-sorting with a lifetime of ~300 fs which allows several energy transfers between parallel nanotubes but also results in 'trapping' of the excitation on minority species. Studies on (partially) polymer-wrapped SWCNT thin films demonstrated similar energy transfer rates and lifetimes of ~1 ps.[103] While the wrapping polymer slows down the rate of downhill exciton energy transfer to the lowest band gap species, transient absorption anisotropy suggests that excitons can move between s-SWCNTs in neighbouring bundles.[100] Thus, polymer-wrapped s-SWCNTs should be beneficial in solar cells and more efficient compared to polymer-free cells with electronically coupled CNT networks and associated exciton delocalization across multiple nanotubes. Overall, energy transfer in a CNT thin

film is a quite complex interplay between rapid downhill exciton transfer and long-range energy transport through a CNT network.

1.3.4.3 Endohedral Filling with Dye Molecules

Instead of polychiral samples, endohedral filling of SWCNT with dye molecules can also enable optimal broadband light harvesting in the UV and visible region. The dyes can complement the light spectrum that can be utilized by SWCNTs which makes filled nanotubes attractive for photoconversion. Thereby, the organic dye has to transfer the photoinduced energy to the SWCNT to contribute to the solar cell current. The principle of energy transfer was already confirmed by photoluminescence and transient absorption measurements.[176, 177] Successful filling was demonstrated with p,p′-dimethylaminonitrostilbene (DANS),[178]quaterthiophene (4T) or α-sexithiophene (6T),[179-181] squarylium dye (SQ),[176, 177, 182] and ferrocenylthiocarbonyl based dyes.[183, 184] The confirmation of the encapsulation is still a challenging part because the characterization requires a combination of spectroscopic information.

The asymmetric dye p,p'-dimethylaminonitrostilbene (DANS) with its non-linear optical response was filled inside the nanotube cavity by Cambré et al.[178] In bulk, the large dipole moments of the dye usually align pairwise antiparallel which cancels out the non-linear optical response. Whereas inside a SWCNT, the DANS molecules perfectly align head-to-tail resulting in a large dipole moment. A first indication for encapsulation is an additional peak in the SWCNT absorption spectrum at the position of the corresponding asymmetric dye, illustrated in Figure 1.3.6A and B.

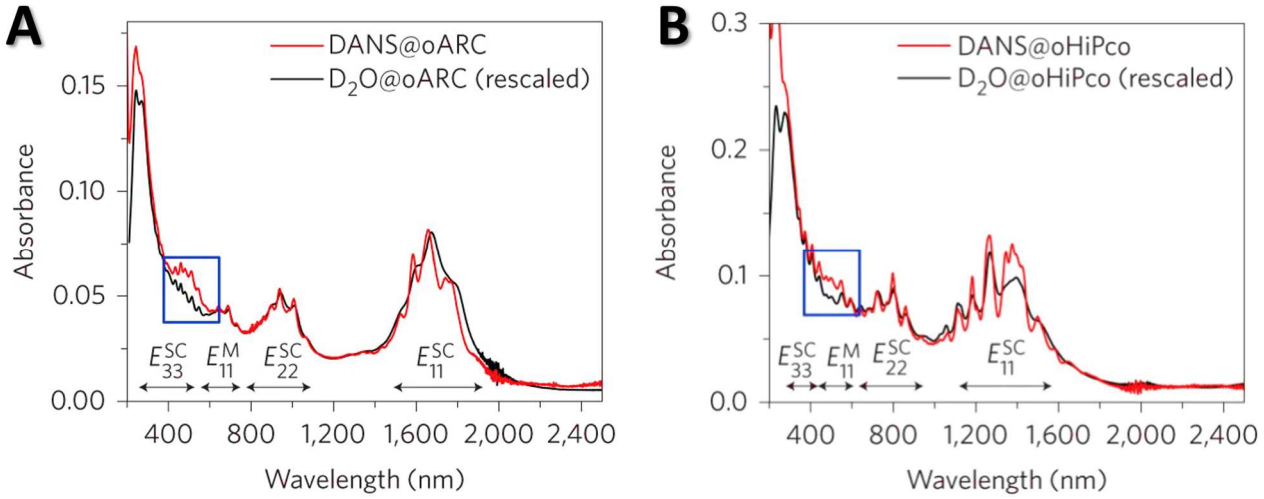

Figure 1.3.6: (A,B) Absorption spectra of DANS-filled ARC discharge or HiPco-SWCNTs compared to the rescaled spectrum of the D_2O-filled samples. The characteristic absorption bands of the semiconducting and metallic SWCNTs are indicated as E^{SC} and E^{M}. In the region around 500 nm, absorption of the encapsulated DANS molecules can be observed (blue boxes).[178] *['Asymmetric dyes align inside carbon nanotubes to yield a large nonlinear optical response', Cambré et al., Nature Nanotechnology, 10, 2015, reproduced with permission from SNCSC]*

The water-filled nanotubes show broader and slightly red-shifted absorption peaks because the dye encapsulation prevents the water filling and hence eliminates the inhomogeneous broadening and dielectric screening induced red-shift.[178]

Squarylium dye was already encapsulated in 2007 by Yanagi [176] confirmed by X-ray diffraction and polarized optical absorption data. It was demonstrated that the dye is located off centre and aligned along the nanotube axis. Ultrafast excitation energy transfer (EET) from the encapsulated squarylium to the SWCNT was observed[176] and transient absorption measurements demonstrate that the majority of SQ excited states undergo EET within approximately 200 fs. Near-complete fluorescence quenching and the comparison of the excited state lifetimes of free and encapsulated SQ dye confirm the close to quantitative EET efficiency.

Figure 1.3.7 shows the PLE maps of (A) SQ-filled SWCNTs and as comparison (B) DCM-filled SWCNTs where the white dashed line highlights the position of the additional EET peak. The (9,8) chirality is the smallest that exhibits an EET peak and that shows a red-shift compared to solvent filling, so the sieving diameter for SQ is 1.15 nm.[177] Excitation of the dye inside the nanotube cavity revealed differences in absorption and photoluminescence spectra due to different stacking of the dye molecules depending on the diameter of the SWCNTs.[177, 182] Theoretical predications approve that dye molecules adopt a close packing geometry for each nanotube diameter resulting in tuneable optical properties of the dyes@SWCNTs.[182]

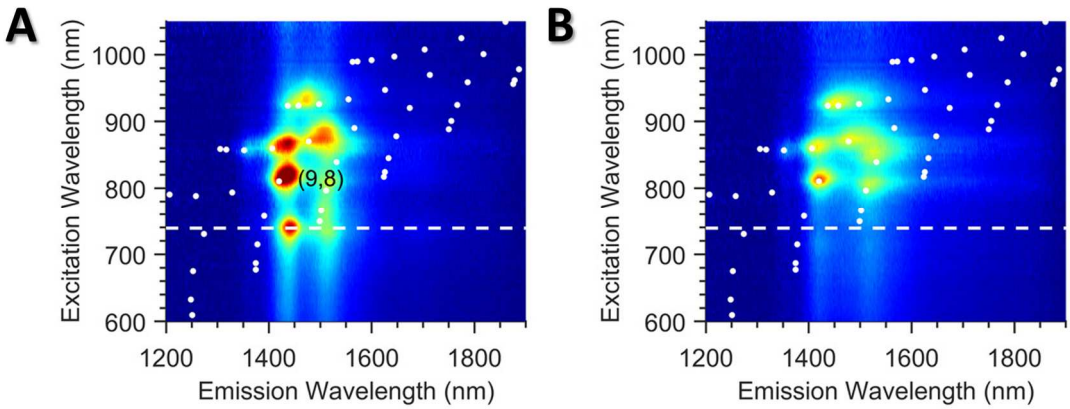

Figure 1.3.7: PLE maps of (A) SQ-filled SWCNTs and as comparison (B) DCM-filled SWCNTs. White points indicate possible peak positions for empty SWCNTs, and the white dashed line highlights the position of the additional EET peak.[177] *[Reproduced from ACS Nano, van Bezouw et al. 'Diameter-Dependent Optical Absorption and Excitation Energy Transfer from Encapsulated Dye Molecules toward Single-Walled Carbon Nanotubes',12, 7, 6881, 2018, under Creative Commons license agreement from Wiley-VCH GmbH]*

Dye filling is only a benefit for broad band light absorption if the SWCNT/acceptor combination itself does not absorb in the same spectral range.

1.3.4.4 Larger diameter CNTs and Other Acceptors

Larger diameter carbon nanotubes, filled or unfilled, have their main optical transition in deeper infrared region and can only be accessed by new acceptor materials. The diameter cut-off for C_{60} is 0.95 nm with the (8,6) chirality as the last one that can contribute to the generated current.[98] The LUMO of C_{60} is -4.05 eV and the thermodynamic driving force ΔG for exciton dissociation vanishes for larger diameters. Separation of the charges can only occur if the large exciton binding energy can be overcome, characteristic E_b values for carbon nanotubes range from 0.2 – 0.5 eV.[185, 186] Thicker CNTs, larger than 0.95 nm, have smaller band gaps and their HOMO is less electronegative compared to small diameter nanotubes like (6,5). (1.8 nm: −4.04 eV vs. (6,5) with 0.78 nm: −3.65 eV)[98] ΔG, calculated as the LUMO-offset of donor and acceptor, is therefore decreasing with increasing CNT diameter.

Acceptors with higher electron affinity are required for these larger diameter SWCNTs, for example, Ihly et al.[187] modified C_{60} with electron withdrawing groups and $C_{60}(CF_3)_4$ showed the best electron transfer rate for (11,9) with 1.35 nm diameter. Non-fullerene acceptors (NFA) are promising in organic photovoltaics and have already proven high efficiencies in thin-film polymer solar cells. In OSC with SCWNT as electron donor, perylene diimide based acceptors or ITIC-2F have been tested by Wang et al.[169] However, their bilayer devices show the highest internal quantum efficiency (IQE) of 50 % still for the smallest diameter nanotubes. Literature LUMO values for ITIC-2F are in the range of -4.14 eV to -4.19 eV which should in principle match with diameters of 1.4 nm.[21] The energy transfer in such devices is still barely understood and more devices of pure chirality SWCNT/NFA solar cells have to be studied.

1.4 References

[1] S. Iijima, *Nature* **1991**, *354*, 56-58.
[2] M.S. Dresselhaus, G. Dresselhaus, R. Saito, *Carbon* **1995**, *33*, 883-891.
[3] M.V. Kharlamova, *Prog Mater Sci* **2016**, *77*, 125-211.
[4] J.W.G. Wilder, L.C. Venema, A.G. Rinzler, R.E. Smalley, C. Dekker, *Nature* **1998**, *391*, 59.
[5] L. Yu, C. Shearer, J. Shapter, *Chem Rev* **2016**, *116*, 13413-13453.
[6] M.S. Dresselhaus, G. Dresselhaus, A. Jorio, *Annu Rev Mater Res* **2004**, *34*, 247-278.
[7] M. Ouyang, J. Huang, C.M. Lieber, *Acc Chem Res* **2002**, *35*, 1018-1025.
[8] S. Reich, C. Thomsen, J. Maultzsch, *Carbon Nanotubes: Basic Concepts and Physical Properties*, Wiley-VCH Verlag GmbH, Berlin, **2004**.
[9] X. Wei, S. Li, W. Wang, X. Zhang, W. Zhou, S. Xie, H. Liu, *Adv Sci* **2022**, *9*, 2200054.
[10] M. Takase, H. Ajiki, Y. Mizumoto, K. Komeda, M. Nara, H. Nabika, S. Yasuda, H. Ishihara, K. Murakoshi, *Nat Photonics* **2013**, *7*, 550-554.
[11] Y. Cao, S. Cong, X. Cao, F. Wu, Q. Liu, M.R. Amer, C. Zhou, *Top Curr Chem (Cham)* **2017**, *375*, 75.
[12] L. Van Hove, *Phys Rev* **1953**, *89*, 1189-1193.
[13] S. Nanot, E.H. Haroz, J.H. Kim, R.H. Hauge, J. Kono, *Adv Mater* **2012**, *24*, 4977-94.
[14] R. Saito, G. Dresselhaus, M.S. Dresselhaus, *Phys Rev B* **2000**, *61*, 2981-2990.
[15] R. Saito, M. Fujita, G. Dresselhaus, M.S. Dresselhaus, *Appl Phys Lett* **1992**, *60*, 2204-2206.
[16] M.J. O'Connell, S.M. Bachilo, C.B. Huffman, V.C. Moore, M.S. Strano, E.H. Haroz, K.L. Rialon, P.J. Boul, W.H. Noon, C. Kittrell, J. Ma, R.H. Hauge, R.B. Weisman, R.E. Smalley, *Science* **2002**, *297*, 593-6.
[17] S.M. Bachilo, M.S. Strano, C. Kittrell, R.H. Hauge, R.E. Smalley, R.B. Weisman, *Science* **2002**, *298*, 2361-6.
[18] M.S. Dresselhaus, G. Dresselhaus, R. Saito, A. Jorio, *Annu Rev Phys Chem* **2007**, *58*, 719-47.
[19] P.T. Araujo, S.K. Doorn, S. Kilina, S. Tretiak, E. Einarsson, S. Maruyama, H. Chacham, M.A. Pimenta, A. Jorio, *Phys Rev Lett* **2007**, *98*, 067401.
[20] M.S. Dresselhaus, G. Dresselhaus, R. Saito, A. Jorio, *Phys Rep* **2005**, *409*, 47-99.
[21] L. Wieland, H. Li, C. Rust, J. Chen, B.S. Flavel, *Adv Energy Mater* **2020**, *11*, 2002880.
[22] A.V. Naumov, S. Ghosh, D.A. Tsyboulski, S.M. Bachilo, R.B. Weisman, *ACS Nano* **2011**, *5*, 1639-48.
[23] V. Perebeinos, J. Tersoff, P. Avouris, *Phys Rev Lett* **2004**, *92*, 257402.
[24] M. Pfohl, D.D. Tune, A. Graf, J. Zaumseil, R. Krupke, B.S. Flavel, *ACS Omega* **2017**, *2*, 1163-1171.
[25] J. Campo, Y. Piao, S. Lam, C.M. Stafford, J.K. Streit, J.R. Simpson, A.R. Hight Walker, J.A. Fagan, *Nanoscale Horizons* **2016**, *1*, 317–324.
[26] N.F. Hartmann, R. Pramanik, A.M. Dowgiallo, R. Ihly, J.L. Blackburn, S.K. Doorn, *ACS Nano* **2016**, *10*, 11449-11458.
[27] Y. Ando, X.L. Zhao, T. Sugai, M. Kumar, *Mater Today* **2004**, *7*, 22-29.
[28] A. Krüger, *Kohlenstoff-Nanoröhren*, Teubner, Wiesbaden, **2007**.
[29] N. Arora, N.N. Sharma, *Diam Relat Mater* **2014**, *50*, 135-150.
[30] T. Guo, P. Nikolaev, A. Thess, D.T. Colbert, R.E. Smalley, *Chem Phys Lett* **1995**, *243*, 49-54.
[31] A. Thess, R. Lee, P. Nikolaev, H. Dai, P. Petit, J. Robert, C. Xu, Y.H. Lee, S.G. Kim, A.G. Rinzler, D.T. Colbert, G.E. Scuseria, D. Tomanek, J.E. Fischer, R.E. Smalley, *Science* **1996**, *273*, 483-7.
[32] M. Kumar, Y. Ando, *J Nanosci Nanotechnol* **2010**, *10*, 3739-58.
[33] M.J. Bronikowski, P.A. Willis, D.T. Colbert, K.A. Smith, R.E. Smalley, *J Vac Sci Technol A* **2001**, *19*, 1800-1805.
[34] B. Kitiyanan, W.E. Alvarez, J.H. Harwell, D.E. Resasco, *Chem Phys Lett* **2000**, *317*, 497-503.

[35] F. Yang, X. Wang, D. Zhang, J. Yang, D. Luo, Z. Xu, J. Wei, J.Q. Wang, Z. Xu, F. Peng, X. Li, R. Li, Y. Li, M. Li, X. Bai, F. Ding, Y. Li, *Nature* **2014**, *510*, 522-4.
[36] H. Wang, L. Wei, F. Ren, Q. Wang, L.D. Pfefferle, G.L. Haller, Y. Chen, *ACS Nano* **2013**, *7*, 614-26.
[37] Y. Yao, C. Feng, J. Zhang, Z. Liu, *Nano Lett* **2009**, *9*, 1673-7.
[38] B. Liu, F. Wu, H. Gui, M. Zheng, C. Zhou, *ACS Nano* **2017**, *11*, 31-53.
[39] S. Deng, Y. Zhang, A.H. Brozena, M.L. Mayes, P. Banerjee, W.A. Chiou, G.W. Rubloff, G.C. Schatz, Y. Wang, *Nat Commun* **2011**, *2*, 382.
[40] A. Nish, J.Y. Hwang, J. Doig, R.J. Nicholas, *Nat Nanotechnol* **2007**, *2*, 640-6.
[41] B.S. Flavel, K.E. Moore, M. Pfohl, M.M. Kappes, F. Hennrich, *ACS Nano* **2014**, *8*, 1817-26.
[42] H. Li, G. Gordeev, O. Garrity, S. Reich, B.S. Flavel, *ACS Nano* **2019**, *13*, 2567-2578.
[43] M. Tange, T. Okazaki, S. Iijima, *ACS Appl Mater Interfaces* **2012**, *4*, 6458-62.
[44] A. Graf, Y. Zakharko, S.P. Schiessl, C. Backes, M. Pfohl, B.S. Flavel, J. Zaumseil, *Carbon* **2016**, *105*, 593-599.
[45] W. Gomulya, G.D. Costanzo, E.J. de Carvalho, S.Z. Bisri, V. Derenskyi, M. Fritsch, N. Frohlich, S. Allard, P. Gordiichuk, A. Herrmann, S.J. Marrink, M.C. dos Santos, U. Scherf, M.A. Loi, *Adv Mater* **2013**, *25*, 2948-56.
[46] D.J. Bindl, M.Y. Wu, F.C. Prehn, M.S. Arnold, *Nano Lett* **2011**, *11*, 455-60.
[47] Y. Joo, G.J. Brady, M.J. Shea, M.B. Oviedo, C. Kanimozhi, S.K. Schmitt, B.M. Wong, M.S. Arnold, P. Gopalan, *ACS Nano* **2015**, *9*, 10203-13.
[48] Y. Joo, G.J. Brady, C. Kanimozhi, J. Ko, M.J. Shea, M.T. Strand, M.S. Arnold, P. Gopalan, *ACS Appl Mater Interfaces* **2017**, *9*, 28859-28867.
[49] K.S. Mistry, B.A. Larsen, J.L. Blackburn, *ACS Nano* **2013**, *7*, 2231-9.
[50] S.K. Samanta, M. Fritsch, U. Scherf, W. Gomulya, S.Z. Bisri, M.A. Loi, *Acc Chem Res* **2014**, *47*, 2446-56.
[51] R. Si, L. Wei, H. Wang, D. Su, S.H. Mushrif, Y. Chen, *Chem Asian J* **2014**, *9*, 868-77.
[52] F. Jakubka, S.P. Schiessl, S. Martin, J.M. Englert, F. Hauke, A. Hirsch, J. Zaumseil, *ACS Macro Lett* **2012**, *1*, 815-819.
[53] X. Tu, A.R. Hight Walker, C.Y. Khripin, M. Zheng, *J Am Chem Soc* **2011**, *133*, 12998-3001.
[54] H. Li, G. Gordeev, O. Garrity, N.A. Peyyety, P.B. Selvasundaram, S. Dehm, R. Krupke, S. Cambre, W. Wenseleers, S. Reich, M. Zheng, J.A. Fagan, B.S. Flavel, *ACS Nano* **2019**.
[55] A.A. Green, M.C. Duch, M.C. Hersam, *Nano Research* **2009**, *2*, 69-77.
[56] H. Li, C.M. Sims, R. Kang, F. Biedermann, J.A. Fagan, B.S. Flavel, *Carbon* **2023**, *204*, 475.
[57] M.S. Arnold, S.I. Stupp, M.C. Hersam, *Nano Lett* **2005**, *5*, 713-8.
[58] H. Li, G. Gordeev, S. Wasserroth, V.S.K. Chakravadhanula, S.K.C. Neelakandhan, F. Hennrich, A. Jorio, S. Reich, R. Krupke, B.S. Flavel, *Nat Nanotechnol* **2017**, *12*, 1176-1182.
[59] M. Zheng, *Top Curr Chem* **2017**, *375*, 13.
[60] J.A. Fagan, E.H. Haroz, R. Ihly, H. Gui, J.L. Blackburn, J.R. Simpson, S. Lam, A.R. Hight Walker, S.K. Doorn, M. Zheng, *ACS Nano* **2015**, *9*, 5377-90.
[61] T.A. Shastry, A.J. Morris-Cohen, E.A. Weiss, M.C. Hersam, *J Am Chem Soc* **2013**, *135*, 6750.
[62] H. Liu, T. Tanaka, Y. Urabe, H. Kataura, *Nano Lett* **2013**, *13*, 1996-2003.
[63] J.G. Clar, C.A. Silvera Batista, S. Youn, J.C. Bonzongo, K.J. Ziegler, *J Am Chem Soc* **2013**, *135*, 17758-67.
[64] N.R. Tummala, A. Striolo, *ACS Nano* **2009**, *3*, 595-602.
[65] C.Y. Khripin, J.A. Fagan, M. Zheng, *J Am Chem Soc* **2013**, *135*, 6822-5.
[66] X. Zeng, D. Yang, H. Liu, N. Zhou, Y. Wang, W. Zhou, S. Xie, H. Kataura, *Adv Mater Interfaces* **2018**, *5*, 1700727.
[67] C.J. Shih, S.C. Lin, M.S. Strano, D. Blankschtein, *J Phys Chem C* **2015**, *119*, 1047-1060.
[68] C.Y. Zhang, P. Wang, B. Barnes, J. Fortner, Y.H. Wang, *Chemistry of Materials* **2021**, *33*, 4551-4557.
[69] K. Moshammer, F. Hennrich, M.M. Kappes, *Nano Research* **2009**, *2*, 599-606.

[70] M.S. Arnold, A.A. Green, J.F. Hulvat, S.I. Stupp, M.C. Hersam, *Nat Nanotechnol* **2006**, *1*, 60.
[71] H. Liu, D. Nishide, T. Tanaka, H. Kataura, *Nat Commun* **2011**, *2*, 309.
[72] S.R. Lustig, A. Jagota, C. Khripin, M. Zheng, *J Phys Chem B* **2005**, *109*, 2559-66.
[73] N.K. Subbaiyan, S. Cambre, A.N. Parra-Vasquez, E.H. Haroz, S.K. Doorn, J.G. Duque, *ACS Nano* **2014**, *8*, 1619-28.
[74] H. Gui, J.K. Streit, J.A. Fagan, A.R. Hight Walker, C. Zhou, M. Zheng, *Nano Lett* **2015**, *15*, 1642-6.
[75] B. Podlesny, T. Shiraki, D. Janas, *Sci Rep* **2020**, *10*, 9250.
[76] J.A. Fagan, *Nanoscale Adv* **2019**, *1*, 3307-3324.
[77] M. Zhang, C.Y. Khripin, J.A. Fagan, P. McPhie, Y. Ito, M. Zheng, *Anal Chem* **2014**, *86*, 3980.
[78] M. Knight, R. Lazo-Portugal, S.N. Ahn, S. Stefansson, *J Chromatogr A* **2017**, *1483*, 93-100.
[79] X. Huang, R.S. McLean, M. Zheng, *Anal Chem* **2005**, *77*, 6225-8.
[80] K.E. Moore, M. Pfohl, F. Hennrich, V.S. Chakradhanula, C. Kuebel, M.M. Kappes, J.G. Shapter, R. Krupke, B.S. Flavel, *ACS Nano* **2014**, *8*, 6756-64.
[81] M.S. Strano, S.K. Doorn, E.H. Haroz, C. Kittrell, R.H. Hauge, R.E. Smalley, *Nano Lett* **2003**, *3*, 1091-1096.
[82] W. Wenseleers, S. Cambré, J. Čulin, A. Bouwen, E. Goovaerts, *Adv Mater* **2007**, *19*, 2274-2278.
[83] S. Cambre, W. Wenseleers, *Angew Chem Int Ed Engl* **2011**, *50*, 2764-8.
[84] J.A. Fagan, J.Y. Huh, J.R. Simpson, J.L. Blackburn, J.M. Holt, B.A. Larsen, A.R. Walker, *ACS Nano* **2011**, *5*, 3943-53.
[85] W. Wenseleers, I.I. Vlasov, E. Goovaerts, E.D. Obraztsova, A.S. Lobach, A. Bouwen, *Adv Func Mater* **2004**, *14*, 1105-1112.
[86] S. Cambre, B. Schoeters, S. Luyckx, E. Goovaerts, W. Wenseleers, *Phys Rev Lett* **2010**, *104*, 207401.
[87] H. Li, G. Gordeev, D. Toroz, D. Di Tommaso, S. Reich, B.S. Flavel, *J Phys Chem C* **2021**, *125*, 7476-7487.
[88] J. Streit, C.R. Snyder, J. Campo, M. Zheng, J.R. Simpson, A.R.H. Walker, J.A. Fagan, *J Phys Chem C* **2018**, *122*, 11577-11585.
[89] L. Yang, J. Han, *Phys Rev Lett* **2000**, *85*, 154-7.
[90] Y.I. Song, G.Y. Kim, H.K. Choi, H.J. Jeong, K.K. Kim, C.M. Yang, S.C. Lim, K.H. An, K.T. Jung, Y.H. Lee, *Chem Vapor Depos* **2006**, *12*, 375-379.
[91] A. Classen, L. Einsiedler, T. Heumueller, A. Graf, M. Brohmann, F. Berger, S. Kahmann, M. Richter, G.J. Matt, K. Forberich, J. Zaumseil, C.J. Brabec, *Adv Energy Mater* **2018**, *8*, 1801913.
[92] L. Wieland, H. Li, X. Zhang, J. Chen, B.S. Flavel, *Small Science* **2022**, *3*, 2200079.
[93] S.L. Guillot, K.S. Mistry, A.D. Avery, J. Richard, A.M. Dowgiallo, P.F. Ndione, J. van de Lagemaat, M.O. Reese, J.L. Blackburn, *Nanoscale* **2015**, *7*, 6556-66.
[94] M. Rdest, D. Janas, *Energies* **2021**, *14*, 1890.
[95] R.C. Tenent, T.M. Barnes, J.D. Bergeson, A.J. Ferguson, B. To, L.M. Gedvilas, M.J. Heben, J.L. Blackburn, *Adv Mater* **2009**, *21*, 3210.
[96] R.M. Jain, R. Howden, K. Tvrdy, S. Shimizu, A.J. Hilmer, T.P. McNicholas, K.K. Gleason, M.S. Strano, *Adv Mater* **2012**, *24*, 4436-4439.
[97] L. Wieland, C. Rust, H. Li, M. Jakoby, I. Howard, F. Li, J. Shi, J. Chen, B.S. Flavel, *Carbon* **2021**, *184*, 828-835.
[98] M. Pfohl, K. Glaser, A. Graf, A. Mertens, D.D. Tune, T. Puerckhauer, A. Alam, L. Wei, Y. Chen, J. Zaumseil, A. Colsmann, R. Krupke, B.S. Flavel, *Adv Energy Mater* **2016**, *6*, 1600890.
[99] Z. Wu, Z. Chen, X. Du, J.M. Logan, J. Sippel, M. Nikolou, K. Kamaras, J.R. Reynolds, D.B. Tanner, A.F. Hebard, A.G. Rinzler, *Science* **2004**, *305*, 1273-6.
[100] D.H. Arias, D.B. Sulas-Kern, S.M. Hart, H.S. Kang, J. Hao, R. Ihly, J.C. Johnson, J.L. Blackburn, A.J. Ferguson, *Nanoscale* **2019**, *11*, 21196-21206.

[101] A.T. Mallajosyula, W. Nie, G. Gupta, J.L. Blackburn, S.K. Doorn, A.D. Mohite, *ACS Nano* **2016**, *10*, 10808-10815.
[102] R.D. Mehlenbacher, J. Wang, N.M. Kearns, M.J. Shea, J.T. Flach, T.J. McDonough, M.Y. Wu, M.S. Arnold, M.T. Zanni, *J Phys Chem Lett* **2016**, *7*, 2024-2031.
[103] R.D. Mehlenbacher, M.Y. Wu, M. Grechko, J.E. Laaser, M.S. Arnold, M.T. Zanni, *Nano Lett* **2013**, *13*, 1495-501.
[104] C. Rust, H. Li, G. Gordeev, M. Spari, M. Guttmann, Q. Jin, S. Reich, B.S. Flavel, *Adv Func Mater* **2021**, *32*, 2107411.
[105] C. Rust, P. Shapturenka, M. Spari, Q. Jin, H. Li, A. Bacher, M. Guttmann, M. Zheng, T. Adel, A.R.H. Walker, J.A. Fagan, B.S. Flavel, *Small* **2022**, *n/a*, e2206774.
[106] K.R. Jinkins, J. Chan, R.M. Jacobberger, A. Berson, M.S. Arnold, *Adv Electron Mater* **2018**, *5*, 1800593.
[107] X. He, W. Gao, L. Xie, B. Li, Q. Zhang, S. Lei, J.M. Robinson, E.H. Haroz, S.K. Doorn, W. Wang, R. Vajtai, P.M. Ajayan, W.W. Adams, R.H. Hauge, J. Kono, *Nat Nanotechnol* **2016**, *11*, 633-8.
[108] R.W. Miles, G. Zoppi, I. Forbes, *Mater Today* **2007**, *10*, 20-27.
[109] A.S. Al-Ezzi, M.N.M. Ansari, *Appl Syst Inno* **2022**, *5*, 67.
[110] K. Yoshikawa, H. Kawasaki, W. Yoshida, T. Irie, K. Konishi, K. Nakano, T. Uto, D. Adachi, M. Kanematsu, H. Uzu, K. Yamamoto, *Nat Energy* **2017**, *2*, 17032.
[111] M.A. Green, E.D. Dunlop, G. Siefer, M. Yoshita, N. Kopidakis, K. Bothe, X.J. Hao, *Prog Photovoltaics* **2022**, *31*, 3-16.
[112] J. He, P. Gao, Z. Yang, J. Yu, W. Yu, Y. Zhang, J. Sheng, J. Ye, J.C. Amine, Y. Cui, *Adv Mater* **2017**, *29*, 1606321.
[113] Y.F. Zhang, F.S. Zu, S.T. Lee, L.S. Liao, N. Zhao, B.Q. Sun, *Adv Energy Mater* **2014**, *4*, 1300923.
[114] C. Battaglia, X. Yin, M. Zheng, I.D. Sharp, T. Chen, S. McDonnell, A. Azcatl, C. Carraro, B. Ma, R. Maboudian, R.M. Wallace, A. Javey, *Nano Lett* **2014**, *14*, 967-71.
[115] J. Dréon, Q. Jeangros, J. Cattin, J. Haschke, L. Antognini, C. Ballif, M. Boccard, *Nano Energy* **2020**, *70*, 104495.
[116] J. Chen, D.D. Tune, K. Ge, H. Li, B.S. Flavel, *Adv Func Mater* **2020**, *30*, 2000484.
[117] G. Qing, J. Yan, H. Li, J. Chen, X. Yang, Y. Bai, X. Zhang, B. Chen, J. Guo, W. Duan, K. Han, F. Li, J. Wang, D. Song, S. Wang, B.S. Flavel, J. Chen, *Carbon* **2022**, *202*, 432-437.
[118] W. Tress, *Organic Solar Cells: Theory, Experiment and Device Simulation*, Springer International Publishing, Cham, **2014**.
[119] L. Sun, Y. Chen, M. Sun, Y. Zheng, *Chem Asian J* **2023**, *n/a*.
[120] J.L. Blackburn, *ACS Energy Lett* **2017**, *2*, 1598-1613.
[121] T.A. Shastry, M.C. Hersam, *Adv Energy Mater* **2017**, *7*, 1601205.
[122] R.A. Marcus, N. Sutin, *Biochim. Biophys. Acta* **1985**, *811*, 265-322.
[123] M. Kuss-Petermann, O.S. Wenger, *Phys Chem Chem Phys* **2016**, *18*, 18657-64.
[124] T.H. Lai, S.W. Tsang, J.R. Manders, S. Chen, F. So, *Mater Today* **2013**, *16*, 424-432.
[125] S.R. Cowan, A. Roy, A.J. Heeger, *Phys Rev B* **2010**, *82*, 245207.
[126] T. Tiedje, E. Yablonovitch, G.D. Cody, B.G. Brooks, *Ieee T Electron Dev* **1984**, *31*, 711-716.
[127] A. Al-Ashouri, E. Kohnen, B. Li, A. Magomedov, H. Hempel, P. Caprioglio, J.A. Marquez, A.B. Morales Vilches, E. Kasparavicius, J.A. Smith, N. Phung, D. Menzel, M. Grischek, L. Kegelmann, D. Skroblin, C. Gollwitzer, T. Malinauskas, M. Jost, G. Matic, B. Rech, R. Schlatmann, M. Topic, L. Korte, A. Abate, B. Stannowski, D. Neher, M. Stolterfoht, T. Unold, V. Getautis, S. Albrecht, *Science* **2020**, *370*, 1300-1309.
[128] NREL, *Best Research-Cell Efficiency Chart*, https://www.nrel.gov/pv/cell-efficiency.html, (accessed Feb 2023).
[129] D. Luo, W. Jang, D.D. Babu, M.S. Kim, D.H. Wang, A.K.K. Kyaw, *J Mater Chem A* **2022**, *10*, 3255-3295.

[130] J. Lee, S. Song, J.F. Huang, Z.F. Du, H. Lee, Z.Y. Zhu, S.J. Ko, T.Q. Nguyen, J.Y. Kim, K. Cho, G.C. Bazan, *Acs Materials Lett* **2020**, *2*, 395-402.
[131] J. Yan, X. Rodriguez-Martinez, D. Pearce, H. Douglas, D. Bili, M. Azzouzi, F. Eisner, A. Virbule, E. Rezasoltani, V. Belova, B. Dorling, S. Few, A.A. Szumska, X. Hou, G. Zhang, H.L. Yip, M. Campoy-Quiles, J. Nelson, *Energ Environ Sci* **2022**, *15*, 2958-2973.
[132] Q.S. Liu, Y.F. Jiang, K. Jin, J.Q. Qin, J.G. Xu, W.T. Li, J. Xiong, J.F. Liu, Z. Xiao, K. Sun, S.F. Yang, X.T. Zhang, L.M. Ding, *Sci Bull* **2020**, *65*, 272-275.
[133] X.N. Zhang, C. Li, J.Q. Xu, R. Wang, J.L. Song, H. Zhang, Y.X. Li, Y.N. Jing, S.L. Li, G.B. Wu, J. Zhou, X. Li, Y.Y. Zhang, X. Li, J.Q. Zhang, C.F. Zhang, H.Q. Zhou, Y.M. Sun, Y. Zhang, *Joule* **2022**, *6*, 444-457.
[134] L. Duan, Y. Zhang, H. Yi, F. Haque, R. Deng, H. Guan, Y. Zou, A. Uddin, *Energy Technol* **2019**, *8*, 1900924.
[135] M. Zhang, L. Zhu, G. Zhou, T. Hao, C. Qiu, Z. Zhao, Q. Hu, B.W. Larson, H. Zhu, Z. Ma, Z. Tang, W. Feng, Y. Zhang, T.P. Russell, F. Liu, *Nat Commun* **2021**, *12*, 309.
[136] G. Yao, Y.S. Ge, X.Y. Xiao, L.F. Zhang, N. Yi, H.Q. Luo, S.S. Yuan, W.H. Zhou, *ACS Appl Energy Mater* **2022**, *5*, 1193-1204.
[137] X. He, C.C.S. Chan, J. Kim, H. Liu, C.J. Su, U.S. Jeng, H. Su, X. Lu, K.S. Wong, W.C.H. Choy, *Small Methods* **2022**, *6*, 2101475.
[138] Y. Su, L. Zhang, Z. Ding, Y. Zhang, Y. Wu, Y. Duan, Q. Zhang, J. Zhang, Y. Han, Z. Xu, R. Zhang, K. Zhao, S. Liu, *Adv Energy Mater* **2022**, *12*, 2103940.
[139] M.S. Arnold, J.L. Blackburn, J.J. Crochet, S.K. Doorn, J.G. Duque, A. Mohite, H. Telg, *Phys Chem Chem Phys* **2013**, *15*, 14896-918.
[140] J.L. Blackburn, T.M. Barnes, M.C. Beard, Y.H. Kim, R.C. Tenent, T.J. McDonald, B. To, T.J. Coutts, M.J. Heben, *ACS Nano* **2008**, *2*, 1266-74.
[141] K.S. Mistry, B.A. Larsen, J.D. Bergeson, T.M. Barnes, G. Teeter, C. Engtrakul, J.L. Blackburn, *ACS Nano* **2011**, *5*, 3714-23.
[142] T.M. Barnes, J.L. Blackburn, J. van de Lagemaat, T.J. Coutts, M.J. Heben, *ACS Nano* **2008**, *2*, 1968-76.
[143] R. Ihly, A.M. Dowgiallo, M.J. Yang, P. Schulz, N.J. Stanton, O.G. Reid, A.J. Ferguson, K. Zhu, J.J. Berry, J.L. Blackburn, *Energ Environ Sci* **2016**, *9*, 1439-1449.
[144] S.N. Habisreutinger, N.K. Noel, B.W. Larson, O.G. Reid, J.L. Blackburn, *ACS Energy Lett* **2019**, *4*, 1872-1879.
[145] I. Jeon, A. Shawky, S. Seo, Y. Qian, A. Anisimov, E.I. Kauppinen, Y. Matsuo, S. Maruyama, *J Mater Chem A* **2020**, *8*, 11141-11147.
[146] M.A. Contreras, T.M. Barnes, J. van de Lagemaat, G. Rumbles, T.J. Coutts, C. Weeks, P. Glatkowski, I. Levitsky, J. Peltola, D.A. Britz, *J Phys Chem C* **2007**, *111*, 14045-14048.
[147] T.M. Barnes, X. Wu, J. Zhou, A. Duda, J. van de Lagemaat, T.J. Coutts, C.L. Weeks, D.A. Britz, P. Glatkowski, *Appl Phys Lett* **2007**, *90*, 243503.
[148] A.B. Phillips, R.R. Khanal, Z. Song, R.M. Zartman, J.L. DeWitt, J.M. Stone, P.J. Roland, V.V. Plotnikov, C.W. Carter, J.M. Stayancho, R.J. Ellingson, A.D. Compaan, M.J. Heben, *Nano Lett* **2013**, *13*, 5224-32.
[149] T.M. Barnes, J.D. Bergeson, R.C. Tenent, B.A. Larsen, G. Teeter, K.M. Jones, J.L. Blackburn, J. van de Lagemaat, *Appl Phys Lett* **2010**, *96*, 243309.
[150] J. van de Lagemaat, T.M. Barnes, G. Rumbles, S.E. Shaheen, T.J. Coutts, C. Weeks, I. Levitsky, J. Peltola, P. Glatkowski, *Appl Phys Lett* **2006**, *88*, 233503.
[151] M.W. Rowell, M.A. Topinka, M.D. McGehee, H.J. Prall, G. Dennler, N.S. Sariciftci, L.B. Hu, G. Gruner, *Appl Phys Lett* **2006**, *88*, 233506.
[152] G.D.M.R. Dabera, K.D.G.I. Jayawardena, M.R.R. Prabhath, I. Yahya, Y.Y. Tan, N.A. Nismy, H. Shiozawa, M. Sauer, G. Ruiz-Soria, P. Ayala, V. Stolojan, A.A.D.T. Adikaari, P.D. Jarowski, T. Pichler, S.R.P. Silva, *ACS Nano* **2013**, *7*, 556-565.

[153] I. Jeon, Y. Matsuo, S. Maruyama, *Single-Walled Carbon Nanotubes in Solar Cells*, Springer International Publishing, Cham, **2018**.
[154] I. Jeon, J. Yoon, U. Kim, C. Lee, R. Xiang, A. Shawky, J. Xi, J. Byeon, H.M. Lee, M. Choi, S. Maruyama, Y. Matsuo, *Advanced Energy Materials* **2019**, *9*, 1901204.
[155] J.H. Chen, K.P. Ge, B.B. Chen, J.X. Guo, L.L. Yang, Y. Wu, G. Coletti, H.X. Liu, F. Li, D.W. Liu, Z.Q. Wang, Y. Xu, Y.H. Mai, *Sol Energ Mat Sol C* **2019**, *195*, 99-105.
[156] J.H. Chen, L. Wan, H. Li, J. Yan, J.K. Ma, B. Sun, F. Li, B.S. Flavel, *Adv Funct Mater* **2020**, *30*, 2004476.
[157] D.D. Tune, N. Mallik, H. Fornasier, B.S. Flavel, *Adv Energy Mater* **2019**, *10*, 1903261.
[158] T.G. Allen, J. Bullock, X.B. Yang, A. Javey, S. De Wolf, *Nat Energy* **2019**, *4*, 914-928.
[159] M. Gong, T.A. Shastry, Y. Xie, M. Bernardi, D. Jasion, K.A. Luck, T.J. Marks, J.C. Grossman, S. Ren, M.C. Hersam, *Nano Lett* **2014**, *14*, 5308-14.
[160] M. Pfohl, K. Glaser, J. Ludwig, D.D. Tune, S. Dehm, C. Kayser, A. Colsmann, R. Krupke, B.S. Flavel, *Adv Energy Mater* **2016**, *6*, 1501345.
[161] M. Gong, T.A. Shastry, Q. Cui, R.R. Kohlmeyer, K.A. Luck, A. Rowberg, T.J. Marks, M.F. Durstock, H. Zhao, M.C. Hersam, S. Ren, *ACS Appl Mater Interfaces* **2015**, *7*, 7428-35.
[162] D.J. Bindl, M.S. Arnold, *J Phys Chem C* **2013**, *117*, 2390-2395.
[163] D.J. Bindl, N.S. Safron, M.S. Arnold, *ACS Nano* **2010**, *4*, 5657-64.
[164] E. Kymakis, G.A.J. Amaratunga, *Rev Adv Mater Sci* **2005**, *10*, 300-305.
[165] S. Ren, M. Bernardi, R.R. Lunt, V. Bulovic, J.C. Grossman, S. Gradecak, *Nano Lett* **2011**, *11*, 5316-21.
[166] D.J. Bindl, A.S. Brewer, M.S. Arnold, *Nano Res* **2011**, *4*, 1174-1179.
[167] M.J. Shea, J.L. Wang, J.T. Flach, M.T. Zanni, M.S. Arnold, *APL Materials* **2018**, *6*, 056104.
[168] M.J. Shea, M.S. Arnold, *Appl Phys Lett* **2013**, *102*, 243101.
[169] J.L. Wang, S.R. Peurifoy, M.T. Bender, F. Ng, K.S. Choi, C. Nuckolls, M.S. Arnold, *J Phys Chem C* **2019**, *123*, 21395-21402.
[170] J.T. Flach, J. Wang, M.S. Arnold, M.T. Zanni, *J Phys Chem Lett* **2020**, *11*, 6016-6024.
[171] J.L. Wang, M.J. Shea, J.T. Flach, T.J. McDonough, A.J. Way, M.T. Zanni, M.S. Arnold, *J Phys Chem C* **2017**, *121*, 8310-8318.
[172] M. Grechko, Y. Ye, R.D. Mehlenbacher, T.J. McDonough, M.Y. Wu, R.M. Jacobberger, M.S. Arnold, M.T. Zanni, *ACS Nano* **2014**, *8*, 5383-94.
[173] D.J. Bindl, M.J. Shea, M.S. Arnold, *Chem Phys* **2013**, *413*, 29-34.
[174] S. Huang, X.F. Du, M.B. Ma, L.L. Xiong, *Nanotechnol Rev* **2021**, *10*, 1592-1623.
[175] D.D. Tune, J.G. Shapter, *Energ Environ Sci* **2013**, *6*, 2572-2577.
[176] K. Yanagi, K. Iakoubovskii, H. Matsui, H. Matsuzaki, H. Okamoto, Y. Miyata, Y. Maniwa, S. Kazaoui, N. Minami, H. Kataura, *J Am Chem Soc* **2007**, *129*, 4992-4997.
[177] S. van Bezouw, D.H. Arias, R. Ihly, S. Cambre, A.J. Ferguson, J. Campo, J.C. Johnson, J. Defillet, W. Wenseleers, J.L. Blackburn, *ACS Nano* **2018**, *12*, 6881-6894.
[178] S. Cambre, J. Campo, C. Beirnaert, C. Verlackt, P. Cool, W. Wenseleers, *Nat Nanotechnol* **2015**, *10*, 248-52.
[179] Y. Almadori, G. Delport, R. Chambard, L. Orcin-Chaix, A.C. Selvati, N. Izard, A. Belhboub, R. Aznar, B. Jousselme, S. Campidelli, P. Hermet, R. Le Parc, T. Saito, Y. Sato, K. Suenaga, P. Puech, J.S. Lauret, G. Cassabois, J.L. Bantignies, L. Alvarez, *Carbon* **2019**, *149*, 772-780.
[180] Y. Almadori, L. Alvarez, R. Le Parc, R. Aznar, F. Fossard, A. Loiseau, B. Jousselme, S. Campidelli, P. Hermet, A. Belhboub, A. Rahmani, T. Saito, J.L. Bantignies, *J Phys Chem C* **2014**, *118*, 19462-19468.
[181] E. Gaufrès, N.Y.W. Tang, F. Lapointe, J. Cabana, M.A. Nadon, N. Cottenye, F. Raymond, T. Szkopek, R. Martel, *Nat Photonics* **2013**, *8*, 72-78.
[182] S. Forel, H. Li, S. van Bezouw, J. Campo, L. Wieland, W. Wenseleers, B.S. Flavel, S. Cambre, *Nanoscale* **2022**, *14*, 8385-8397.

[183] N. Murakami, H. Miyake, T. Tajima, K. Nishikawa, R. Hirayama, Y. Takaguchi, *J Am Chem Soc* **2018**, *140*, 3821-3824.
[184] Y. Takaguchi, H. Miyake, T. Izawa, D. Miyamoto, R. Sagawa, T. Tajima, *Phosphorus Sulfur* **2019**, *194*, 707-711.
[185] L. Lüer, S. Hoseinkhani, D. Polli, J. Crochet, T. Hertel, G. Lanzani, *Nat Phys* **2008**, *5*, 54-58.
[186] F. Wang, G. Dukovic, L.E. Brus, T.F. Heinz, *Science* **2005**, *308*, 838-41.
[187] R. Ihly, K.S. Mistry, A.J. Ferguson, T.T. Clikeman, B.W. Larson, O. Reid, O.V. Boltalina, S.H. Strauss, G. Rumbles, J.L. Blackburn, *Nat Chem* **2016**, *8*, 603-609.

- this page left intentionally blank -

2 Experimental Methods

In this chapter all general experimental methods are explained, beginning with the preparation of two different (6,5) solutions either in toluene or water and the necessary separation procedure. The differences in film fabrication based on these two solutions are outlined. However, the incorporation of these films into the solar cell architecture is not included in this general methods section mainly due to the small changes and improvements for every chapter. Instead, it is listed after every results part as a subchapter, the most general description is given in the experimental details section 3.4. The characterization methods are on the other hand the same for all devices, thus they are summarized here in the last paragraphs.

2.1 (6,5) SWCNT in Toluene

The (6,5) suspension was prepared by shear-force mixing[1] with the raw material CoMoCAT® (Sigma-Aldrich, 773735 lot no. MKBZ1159V) and the dispersant and sorting polymer PFO-BPy[2], poly[(9,9-dioctylfluorenyl-2,7diyl)-alt-co-(6,6'-(2-20-bipyridine))] (American Dye Source, lot no. 19L014A1). 40 mg CoMoCAT® enriched in (6,5) and 55 mg PFO-BPy were added into 110 mL toluene and shear-force mixed for 65 h. Afterwards the suspension was ultra-centrifuged at 45560 g for 30 minutes at 20°C (SW-40-Ti rotor, Beckman-Coulter, Optima L-80 XP). The spectrum of the (6,5) solution in Figure 2.1A shows the main absorbance signal at 360 nm which is assigned to the PFO-BPy and the (6,5) optical density (OD) is 0.03 in a 1 mm quartz cuvette.

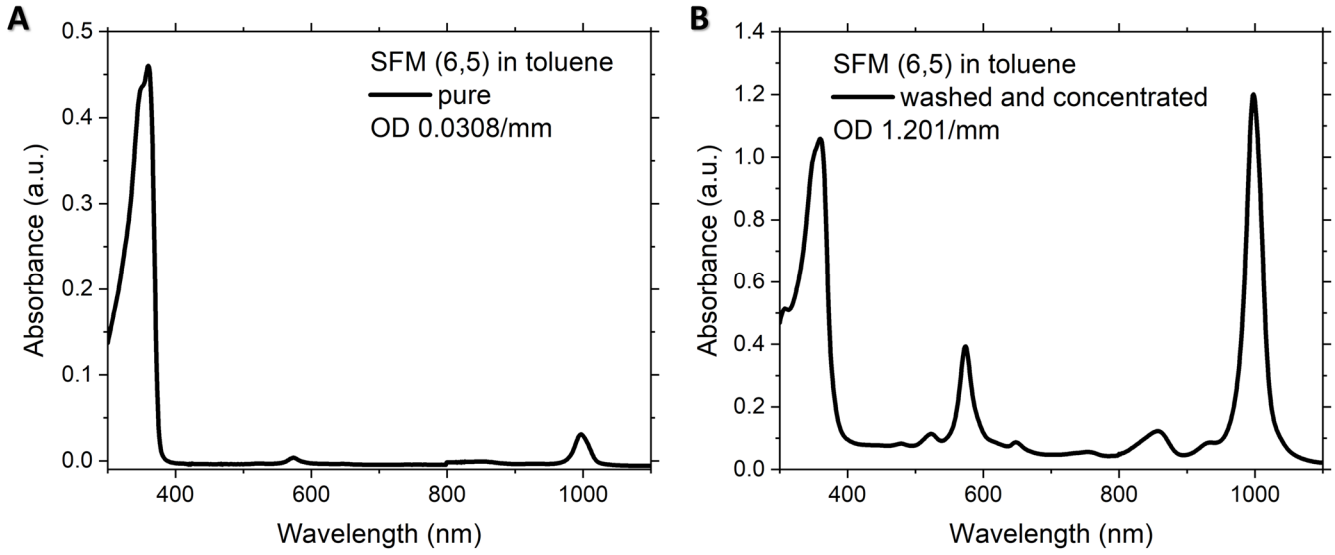

Figure 2.1: Absorbance spectra of (A) (6,5) SWCNTs in toluene directly after shear-force mixing (SFM) and (B) after an additional concentration and washing step to remove most of the wrapping polymer PFO-BPy. Removal of excess PFO-BPy is evidenced by a reduction in the peak at 360 nm. (1 mm pathlength) Figure reproduced from [3]

By Filtration on a nylon membrane (0.2 mm pore size) the supernatant of the centrifugation was rinsed with toluene to reduce the excess polymer and was concentrated by redispersion of the (6,5) filter cake in a smaller amount of toluene. The resulting absorbance spectrum is shown in Figure 2.1B with an OD of 1.2/mm for (6,5) while the polymer peak is even lower. The two spectra are characteristic for the preparation of (6,5) SWCNT solutions. The results in this thesis are based on several (6,5) solutions, for comparison the maximum optical density of (6,5) SWCNTs around 1000 nm will be stated or alternatively the concentration.

The concentration of the (6,5) solutions can be estimated by the following relation[4] where 1 $OD_{@990nm}$ is equal to 5-10 µg (6,5) tubes/mL measured with a 10 mm optical path. For example, the high concentrated (6,5) solution in Figure 2.1B has an $OD_{@990nm}$ of 0.9015/mm resulting in a concentration of 45-90 µg/mL.

2.2 Aqueous SWCNT Dispersion

Surfactant dispersed SWCNTs in aqueous solution were sorted by ATPE (aqueous two phase extraction) using a previously reported method.[5, 6] The SWCNTs (6,5), (7,6) and (10,3) were prepared from raw soot from three different sources: CoMoCAT® SG65i (Chasm, lot no. SG65i-L58), CoMoCAT® SG76i (Chasm, lot no. SG76-L39) and HiPco (Nano Integris, lot no. HR-29-073), respectively. 40 mg of SWCNT powder was first dispersed in 40 mL of 2 % sodium deoxycholate (DOC) (BioXtra 98+%, Sigma Aldrich) by 45 min tip sonication (0.9 W/mL) in an ice bath followed by centrifugation at 45560 g for 1 hour (Beckman Optima L-80 XP, SW 40 Ti rotor).

The supernatant was collected and ATPE separation performed using the conditions described by Fagan et al.[7] Materials like SDS (>99%), SC (>99%), and iodixanol (sold as Opti-Prep, 60% volume fraction stock solution) were acquired from Sigma-Aldrich and used without further purification. NaClO (10–15% solution) was acquired from Sigma-Aldrich and diluted 1:99 with 18.1 MΩ H_2O to generate a working NaClO stock solution. Poly(ethylene glycol) (PEG, Mw 6 kDa) was acquired from Alfa Aesar. Dextran 70 (DX, Mw 70 kDa) was purchased from TCI.
In step 1, the DOC concentration was adjusted to 0.05 % and a diameter sorting was performed by gradually increasing the sodium dodecylsulfate (SDS) concentration. All SWCNTs with a diameter larger than the target species were partitioned to the top phase before adding fresh top phase and

adjusting SDS concentrations to 1.5 %, 0.95 % and 0.5 % for the partitioning of (6,5), (7,6) and (10,3) respectively. In step 2, the top phase containing the enriched single chirality were collected and a metallic-semiconducting separation performed. This was achieved with a sodium cholate (SC) concentration of 0.9 % and 1 % SDS with 5 µL/mL NaClO. Each of the different species were finally concentrated and adjusted to 1% DOC (10 g/L) in a pressurized ultrafiltration stirred cell (Millipore) with a 300 kDa molecular weight cut-off membrane. The resulting absorbance spectra of separated (6,5), (7,6) or (10,3) SWCNTs are shown in Figure 2.2. The (6,5) solution with an $OD_{@990nm}$ of 5.202/mm has a concentration of 260-520 µg/mL. If the concept is transferred on the other species and their main S_{11} absorbance, the concentration of (7,6) is roughly 51-102 µg/mL ($OD_{@1029nm}$ 1.024/mm) and for (10,3) it is 25-50 µg/mL ($OD_{@1260nm}$ 0.505/mm).

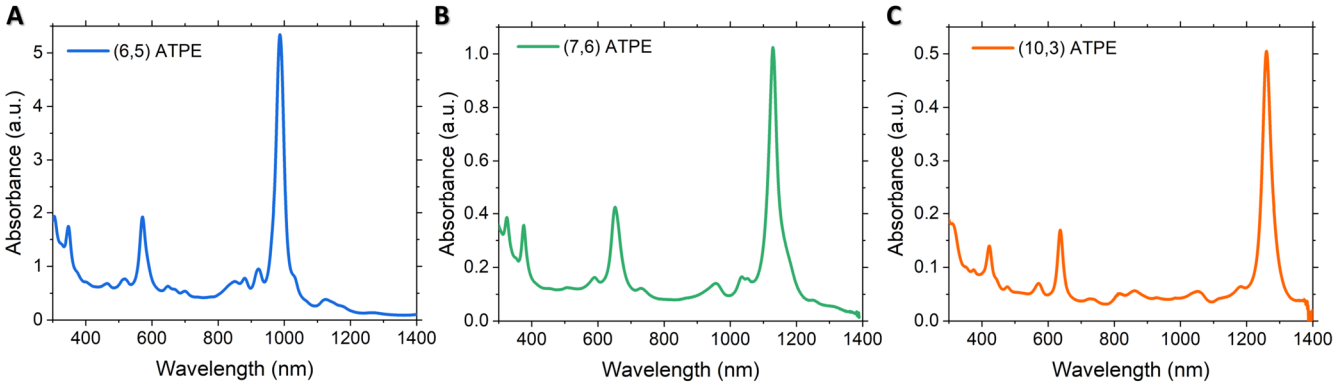

Figure 2.2: Absorbance spectra of the ATPE-sorted chiralities (6,5), (7,6) and (10,3) in water/DOC. (1 mm pathlength)

2.3 Thin Film Preparation

Separated single walled carbon nanotubes can only be incorporated into applications e.g., solar cells, if films or layers can be prepared from a CNT dispersion. The different dispersants enable film formation for either aqueous or organic solutions but in all solvents SWCNT concentration is a key parameter.

The use of organic solvents simplifies film formation because SWCNT/polymer toluene dispersions can directly be used to spin cast thin films within a solar cell layer stack. A high concentrated SWCNT dispersion is fundamental for spin coating which relies on controlling the rotation speed and duration of casting. Usually, 50-60 µL of the prepared polymer-sorted solution is spin cast at 600 rpm for 20 s followed by 1500 rpm for 5 s to remove the excess material and reach homogeneity. After annealing at 110 °C for 7 minutes, the next layer can be applied considering that the following solvents do not redissolve the layers underneath.

Material incompatibilities usually prohibit that films from aqueous dispersions can be incorporated directly. Thus, films are prepared separately by filtration and laminated onto the device by dissolving a membrane. A specific amount of aqueous SWCNTs (1, 2, 4 or 8 µg) is diluted to a total volume of 1 mL and filtered on an 80 nm pore polycarbonate membrane (47mm, it4ip, $\varepsilon_{porosity} = 6 \times 10^{12}$ m^{-2}). Therefore, a calibrated positive pressure microfluidic dead-end filtration setup is used which facilitated the SWCNT filtration by employing constant pressure. The setup is capable of in situ measurements of transmembrane pressure, volume rate and membrane retention, this allows to vary the volume rate of filtration with high accuracy (± 1.7 µL/min at 100 µL/min). Flow rate was set to 220 µL/min for the first 250 µL and then increased to 1150 µL/min for the remaining volume to adhere the SWCNTs to the membrane surface. For detailed information on the dead-end filtration setup and optimized parameter for other raw materials see Rust et al.[8, 9] The resulting film had a diameter of 22 mm. Aqueous SWCNT films on polycarbonate are transferred onto the layer stack in air, by turning it upside down and then wetting and heating (70 °C, 5 min) the film to adhere it to the layer stack. The polycarbonate membrane was then dissolved by propylamine (≥99%, Sigma-Aldrich) followed by washing with acetone and isopropanol to remove membrane or solvent residues that could contaminate the layer stack.

2.4 Characterization

2.4.1 Solar Cell Characteristics

All devices were characterized under ambient conditions. The current density-voltage characteristics (J-V curves) were measured with a Keithley 2601B source meter under AM1.5G illumination from a LOT-QuantumDesign solar simulator (450-1000 W Xe Arc Lamp). A silicon reference cell was used to check the solar simulator and calibrate the distance between the solar cell and the lamp. EQE measurements were conducted using the integrated system SpeQuest Quantum Efficiency from Rera solutions. Calibration was performed with Si 250 – 100 nm and Ge 700 – 1800 nm diodes.

2.4.2 Absorbance Measurement

UV-vis-NIR absorbance spectra of the polymer-wrapped SWCNT solutions were collected on a Cary 500 spectrometer from 1400 nm to 200 nm in a 1 mm quartz cuvette. Films for absorbance

measurements were prepared on glass microscope slides following the same spin coating or transfer procedures mentioned above.

2.4.3 Atomic Force Microscopy (AFM)

Topographies were recorded with a Dimension Icon, Bruker with NSC 19 cantilevers (µmasch) with a resonance frequency of 65 kHz and a force constant of 0.5 Nm^{-1}. Imaging was performed in the repulsive regime with standard tapping mode in air and a resolution of 1024 lines. All topographies were evaluated using open-source Gwyddion for example the determination of the root mean square (RMS).

2.4.4 Transient absorption (TA)

TA spectra were recorded by using a home-made pump-probe setup with a resolution of ≈ 200 fs. Pump pulses (745 nm, 1 kHz) were provided by the second harmonic of the signal beam of a collinear optical parametric amplifier (Light Conversion, Orpheus). White light continuum pulses (550 – 1100 nm) were generated by pumping a 2 mm thick sapphire crystal, using the output of a commercial ytterbium pumped oscillator – amplifier system (1028 nm, 1 mJ, 2 kHz, 200 fs, Light Conversion, Pharos). The white light pulses were dispersed onto a linear CCD image sensor and read out at 2 kHz. Adjacent spectra correspond to the transmission of the sample with and without pump pulse and were used to calculate ΔT/T. The delay between pump and white light pulses was controlled by a linear delay stage. All transients were collected at a pump fluence of 4.5 micro joule per centimeter squared. As a detector a compact monolithic miniature spectrometer (Zeiss, MMS 1) was used with a spectral resolution of ≈ 10 nm and an active range of 310 – 1100 nm. The PL kinetics were measured with a universal streak camera (C10910-02, Hamamatsu) with a S-1 photocathode coupled to a spectrometer (SpectraPro 300i, Acton). For the excitation the output of the collinear optical parametric amplifier was used (745 nm, 1 kHz, 4.5 micro joule per centimeter squared).

2.5 References

[1] A. Graf, Y. Zakharko, S.P. Schiessl, C. Backes, M. Pfohl, B.S. Flavel, J. Zaumseil, *Carbon* **2016**, *105*, 593-599.
[2] A. Nish, J.Y. Hwang, J. Doig, R.J. Nicholas, *Nat Nanotechnol* **2007**, *2*, 640-6.
[3] L. Wieland, H. Li, X. Zhang, J. Chen, B.S. Flavel, *Small Science* **2022**, *3*, 2200079.
[4] M. Zheng, B.A. Diner, *J Am Chem Soc* **2004**, *126*, 15490-4.
[5] H. Li, G. Gordeev, O. Garrity, S. Reich, B.S. Flavel, *ACS Nano* **2019**, *13*, 2567-2578.
[6] J.A. Fagan, C.Y. Khripin, C.A. Silvera Batista, J.R. Simpson, E.H. Haroz, A.R. Hight Walker, M. Zheng, *Adv Mater* **2014**, *26*, 2800-4.
[7] J.A. Fagan, *Nanoscale Adv* **2019**, *1*, 3307-3324.
[8] C. Rust, H. Li, G. Gordeev, M. Spari, M. Guttmann, Q. Jin, S. Reich, B.S. Flavel, *Adv Func Mater* **2021**, *32*, 2107411.
[9] C. Rust, P. Shapturenka, M. Spari, Q. Jin, H. Li, A. Bacher, M. Guttmann, M. Zheng, T. Adel, A.R.H. Walker, J.A. Fagan, B.S. Flavel, *Small* **2022**, *n/a*, e2206774.

- this page left intentionally blank -

- this page left intentionally blank -

3 SWCNT/Fullerene Solar Cells

3.1 (6,5)/ Fullerene Solar Cells

3.1.1 Organic vs. Aqueous Sorted (6,5)

The organic solar cell design used in this thesis is similar to previous work[1-4] with the SWCNT/C_{60} active layer sandwiched between hole and electron selective layers on a indium tin oxide (ITO) substrate with a silver top contact. Pre-structured ITO is first cleaned and acts as the transparent anode followed by spin coating and annealing of the standard hole transport layer (HTL) PEDOT:PSS. In the past, most groups have used PEDOT:PSS as the hole-selective layer in their design as shown in Figure 3.1A but for the aqueous sorted SWCNTs it is replaced by PolyTPD as displayed in Figure 3.1B. PEDOT:PSS as standard HTL is soluble in water so that it provides a wide degree of freedom in selecting the solvents for solution coating of subsequent layers on the PEDOT:PSS layer. However, it has several limitations such as high acidity, inefficient blocking of electrons, and thermal instability. Additionally, corrosion of the ITO electrode leads to migration of indium to the PEDOT:PSS and the degradation of the device due to water absorption.[5] Therefore, many researchers have investigated alternative hole transport layers, for example poly(N,N'-bis(4-butylphenyl)-N,N'-bis (phenyl)benzidine) or short PolyTPD with its high hole mobility and reasonable HOMO level to inject holes (5.2 eV).[6] Additionally, it is solution processable and soluble in common organic solvents like toluene and chlorobenzene which unfortunately limits the solvents for subsequent layers but enables to work with aqueous solutions. However, solvent resistance was significantly improved for chlorobenzene by annealing at about glass transition temperature.[7]

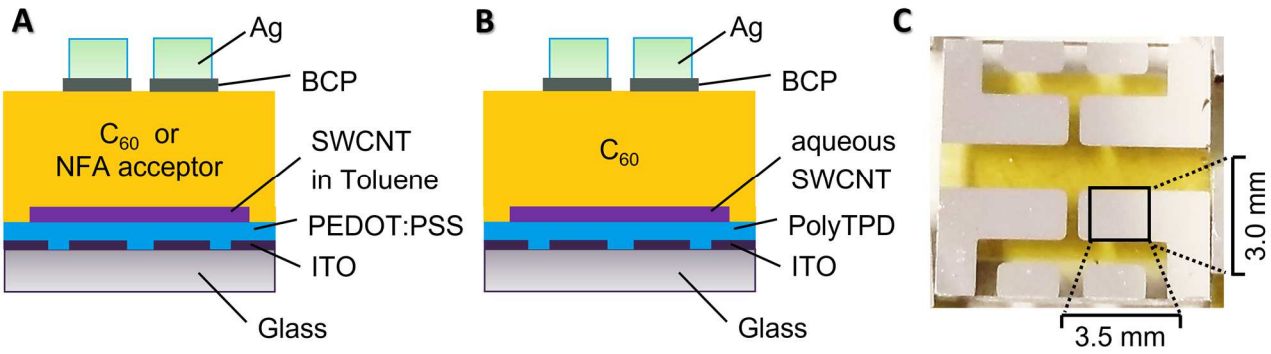

Figure 3.1: Schematic of a bilayer SWCNT based solar cell made of (A) SWCNTs dispersed in toluene or (B) aqueous dispersed SWCNTs. (C) Photograph of a bilayer solar cell highlighting the active area by a black box. Figure adapted from [8]

SWCNT/C_{60} solar cells for two different types of (6,5) are fabricated, those prepared by shear-force mixing in PFO-BPy and those sorted by aqueous two-phase extraction (ATPE). The composition of the raw soot was identical and absorption spectra of the dispersions used can be

found in Figure 3.2. While the (6,5) ATPE separated sample attained an OD of 5.34 (@987 nm), the polymer sample is concentrated to an optical density of 1.33 (@997 nm). During device assembly the polymer-wrapped SWCNTs could be directly deposited on top of the PEDOT:PSS by spin-coating four times 40 µL suspension whereas the aqueous SWCNTs first had to be filtered on a membrane before transferring on the PolyTPD. 2 µg of a single chirality ATPE-sorted (6,5) dispersion were filtered onto a polycarbonate membrane (22 mm diameter) to produce a 12 ± 4 nm thick SWCNT film, which is in line with other SWCNT/C_{60} cells in the literature.[3, 4, 9] Afterwards the film was transferred onto the layer stack by dissolving the membrane with propylamine.

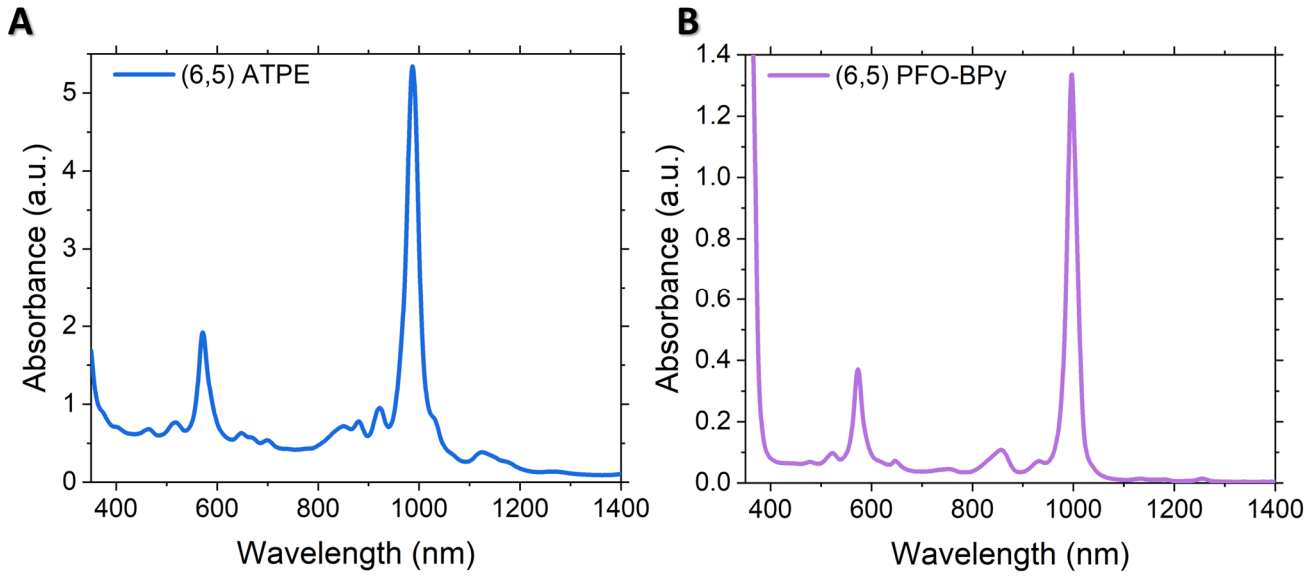

Figure 3.2: Absorbance measurement of (A) the ATPE-sorted (6,5) in water/DOC and (B) (6,5) PFO-BPy in toluene.

After annealing the CNT films, 100 nm C_{60} fullerene are evaporated on the SWCNTs. To complete device fabrication, 10 nm of Bathocuproine (BCP) were thermally evaporated as electron transport layer followed by the 100 nm thick silver electrode. The active area of all cells was 0.105 cm^2, as indicated in Figure 1.2C by a black rectangle in the photograph. Each ITO substrate contained four separate devices.

Current density-voltage (J-V) curves for both (6,5)-types in the fullerene solar cells are shown in Figure 3.3A. The PFO-BPy wrapped (6,5) solar cells have a PCE of 0.7 %, J_{SC} of 2.88 mA/cm^2, V_{OC} of 514 mV and FF of 47 % whereas the ATPE sorted (6,5) cells have the following parameters summarized in Table 1: PCE 0.05 %, J_{SC} 1.16 mA/cm^2, V_{OC} 138 mV and FF 33 %. Despite their difference both are close to the best in the field for their respective type[2, 10, 11] and serve the purpose of this work, which is to investigate the practicality of extending the light absorption of a solar cell with carbon nanotubes.

Table 1: Solar cell performance parameters of (6,5)/C_{60} solar cells with different (6,5) dispersions and film preparation methods.

Layer stack ITO/…/C_{60}/BCP/Ag	J_{SC} [mA/cm²]	V_{OC} [mV]	FF [%]	Efficiency [%]	Peak EQE at S_{11} of (6,5) [%]
PEDOT:PSS/(6,5) PFO-BPy	2.88	514.4	46.9	0.695	24.20
PolyTPD/(6,5) ATPE	1.16	138.5	33.2	0.053	6.22

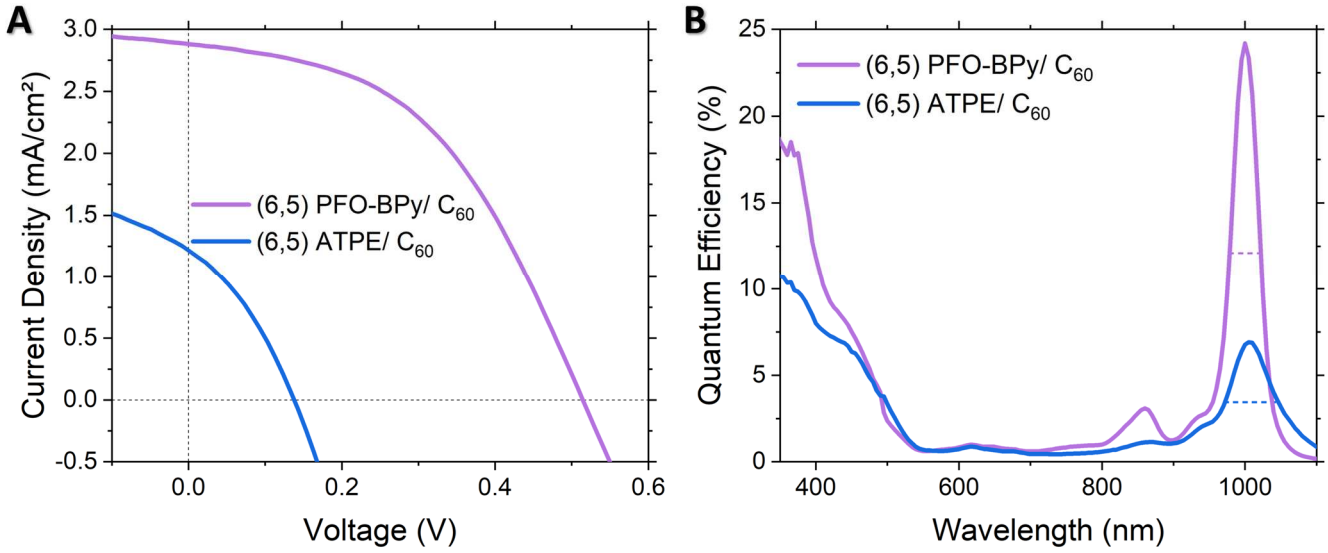

Figure 3.3: (A) Current density-voltage curve of (6,5)/C60 solar cells with (6,5) either polymer sorted with PFO-BPy (purple) or by aqueous two-phase extraction (blue) (B) Corresponding EQE of the (6,5)/C60 devices. The dashed lines indicate the FWHM of 43 nm or 74 nm, respectively. Figure reproduced from[8]

The difference in J_{SC} between the two types of (6,5) can also be seen in the external quantum efficiency (EQE) measurement in Figure 3.3B. The EQE at the S_{11} peak of (6,5) for the polymer wrapped species (1000 nm) was 24.2 % compared to 6.2 % for the ATPE (1010 nm) based films. Over the 300 – 1100 nm range this results in an integrated current density of 1.37 mA/cm² and 0.88 mA/cm², respectively. The red shift of S_{11} in EQE and absorption as well as the increase in FWHM (43 nm vs. 70 nm) in Figure 3.3B for the ATPE sample is an evidence for water filling.[12, 13] This is in agreement with the recent work of Li et al. showing that PFO-BPy tends to disperse empty species.[14]

An indication as to why the two types of (6,5) perform differently can be obtained from time resolved spectroscopy. In Figure 3.4A transient absorption (TA) measurements of ATPE sorted (6,5) suspended by 1 % DOC in H_2O afford an excitonic lifetime (τ) of 2.6 ps, which is 12 times shorter than for PFO-BPy wrapped (6,5) with τ = 30.7 ps measured with a streak camera, Figure 3.4B.

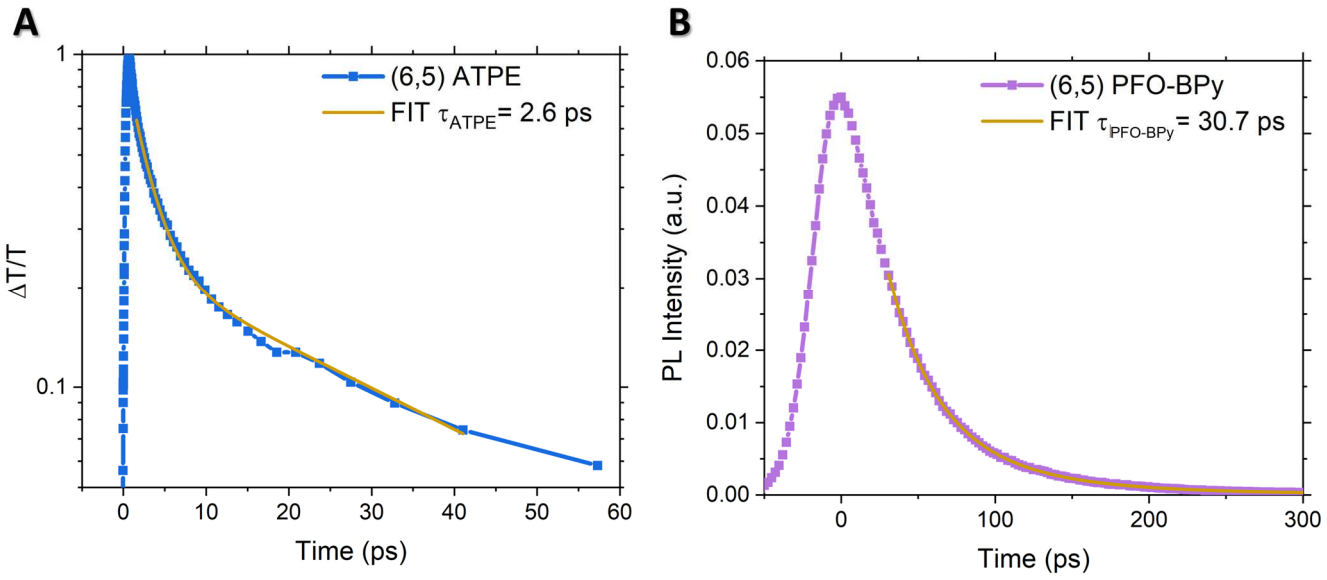

Figure 3.4: (A) Fitted decay of the (6,5) ATPE solution by transient absorption spectroscopy and (B) PL decay of from (6,5) PFO-BPy in toluene solution. Figure reproduced from[8]

The resolution of the TA setup (≈ 200 fs) could not resolve the fastest decay component of the SWCNTs in solution. For reference, Graham et al.[15] revealed for aqueous (6,5) two fast decay components (122 fs and 1.3 ps) as well as slower (22 ps or 300 ps) relaxation processes. Mehlenbacher et al.[16] traced the ultrafast energy transfer between bare ATPE-sorted carbon nanotubes in a thin film by two-dimensional (2D) white-light spectroscopy and reported lifetimes of ≈ 300 fs, whereas for polymer-wrapped SWCNTs it was approximately 1 ps.[17]

3.1.2 Film Thickness

A 2 µg film of monochiral (6,5) ATPE-sorted dispersion discussed in the last section has a thickness of approximately 12 nm. Atomic force microscopy (AFM) of this film in Figure 3.5A reveals a densely packed carbon nanotube network. In contrast, a 1 µg film results in a thickness of 9 ± 2 nm but has holes in the CNT network after dissolving the membrane. Figure 3.5B displays the dependency of the film thickness on the mass of filtered (6,5) ATPE. The (6,5) dispersion method can influence solar cell performance due to significant impact on the exciton lifetime.[18] Thus, an aqueous shear-force mixed and an aqueous sonicated sample were prepared and both sorted by ATPE. Several films with varying mass were fabricated by filtration and transferred on glass giving film absorbance spectra displayed in Figure 3.5C and D. The mass of (6,5) used for film formation was varied from 1 – 8 µg to afford thicknesses of 9 ± 2 nm up to 28 ± 10 nm for the SFM dispersion. On the other hand, the sonicated sample was varied from 1 – 4 µg with thicknesses reaching 9 ± 4 nm to 19 ± 7 nm.

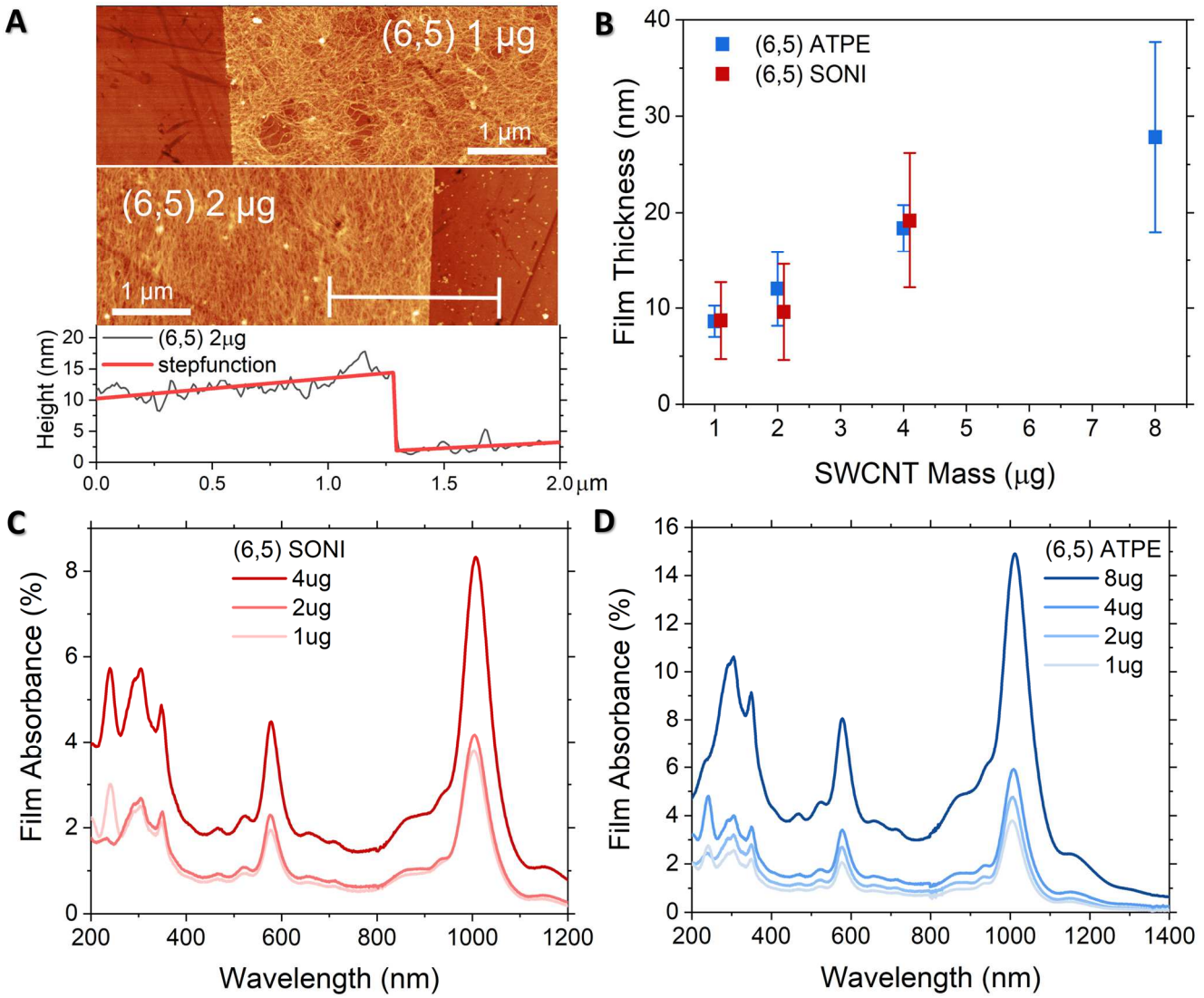

Figure 3.5: (A) AFM images of films from 1 µg and 2 µg of (6,5) with the cross section indicated by a white line in the 2 µg film. (B) A plot of the mass of SWNCTs filtered and the resulting film thickness. Film absorbance measurement of (6,5) on glass either sonicated (C) or shear-force mixed (D) with variable mass and film thickness. The greater the mass of filtered SWCNTs the higher the film absorbance and thickness. Figure reproduced from[8]

For the high mass films the scattering background in the film absorbance measurements are tremendous which reduces the measured J_{SC} and overall EQE. Thus, the maximum efficiency is attained for film thicknesses of 9-12 nm which is in agreement with the reported exciton diffusion lengths. The 2 µg sample (6,5) SFM has reached 0.053 % efficiency and for the sonicated devices 1 µg is slightly more efficient with 0.044 % compared to the 2 µg film with 0.040 %. An overview of all solar cell parameter is given in Table 2 and the corresponding J-V curves and EQE spectra in Figure 3.6 and Figure 3.7.

The V_{OC} tend to correlate inversely with the mass, lower SWCNT content yields higher open circuit voltages as shown in Figure 3.6A. One explanation for this trend is that with increasing film thickness the barrier for holes separated at the SWCNT/fullerene interface becomes larger.

Table 2: Solar cell performance parameters of aqueous (6,5) ATPE/C_{60} solar cells with different (6,5) dispersions techniques and varied mass.

Layer stack ITO/PTPD/…/C_{60}/BCP/Ag	J_{SC} [mA/cm²]	V_{OC} [mV]	FF [%]	Efficiency [%]	Peak EQE at S_{11} of (6,5) [%]
(6,5) ATPE **8ug**	0.89	94.2	30.9	0.026	4.37
(6,5) ATPE **4ug**	1.06	102.7	34.4	0.038	8.09
(6,5) ATPE **2ug**	1.16	138.5	33.2	0.053	6.22
(6,5) ATPE **1ug**	0.63	144.7	26.6	0.024	5.51
(6,5) ATPE, SONI **4ug**	0.88	86.8	29.6	0.019	2.76
(6,5) ATPE, SONI **2ug**	1.04	106.9	36.3	0.040	5.91
(6,5) ATPE, SONI **1ug**	1.11	109.2	36.0	0.044	5.93

Short circuit current density is as well decreasing with the film thickness, except the 1 µg film that has the lowest J_{SC} value due to the holes in the CNT network. The EQE of (6,5) SFM in Figure 3.6B reveals that the 4 µg films with a thickness of 18 nm perform best with an S_{11} EQE of 8.1%. In general, a thicker (6,5) film leads to an increased EQE signal at S_{11} (1 µg: 5.5 %, 2 µg: 6.2 %, 4 µg: 8.1 %) except for the thickest film tested (8 µg: 4.4 %) with a film thickness more than double of the exciton diffusion length.[16, 19, 20]

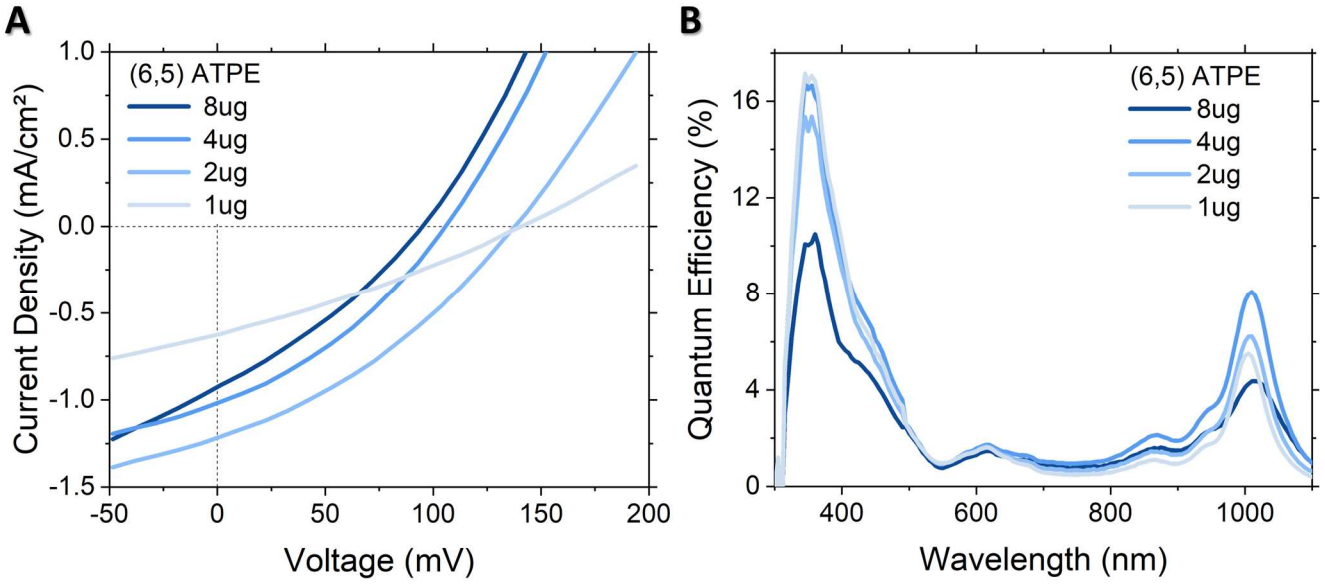

Figure 3.6: (A) Current density-voltage curve of (6,5)/C_{60} solar cells with (6,5) SFM and sorted by aqueous two-phase extraction with increased film thickness from 1 µg to 8 µg. The best performance is from a 2 µg film with a thickness of 12 nm. (B) Corresponding EQE spectra with the maximum signal of (6,5) at 1000 nm for the 4 µg film. Figure reproduced from[8]

The sonicated (6,5) films of 1 µg and 2 µg have already shown a quite similar film absorbance in Figure 3.5C leading to similar J-V and EQE curves represented in Figure 3.7. Although, the film thickness of the 4 µg film is only slightly increased compared to the (6,5) ATPE SFM sample (Figure 3.5B), it already follows the decreasing V_{OC} and J_{SC} trends discussed for the 8 µg (6,5) SFM.

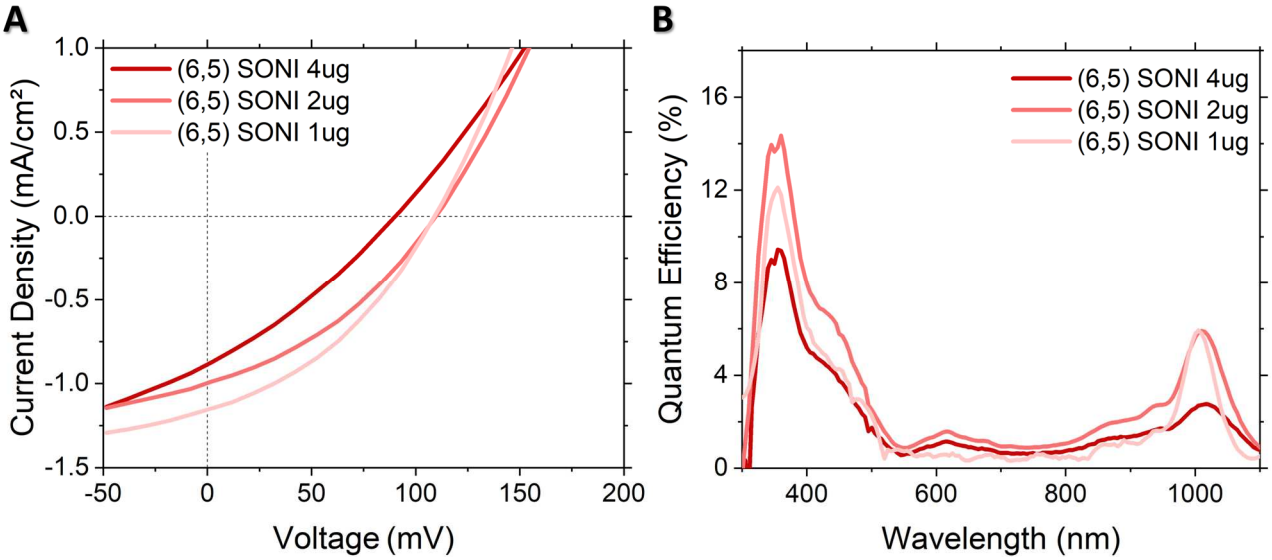

Figure 3.7: (A) Current density-voltage curve of (6,5)/C_{60} solar cells with sonicated (6,5) sorted by aqueous two-phase extraction with increased film thickness from 1 µg to 4 µg. (B) Corresponding EQE spectra with the maximum signal of (6,5) at 1000 nm for the 1 and 2 µg film.

The sonication processing is known to shorten the SWCNT inducing more quenching sites compared to SFM resulting in lower exciton lifetimes.[18] Thus, the 19 nm film (4 µg) is already too thick for most of the photogenerated excitons to reach the donor/acceptor interface. On the other hand, the 18 nm thickness of the 4 µg (6,5) SFM sample seems to coincide with the exciton diffusion length in the device yielding the best (6,5) EQE signal.

In agreement with literature, the performance values of solar cells from (6,5) in aqueous solution or polymer-wrapped in organic solvents were different and the polymer wrapped SWCNTs outperformed those from aqueous sorting. The gentler shear-force mixing method is preferred over sonication because it enables higher efficiency with thicker SWCNT films.

3.2 Larger Diameter SWCNT/Fullerene Solar Cells

ATPE makes it is possible to isolate other single chiral SWCNT species whose S_{11} transition lies deeper in the IR region at wavelengths higher than 1000 nm. SWCNT films were thus prepared from (7,6) and (10,3) dispersions, which have S_{11} at 1130 nm and 1260 nm (Figure 3.8A), respectively.

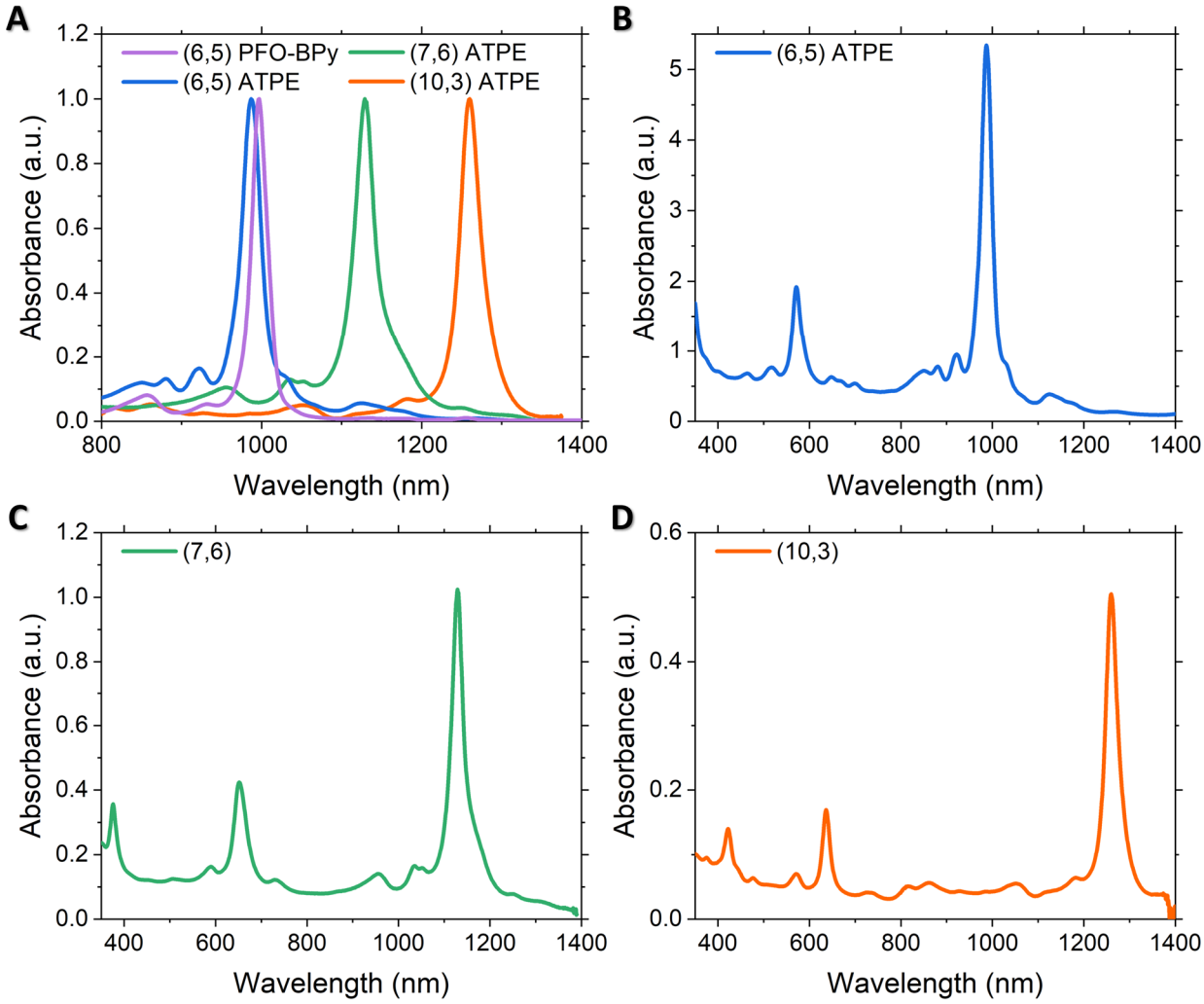

Figure 3.8: (A) Normalized absorbance spectra of the single chirality dispersions used in this section. (B)-(D) Absorbance measurement of the ATPE-sorted chiralities (6,5), (7,6) and (10,3) in water/DOC. (1 mm pathlength) Figure reproduced from[8]

All ATPE samples were prepared by sonication while the polymer-wrapped (6,5) is shear-force mixed. The SWCNTs (6,5), (7,6) and (10,3) were prepared from three different raw soot where (6,5) and (7,6) are made from enriched material. The amount of SWCNT is therefore significantly higher in the concentrated (6,5) solution with an optical density over 5 compared to (7,6) and (10,3) with an OD of approximately 1 and 0.5. The corresponding absorption spectra are displayed in Figure 3.8B to D.

Although the fabricated (7,6) films have similar but slightly reduced film thicknesses, the film absorbance measurements in Figure 3.9B reveal that the 2 µg (6,5) film is absorbing more than double compared to the 2 µg (7,6) sample. The (10,3) 2 µg film absorbance is even lower due a miscalculation of the concentration.

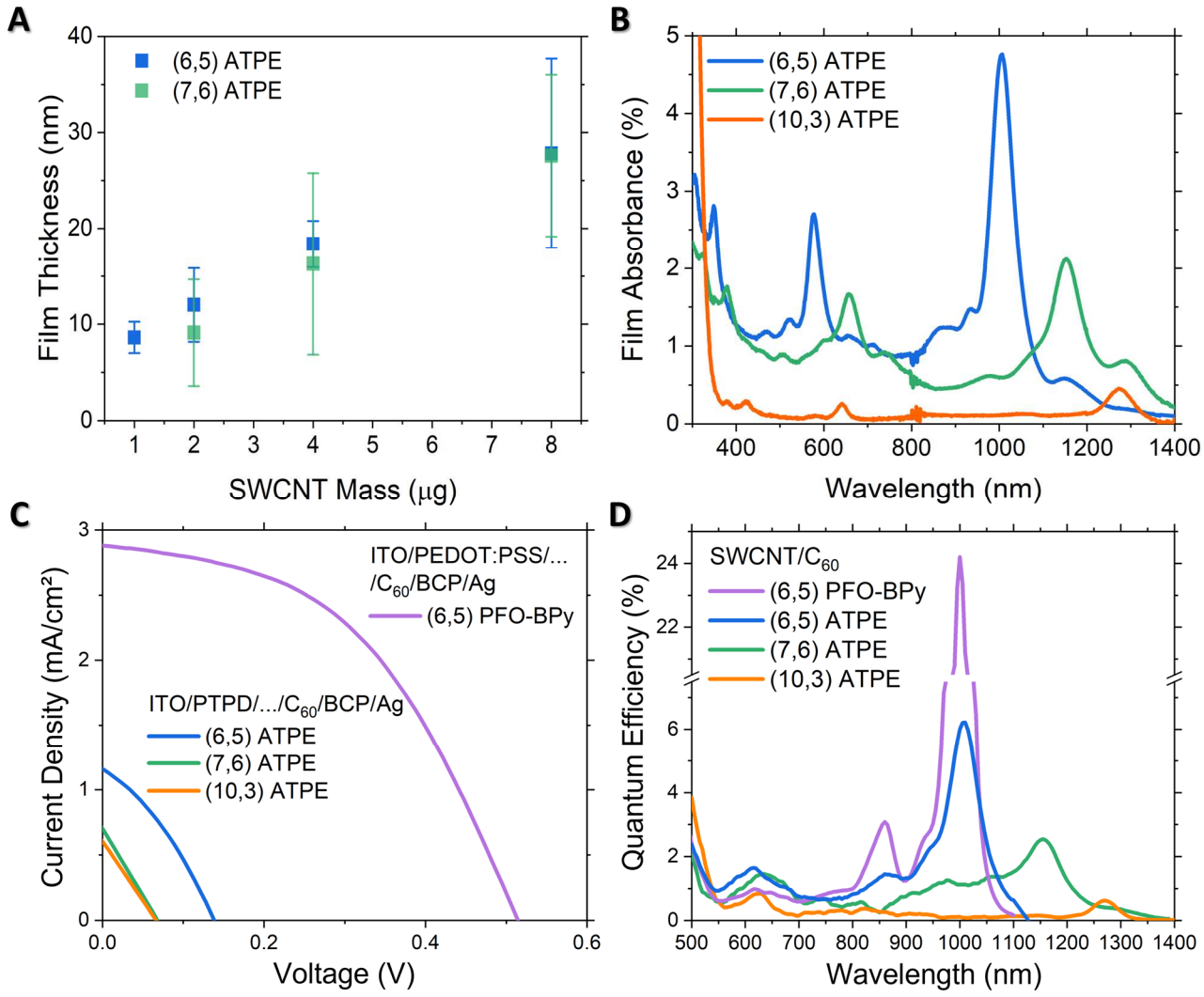

Figure 3.9: (A) A plot of the mass of SWNCTs filtered and the resulting film thickness. (B) Film absorbance measurement of 2 µg (6,5), (7,6) and (10,3) on glass. (C) Current density-voltage curve of s-SWCNT/C_{60} solar cells with (6,5) PFO-BPy or (6,5), (7,6) and (10,3) sorted by aqueous two-phase extraction. (D) Corresponding EQE of the s-SWCNT /C_{60} devices with the maximum EQE signal of polymer-sorted (6,5). Figure reproduced from[8]

Table 3: Solar cell performance parameters of SWCNT/C_{60} solar cells with single chirality dispersions of different diameters. All prepared with a 2 µg film.

Layer stack	J_{SC} [mA/cm²]	V_{OC} [mV]	FF [%]	Efficiency [%]	Peak EQE (or IQE) at S_{11} [%]
(6,5) PFO-BPy	2.88	514.4	46.9	0.695	24.20
(6,5) ATPE	1.16	138.5	33.2	0.053	6.22 (59.92)
(7,6) ATPE	0.70	67.7	25.0	0.012	2.54 (53.31)
(10,3) ATPE	0.61	66.5	25.3	0.010	0.63 (61.12)

The large diameter SWCNT films were integrated into SWCNT/C_{60} layer stacks as described in the previous section for the aqueous (6,5) ATPE sample. Performance parameters for these solar cells are provided in

Table 3 and the J-V curves are presented in Figure 3.9C. Overall, the efficiency of (7,6) and (10,3) solar cells are comparable but reduced to a fifth in relation to the (6,5) ATPE. When the external quantum efficiency is measured (Figure 3.9D) it can be seen that the signal at S_{11} decreases with increasing diameter: 6.2 % for (6,5) with d = 0.75 nm, 2.5 % for (7,6) with d = 0.88 nm, and 0.63 % for (10,3) with d = 0.92 nm.

The diameter dependence is a result of the reduction in the energetic offset between the LUMO of the SWCNT and that of C_{60} leading to a smaller driving force that cannot overcome the exciton binding energy.[1, 19, 21] Besides, the internal quantum efficiency (IQE) can be calculated for the devices to address the differences in film absorbance. IQE is defined as the ratio of the number of charge carriers generated to the number of photons absorbed, within the active layer of the device. It can be calculated from the EQE and the transmittance τ and reflectance ρ of the layers.

$$IQE\ (\%) = \frac{EQE\ (\%)}{1 - \tau(\lambda) - \rho(\lambda)} = \frac{EQE\ (\%)}{1 - 10^{-Abs(\lambda)} - \rho(\lambda)} \qquad (1)$$

The transmittance can be deduced from the film absorbance in Figure 3.9B and the reflectance is usually quite low for CNT layers and will be neglected. The IQE results at the corresponding S_{11} transitions are all around 60 % listed in

Table 3 in the brackets after the EQE value. For the IQE values no diameter dependence can be observed, only the (7,6) IQE is a little lower due to the higher scattering background in the film absorbance. For the polymer-wrapped sample a film absorbance measurement was not taken so IQE could not be calculated.

3.3 Summary

SWCNT/C_{60} solar cells were fabricated from two different types of (6,5), those prepared by shear-force mixing in PFO-BPy and those sorted by aqueous two-phase extraction. For the aqueous sorted SWCNTs the standard hole transport layer PEDOT:PSS was replaced by PolyTPD and for device integration SWCNTs first had to be filtered on a membrane before transferring on the

PolyTPD. In contrast, polymer-wrapped SWCNTs could be directly spin cast on the PEDOT:PSS. Despite their efficiency difference both are close to the best in the field for their respective type.[2, 10, 11] Time resolved spectroscopy revealed that the excitonic lifetime of ATPE sorted (6,5) in solution is 12 times shorter than for PFO-BPy wrapped (6,5). In thin films, ultrafast energy transfer[16] between bare ATPE-sorted carbon nanotubes has been reported resulting in lifetimes of ≈ 300 fs, whereas for polymer-wrapped SWCNTs it was approximately 1 ps.[17] Additionally, the (6,5) dispersion method can also influence solar cell performance due to significant impact on the exciton lifetime.[18] The comparison of an aqueous shear-force mixed and an aqueous sonicated sample (both sorted by ATPE) demonstrated that SFM facilitates thicker films in a device leading to slightly more efficient solar cells and higher external quantum efficiency. Several films thickness between 9 and 28 nm were tested and the maximum efficiency is attained for 9-12 nm thick films which is in line with the reported exciton diffusion lengths. In general, thicker (6,5) films lead to an increased EQE signal at S_{11} until the thickness exceeds the exciton diffusion length.[16, 19, 20]

Other single chiral SWCNT species whose S_{11} transition lies deeper in the IR region than 1000 nm were integrated in the same device stack to investigate the practicality of extending the light absorption of a solar cell with carbon nanotubes. SWCNT films were prepared from ATPE sorted (7,6) and (10,3) dispersions, which have S_{11} at 1130 nm and 1260 nm, respectively. The efficiency of (7,6) and (10,3) solar cells are comparable to each other but reduced to a fifth in relation to the (6,5) ATPE. In the EQE spectra the S_{11} signal decreases with increasing diameter because of the reduction in the energetic offset between the LUMO of the SWCNT and that of C_{60} leading to a smaller driving force that cannot overcome the exciton binding energy.[1, 19, 21] The calculation of internal quantum efficiency (IQE) addresses the differences in film absorbance resulting in IQE values around 60 % for all devices.

3.4 Experimental Details

3.4.1 SWCNT Dispersion and Separation

The (6,5) PFO-BPy suspension was prepared by shear-force mixing[22] in toluene with the raw material CoMoCAT® (Sigma-Aldrich, 773735 lot no. MKBZ1159V) and the dispersant and sorting polymer PFO-BPy[23] (American Dye Source, lot no. 19L014A1). All details are described in the experimental section, briefly, shear-force mixing is followed by ultra centrifugation and a filtration step to wash off excess polymer and simultaneously concentrate the (6,5) by redispersion in a smaller amount of toluene. The (6,5) PFO-BPy sample has a concentration between 45-90 µg/mL.

The surfactant dispersed SWCNTs in aqueous solution (6,5), (7,6) and (10,3) were prepared from raw soot from three different sources: CoMoCAT® SG65i (Chasm, lot no. SG65i-L58), CoMoCAT® SG76i (Chasm, lot no. SG76-L39) and HiPco (Nano Integris, lot no. HR-29-073), respectively. First, the raw material was dispersed in sodium deoxycholate (DOC) by tip sonication and subsequently ultracentrifuged. The supernatant was collected and ATPE separation performed using the conditions described already in the experimental section. Each separated species was finally concentrated and adjusted to 1% DOC (10 g/L), resulting in concentrations of 260-520 µg/mL for (6,5), 51-102 µg/mL for (7,6) and 25-50 µg/mL for (10,3).

3.4.2 Device Fabrication

The fabrication of SWCNT based solar cells in bilayer architecture depends on the dispersant of the carbon nanotubes. Although, the layer stack at the end is quite similar for aqueous or toluene SWCNT solutions the underlying hole transport layer can vary due to solubility sequences.
In both cases, pre-structured indium tin oxide substrates (Psiotec, 15 Ω/sq) is the transparent anode, starting by cleaning those substrates with acetone and detergent, followed by water and isopropanol. After drying, the ITO substrates were oxygen plasma cleaned for 30 s to 1 min (ATTO, diener electronic) to facilitate the homogeneous distribution of the next layer. The standard hole transport layer PEDOT:PSS (AI 4083, Ossila) was filtered (Millex-HV, 0.45 µm, Merck) and subsequently spin cast on the ITO at 3000 rpm for 30 s followed by an annealing at 150 °C for 15 min. For the SWCNTs dispersed in organic solvents like toluene, 55 µL of the prepared polymer-sorted (6,5) solution was spin cast on top of the PEDOT:PSS at 600 rpm for 20 s followed by 1500 rpm for 5 s. After annealing at 110°C for 7 min, usually 100 nm C_{60} fullerene (99.9+%;

Sigma–Aldrich, lot. MKCK0541) are evaporated on the SWCNT film. To complete device fabrication, and 10 nm of Bathocuproine (BCP, > 99.5%, Ossila) were thermally evaporated followed by the 100 nm thick silver electrode. The active area of all cells is 0.105 cm^2.

For the aqueous dispersed SWCNTs, the layer stack (Figure 3.1B) is based on cleaned ITO without plasma cleaning. Then, PolyTPD (M_w = 100,000 – 150,000, Ossila) 10 mg/mL in chlorobenzene (anhydrous, 99.8%, Sigma-Aldrich) was spin cast as hole transport layer and annealed at 230°C for 30 min in a glove box. Aqueous SWCNT films were transferred onto the PolyTPD layer in air, by first wetting and heating (70°C, 5 min) the film to adhere it to the layer stack. The polycarbonate membrane was then dissolved by propylamine (≥ 99%, Sigma-Aldrich) followed by washing with acetone and isopropanol. Like in the organic solvent case, the following layers of C_{60}, BCP and silver were evaporated to complement the device.

3.5 References

[1] M. Pfohl, K. Glaser, A. Graf, A. Mertens, D.D. Tune, T. Puerckhauer, A. Alam, L. Wei, Y. Chen, J. Zaumseil, A. Colsmann, R. Krupke, B.S. Flavel, *Adv Energy Mater* **2016**, *6*, 1600890.

[2] R.M. Jain, R. Howden, K. Tvrdy, S. Shimizu, A.J. Hilmer, T.P. McNicholas, K.K. Gleason, M.S. Strano, *Adv Mater* **2012**, *24*, 4436-4439.

[3] S.L. Guillot, K.S. Mistry, A.D. Avery, J. Richard, A.M. Dowgiallo, P.F. Ndione, J. van de Lagemaat, M.O. Reese, J.L. Blackburn, *Nanoscale* **2015**, *7*, 6556-66.

[4] A.T. Mallajosyula, W. Nie, G. Gupta, J.L. Blackburn, S.K. Doorn, A.D. Mohite, *ACS Nano* **2016**, *10*, 10808-10815.

[5] M. Jørgensen, K. Norrman, F.C. Krebs, *Sol Energ Mat Sol C* **2008**, *92*, 686-714.

[6] D. Zhao, M. Sexton, H.-Y. Park, G. Baure, J.C. Nino, F. So, *Adv Energy Mater* **2015**, *5*.

[7] T.Y. Kim, J.H. Jung, J.B. Kim, D.G. Moon, *Synthetic Metals* **2017**, *232*, 167-170.

[8] L. Wieland, C. Rust, H. Li, M. Jakoby, I. Howard, F. Li, J. Shi, J. Chen, B.S. Flavel, *Carbon* **2021**, *184*, 828-835.

[9] D.J. Bindl, M.S. Arnold, *J Phys Chem C* **2013**, *117*, 2390-2395.

[10] M.J. Shea, M.S. Arnold, *Appl Phys Lett* **2013**, *102*, 243101.

[11] A. Classen, L. Einsiedler, T. Heumueller, A. Graf, M. Brohmann, F. Berger, S. Kahmann, M. Richter, G.J. Matt, K. Forberich, J. Zaumseil, C.J. Brabec, *Adv Energy Mater* **2018**, *8*, 1801913.

[12] J. Gao, W. Gomulya, M.A. Loi, *Chem Phys* **2013**, *413*, 35-38.

[13] J. Campo, S. Cambre, B. Botka, J. Obrzut, W. Wenseleers, J.A. Fagan, *ACS Nano* **2020**.

[14] H. Li, G. Gordeev, D. Toroz, D. Di Tommaso, S. Reich, B.S. Flavel, *J Phys Chem C* **2021**, *125*, 7476-7487.

[15] M.W. Graham, J. Chmeliov, Y.Z. Ma, H. Shinohara, A.A. Green, M.C. Hersam, L. Valkunas, G.R. Fleming, *J Phys Chem B* **2011**, *115*, 5201-11.

[16] R.D. Mehlenbacher, J. Wang, N.M. Kearns, M.J. Shea, J.T. Flach, T.J. McDonough, M.Y. Wu, M.S. Arnold, M.T. Zanni, *J Phys Chem Lett* **2016**, *7*, 2024-2031.

[17] R.D. Mehlenbacher, M.Y. Wu, M. Grechko, J.E. Laaser, M.S. Arnold, M.T. Zanni, *Nano Lett* **2013**, *13*, 1495-501.

[18] M.J. Shea, J.L. Wang, J.T. Flach, M.T. Zanni, M.S. Arnold, *APL Materials* **2018**, *6*, 056104.

[19] D.J. Bindl, M.Y. Wu, F.C. Prehn, M.S. Arnold, *Nano Lett* **2011**, *11*, 455-60.

[20] D.J. Bindl, M.J. Shea, M.S. Arnold, *Chem Phys* **2013**, *413*, 29-34.

[21] J.L. Wang, S.R. Peurifoy, M.T. Bender, F. Ng, K.S. Choi, C. Nuckolls, M.S. Arnold, *J Phys Chem C* **2019**, *123*, 21395-21402.

[22] A. Graf, Y. Zakharko, S.P. Schiessl, C. Backes, M. Pfohl, B.S. Flavel, J. Zaumseil, *Carbon* **2016**, *105*, 593-599.

[23] A. Nish, J.Y. Hwang, J. Doig, R.J. Nicholas, *Nat Nanotechnol* **2007**, *2*, 640-6.

- this page left intentionally blank -

- this page left intentionally blank -

4 Endohedral Filling of SWCNTs

SWCNT/C_{60} solar cells only absorb in the infrared and roughly between 350 to 550 nm but they are missing the main visible part with the highest solar irradiation. Therefore, the idea is to encapsulate (dye) molecules that absorb in this region to complement the solar cell absorption. The energy transfer from dyes to SWCNTs has been demonstrated to be fast, so the generated charges can contribute to the device current.[1, 2]

The general principle of liquid phase filling[3] is confirmed for different solvents encapsulated in the standard (6,5) chirality which are incorporated in SWCNT/C_{60} devices. For the same CoMoCAT raw material different filling procedures are tested with small molecules like anthracene. Dyes absorbing in the visible like squarylium have already been encapsulated by others showing a sieving diameter around 1.15 nm.[1, 2] Other raw materials with larger diameter carbon nanotubes are combined with this squarylium dye for endohedral filling. However, these chiralities are not compatible with the standard C_{60} acceptor.[4] Other possible acceptors have their main absorbance in the visible, so dyes absorbing in the ultraviolet or blue region are necessary to gain broadband light absorption.

4.1 Solvent Filling in (6,5)

SWCNT/C_{60} solar cells of four different ATPE-sorted (6,5) are fabricated either empty nanotubes, partially water-filled, completely water-filled, or hexane-filled CNTs. Usually, CoMoCAT raw material is used to prepare (6,5) samples because it is enriched in this chirality and high yields can be achieved. The filling is performed by spontaneous liquid-phase filling[3] which is basically the addition of raw SWCNT powder to 2-3 mL of the selected liquid such as water or hexane. After incubation for about 1 hour in the liquid, the mixture is filtered and washed with heptane to remove residual alkane on the outside of the SWCNTs. The filter cake is dried in air before the modified starting material is dispersed in DOC by tip sonication and centrifuged to remove bundles and residues from synthesis. The supernatant undergoes rate-zonal ultracentrifugation resulting in one or several bands containing individualized CNTs with and without the selected liquid inside. The top band has been shown to comprise empty and closed SWCNTs, while the lower band(s) consist of filled species.[5] After washing steps and concentration the obtained solutions are separated by ATPE as already reported[6-8], all details from the filling to the sorting are described in 4.4 Experimental Details.

The samples, water- and hexane-filled (6,5), are made of CoMoCAT and yield concentrations of 64-128 µg/mL and 52-104 µg/mL, however this raw material does not contain many closed nanotubes. For the empty (6,5), HiPco and Nopo material are used as starting material which is dispersed in DOC and sorted first by rate-zonal ultracentrifugation to gain all empty species followed by ATPE to yield the (6,5) chirality. If the tip sonication necessary for dispersing the CNTs is opening some nanotubes or breaks them, the density dependent ultracentrifugation enables separation of the empty and unintentionally water-filled species. The concentration of the (6,5) from HiPco is 117-233 µg/mL and 55-110 µg/mL for the empty (6,5) from Nopo. The absorbance spectra of all four (6,5) solutions are normalized and exhibit only minimal differences as displayed in Figure 4.1A. The first transition peaks (S_{11}) of the water@(6,5) and hexane@(6,5) samples are slightly red shifted by 4 and 7 nm, respectively, compared to the empty (6,5) from Nopo, illustrated in Figure 4.1B. The S_{11} peak position of (6,5) from HiPco lies in between the empty (6,5) and water-filled sample suggesting partial filling with water.

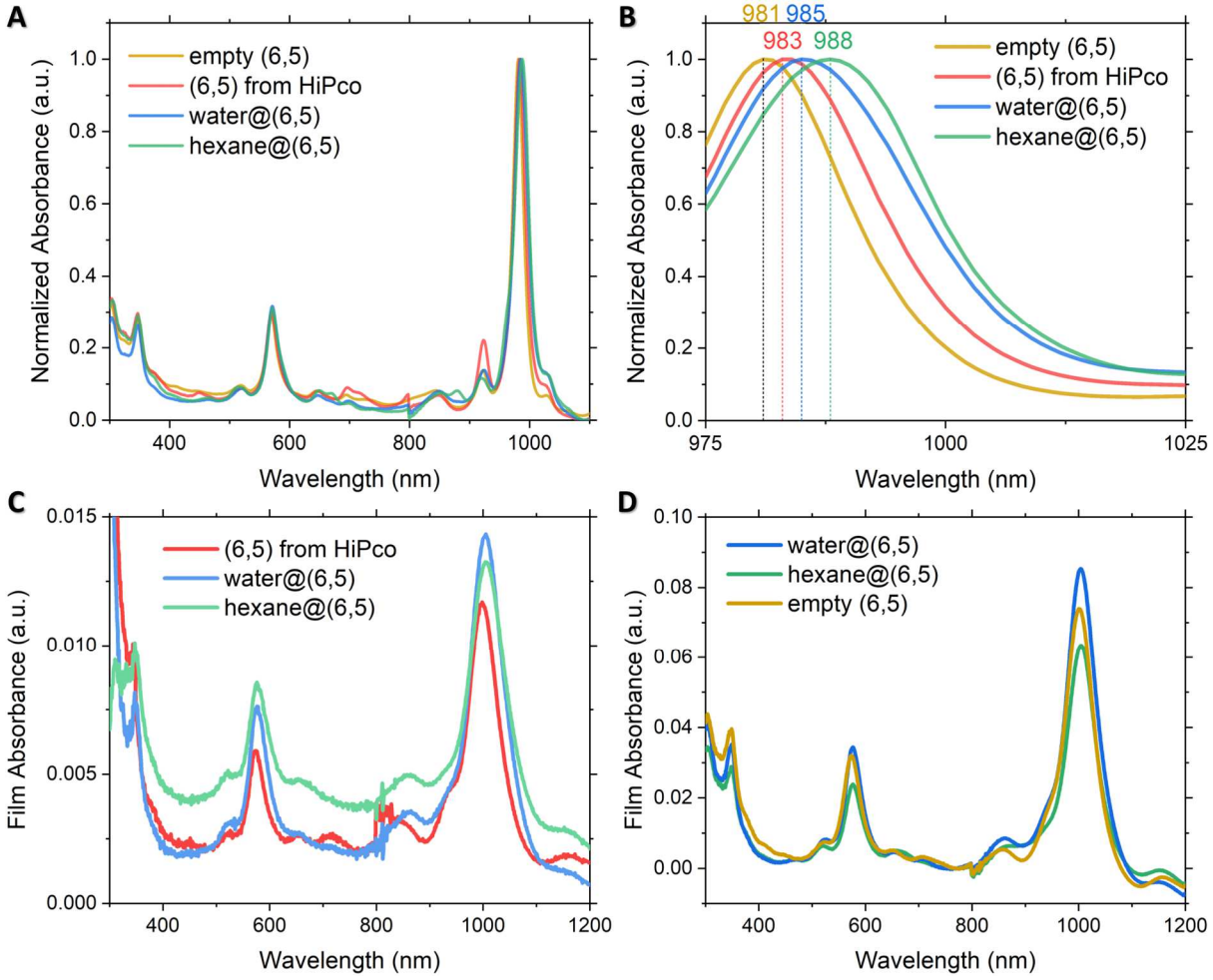

Figure 4.1: (A) Normalized absorbance measurement of ATPE-sorted (6,5) in water/DOC with different fillings: empty (6,5), partially water filled (6,5) from HiPco, complete water or hexane filling.(B) Zoom in (A) to highlight the red shifts of the fillers compared to the empty (6,5). Film absorbance measurement of (C) comparably thin (6,5) films with different filling and (D) thicker films of (6,5) either empty or water/hexane filled.

Films are fabricated from all (6,5) suspensions by filtration on polycarbonate membranes and subsequent dissolution of the membrane to the transfer the (6,5) layer on a substrate. Two sets of experiments are performed, the first with (6,5) from HiPco in comparison to completely water-filled and (6,5)@hexane and the second with truly empty (6,5) from Nopo in comparison to the two fillings. In the first set comparably thin films are used that absorb 5 times less light in comparison to the second set of experiments, as shown by the film absorbance measurements in Figure 4.1C and D.

(6,5) films are integrated into SWCNT based solar cells with an active layer of the (6,5) as donor and C_{60} as acceptor. ITO as transparent electrode is the basis for the hole transport layer PolyTPD where the (6,5) is transferred on followed by evaporation of C_{60}, the electron transport layer BCP and the silver back electrode. The fabrication is similar to standard SWCNT/Fullerene solar cells and details are summarized in 4.4 Experimental Details. J-V curves of the devices in Figure 4.2A reveal that they are 3-4 times less efficient than the reference without any CNTs. The filling of the devices has a minor influence on the open circuit voltage, but J_{SC} is slightly increased for the partially filled (6,5) from HiPco (red line). The higher J_{SC} value for the water filling compared to the hexane filled SWCNTs can be attributed to the lower scattering background in the film absorbance and therefore less bundles or liquid residues.

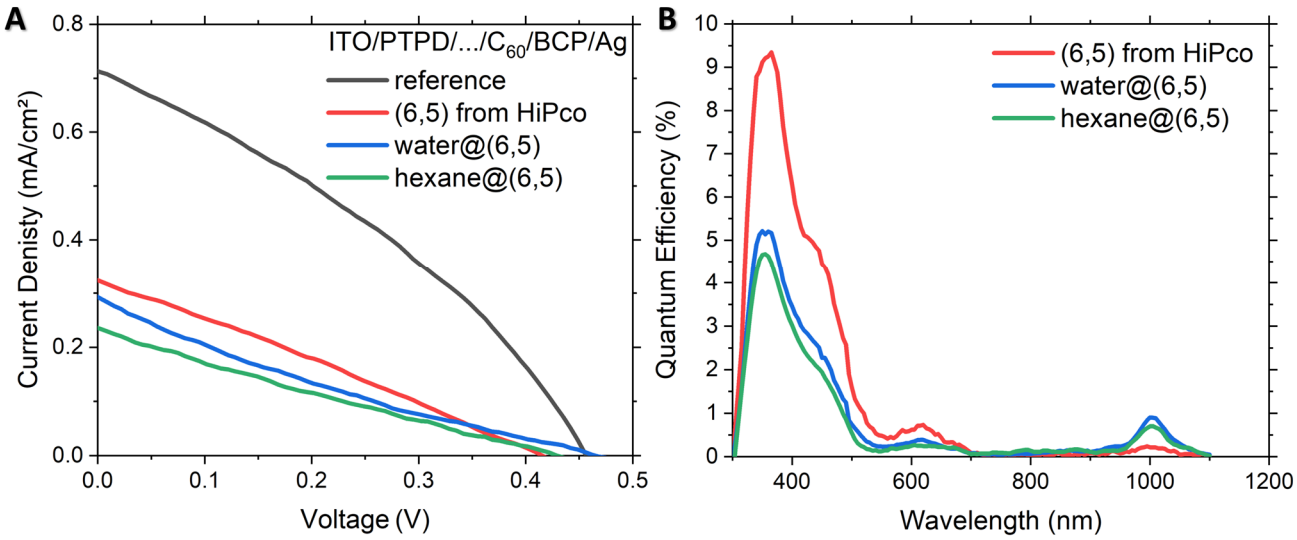

Figure 4.2: (A) Current density-voltage curve of (6,5)/C_{60} solar cells with partially water-filled (6,5) from HiPco(red) in comparison to complete water- (blue) and hexane-filling (green). (B) Corresponding EQE of the (6,5)/C_{60} devices.

The spectra of external quantum efficiency in Figure 4.2B show that the higher current of the (6,5) from HiPco arises from the C_{60} acceptor and not the SWCNTs. One explanation could be the comparably thin layers in this experiment where the (6,5) from HiPco film absorbs least. Whereas the water@(6,5) film absorbance at S_{11} is little bit increased compared to hexane filling leading to

an EQE signals of 0.90 % and 0.70 %, respectively. An overview about the solar cell performance of the (6,5)/C_{60} devices are given in Table 1.

Table 1: Performance parameters of (6,5)/C_{60} solar cells with different filling: partially water-filled (6,5) from HiPco in comparison to complete water- and hexane-filling.

Layer stack ITO/PTPD/.../C_{60}/BCP/Ag	J_{SC} [mA/cm²]	V_{OC} [mV]	FF [%]	Efficiency [%]	Peak EQE at S_{11} of (6,5) [%]
reference	0.711	454.9	34.0	0.110	-
(6,5) from HiPco	0.323	414.2	27.2	0.036	0.24
water@(6,5)	0.293	465.2	19.9	0.027	0.90
hexane@(6,5)	0.233	430.1	23.3	0.023	0.70

The second set of experiments with higher film absorbance of the (6,5) films shows tremendously reduced V_{OC} all below 100 mV as depicted in Figure 4.3A for the different fillings. Whether or not the (6,5) nanotubes are water-filled, makes nearly no difference in the current density-voltage characteristics. The hexane-filled J-V performance values listed in Table 2 are slightly reduced due to the lower film absorbance at the characteristic CNT transitions in comparison to the empty and especially to the water-filled (6,5). The trend of the film absorbance at S_{11} is given in Figure 4.1D with 0.063 for hexane@(6,5), 0.075 for empty and 0.085 for water-filled (6,5). As illustrated in Figure 4.3B, EQE at S_{11} is following this trend with values of 1.56 %, 3.56 % and 4.59 % for hexane, empty and water@(6,5).

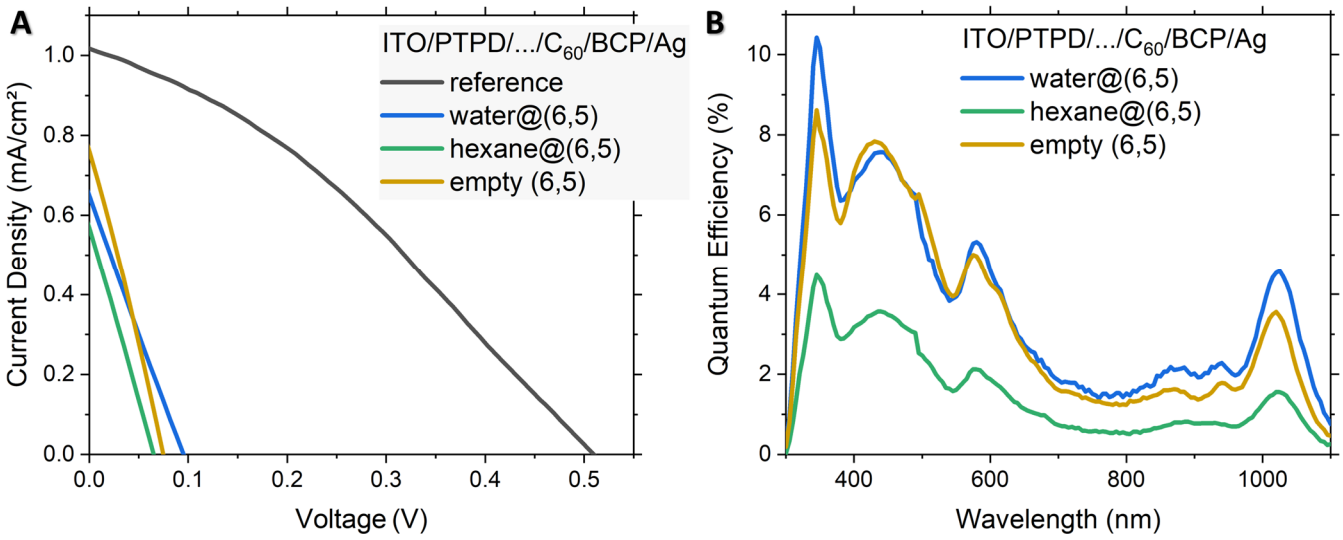

Figure 4.3: (A) Current density-voltage curve of (6,5)/C_{60} solar cells with different filling: empty (6,5) from Nopo (gold) in comparison to water (blue) and hexane filling (green). (B) Corresponding EQE of the (6,5)/C_{60} devices.

The C_{60} thickness in this second set of experiments is roughly 60 nm and thus lower than the standard thickness of 90-100 nm. As a result, the C_{60} signal in the EQE spectrum between 400 and 550 nm is not so present and more comparable to the intensity of the CNT peaks. The thinner acceptor layer can lead to the lower V_{OC} and more shorts if the CNT network is not completely covered and individual CNTs are sticking out directly contacting the back electrode.

Table 2: Performance parameters of (6,5)/C_{60} solar cells with different filling: empty (6,5) from Nopo in comparison to complete water and hexane filling.

Layer stack ITO/PTPD/…/C_{60}/BCP/Ag	**J_{SC} [mA/cm²]**	**V_{OC} [mV]**	**FF [%]**	**Efficiency [%]**	**Peak EQE at S_{11} of (6,5) [%]**
reference	1.016	509.7	32.4	0.168	-
water@(6,5)	0.651	95.2	24.5	0.015	4.59
hexane@(6,5)	0.571	65.3	25.6	0.010	1.56
empty (6,5)	0.765	74.8	27.1	0.015	3.56

In summary, absorbance peaks of (6,5) with different fillings are shown to be red shifted for several nanometer due to other dielectric constants of the liquids inside. The outer environment is for all species 1% DOC solution and the sorting and solar cell fabrication procedures are identical. Incorporated in the layer stack ITO/PolyTPD/(6,5)/C_{60}/BCP/Ag, the empty (6,5) might be minimal more efficient compared to filled devices but empty lag behind in the EQE intensity at S_{11}. Overall, the filling of the (6,5) seem to make no significant difference.

4.2 Dye Filling

After accomplishing the solvent filling in the (6,5) chirality, the CoMoCAT raw material is mixed with anthracene to test different filling procedures. Similar steps are performed for the HiPco raw material with tetracene. To address the issue of dyes absorbing in the visible, squarylium dye is encapsulated in larger diameter raw materials such as P2 or TUBALL. All these dyes are soluble in organic solvents like chloroform or toluene. In addition, 3-Hydroxyisonicotinealdehyde (HINA) as aqueous dye is tested in CoMoCAT due to its small size.

4.2.1 Anthracene and Tetracene

Like for the solvent filling in (6,5), the CoMoCAT raw material is mixed with anthracene because these are both powders solvents are used as transfer agent. Three different filling sequences are tested all based on the liquid-phase filling with an overload of anthracene compared to SWCNTs in a ratio of 3:1. The concentration of carbon nanotubes is always hold at 1 mg/mL.

(1) tip sonication: Toluene was used as solvent and the mixture was tip sonicated for 25 minutes not only incubated as for the liquid-phase filling. Filtration and washing followed as usual to remove excess anthracene molecules, here toluene and chloroform were rinsed through the filter cake. Chloroform is able to dissolve more anthracene and is ideal to wash away the overdosed filler. After evaporation of the residual chloroform, the dried filter cake was dispersed in 1 % DOC as usual by tip sonication for 30 minutes.
(2) tip sonication + incubation: Chloroform was directly used in the first step and tip sonication of the mixture was only applied for 10 minutes (instead of 25). Additionally, the dispersion was stirred at 65°C for about 3 days. Filtration and washing were similar to the previous method except for the rinsing solvent which was here only chloroform. Redispersion in DOC was identical.
(3) tip sonication + evaporation: Like in method (2) the CNT and anthracene were tip sonicated in chloroform but for 30 minutes followed by complete evaporation of the solvent to force the molecules to move in the cavity. Transfer on the filter, washing and redispersion in DOC completed the procedure.

The reference sample was prepared by the third method beginning from the tip sonication in chloroform of course without any filler molecule, to evaporation, chloroform rinsing, drying and finally tip sonication in DOC. The absorbance measurements in Figure 4.4A represent all chiralities in the CoMoCAT sample with the maximum intensity for the (6,5) S_{11} around 1000 nm. However, no additional peak can be observed for all methods but a higher background in visible and UV for method (1) with just tip sonication. Overall anthracene is quite challenging to observe by absorbance because of its main peak below 300 nm and some excitonic signals up to 400 nm.

Method (2) with the extra incubation time shows sharper CNT signals especially in the IR region which can be a sign for filling. There might be an overlap with the increasing background of the CNT sample in the UV that can hide an extra peak or the filler molecule is chloroform from processing.

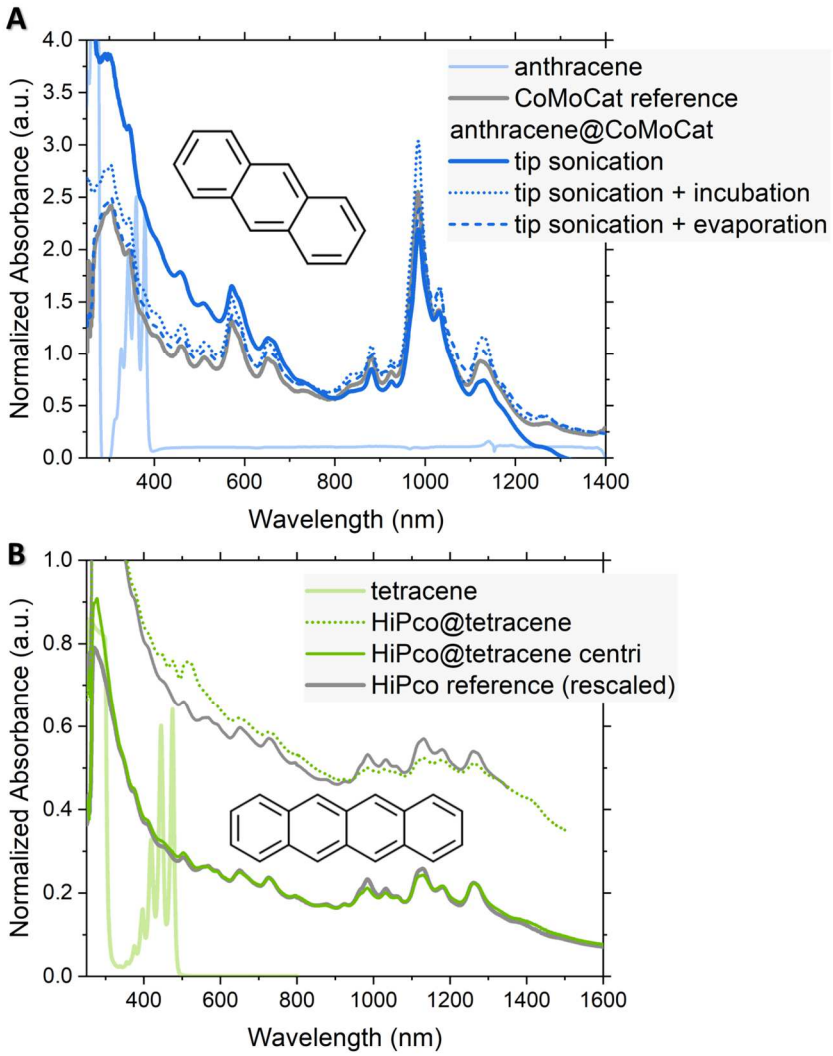

Figure 4.4: Normalized absorbance measurement in water/DOC of (A) CoMoCAT treated with anthracene and (B) HiPco mixed with tetracene focussing on different filling procedures.

Tetracene is tested with its characteristic exitonic peaks between 400 and 500 nm, to prevent the detection problem and HiPco material that contains more larger diameter chiralities facilitates the encapsulation. The same overload of 3:1 for filler molecules to SWCNTs is used in toluene executing filling method (1). An additional broad peak around 520 nm is measured in absorbance for the tetracene@HiPco, see Figure 4.4B, although after centrifugation of the sample the extra peak is gone. Centrifugation as instrument to narrow the peak positions of individual nanotubes also remove bundles and other heavier CNTs. In general, the tetracene molecules inside a carbon nanotube should not be so heavy that they are removed by centrifugation, but rate zonal ultracentrifugation as demonstrated by solvent filling (6,5) was not performed. Extensive washing was performed during sample preparation to reduce excess molecules on the outside, that could attach due to van der Waals interaction. Such tetracene/SWCNT complexes could also be an explanation for the observed peak.

4.2.2 Squarylium Dye (SQ)

Squarylium dye have already been filled in SWCNTs by others showing a sieving diameter around 1.15 nm[1, 2] thus CoMoCAT is not sufficient as raw material. Larger diameter carbon nanotubes in raw materials such as P2 or TUBALL are combined with SQ to enable endohedral filling. A 1:1 mixture of SWCNTs and SQ in dichloromethane (DCM) was briefly bath sonicated for 5 minutes and incubated for 1 hour by refluxing. Afterwards. the SQ@SWCNT powder is filtered and extensively washed with DCM followed by drying and dispersion in DOC. The absorbance spectra in Figure 4.5A highlight that SQ filling works for different raw materials with the additional peak around 705 nm, as expected, only the CoMoCAT is too small to encapsulate the molecules.

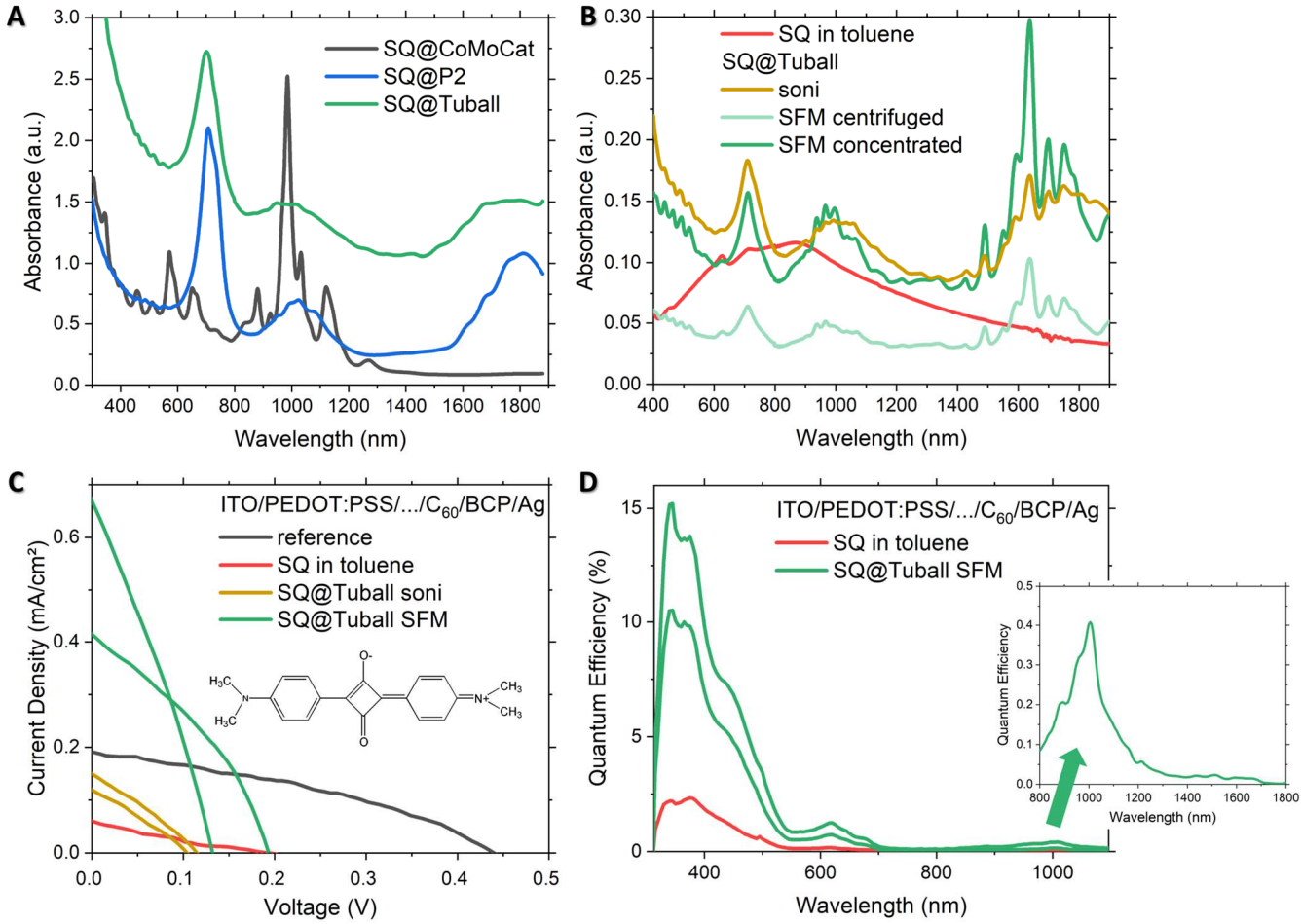

Figure 4.5: Absorbance spectra of (A) different raw materials filled with SQ except the CoMoCAT due to its small diameter and (B) SQ@Tuball samples used for solar cell fabrication. (C) J-V curves of ITO/PEDOT:PSS/.../C_{60}/BCP/Ag with pure SQ or SQ@Tuball (soni or SFM) in the stack. Inset: chemical formula of SQ (D) Corresponding EQE spectra of the SQ@Tuball SFM devices.

For solar cell fabrication, only semiconducting nanotubes are necessary, so as next step polymer-sorting with PFO-BPy was performed with the filled raw material to gain individualized SQ@CNTs in toluene either by shear-force mixing or tip sonication. The absorbance spectra shown in Figure 4.5B are obtained after centrifugation of the toluene dispersions and in addition, the SFM

sample was concentrated. All spectra still display the SQ absorbance signal at 711 nm and the maximum absorbance in the IR at 1637 nm corresponds to the (14,6) chirality.[8]

The device fabrication is identical to the procedure already discussed in chapter 3 for CNT dispersions in toluene that can directly be spin cast on the transparent ITO with PEDOT:PSS. The standard C_{60} acceptor is used, although it is known that this fullerene acceptor has a diameter limit of roughly 1 nm to separate charges. Albeit the (14,6) chirality has a diameter of 1.4 nm, there is a detectable but low J-V performance illustrated in Figure 4.5C. The EQE measurements of the SQ@Tuball SFM in Figure 4.5D can clarify this issue because in IR only one peak at 1000 nm is detected corresponding to (6,5) chirality. The signals at 620 nm of SQ@Tuball with intensities of 1.26 % or 0.81 % can rather be attributed to the C_{60} than SQ because the SQ in toluene (red) has no significant EQE response at this wavelength and other (6,5)/C_{60} cells like in Figure 4.2B show there signals as well. All the numbers are provided in Table 3, which confirm again that the SFM SQ@Tuball has a better performance than the sonicated sample.

Table 3: Performance parameters of SQ@Tuball/C_{60} solar cells with different dispersion methods either shear-force mixing or tip sonication, and references with just C60 or pure SQ without nanotubes.

Layer stack ITO/PEDOT:PSS/…/C_{60}/BCP/Ag	**J_{SC} [mA/cm²]**	**V_{OC} [mV]**	**FF [%]**	**Efficiency [%]**	**Peak EQE at S_{11} of (6,5) [%]**
reference (only C_{60})	0.196	437.8	36.3	0.030	-
SQ in toluene	0.060	190.6	22.6	0.0026	-
SQ@Tuball soni	0.150 0.120	114.5 104.3	28.9 27.7	0.0050 0.0035	?
SQ@Tuball SFM (dev04-4) (dev06-3)	0.668 0.414	130.9 192.4	29.3 34.6	0.026 0.028	0.41 0.15

In summary, filling squarylium into Tuball or P2 was successful but the sorting should be done by aqueous based methods to gain a variation of filled chiralities, as demonstrated in the paper of Forel et al.[9] The incorporation of the dye filled SWCNTs is challenging because a minimum diameter of roughly 1.15 nm is required for the encapsulation[1] whereas the standard fullerene acceptor is limited to diameters of up to 0.95 nm in SWCNT/C_{60} solar cells.[4]

4.2.3 3-Hydroxyisonicotinealdehyde (HINA):

Many dyes are soluble in organic solvents like chloroform or toluene and require larger diameter SWCNTs because their molecular structure is more complex compared to solvents that fit inside

nearly every chirality. In contrast, 3-Hydroxyisonicotinealdehyde (HINA) is an aqueous dye and so small that it can fit inside CoMoCAT.

The absorbance of HINA is pH dependent as displayed in Figure 4.6A due to its hydroxy group and the pyridine ring shown in panel B. For an pH below 3.9 the cationic species with an absorbance at 286 nm is dominant whereas in the basic regime (pH > 7.1) HINA is anionic with the main absorbance peak at 385 nm. The neutral HINA molecule absorbs in equal shares at 385 nm and additionally at 325 nm. The green emission for the anionic dye is relative intense at 525 nm, HINA is therefore the smallest green-emissive fluorophore.[10] Over the time, the basic solutions show lower absorbance and in the case of the neutral solution the intensity shifts to the cationic HINA, as shown in Figure 4.6C.

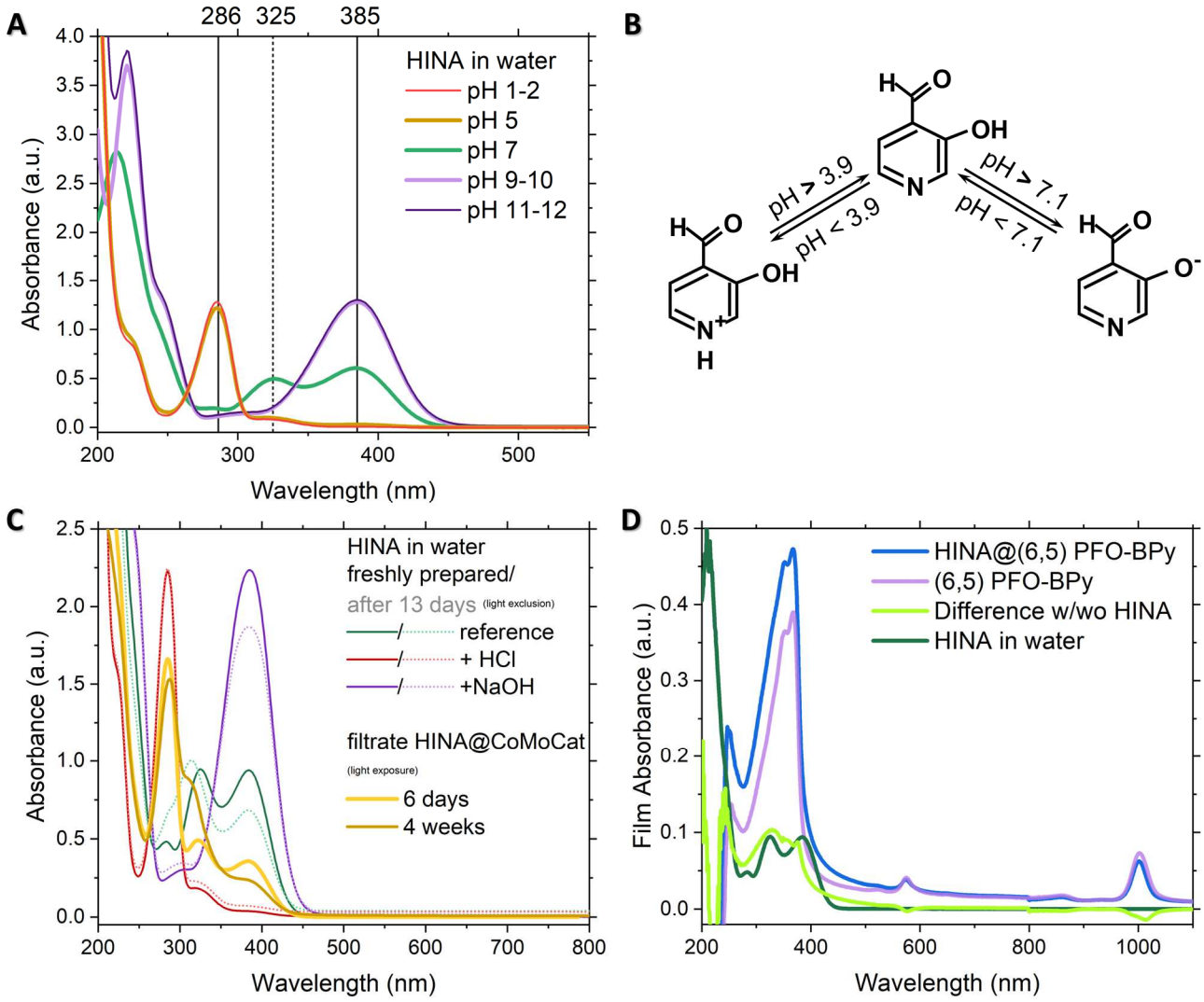

Figure 4.6: (A) Absorbance of HINA depending on the pH and (B) the corresponding cationic or anionic molecular structures. (C) Intensity differences in absorbance of freshly prepared solutions and after 13 days. The filtrate of HINA@CoMoCAT showing mainly cationic response even after several weeks. (D) The film absorbance of HINA@(6,5) (blue) and a reference sample (purple) are similar but the signal of the differential at 328 nm can be assigned to the HINA dye.

The standard procedure for encapsulation is used where the aqueous HINA solution is stirred with the CoMoCAT material, followed by washing and drying the filter cake. The absorbance of the filtrate is mainly cationic as displayed in Figure 4.6C but over several weeks a shoulder is occurring that can be ascribed to the neutral species. The soaked raw material HINA@CoMoCAT was subsequently polymer sorted with PFO-BPy in toluene using the shear-force mixer. The resulting film absorbance in Figure 4.6D highlights the selectivity of the PFO-BPy polymer which only wraps the (6,5) chirality absorbing around 1000 nm. The difference of the HINA@(6,5) and the reference sample is displayed in Figure 4.6D as green line but it is hard to tell if there is an additional peak due to overlap with PFO-BPy absorbing at 365 nm. However, the intensity at 328 nm of the differential line can be assigned to the neutral HINA molecule.

The HINA absorbance in the UV and the (6,5) main signal in the infrared gives rise to a gap in the visible region. Thus, an acceptor absorbing in this range would be favourable in solar cell fabrication but C_{60} is only capturing the light up to 500 nm. ITIC-2F, a non-fullerene acceptor, was already tested by Wang et al.[11] in combination with (6,5) and has its absorbance maximum at 725 nm.[12] In the solar cell fabrication process, ITIC-2F is dissolved in chlorobenzene and directly spin cast on top of the (6,5) film. The J-V curves of completed (6,5)/ITIC-2F devices shown in Figure 4.7A reveal that the HINA filling is detrimental to the cell performance.

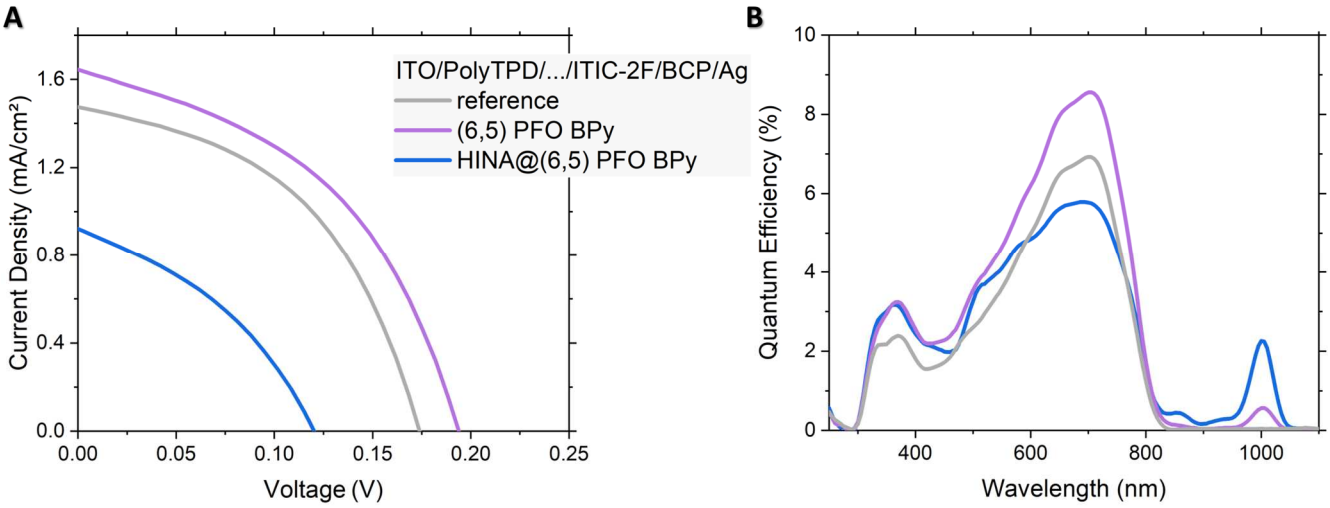

Figure 4.7: (A) J-V curves of polymer-sorted HINA@(6,5) (blue) or (6,5) (purple) in comparison to the reference sample without CNTs. (B) Corresponding EQE spectra of all devices.

The EQE signal of ITIC-2F around 705 nm is 5.78 % with the HINA dye whereas it is 8.56 % in combination with polymer-wrapped (6,5) shown in Figure 4.7B. An extra EQE peak in the blue region is not observed, meaning no or only partial filling is accomplished due to the absorbance

results. Nevertheless, the EQE spectrum of HINA@(6,5) exhibits an increased S_{11} intensity of 2.26 % compared to 0.56 % for (6,5) at 1000 nm.

Table 4: Solar cell parameters of HINA@(6,5) or just (6,5) in combination with ITIC-2F in comparison to the reference sample without any SWCNTs.

Layer stack ITO/PolyTPD/.../ITIC-2F/BCP/Ag	J_{SC} [mA/cm²]	V_{OC} [mV]	FF [%]	Efficiency [%]	Peak EQE at S_{11} of (6,5) [%]
Reference (pure ITIC-2F)	1.47	173.7	46.8	0.120	-
(6,5) PFO-BPy	1.64	193.4	44.7	0.142	0.56
HINA@(6,5) PFO-BPy	0.92	119.4	37.3	0.041	2.26

The encapsulation of HINA is promising due to its small size, water solubility and green emission. However, the green emission is only found for the anionic HINA in a basic environment of a pH over 7.1, the neutral and cationic molecules show blue emissions of 382 and 395 nm, respectively.[10] As shown in Figure 4.6C, mainly the cationic species occurred in this experiment most likely due to the slightly acidic deionized water used as solvent for HINA. The dye encapsulation is hard to conform just with absorbance measurements due to the overlap of the polymer peak and the HINA signals. The creation of an intentionally basic environment for the HINA molecules during the filling procedure could be one option to facilitate the distinction between dye and polymer. Alternatively, aqueous sorting methods can be performed but here the risk is to flush out the dye during processing or to change the conformation due to pH variation.

4.3 Summary

The encapsulation of several solvents in (6,5) and dye molecules like squarylium in larger diameter SWCNTs was successful using the liquid phase filling[3] technique. A good indication of accomplished filling is an extra peak in the absorbance spectrum, however, overlapping signals especially in the case of filled raw materials makes it hard to confirm encapsulation. Low dye content or partial filling is another obstacle which is often observed if the size of the dye is close to the SWCNT diameter and is just fitting in the cavity.

Filled raw material can be separated as usual by aqueous methods as well as polymer sorting. Depending on the solubility of the dye, the sorting method should be chosen carefully to avoid a flushing out during the sorting procedure. In general, most dyes are soluble in organic solvents, so

aqueous two-phase extraction is favoured. For aqueous dyes like HINA, polymer sorting is the better choice to yield individual filled chiralities.

These dye@SWCNT samples can be incorporated into solar cells in the same way as their reference solutions with water-filling or an empty cavitiy depending on the separation procedure. The solvents encapsulated in (6,5) seem to make no significant difference in solar cell performance, just the empty (6,5) are minimal more efficient compared to water- or hexane-filling. Those SWCNT/C_{60} solar cells only absorb in the infrared region and around 350 to 550 nm due to the fullerene acceptor but they are missing the main visible part of the solar irradiation. Dye molecules absorbing in this region can complement the solar cell absorption such as squarylium dye encapsulated in larger diameter CNTs. The problem of SQ is that a minimum diameter of 1.15 nm is required for the encapsulation[1] whereas C_{60} is limited to diameters of up to 0.95 nm in SWCNT based solar cells.[4] Other smaller sized dye molecules with absorption in the visible are necessary or acceptors suitable for larger diameter nanotubes but their absorption should then not overlap with the dye. Instead of optimizing the light capture of the SWCNT solar cells, already established broad band light absorbing solar cells can be combined with SWCNT/C_{60} solar cells for absorption extension into the infrared.

4.4 Experimental Details

4.4.1 Raw Materials

SWCNT raw materials are procured from several manufacturers and utilized without modification. CVD grown CNTs like CoMoCAT® (773735 lot no. MKBZ1159V) from Sigma-Aldrich, or HiPco nanotubes either from NanoIntegris (batch# HR29-073) or Nopo Nanotechnologies (batch# Aug 2020). Larger diameter tubes likeTuball™ (batch#: 109-16092015) from OCaSiAl with an average diameter of 1.6 nm or electric arc CNTs (P2-SWCNT, Lot# 02-A011) from Carbon Solution.

4.4.2 Endohedral Filling

Solvent filling was performed by liquid phase filling[3] which means adding the raw CoMoCAT® powder (40 mg) to 2-3 mL of n-hexane (C_6H_{14}) or water and incubating them for 1 hour in the liquid state at room temperature. After incubation, the mixtures were filtered (Millipore VVLP membrane, 0.1 µm pore size) and washed by heptane to remove the residual alkane on the outside of the SWCNTs. The resulting filter cakes were placed in a fume hood to allow the heptane to evaporate prior to the dispersion with surfactants.

For anthracene and tetracene several filling procedures are tested, all details are given in the main text. Here the product specification and mass ratios are depicted. Method 1'tip sonication' is staring with 8.8 mg CoMoCAT® material in 8 mL toluene mixed with 25 mg anthracene (Sigma Aldrich, lot#MKCC7378) and tip sonicated for 25 min. The mixture is filtered on a regenerated cellulose membrane (RC-membrane, it4ip, 0.2 µm pore size) and washed with 5 ml toluene and 15 mL chloroform. In method 2, 64.6 mg anthracene are mixed with 13.3 mg CoMoCAT® in 13 mL chloroform before 10 min tip sonication and incubation time. Similar to the first method, the mixture is filtered on RC and now washed with in total 27 mL chloroform. The third procedure is based on 12.1 mg CoMoCAT® with 38.9 mg anthracene in 12 mL chloroform. After tip sonication, the complete chloroform is evaporated in an oven at 150°C followed by redispersion in 10 mL and washing with 17 mL chloroform.

Tetracene filling is tested with HiPco material, here 13.6 mg CNTs are combined with 44.0 mg tetracene (Sigma Aldrich, lot#SHBJ8238) in 14 mL chloroform and tip sonicated for 25 min. After evaporation of the chloroform, as in method 3, the powder is dispersed in 12 mL chloroform by

few minutes bath sonication and washed with in total 226 mL chloroform. The sample was centrifuged (SW-40-Ti rotor, Beckman-Coulter, Optima L-80 XP) at 19000rpm and 20°C.

Filling of SWCNTs with the squarylium dye 1,3-bis[4-(dimethylamino)phenyl]-2,4 dihydroxycyclobutenediylium dihydroxide, bis(inner salt) (SQ) was carried out using a similar strategy as for solvent filling. 20 mg SWCNTs (EA-P2, TUBALL™ or CoMoCAT®) were mixed with 20 mg of the SQ dye (lot# MKBG1223 V, Sigma-Aldrich) in 5 mL dichloromethane (DCM, Sigma-Aldrich) bath sonicated for 5 min and incubated for 1 hour by refluxing. The filled SWCNT powders (denoted SQ@SWCNT) were filtered (PTFE membrane, 0.45 µm pore size, Phenex) and washed with copious amounts of DCM to remove the non-encapsulated SQ. The filter cake was then placed in an oven at 100°C to evaporate all the DCM, before further dispersion.

HINA filling in CoMoCAT® was accomplished similar to the SQ encapsulation. First 16.5 mg Hydroxyisonicotinealdehyde (HINA) are dissolved in 6 ml deionized water and stirred with 30 mg CoMoCAT® raw material for 3 days at 60 C. The filled nanotubes were filtered (Nylon membrane, 0.2 mm pore size) and washed with water followed by drying in an oven at 120°C.

4.4.3 SWCNT Dispersion and Separation

For aqueous suspension, the filled (or unfilled) SWCNT powder (1 mg/mL) was dispersed in 2 % DOC (20 g/L) solution via tip sonication (45 min) in an ice bath, followed by centrifugation (Beckman J-2 centrifuge, JA-20 rotor, 1884 rad/s, 2 h), followed by the collection of the supernatant. For Rate-Zonal Centrifugation, 8.2 mL aliquots of the supernatant were layered on top of 28 mL of 10 % (volume/volume) iodixanol containing 1 % DOC (10 g/L) and ultracentrifuged for 2 h 45 min in a VTi-50 rotor (Beckman-Coulter) at 5240 rad/s (50 000 rpm) at 20°C. Primary bands in the middle of each centrifuge tube containing well-individualized SWCNTs were collected. All SWCNT populations were concentrated and adjusted toward a 1 % DOC (10 g/L) concentration using iterative concentration dilution cycles in a pressurized ultrafiltration stirred cell (Millipore) with either a 100 or 300 kDa molecular weight cut-off membrane.

These concentrated aqueous solutions are the parent suspension for aqueous two-phase extraction which was already described in detail in the experimental section. The individual (6,5)

nanotube solutions achieve concentrations of 64-128 µg/mL and 52-104 µg/mL for water- or hexane-filling and 117-233 µg/mL for (6,5) HiPco and 55-110 µg/mL for the completely empty (6,5) from Nopo.

SQ- and HINA filled SWCNT powders were further treated by polymer-sorting in toluene instead of the aqueous separation. 29.1 mg HINA@CoMoCAT are shear-force mixed with 36.6 mg PFO-BPy (American Dye Source, lot no. 19L014A1) in ca. 100 mL toluene. The details are described in the experimental section, briefly, shear-force mixing is followed by ultra centrifugation and a filtration step to wash off excess polymer and simultaneously concentrate the polymer-wrapped and filled SWCNTs by redispersion in a smaller amount of toluene.

4.4.4 Device Fabrication

The fabrication of SWCNT based solar cells from (6,5) with different solvent filling is the same as already described in the experimental details of chapter 3.

Briefly, pre-structured indium tin oxide substrates (Psiotec, 15 Ω/sq) are first cleaned followed by spin coating PolyTPD (M_w = 100,000 – 150,000, Ossila, 10 mg/mL in chlorobenzene) as hole transport layer. After annealing at 230°C for 30 min in a glove box, the SWCNT films from aqueous solutions were transferred onto the PolyTPD layer in air. The details of the film preparation are already noted in the experimental section (chapter 2). The filter membrane made of polycarbonate was then dissolved by propylamine (≥ 99%, Sigma-Aldrich) followed by washing with acetone and isopropanol. To complete device fabrication, 100 nm C_{60} fullerene (99.9+%; Sigma–Aldrich, lot. MKCK0541) are evaporated on the SWCNT film. Subsequently, 10 nm of Bathocuproine (BCP, > 99.5%, Ossila) were thermally evaporated followed by the 100 nm thick silver electrode. The active area of all cells is 0.105 cm^2.

The HINA@CoMoCAT devices are fabricated with the same procedure except the C_{60} acceptor layer is replaced by ITIC-2F 3,9-bis(2-methylene-((3-(1,1-dicyanomethylene)-6,7-difluoro)-indanone))-5,5,11,11-tetrakis(4-hexylphenyl)-dithieno[2,3-d:2',3'-d']-s-indaceno[1,2-b:5,6-b']dithiophene (Ossila, lot M2075A1). Here the acceptor layer is spin cast from a 10 mg/mL ITIC-2F solution in chlorobenzene. (1000 rpm for 20 s)

For the PFO-BPy wrapped SQ@Tuball, the solar cell design is the same but the hole transport layer is exchanged by PEDOT:PSS (AI 4083, Ossila) which is placed on the plasma cleaned ITO. PEDOT:PSS is first filtered (Millex-HV, 0.45 µm, Merck) and subsequently spin cast at 3000 rpm for 30 s followed by an annealing at 150°C for 15 min. 55 µL of the polymer-wrapped SWCNTs dispersed in toluene are directly spin cast on top of the PEDOT:PSS with 600 rpm for 20 s followed by 1500 rpm for 5 s. After annealing at 110°C for 7 min, the C_{60} acceptor layer was evaporated like in the aqueous case, and BCP plus silver on top to finish the device.

4.5 References

[1] S. van Bezouw, D.H. Arias, R. Ihly, S. Cambre, A.J. Ferguson, J. Campo, J.C. Johnson, J. Defillet, W. Wenseleers, J.L. Blackburn, *ACS Nano* **2018**, *12*, 6881-6894.

[2] K. Yanagi, K. Iakoubovskii, H. Matsui, H. Matsuzaki, H. Okamoto, Y. Miyata, Y. Maniwa, S. Kazaoui, N. Minami, H. Kataura, *J Am Chem Soc* **2007**, *129*, 4992-4997.

[3] J. Campo, Y. Piao, S. Lam, C.M. Stafford, J.K. Streit, J.R. Simpson, A.R. Hight Walker, J.A. Fagan, *Nanoscale Horizons* **2016**, *1*, 317–324.

[4] M. Pfohl, K. Glaser, A. Graf, A. Mertens, D.D. Tune, T. Puerckhauer, A. Alam, L. Wei, Y. Chen, J. Zaumseil, A. Colsmann, R. Krupke, B.S. Flavel, *Adv Energy Mater* **2016**, *6*, 1600890.

[5] S. Cambre, W. Wenseleers, *Angew Chem Int Ed Engl* **2011**, *50*, 2764-8.

[6] J.A. Fagan, *Nanoscale Adv* **2019**, *1*, 3307-3324.

[7] H. Li, G. Gordeev, O. Garrity, S. Reich, B.S. Flavel, *ACS Nano* **2019**, *13*, 2567-2578.

[8] H. Li, G. Gordeev, O. Garrity, N.A. Peyyety, P.B. Selvasundaram, S. Dehm, R. Krupke, S. Cambre, W. Wenseleers, S. Reich, M. Zheng, J.A. Fagan, B.S. Flavel, *ACS Nano* **2019**.

[9] S. Forel, H. Li, S. van Bezouw, J. Campo, L. Wieland, W. Wenseleers, B.S. Flavel, S. Cambre, *Nanoscale* **2022**, *14*, 8385-8397.

[10] R. Kang, L. Talamini, E. D'Este, B.M. Estevao, L. De Cola, W. Klopper, F. Biedermann, *Chem Sci* **2020**, *12*, 1392-1397.

[11] J.L. Wang, S.R. Peurifoy, M.T. Bender, F. Ng, K.S. Choi, C. Nuckolls, M.S. Arnold, *J Phys Chem C* **2019**, *123*, 21395-21402.

[12] X. Liu, X. Li, Y. Zou, H. Liu, L. Wang, J. Fang, C. Yang, *J Mater Chem A* **2019**, *7*, 3336-3343.

- this page left intentionally blank -

- this page left intentionally blank -

5 Tandem approach: Silicon/SWCNT Solar Cell

Here the practical possibility of SWCNT/fullerene solar cells is investigated to function as infrared extension for light absorption of silicon solar cells. For this purpose, a bifacial silicon solar cell is employed as the top cell because it ensures that most of infrared light passes to the SWCNTs/fullerene cell underneath. The bifacial silicon cell is efficient for above-bandgap light (< 1100 nm) and highly transparent to below-bandgap light which is an important pre-requisite for this concept. In addition, a bifacial design profits from backside scattered light collection[1-3] and this leads to an overall optical gain that is greater than the heating losses of the design.[4, 5] The first optical transitions of few (n,m) pure SWCNTs are used to best complement to the absorption of silicon. In general, the concept to utilize SWCNTs as IR absorber on the backside of a bifacial silicon solar cell can possibly lead to further reductions of device temperature in the silicon and a simultaneous increase in performance.

5.1 Silicon Cell

In Figure 5.1A the schematic of the bifacial silicon solar cell is shown alongside photographs (Figure 5.1B) of the front and back side of the completed device. The bifacial silicon solar cell was prepared from a 170 µm thick n-type wafer with a boron diffused (p^+) region to form a p-n junction on the front. A silicon nitride layer was used for passivation and antireflection. On the back, phosphorous doped polycrystalline silicon (n^+) with an ultrathin SiO_2 passivation layer and a silicon nitride antireflection coating were used. Either a AgAl or Ag paste was used for firing to ensure low contact resistance between the p^+ or n^+ regions and the silver fingers, respectively.

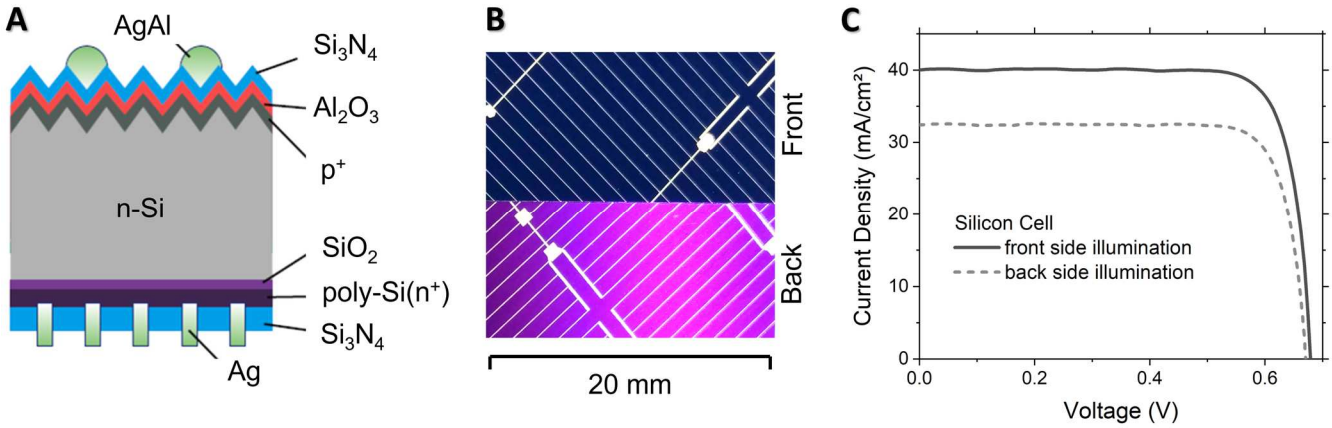

Figure 5.1: (A) Schematic of the bifacial silicon solar cell and (B) photograph of the final device with the metallic fingers on the front and rear side. (C) The corresponding J-V curves for front or back side illumination. Figure reproduce from [6]

The active area was defined by the wafer size and this was cut to 4 cm^2 in order to simultaneously cover all four SWCNT/C_{60} cells on the ITO substrate.

Current density-voltage (J–V) curves of the bifacial solar cell are shown in Figure 5.1C. When illuminated from the front, the bifacial silicon cell has a PCE of 22.1%, and a short circuit current density (J_{SC}) of 40.1 mA/cm^2. (Table 1) The performance values for backside illumination are comparable in V_{OC} and fill factor but only show a PCE of 17.8 % and J_{SC} of 32.4 mA/cm^2. Overall, this makes the bifacial solar cell comparable to the current state-of-the-art.[7, 8]

Table 1: Solar cell performance parameters of a bifacial silicon solar cell.

Layer stack	J_{SC} [mA/cm^2]	V_{OC} [mV]	FF [%]	Efficiency [%]
Si front side	40.05	679.1	81.7	22.07
Si back side	32.42	670.6	82.0	17.76

5.2 Tandem Approach

In the inset of Figure 5.2B the schematic of the 4-probe tandem idea is depicted made of a bifacial silicon solar combined with a monochiral SWCNT/C_{60} device. The organic solar cells used for the tandem are already discussed in chapter 3 with S_{11} transitions that lie either on the edge or outside the absorption range of silicon. Figure 5.2A shows the AM1.5 solar irradiance spectrum overlaid with the absorption of silicon (gray) in the visible and near-IR as well as the absorption of the SWCNTs. The (6,5), (7,6) and (10,3) are shown with their S_{11} at 1000 nm, 1130 nm and 1260 nm, respectively. If C_{60} is used as acceptor, there is an upper diameter limit of 0.95 nm[9] (shown as a dashed line, 1320 nm). Besides the upper limit, a minimum diameter of ≈ 0.88 nm is necessary (shown as a dotted line, 1100 nm) to ensure minimal overlap with silicon and best absorption extension.

In fact, a closer look on the AM1.5 solar irradiance spectrum in Figure 5.2A reveals that the selection of possible chiral species may indeed be even further restricted. If discussion of the absorption tail left and right of the S_{11} peak is neglected, dips at 1135 nm and 1350 nm in the AM1.5 spectrum mean that the best choice for SWCNTs will be those with a S_{11} from 1170 – 1320 nm. Only (9,4), (8,6), (10,2), (11,0), (9,5), (10,3), (8,7), (11,1), and (10,5) meet these criteria. On the other hand, there is a considerable window of opportunity for SWCNTs in the range

1500 – 1800 nm, where the S_{11} of large diameter species like (14,6) is located,[10] but this will require the identification of new acceptors.

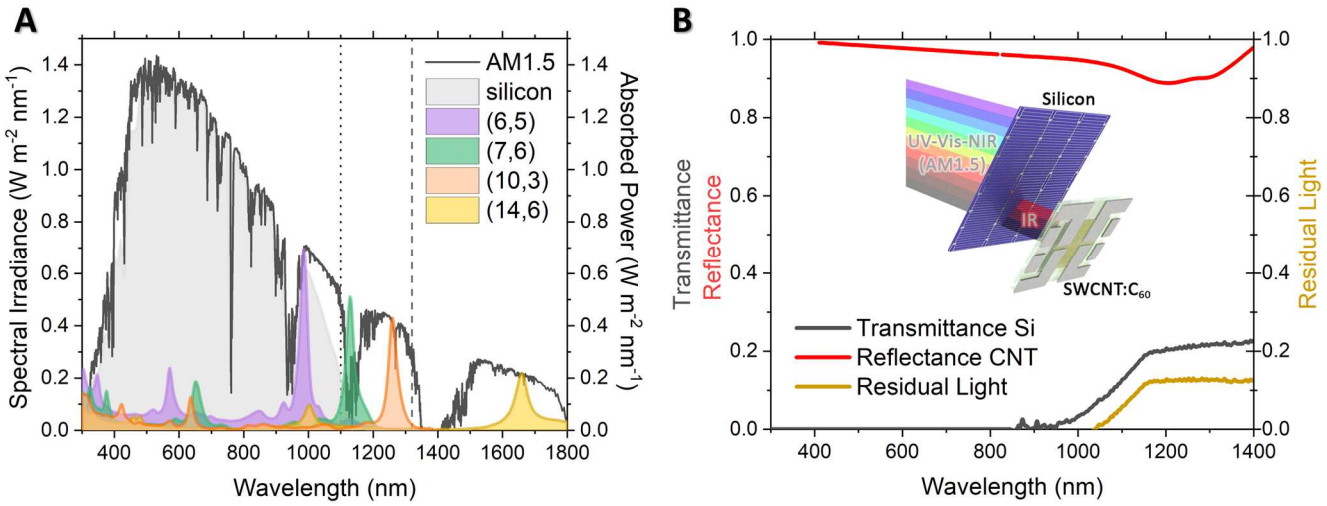

Figure 5.2: (A) Spectral overlap of silicon and SWCNTs with the AM1.5G solar irradiance spectrum. (B) Transmittance of silicon and reflectance of CNTs and the calculated residual light. Figure reproduce from [6]

The transmittance spectrum of pure silicon in Figure 5.2B reveals that a maximum of 23% of the IR light passes through the bifacial cell and begins to increase at 950 nm before reaching a plateau at ≈ 1150 nm. The current density of this residual part of the light after the silicon cell is calculated to be 2.08 mA/cm^2. This highlights the small amount of residual light that could be captured and the reflectance of CNTs in that spectral range also have to be considered.

The disparity of PCE for the silicon and SWCNT/C_{60} solar cells is apparent with 22 % compared to maximum 0.7 % and highlighted as well in the EQE spectra shown in Figure 5.3A. Silicon absorbs light throughout the entire visible range (350 – 1200 nm) and has a flat EQE of ≈ 95 % from 550 – 850 nm. In contrast, SWCNT cells capture far less light with narrow IR absorption and a UV component (330 – 500 nm) associated with C_{60}. Despite being the chiral species of choice for high performance CNT solar cells,[11] it also becomes clear that PFO-BPy wrapped (6,5) SWCNTs are poorly suited to extend the light absorption of a silicon solar cell. The EQE of the silicon cell at 1000 nm is ≈ 85% (compared to 24 % for the SWCNT) and the spectral absorption by the nanotube is entirely overlapped with that of silicon. Consequently, when the PFO-BPy (6,5)/C_{60} cell is measured in combination with the bifacial cell the peak EQE from the nanotube is reduced from 24.20 % to 0.18 %, as shown in Figure 5.3B.

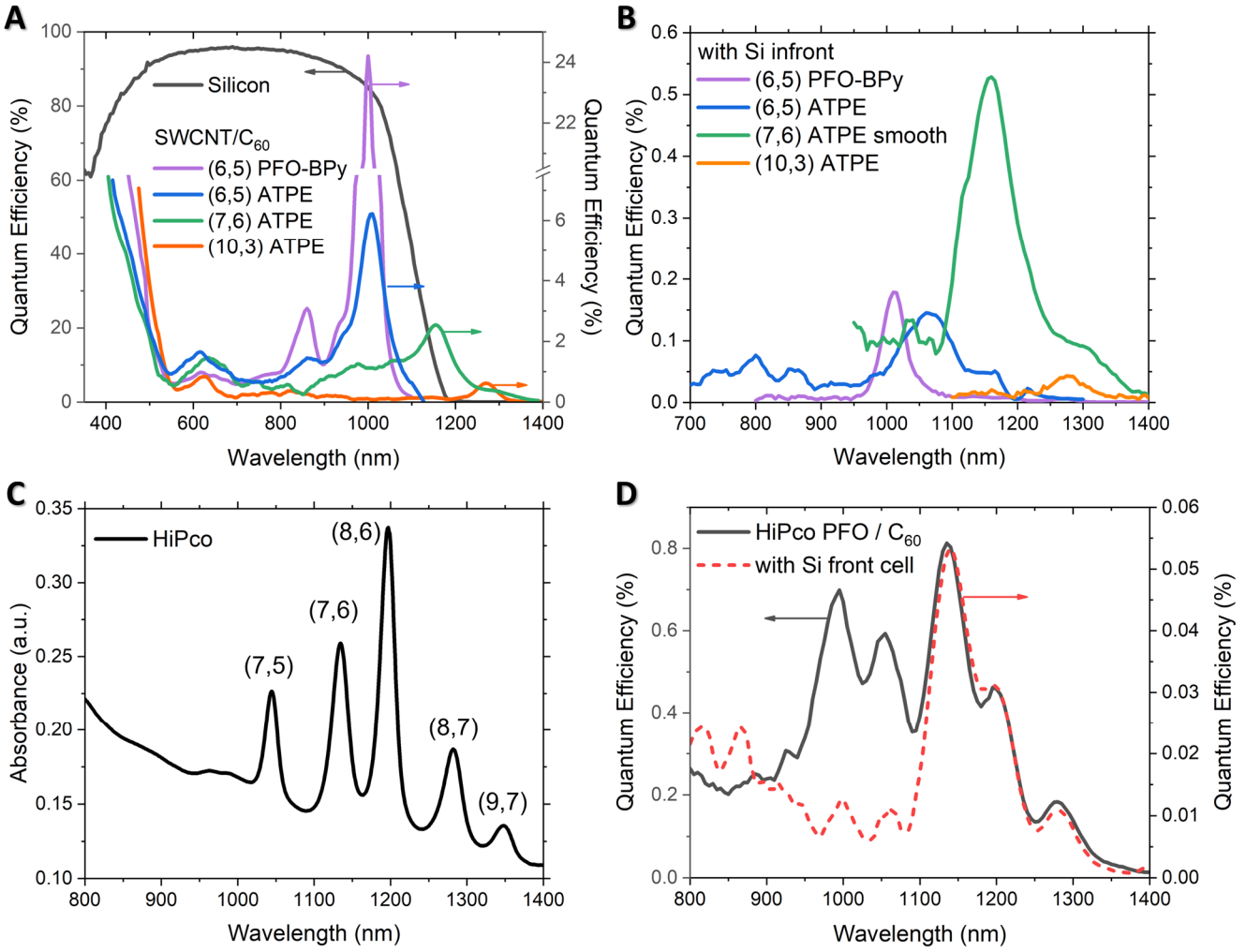

Figure 5.3: (A) EQE of the bifacial silicon solar cell and SWCNT cells. (B) EQE of organic SWCNT solar cells from different chiralities when measured at the rear of the bifacial silicon solar cell in comparison to the transmittance of the silicon cell. (C) The absorption spectrum of a PFO-wrapped HiPco dispersion. (D) EQE of HiPco/C_{60} device with and without the silicon solar cell. Figure reproduce from [6]

Upon comparison of Figure 5.3A and B, the peak EQE for all cells has now been reduced by approximately an order of magnitude with the bifacial cell in the light path. However, now instead of the smallest diameter SWCNT having the highest EQE, it is in fact the (7,6) device which performs the best. This is related to the two competing factors of transmittance of light through the silicon and the energetic offset of the SWCNTs to C_{60}. For (10,3), the decrease in energetic driving force for exciton separation far outweighs any improvement of reduced spectral overlap with silicon. A further example of this effect can be seen in Figure 5.3C and D, where poly(9,9-di-n-octylfluorenyl-2,7-diyl) (PFO) is used to wrap HiPco raw soot which results in the extraction of predominately (7,5) (7,6) (8,6) (8,7) and (9,7).[12] Although the maximum in absorbance (≈ 1200 nm) in Figure 5.3C can be attributed to (8,6), the main EQE peak is caused by (7,6) at 1135 nm due to the better excitonic dissociation with C_{60}. (Figure 5.3D) In combination with the

bifacial silicon solar cell (red dashed line), an EQE from only (7,6), (8,6), (8,7) remain with all others suppressed by the silicon.

If the absorption tails left and right of the central S_{11} peak are included it can clearly be seen in Figure 5.3B, that for (7,6) additional light can be collected from 1150 – 1400 nm. However, the additional current gained by the SWCNT solar cells is limited questioning the realization of an elaborate tandem architecture. The integrated current density from EQE data with and without the silicon cell is summarized in Table 2. For the best performing (7,6) devices, an additional 0.156 mA/cm^2 (value obtained from integration over 300 – 1500 nm) can be expected.

Table 2: Calculated total current density of the silicon cell and the additional contribution from different single chirality SWCNT based PVs.

Current density [mA/cm^2]	**Silicon**	**(6,5) PFO-BPy**	**(6,5) ATPE**	**(7,6) ATPE**	**(10,3) ATPE**
J_{SC} (device)	35.881 [a]	1.367 [b]	0.881 [b]	0.775 [a]	0.584 [a]
J_{SC} (with Si in front)		0.018 [b]	0.022 [b]	0.156 [a]	0.020 [a]

Integration over the range of a) 300-1500 nm or b) 300-1100 nm

Here it is important to state that such a small potential contribution to J_{SC} is far below that of the silicon cell alone (≈ 40 mA/cm^2) and thus a tandem stack with SWCNTs is not expected to be feasible. Even if the current best performing devices with J_{SC} of 8.8 mA/cm^2 for single chirality (6,5)[11] or 10.4 mA/cm^2 for a multi-chiral HiPco sample[13] are taken, this is still 3 – 4 times smaller than that of the silicon cells and will only further be reduced once the cell is placed on the rear as we have shown. More critical to this discussion is an integration of the AM1.5 spectrum from 1100 – 2500 nm which affords an upper limit of an extra ≈ 22.5 mA/cm^2, and which is still below that of the silicon solar cell. Furthermore, if the spectral region is constrained to 1100 – 1320 nm in accordance with the SWCNT diameter/spectral-overlap discussion, then, in the best case there is only an extra ≈ 7.6 mA/cm^2 to be gained from the use of SWCNTs.

Table 3 provides a comparison of the performance data of other types of silicon tandem cells. These architectures all have a PCE > 20 % and the key to their success, has been the use of silicon to extend an otherwise highly efficient front cell towards the IR. In the case organic SWCNT solar cells, these are currently too inefficient to be used on the front side and the spectral overlap of C_{60} (300 – 600 nm) with silicon will only act to reduce the performance of the silicon solar cell.

Table 3: Comparison of the performance values of heterogeneous tandem silicon solar cells.

Tandem Architecture	V_{OC} [V]	J_{SC} [mA/cm²]	FF [%]	PCE [%]
III-V/ Si				
GaAsP/Si (2-terminal) [14]	1.73	17.34	77.7	23.4
GaAs/Si (4-terminal) [15]	1.09	28.9	85.0	32.8
GaInP/GaInAsP/Si [16]	3.25	13.11	84.3	35.9
Monolithic Perovskite/Silicon[17]	1.98	?	81.2	32.5
Bifacial monolithic perovskite/ Silicon [18]	1.80	18.46	75.9	25.2

5.3 Summary

Extending the light absorption of silicon solar cells has been investigated by using the optical transitions of SWCNTs, particularly in the IR. Given the current constraints of C_{60} as an acceptor and the amount of light eventually reaching a SWCNT/C_{60} cell, it was found that (7,6) is currently the best choice for this purpose. However, a large mismatch in current density from the SWCNT-based and silicon solar cells prohibit the realistic use of these two cells in a tandem architecture. Despite the decreasing spectral response of silicon in the range 950 – 1200 nm, traditional approaches such as reducing the absorption of the window layer in the long wavelength range, improving passivation, increasing the internal reflectance at back interface, are more likely to lead to performance gains in this spectral region.

5.4 Experimental Details

A 4-probe tandem approach was realized by combination of chirality specific SWCNT-based solar cells, made from polymer-sorted or aqueous solution, with a bifacial TOPCon silicon solar cell.

The SWCNT/fullerene devices used here, are already discussed in detail in chapter 3. Briefly, the layer stack is based on the active layer sandwiched between a transparent indium tin oxide electrode with a hole transport layer and the electron selective layer BCP (10 nm) completed by the silver electrode (100 nm). The HTL is spin cast on ITO, for the toluene suspension PEDOT:PSS is used and for CNT films from aqueous dispersions PolyTPD is the underlying layer. While the toluene suspension can directly be spin cast on the HTL, the aqueous dispersion is filtered on a polycarbonate membrane. That filtered CNT film is placed upside down on the layer stack and the membrane is dissolved by propylamine and rinsed with acetone and isopropanol to remove membrane and solvent residues. The electron transport layer BCP and the silver electrode are evaporated on top to complement the device.

N-type CZ wafers were used with a thickness of 170 µm, resistivity of 1 – 2 Ω·cm and area of 252 cm^2. The main processes of TOPCon cell fabrication included: 1) saw damage removal and texturing with 2 – 3% KOH (80°C, 20 min) to form random pyramids surface with an average size of 3 µm; 2) formation of the p^+ emitter with a sheet resistance of 150 Ω/□ in a high-temperature diffusion tube; 3) back side polishing using an alkaline solution and subsequent deposition of a 1.5 nm SiO_2 thin film and a 150 nm thick undoped poly-Si layer using low pressure chemical vapor deposition (LPCVD); 4) formation of a heavy phosphorus doped n^+ region on the back side with $POCl_3$ diffusion in a high temperature diffusion tube; 5) silicon oxide glass (boron/phosphorus silicon glass) removal by a HF; 6) AlO_x/SiN_x passivation film deposition using ALD and PECVD; 7) screen printing with silver-aluminium and silver pastes combined with a high temperature firing process to form the metal electrodes on the front and back side, respectively. For the bifacial silicon solar cell, the active area was defined by the wafer size cut to 4 cm^2.

The external quantum efficiency of the SWCNT/fullerene cells is measured in air with the silicon cell right in front and as reference value without it. Other solar cell parameters like J-V curves became too small to be detected with the Silicon in the light path.

5.5 References

[1] A. Hubner, A. Aberle, R. Hezel, in *Conf Rec Twenty Sixth IEEE Photovolt Spec Conf*, Anaheim, CA, USA **1997**. p. 223-226.

[2] R. Guerrero-Lemus, R. Vega, T. Kim, A. Kimm, L.E. Shephard, *Adv Mater Res-Switz* **2016**, *60*, 1533-1549.

[3] T.S. Liang, M. Pravettoni, C. Deline, J.S. Stein, R. Kopecek, J.P. Singh, W. Luo, Y. Wang, A.G. Aberle, Y.S. Khoo, *Energ Environ Sci* **2019**, *12*, 116-148.

[4] M.T. Patel, R.A. Vijayan, R. Asadpour, M. Varadharajaperumal, M.R. Khan, M.A. Alam, *Appl Energ* **2020**, *276*, 115405.

[5] M.W.P.E. Lamers, E. Ozkalay, R.S.R. Gali, G.J.M. Janssen, A.W. Weeber, I.G. Romijn, B.B. Van Aken, *Sol Energ Mat Sol C* **2018**, *185*, 192-197.

[6] L. Wieland, C. Rust, H. Li, M. Jakoby, I. Howard, F. Li, J. Shi, J. Chen, B.S. Flavel, *Carbon* **2021**, *184*, 828-835.

[7] J. Chen, D.D. Tune, K. Ge, H. Li, B.S. Flavel, *Adv Func Mater* **2020**, *30*, 2000484.

[8] K. Yoshikawa, H. Kawasaki, W. Yoshida, T. Irie, K. Konishi, K. Nakano, T. Uto, D. Adachi, M. Kanematsu, H. Uzu, K. Yamamoto, *Nat Energy* **2017**, *2*, 17032.

[9] M. Pfohl, K. Glaser, A. Graf, A. Mertens, D.D. Tune, T. Puerckhauer, A. Alam, L. Wei, Y. Chen, J. Zaumseil, A. Colsmann, R. Krupke, B.S. Flavel, *Adv Energy Mater* **2016**, *6*, 1600890.

[10] H. Li, G. Gordeev, O. Garrity, N.A. Peyyety, P.B. Selvasundaram, S. Dehm, R. Krupke, S. Cambre, W. Wenseleers, S. Reich, M. Zheng, J.A. Fagan, B.S. Flavel, *ACS Nano* **2019**.

[11] A. Classen, L. Einsiedler, T. Heumueller, A. Graf, M. Brohmann, F. Berger, S. Kahmann, M. Richter, G.J. Matt, K. Forberich, J. Zaumseil, C.J. Brabec, *Adv Energy Mater* **2018**, *8*, 1801913.

[12] A. Nish, J.Y. Hwang, J. Doig, R.J. Nicholas, *Nat Nanotechnol* **2007**, *2*, 640-6.

[13] M. Gong, T.A. Shastry, Q. Cui, R.R. Kohlmeyer, K.A. Luck, A. Rowberg, T.J. Marks, M.F. Durstock, H. Zhao, M.C. Hersam, S. Ren, *ACS Appl Mater Interfaces* **2015**, *7*, 7428-35.

[14] T.J. Grassman, D.J. Chmielewski, S.D. Carnevale, J.A. Carlin, S.A. Ringel, *IEEE J Photovolt* **2016**, *6*, 326-331.

[15] S. Essig, C. Allebé, T. Remo, J.F. Geisz, M.A. Steiner, K. Horowitz, L. Barraud, J.S. Ward, M. Schnabel, A. Descoeudres, David L. Young, M. Woodhouse, M. Despeisse, C. Ballif, A. Tamboli, *Nat Energy* **2017**, *2*, 17144.

[16] M.A. Green, E.D. Dunlop, J. Hohl-Ebinger, M. Yoshita, N. Kopidakis, X. Hao, *Progress in Photovoltaics: Research and Applications* **2021**, *29*, 657-667.

[17] NREL, *Best Research-Cell Efficiency Chart*, https://www.nrel.gov/pv/cell-efficiency.html, (accessed Feb 2023).

[18] M. De Bastiani, A.J. Mirabelli, Y. Hou, F. Gota, E. Aydin, T.G. Allen, J. Troughton, A.S. Subbiah, F.H. Isikgor, J. Liu, L. Xu, B. Chen, E. Van Kerschaver, D. Baran, B. Fraboni, M.F. Salvador, U.W. Paetzold, E.H. Sargent, S. De Wolf, *Nat Energy* **2021**, *6*, 167-175.

- this page left intentionally blank -

- this page left intentionally blank -

6 SWCNT/ Non-Fullerene Solar Cells

6.1 (6,5)/ Non-Fullerene Solar Cells

Bilayer cells of polymer-wrapped (6,5) SWCNTs with three different non-fullerene acceptors (NFA) will be discussed in this section and compared with the standard (6,5)/C_{60} solar cells. The schematic of the layer stack in Figure 6.1A was already discussed in chapter 3 about SWCNT/fullerene solar cells. Briefly, the solar cell consists of (6,5) SWCNTs as donor and a (non) fullerene acceptor sandwiched in between the hole transport layer (HTL) PEDOT:PSS and the transparent cathode made of ITO on glass and on the other side the electron transport layer BCP plus the silver back electrode. All details are summarized in the experimental details at the end of this chapter.

The (6,5) SWCNT solution was prepared by shear-force mixing with the selective polymer PFO-BPy to achieve longer and less defected carbon nanotubes which minimizes quenching sites. This ensures longer exciton lifetimes and higher quantum yields.[1-3] A low concentration of (excess) polymer facilitates charge separation and transfer due to better contact areas between the SWCNTs and the acceptor.[4, 5] The (6,5) SWCNT films were fabricated by multiple spin coating steps from the concentrated toluene solution resulting in thicknesses between a few nanometer up to 18 nm. In the bilayer stack the (6,5) films are combined with three different non-fullerene acceptors: 3,9-bis(2-methylene-((3-(1,1-dicyanomethylene)-6,7-difluoro)-indanone))-5,5,11,11-tetrakis(4-hexylphenyl)-dithieno[2,3-d:2’,3’-d’]-s-indaceno[1,2-b:5,6-b’]dithiophene or short ITIC-2F, N,N'-Dioctyl-3,4,9,10-perylene dicarboximide or PTCDI-C8 and Y6, 2,2'-((2Z,2'Z)-((12,13-bis(2-ethylhexyl)-3,9-diundecyl-12,13-dihydro-[1,2,5]thiadiazolo[3,4-e]thieno[2",3’’:4’,5']thieno [2',3':4,5]pyrrolo[3,2-g]thieno[2',3':4,5]thieno[3,2-b]indole-2,10-diyl)bis(methanylylidene)) bis(5,6-difluoro-3-oxo-2,3-dihydro-1H-indene-2,1-diylidene))dimalononitrile. Their chemical structures are shown in Figure 6.1 as well as the additional PM6 donor for ternary solar cell fabrication (see chapter 6.2). These NFA are designed to absorb most of the visible and near infrared light, maximizing their solar cell efficiencies. Transmittance measurements of spin cast ITIC-2F and Y6 thin films in Figure 6.1B show that their minima is located at 725 nm[6] and 810 nm[7], respectively. The light absorption of ITIC-2F is mainly up to 850 nm, while Y6 has an absorption tail reaching 1000 nm.

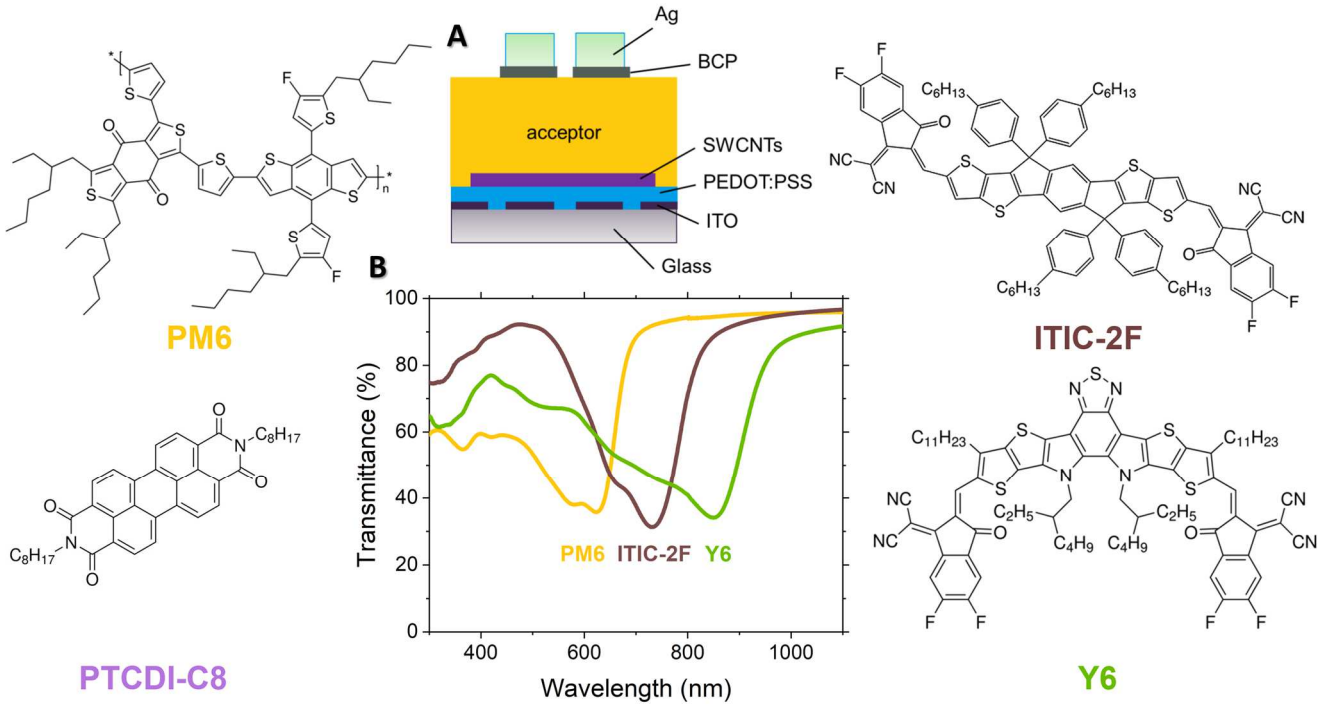

Figure 6.1: Chemical structures of the donor PM6 and the non-fullerene acceptors ITIC-2F, PTCDI-C8 and Y6. (A) Schematic of the solar cell bilayer architecture employed and (B) film transmittance spectra of PM6, ITIC-2F and Y6 on glass. Figure reproduced from [8]

Each acceptor forms a type II heterojunction in combination with the (6,5) SWCNTs as illustrated in the energy level diagram in Figure 6.2A. In the simplest model, the energetic offset between the lowest unoccupied molecular orbitals (LUMOs) of the (6,5) donor and the different acceptors is an indicator for charge separation at their interface. (see chapter Solar Cells: Working Principle) The LUMO position of the (6,5) SWCNT in Figure 6.2A was calculated based on the optical bandgap and already includes E_b.[9] Exciton binding energies within SWCNTs have been estimated to range from 0.2 eV – 0.5 eV[10, 11] and a reorganization energy of 130 meV has been shown to be required.[12] The LUMO offsets for C_{60}, ITIC-2F and Y6 range all between 0.45 and 0.54 eV which is in agreement with the literature values for E_b that need to overcome. PTCDI-C8 has a relatively large LUMO offset of 0.7 eV which should in principle facilitate the charge separation. However, following the Marcus theory more electronegative potentials leading to increasing energy barriers if these potentials are larger than the reorganization energy of the surrounding solvent molecules. This counter intuitive trend is the so-called Marcus inverted region.

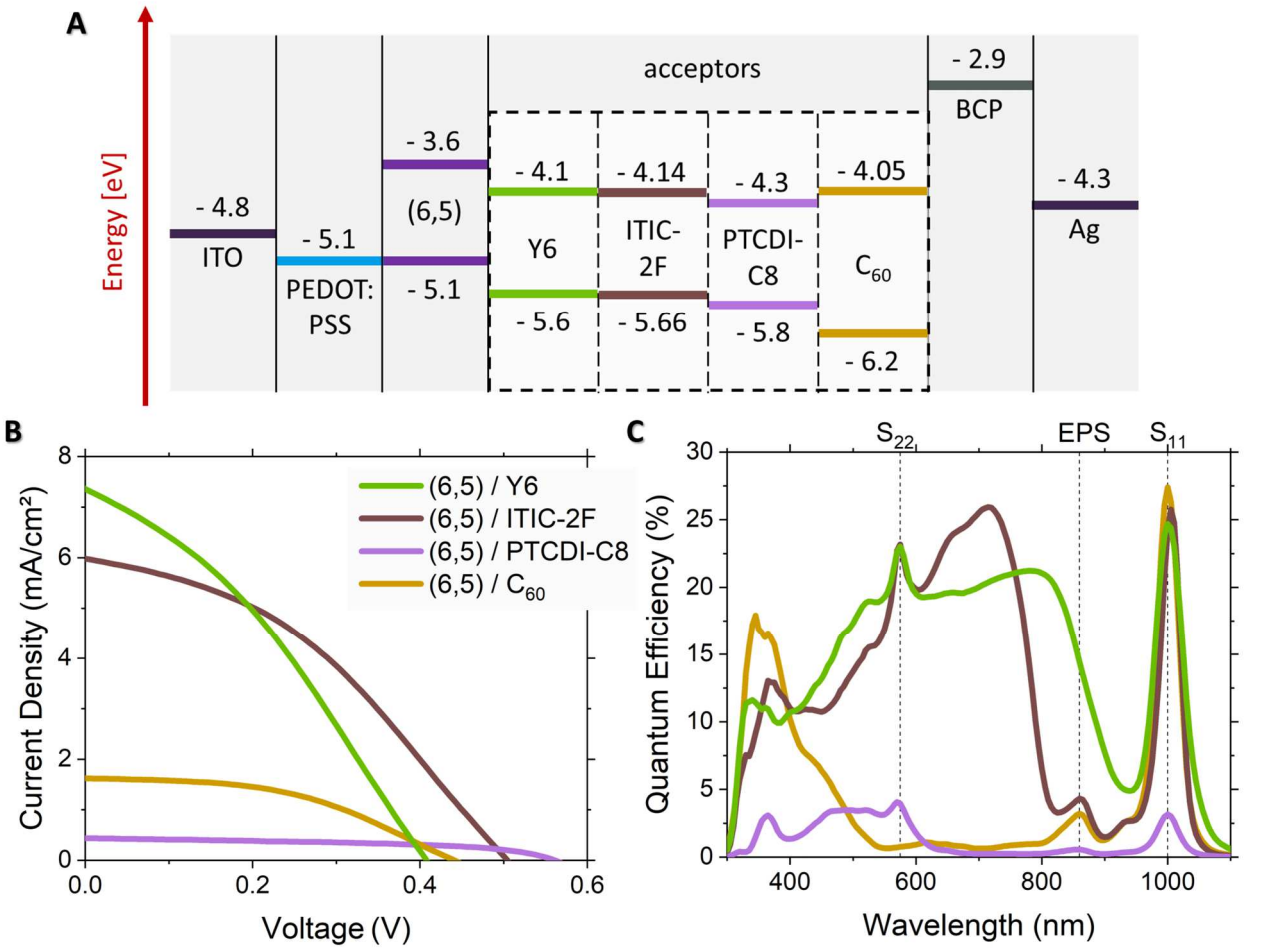

Figure 6.2: (A) An energy level diagram for each of the 4 acceptors used in the bilayer architecture. (B) Current density-voltage (J-V) and (C) external quantum efficiency (EQE) measurements of the assembled solar cells. Figure reproduced from [8]

The current density-voltage (J-V) curves in Figure 6.2B reveal that the PTCDI-C8 has a good fill factor of 51 % and a V_{OC} of 561 mV, however the current density is low and therefore the efficiency is compared to the other NFA 7 to 9 times smaller. The best performing solar cells were the (6,5)/ITIC-2F and (6,5)/Y6 with efficiency values of 1.16 % and 1.09 %, respectively. The main attribution has the improved short circuit current density (J_{SC}), which was almost 4 times higher than for C_{60} acceptor. All performance parameters for each (6,5)/acceptor combination are given in Table 1. Efficiencies in the range of ≈ 1 % are quite low in the organic solar cell community or in the general field of solar cells, where even mass-produced roof top silicon cells are about 20 %.[13] Nevertheless, in the field of SWCNT solar cells the benchmark is at ≈ 3 %[14, 15] for the fullerene derivate $PC_{71}BM$ and 1 % for SWCNT/C_{60} devices.[16] Overall a significant improvement was observed by using NFA instead of C_{60}.

Table 1: Solar cell performance parameters for the ITO/PEDOT:PSS/(6,5)/acceptor/ BCP/Ag devices.

Layer stack ITO/PEDOT:PSS/(6,5)/…/BCP/Ag	**J_{SC} [mA/cm²]**	**V_{OC} [mV]**	**FF [%]**	**Efficiency [%]**	**Peak EQE at S_{11} of (6,5) [%]**
Y6	7.35	408.2	33.5	1.01	24.67
ITIC-2F	5.97	502.9	38.6	1.16	25.75
PTCDI-C8	0.44	560.8	51.0	0.13	3.15
C_{60}	1.62	441.6	46.0	0.33	27.39

The external quantum efficiency spectra in Figure 6.2C for each SWCNT bilayer solar cell show distinct peaks at ≈ 1000 nm and ≈ 575 nm that are associated with the first (S_{11}) and second (S_{22}) optical transitions of (6,5) SWCNTs. The broad peak at ≈ 860 nm is the exciton-phonon side band (EPS) of the S_{11} transition and all other major features are associated with the different acceptors used. Apparently, the improved J_{SC} and efficiency of the NFA is based on the wide range of light capture in the visible and near IR compared to the (6,5)/ C_{60} cells which mainly absorb the UV up to yellow/ green light. The integrated current density of Y6 and ITIC-2F in the visible region (400 - 800 nm) was calculated as described in the introduction resulting in 4.34 mA/cm² and 4.31 mA/cm², respectively. The superiority of the NFAs compared to C_{60} with integrated J_{SC} of 0.41 mA/cm² is obvious.

Another figure of merit in the SWCNT solar cell community is the peak EQE at the S_{11} position of the carbon nanotubes. The (6,5)/Y6, (6,5)/ITIC-2F and (6,5)/C_{60} solar cells achieve a peak EQE at S_{11} of 24.7 %, 25.8 % and 27.4 %, respectively, due to their similar LUMO offset of ≈0.5 eV. These EQE values are in agreement with the highly efficient SWCNT solar cells from Classen et al.[14], who achieved 26 % with their (6,5)/$PC_{71}BM$ devices. The (6,5)/ PTCDI-C8 solar cell on the other hand has a LUMO offset of 0.7 eV, which means that junction is in the Marcus inverted region and the peak EQE is consequently considerably lower at only 3.2 %.

In summary, the non-fullerene acceptors ITIC-2F and Y6 are promising candidates for efficient SWCNT/NFA solar cells due to their appropriate LUMO offset for charge separation and the broad light absorption. Among the tested (6,5)/NFA solar cells, ITIC-2F has the best performance in terms of efficiency, while Y6 has the broadest spectral absorbance and thus the highest J_{SC}. However, only fractions of the high energetic light from UV up to 600 nm is captured by those SWCNT/NFA devices. Ternary structures with a third material absorbing in this region can

optimize light capture and increase efficiency. In the next section the standard PM6:Y6 donor-acceptor pair is combined with (6,5) SWCNTs as second donor, where PM6 absorbs light from 500 – 700 nm (max 610 nm),[7] Y6 from 600 – 1000 nm and (6,5) SWCNTs mainly in the IR. (see Figure 6.1B)

6.2 Ternary PM6:Y6:SWCNT Solar Cells

Two different solar cell architectures as shown in Figure 6.3A were tested for the ternary PM6:Y6:SWCNT approach, details of the preparation are given in chapter 6.4.2. Briefly, the first architecture is a layered stack in which PM6:Y6 was directly spin cast on top of the (6,5) SWCNT film sitting on the transparent electrode and PEDOT:PSS as HTL. The (6,5) film thickness can be varied by multiple spin coating steps; the following results are based on an 18 nm thick film. While the second approach was a bulk heterojunction, here 75 µg of (6,5) SWCNTs[17] were directly mixed into the PM6:Y6 chloroform solution in a 5:3 ratio. The three-component solution was spin-cast as well on the ITO/PEDOT:PSS substrate and both device stacks were finished by evaporation of BCP as ETL and a silver electrode.

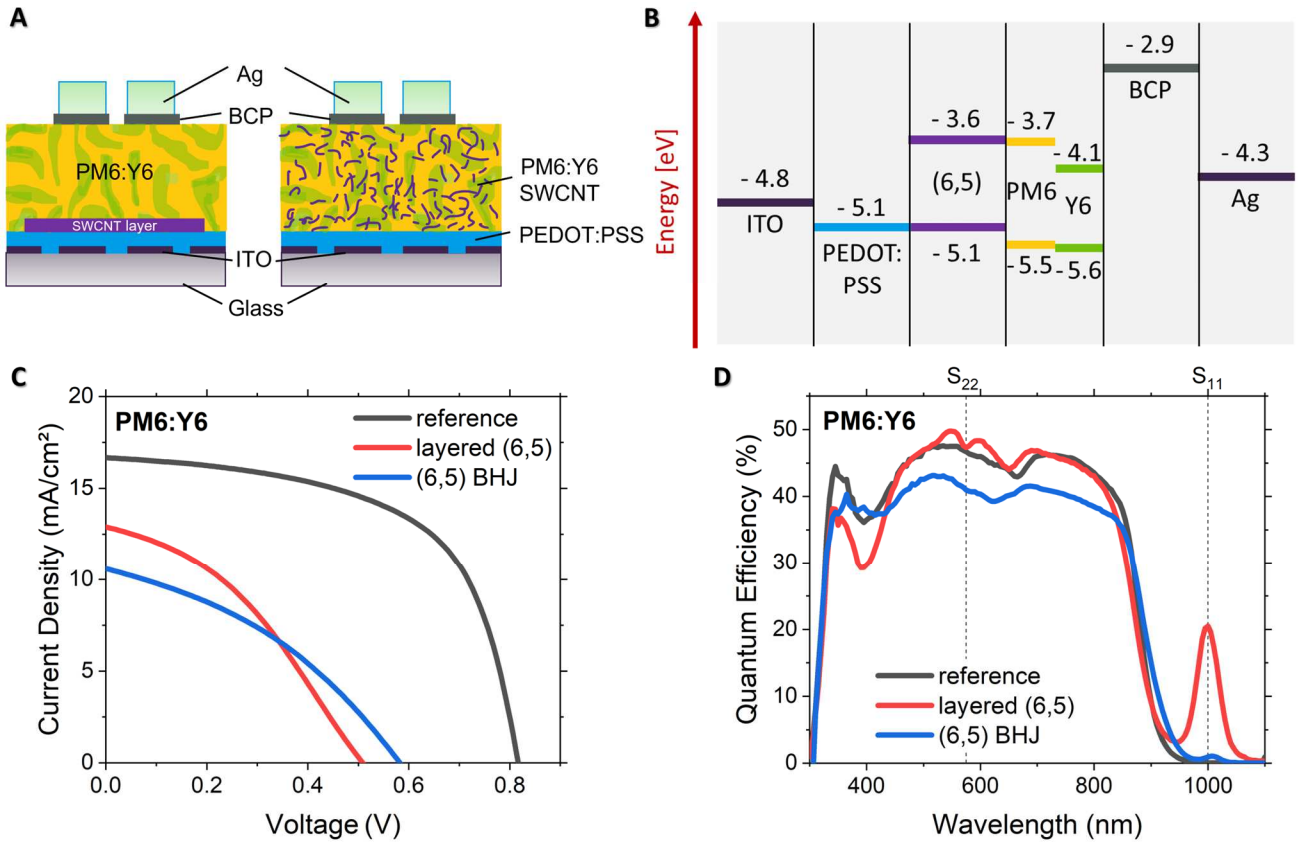

Figure 6.3: (A) Schematic of the ternary polymer/(6,5) solar cell architecture with (6,5) layer underneath the PM6:Y6 (left) or a bulk heterojunction of PM6:Y6:(6,5) (right). (B) The corresponding energy level diagram. (C) Current density-voltage (J-V) and (D) external quantum efficiency (EQE) measurements of the assembled solar cells. Figure reproduced from [8]

In the energy level diagram, illustrated in Figure 6.3B, the HOMOs and LUMOs are arranged like a cascade facilitating charge separation and the hole or electron transfer to the ITO anode or silver cathode, respectively. PM6 is perfectly fitting in between (6,5) and Y6, so excitons generated by CNTs can relax to the lower PM6-HOMO to enable charge splitting.

In Figure 6.3C the J-V curves of the ternary architectures and a PM6:Y6 reference cell reveal the reduction in efficiency by adding (6,5) SWCNTs into the tailored PM6:Y6 donor-acceptor pair. While the PM6:Y6 solar cell reached an efficiency of 8.07 %, the layered ternary structure achieved 2.44 % and the bulk heterojunction with (6,5) 2.27 % . The layered device also showed the higher J_{SC} of 12.9 mA/cm^2 compared to 10.6 mA/cm^2 for the bulk heterojunction, however the V_{OC} is reduced about 70 mV for the layered architecture. All solar cell performance parameters are summarized in Table 2. The efficiency values are close to the best in the field of SWCNT solar cells with ≈ 3 %. The champion device from Gong et al. reached 3.2 % with a polychiral SWCNT sample in a BHJ, whereas the bilayer (6,5)/$PC_{71}BM$ cell from Classen reported 2.9 %.

Table 2: Solar cell performance of layered and bulk heterojunction ITO/PEDOT:PSS/(6,5)/PM6:Y6/BCP/Ag devices.

Layer stack ITO/PEDOT:PSS/…/ BCP/Ag	**J_{SC} [mA/cm^2]**	**V_{OC} [mV]**	**FF [%]**	**Efficiency [%]**	**Peak EQE at S_{11} of (6,5) [%]**
PM6:Y6 (bulk-heterojunction)	16.65	816.1	59.4	8.07	-
(6,5) layered	12.86	511.0	37.1	2.44	20.49
(6,5) bulk heterojunction	10.57	581.8	36.9	2.27	1.04

The EQE measured for the layered device follows a similar shape than the PM6:Y6 reference cell albeit the extra IR peak at ≈ 1000 nm from the (6,5) SWCNTs, as demonstrated in Figure 6.3D. The peak EQE at S_{11} has already achieved 20.5 %. Calculating the J_{SC} of this additional peak by integration of the EQE curve from 900 – 1100 nm results in an additional current density of 0.65 mA/cm^2 for the SWCNTs in the IR. Apparently, a dip at 575 nm occurred in the EQE spectrum of the layered device which corresponds to the S_{22} transition of (6,5) and is a result of the light first passing through the SWCNT before reaching the PM6:Y6. The probability of charge transfer from S_{22} to C_{60} is much lower than the relaxation to S_{11} and then to C_{60} due to the different time scales for excitonic relaxation and charge transfer. While excitonic relaxation from S_{22} to S_{11} takes ≈ 40 fs,[18, 19] the charge transfer from (6,5) CNTs to C_{60} occurs within ≈ 120 fs.[20] Nevertheless, photocurrent generation for S_{22} has been reported[21-23] but only over an intermediate transition to S_{11}. The minimal loss in current at S_{22} is dominated by the reduced PM6:Y6 absorbance due to

(6,5) light capture. The absorbed photons by SWCNTs mainly relax first to the ground state and generate current in the lower energetic IR region. Similar trends can be seen in the EQE of the bulk heterojunction PM6:Y6:(6,5), positive as well as negative influence of (6,5) with its S_{11} and S_{22} transitions, albeit the magnitude of these peaks is significantly reduced.

Primarily, the difference in EQE between the two architectures are based on the relative concentrations of (6,5) SWCNTs in those devices. In the layered device 330 µL of (6,5) SWCNTs with an estimated concentration of max. 74 µg/mL[17] were used whereas for the bulk heterojunction, 500 µL (max. 90 µg/mL) of SWCNTs were dried and redissolved in the PM6:Y6 solution. The number of CNTs per cm^2 was estimated to be higher for the layered than for the bulk heterojunction devices due to the increased film absorptivity of the (6,5) SWCNTs at S_{11}.Figure 6.4 illustrates the higher optical density at ≈ 1000 nm for the (6,5) film in the layered architecture (red line) compared to the ternary bulk heterojunction PM6:Y6:(6,5) (blue line).

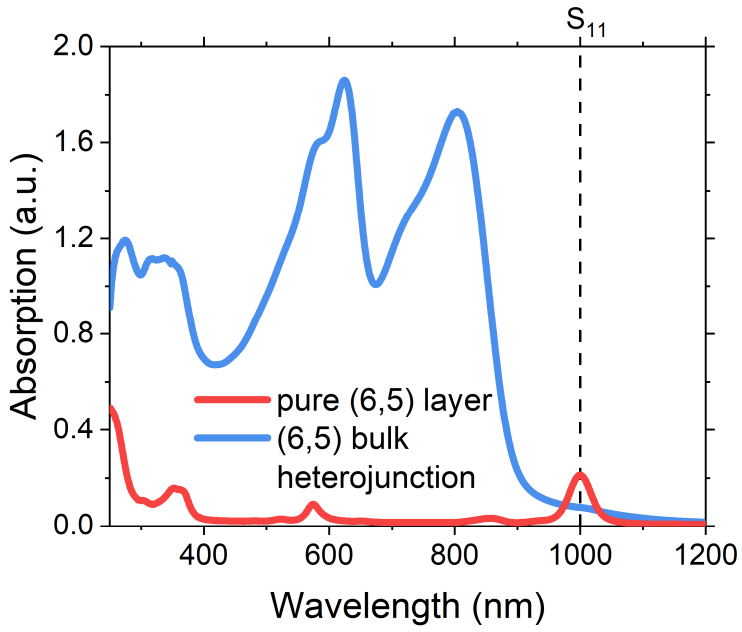

Figure 6.4: Absorption spectra of films made of polymer-wrapped (6,5) SWCNTs (red line) or (6,5) mixed together with PM6:Y6 for the ternary device (blue line). The maximum S_{11} absorptivity of the (6,5) at 1000 nm is higher for the pure SWCNT film of the layered device compared to the bulk heterojunction.

The EQE performance in the IR of such layered architectures apparently depends on the (6,5) film thickness which was determined by AFM and correlated to the film absorption. As shown in Figure 6.5A, the increase in optical density is about 0.013 per nanometer. Besides the results on the 18 nm thick (6,5) film, 10 and 8 nm are studied as well, all with a close packed SWCNT network as displayed in Figure 6.5B. Increasing the (6,5) film thickness resulted in reduced J_{SC} and V_{OC} values and by extension, in lower efficiencies, demonstrated in Figure 6.5C and summarized in Table 3. Despite the minimal decrease in J-V parameters, increasing film thickness from ≈ 8 nm to

10 nm and 18 nm of SWCNTs rises the peak EQE at S_{11} from 6.7 % to 10.9 % up to 20.5 % in Figure 6.5D.

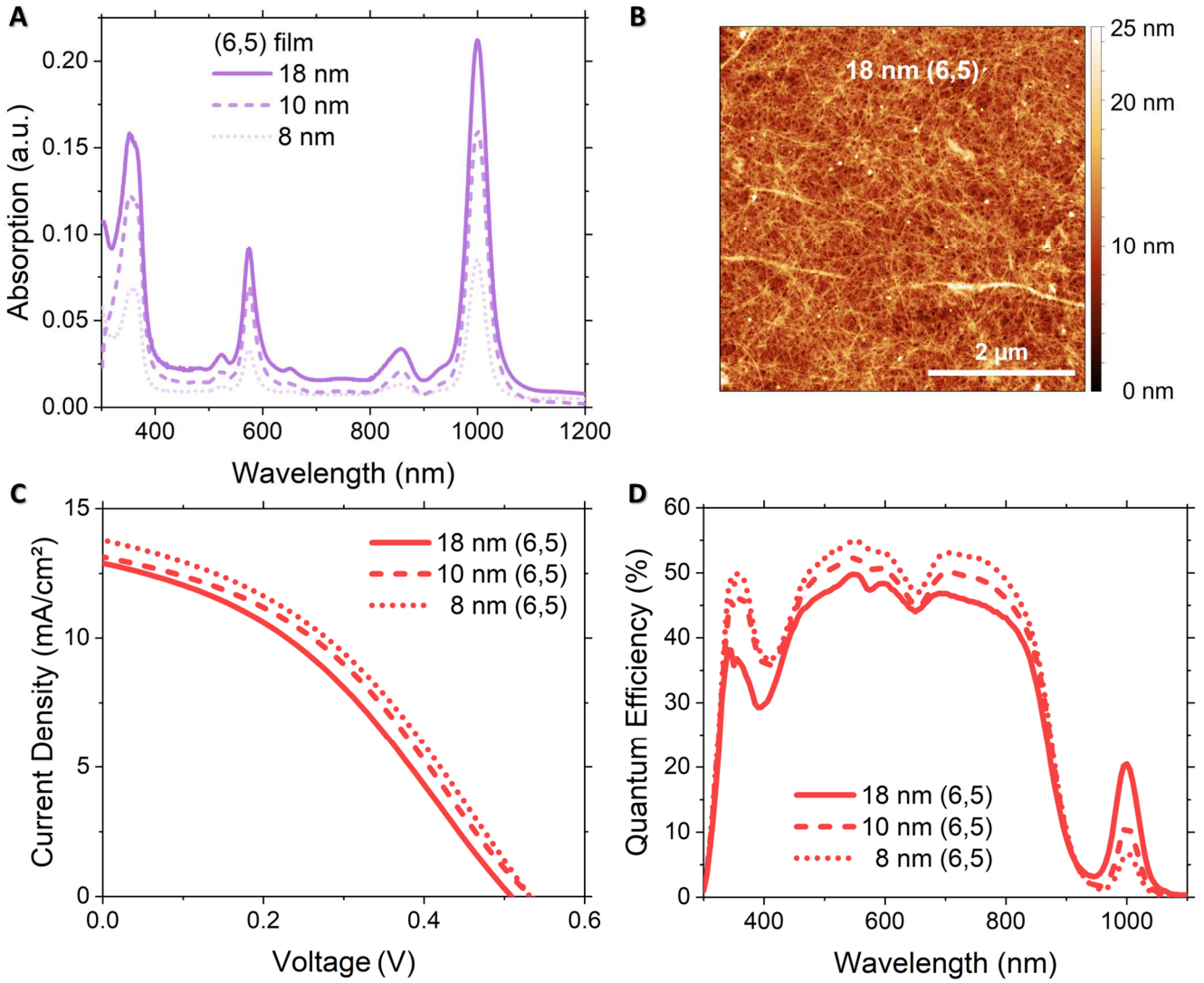

Figure 6.5: (A) Film absorption measurements for different film thickness of (6,5) SWCNTs (B) AFM image of the interwoven CNT network for an 18 nm thick layer of (6,5) SWCNTs. (C) Current density-voltage and (D) EQE measurements of ITO/PEDOT:PSS/(6,5):PM6:Y6/ BCP/Ag bilayer devices with increasing thickness of the spin-cast (6,5) nanotubes. Figure reproduced from [8]

Table 3: Solar cell performance parameters for layered ITO/PEDOT:PSS/(6,5)/PM6:Y6/BCP/Ag devices with varying thickness of the SWCNT layer.

(6,5) Layer Thickness ITO/PEDOT:PSS/(6,5)/PM6:Y6 /BCP/Ag	**J_{SC} [mA/cm²]**	**V_{OC} [mV]**	**FF [%]**	**Efficiency [%]**	**Peak EQE at S_{11} of (6,5) [%]**
18 nm	12.86	511.0	37.1	2.44	20.49
10 nm	13.11	539.2	38.2	2.70	10.85
8 nm	13.75	531.4	38.7	2.83	6.70

Thicker SWCNT films are also associated with an increased scattering background, as shown in Figure 6.5A, which can reduce the generated J_{SC} leading to lower EQE values in the visible part of the spectrum in Figure 6.5D. The SWCNT films are an additional barrier for the separated positive charges from the PM6:Y6 interface resulting again in a reduced EQE signal. The optimum SWCNT film thickness is defined by the exciton diffusion length which has been determined by ultrafast spectroscopy[24, 25] or photocurrent measurements in bilayer devices.[25-27] Thereby J_{SC} or the EQE signal of the SWCNTs is monitored with increasing film thickness, first its linearly increasing up to 5 - 18 nm and then falls abrupt for even thicker films.[16, 26, 28, 29] The 18 nm thick film with the highest EQE response of 20.5 % is therefore close to the maximum.

The challenges of limited film thickness due to exciton diffusion length and the (6,5) film as light filter for the PM6:Y6 are subordinate issues for bulk heterojunction solar cells. A ternary phase of intermixed PM6:Y6 including the carbon nanotubes are studied in the following paragraphs and is mainly affected by the amount of (6,5) in the bulk layer. The ratio of (6,5) to PM6:Y6 solution was varied from 1:4 to 2:3, an overview of all solar cell parameters is given in Table 4. The J-V curves in Figure 6.6A illustrate a reduction of J_{SC} and V_{OC} of up to a third for the increase in (6,5) content from a ratio of 1:4 to 2:3. For example, J_{SC} is reduced from 15.0 mA/cm^2 for the reference PM6:Y6 device to 9.3 mA/cm^2 for a 2:3 ratio of SWCNTs.

Table 4. Solar cell performance parameters for bulk heterojunction ITO/PEDOT:PSS/(6,5):PM6:Y6/BCP/Ag devices with varying SWCNT content.

Layer stack ITO/PEDOT:PSS/…/ BCP/Ag	**J_{SC} [mA/cm^2]**	**V_{OC} [mV]**	**FF [%]**	**Efficiency [%]**	**Peak EQE at S_{11} of (6,5) [%]**
PM6:Y6	15.01	700.0	50.3	5.28	-
(6,5)C_7H_8 in PM6:Y6 (1:4)	13.36	570.8	43.1	3.29	0.79
(6,5)C_7H_8 in PM6:Y6 (1:2)	11.08	500.3	41.6	2.31	1.41
(6,5)C_7H_8 in PM6:Y6 (2:3)	9.30	500.2	38.4	1.78	1.52
PM6:Y6	12.24	565.4	47.6	3.29	-
(6,5)$CHCl_3$ in PM6:Y6 (5:3)	10.57	581.8	36.9	2.27	1.04

All these devices were prepared by direct addition of the (6,5) solution in toluene to the PM6:Y6 mixture in chloroform at the specific volume:volume ratios listed above. Obviously, this equates to a dilution of the PM6:Y6 solution leading to lower current generation. Simultaneously, a significant reduction in V_{OC} is observed presumably due to trap states that facilitate non-radiative

recombination. I_{SC} and V_{OC} decrease results in an overall diminishing EQE spectra as shown in Figure 6.6B.

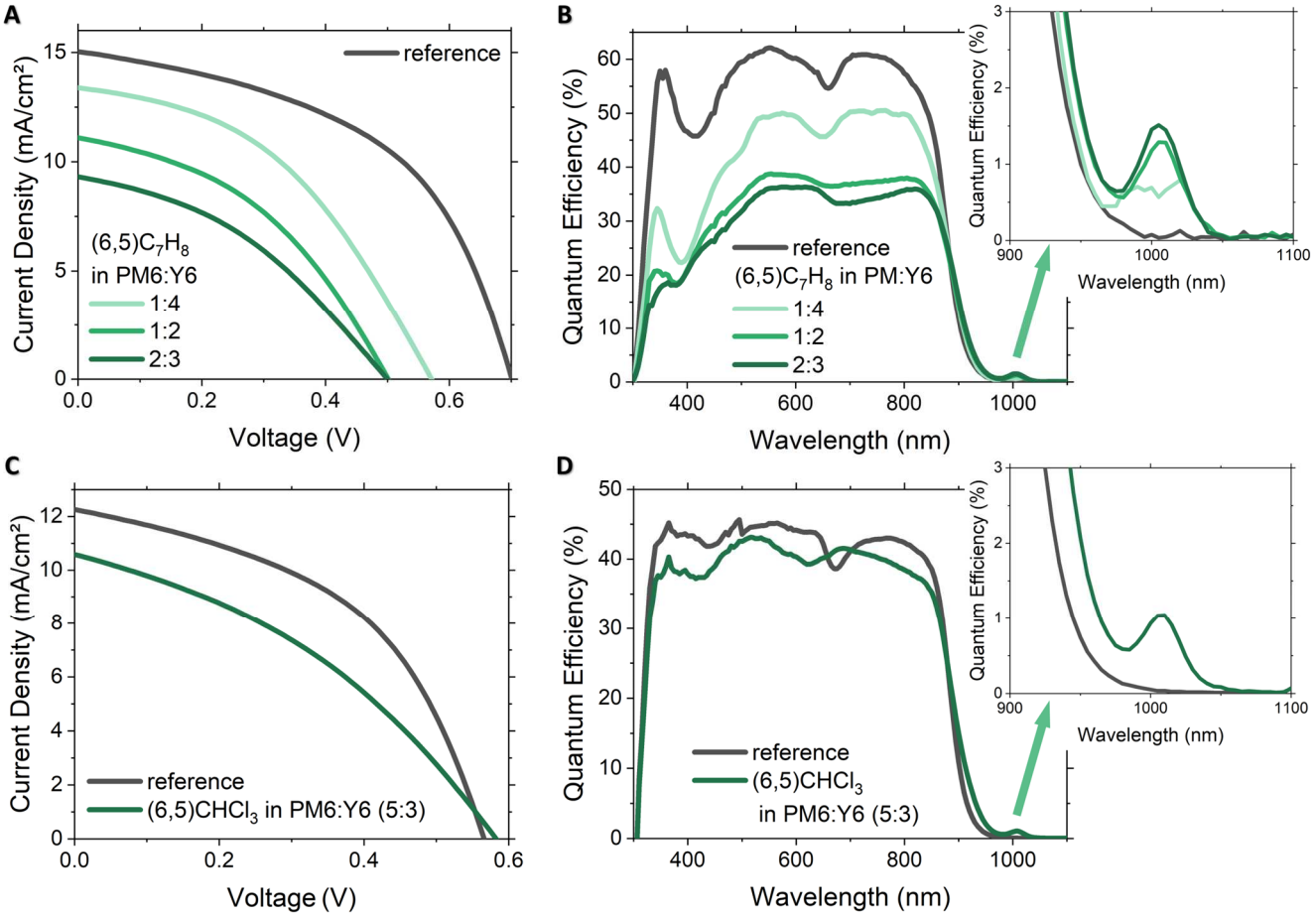

Figure 6.6: (A) Current density-voltage measurements of bulk heterojunction (6,5):PM6:Y6 solar cells prepared with a different ratio of PM6:Y6 and with the SWCNTs in toluene (C_7H_8). (B) The corresponding external quantum efficiency measurements. (C) Current density-voltage measurements of bulk heterojunction (6,5):PM6:Y6 solar cells prepared with the SWCNTs in chloroform ($CHCl_3$) and used to disperse PM6/Y6. (D) The corresponding external quantum efficiency measurements. Figure reproduced from [8]

The 1:2 and 2:3 ratio have a similar external quantum efficiency in the PM6:Y6 absorbance range from 400 – 900 nm that is based on a nearly identical film absorption shown in Figure 6.7A. Despite the dilution issue, the external quantum efficiency at S_{11} is increasing with higher (6,5) content, more precisely from 0.80 % for the 1:4 ratio up to 1.29 % (1:2) and 1.51 % (2:3).

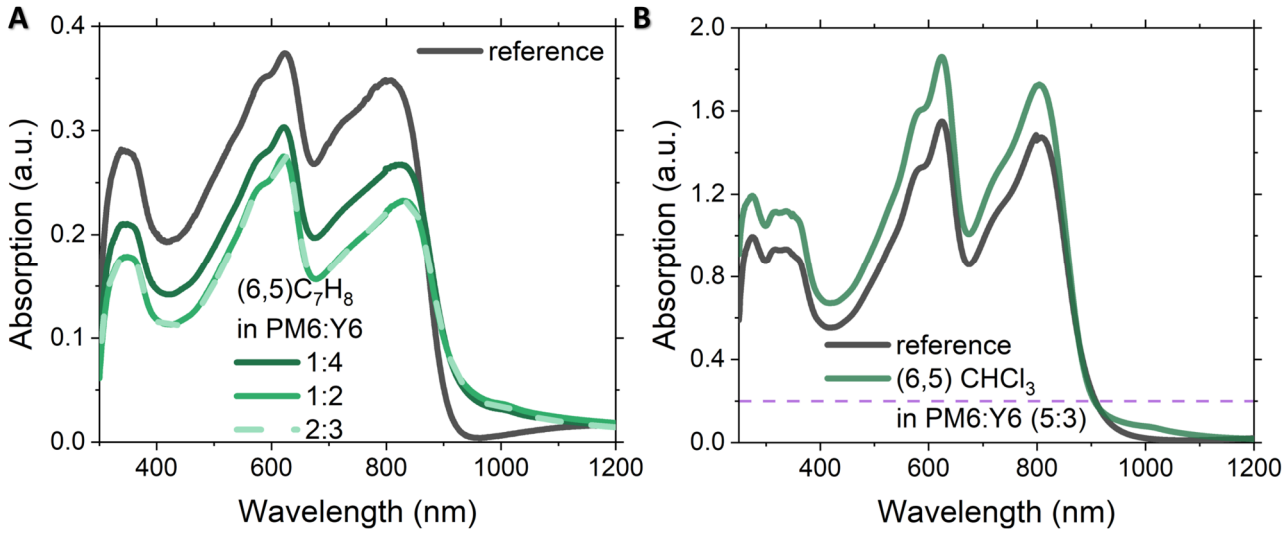

Figure 6.7: Film absorption spectra of (A) (6,5) SWCNTs in toluene (C7H8) added directly to PM6:Y6 in chloroform and (B) of (6,5) SWCNTs in chloroform and used to disperse PM6:Y6 in a ratio of 5:3. The dashed line at 0.2 OD highlights the maximum S_{11} absorptivity of SFM (6,5) films as shown in Figure 6.5A. Figure reproduced from [8]

As control experiment, the PM6:Y6 solution was diluted just with toluene and no nanotubes, more precisely in the 1:2 and 2:3 ratio. A similar trend in the reduction of J_{SC} is observed for the toluene control samples in Figure 6.8A and the ternary bulk heterojunction PM6:Y6:(6,5) already discussed above in Figure 6.6A. The same is true for the decrease in EQE intensity in the visible part of the light spectrum where PM6:Y6 absorb.

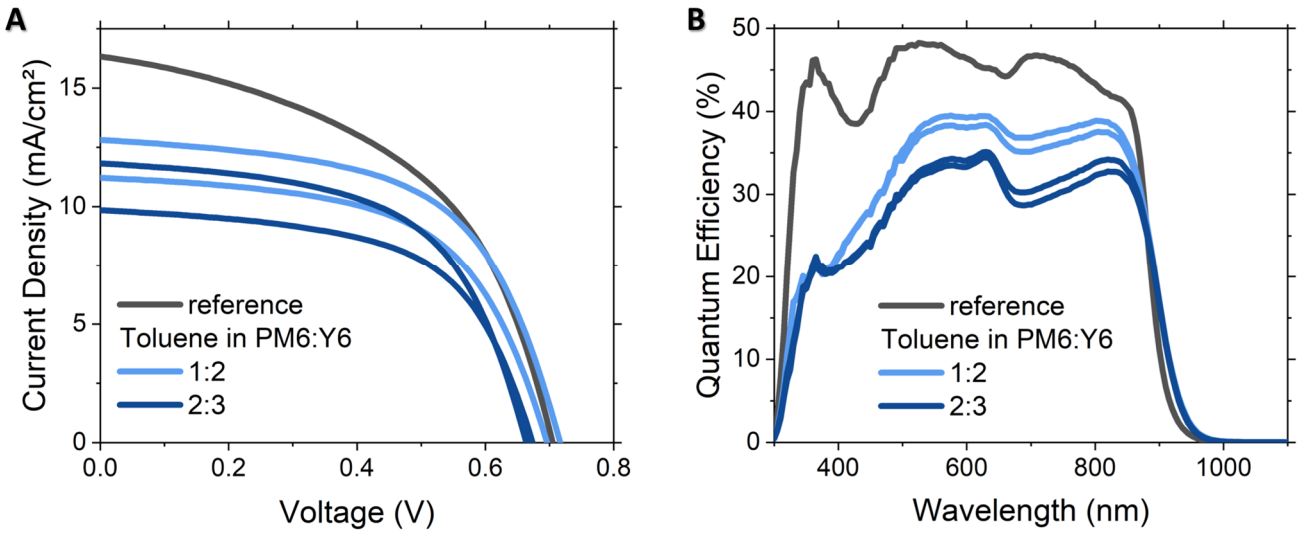

Figure 6.8: J-V measurements of the reference PM6:Y6 heterojunction in comparison to bulk heterojunctions with additional toluene (but no carbon nanotubes) in the ratios 1:2 and 2:3. Figure reproduced from [8]

However, the V_{OC} is less effected by the dilution with pure toluene than with the (6,5) SWCNT solution. While the V_{OC} is significantly reduced from 700 mV to 500 mV by (6,5), it is nearly the same for the toluene dilution only 40 mV reduction. (Table 5) The interface between PM6 and Y6 might be less effected by solvents than by the addition of a third material like CNTs which can induce trap states in the polymer solar cell.

Table 5. Solar cell performance parameters for bulk heterojunction ITO/PEDOT:PSS/C_7H_8:PM6:Y6/BCP/Ag devices with varying toluene content.

Layer stack ITO/PEDOT:PSS/.../ BCP/Ag	**J_{SC} [mA/cm^2]**	**V_{OC} [mV]**	**FF [%]**	**Efficiency [%]**
PM6:Y6	16.30	703.9	49.0	5.62
C_7H_8 in PM6:Y6 (1:2)	12.80 11.21	715.6 695.9	57.9 57.8	5.30 4.51
C_7H_8 in PM6:Y6 (2:3)	9.84 11.82	672.8 662.3	58.3 57.3	3.86 4.49

The mixture of toluene and chloroform solution was found to introduce morphology changes in the spin cast PM6:Y6 layers. AFM pictures of the surface of these PM6:Y6:(6,5) films are depicted in Figure 6.9. Panel A shows a homogeneous film for the PM6:Y6 reference in contrast to panel C-E where the surface roughness is increasing with a higher (6,5) content. This is reflected in the root mean square (RMS) values which rise from 15.4 nm (1:4) to 17.6 nm (1:2) and 20.7 nm (2:3), which is an order of magnitude higher compared to the PM6:Y6 reference with 1.28 nm. The addition of (6,5) in toluene into the PM6:Y6 chloroform solution has caused the formation of polymer aggregates leading to these rougher surfaces.

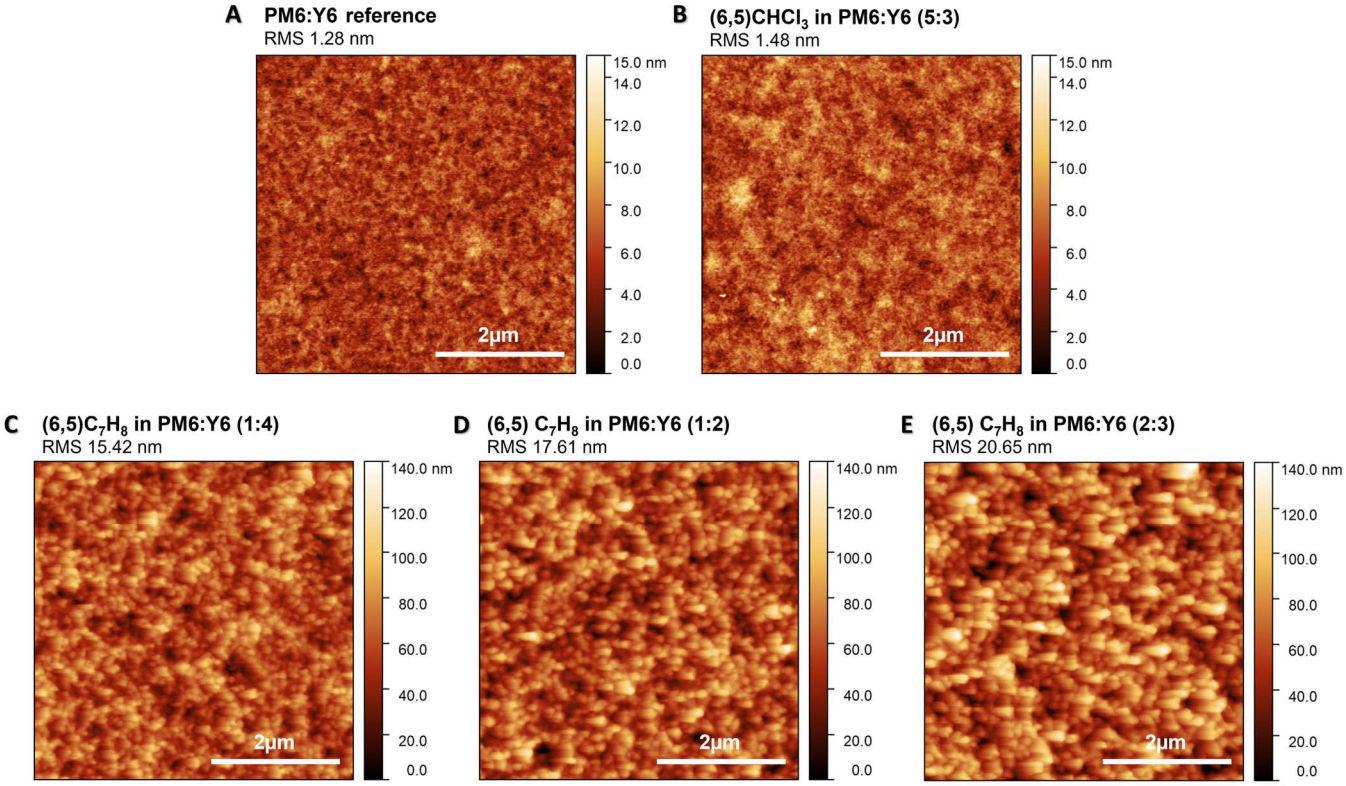

Figure 6.9: AFM images of PM6:Y6 spin case onto a glass substrate and with the addition of (6,5) SWCNTs either in toluene (C_7H_8) or chloroform ($CHCl_3$). Figure reproduced from [8]

Literature values for exciton diffusion length in Y6 range from 29 – 37 nm[30-32] and in optimized PM6:Y6 solar cells the domain size of Y6 was estimated at 44 nm.[33] Larger domain sizes can hinder the exciton diffusion and reduce the generated current, nevertheless, active layers of 100 -200 nm are necessary to absorb light effectively.[34] For bulk heterojunction PM6:Y6 solar cells, Tokmoldin et al.[35] reported an extraordinarily long diffusion length of 330 nm for Y6 due to high doping level in PM6 and space-charge effect.

To avoid dilution and phase separation in the PM6:Y6:(6,5) solar cells, the toluene solvent has been evaporated before the (6,5) SWCNTs were dispersed in chloroform by sonication. This (6,5) chloroform solution was then the stock solution for the addition of PM6:Y6 powders in their 1:1.2 ratio. The morphology of the (6,5)$CHCl_3$ in PM6:Y6, Figure 6.9B, is similar to the PM6:Y6 reference but the surface is still a bit rougher with a RMS of 1.48 nm compared to 1.28 nm. The integration of the (6,5)$CHCl_3$ SWCNTs didn't show larger polymer aggregates as the (6,5)C_7H_8 and resulted in a V_{OC} comparable to the reference cell, see Figure 6.6C. The J_{SC} is slightly reduced from 12.2 mA/cm^2 to 10.6 mA/cm^2, as well as the EQE in the visible region due to disruption of the tailored morphology of PM6:Y6 by the carbon nanotubes. In Figure 6.6D, the external quantum efficiency at the S_{11} transition is diminished to 1.0% for the (6,5)$CHCl_3$ although the concentration ratio is 5:3 in the device. This ratio is calculated from the amount of SWCNTs in the original toluene solution before transferring it into chloroform solvent, processing losses are therefore not included. The film absorbance of PM6:Y6:(6,5)$CHCl_3$ in Figure 6.7B clearly shows the dominance of the PM6:Y6 components over the (6,5) contribution. For comparison, the concentration of (6,5)C_7H_8 solution was 145 µg/mL while the (6,5)$CHCl_3$ was 90 µg/mL before changing the solvent. Higher concentrated SWCNT solutions in chloroform are desired to adjust the ratio of (6,5) to PM6:Y6, however the changes in morphology especially in domain size have to be balanced as well.

6.3 Summary

Ternary architectures composed of PM6:Y6 and (6,5) SWCNTs as second donor were investigated. In the layered stack an EQE over 20 % was achieved with an 18 nm thick (6,5) film underneath the bulk of PM6:Y6. The maximum SWCNT film thickness is limited by the short exciton diffusion length of carbon nanotubes to approximately 18 nm thus the light capture in the infrared is confined as well. Bulk heterojunctions can overcome this limitation but suffer from phase

separation by directly adding the (6,5) toluene solution into the PM6:Y6 in chloroform. The preparation in a single solvent resolved the morphology issue but the additional transfer step of the SWCNTs from toluene into chloroform makes it more difficult to gain high concentrated (6,5) SWCNT solutions and therefore significant EQE intensity at the S_{11} transition. Nevertheless, all prepared devices have shown absorption extension into the IR to some extent whereby the layered stack achieved the best EQE values for (6,5).

Bulk heterojunctions are promising architectures if their bottle neck of high concentrated SWCNT is solved and larger amounts of carbon nanotubes can be incorporated into the solar cells without causing dramatic morphology changes. Modifications to the side chains of PM6 or Y6 could make these molecules more compatible with the SWCNTs. In the future, new designed NFA or polymer donors could be able to directly disperse or even sort the carbon nanotubes making PFO-BPy as fourth component in the active layer redundant.

6.4 Experimental Details

6.4.1 Device Fabriaction: (6,5)/Non-Fullerene Acceptor Solar Cells

Bilayer cells of polymer-wrapped (6,5) SWCNTs with non-fullerene acceptors (NFA) are fabricated like the standard (6,5)/C_{60} solar cells discussed in chapter 3 by just replacing the acceptor layer. The schematic of the layer stack is illustrated in Figure 6.1A. where (6,5) SWCNTs and a (non) fullerene acceptor are sandwiched in between PEDOT:PSS, the transparent ITO cathode and on the other side the electron transport layer BCP plus the silver back electrode.

All devices are based on glass with a pre-structured ITO layer (Psiotec, 15 Ω/sq) which is first cleaned, dried and oxygen plasma cleaned. The standard hole transport layer PEDOT:PSS (AI 4083, Ossila) is filtered (Millex-HV, 0.45 µm, Merck) and subsequently spin cast on the ITO at 3000 rpm for 30 s followed by an annealing at 150°C for 15 min. The (6,5) SWCNT solution is prepared by shear-force mixing in toluene with the selective polymer PFO-BPy as described in the experimental section. 55 µL of this solution is spin cast on top of the PEDOT:PSS at 600 rpm for 20 s followed by 1500 rpm for 5 s. The (6,5) films are fabricated by multiple spin coating steps resulting in thicknesses between a few nanometer up to 18 nm. After annealing at 110°C for 7 min, the acceptor layer was applied usually 100 nm C_{60} fullerene (99.9+%; Sigma–Aldrich, lot. MKCK0541). As alternative to the fullerene acceptor, non-fullerene acceptors (NFA) are tested in the active layer, their chemical structures are shown in Figure 6.1. PTCDI-C8 (N,N'-Dioctyl-3,4,9,10-perylene dicarboximide, Sigma-Aldrich, lot MKBV5102V) can also be evaporated achieving layer thicknesses of 40 nm whereas the other non-fullerene acceptors ITIC-2F and Y6 are spin cast from chlorobenzene solutions. A solution of 10 mg/mL ITIC-2F or 3,9-bis(2-methylene-((3-(1,1-dicyanomethylene)-6,7-difluoro)-indanone))-5,5,11,11-tetrakis(4-hexyl phenyl)-dithieno[2,3-d:2’,3’-d’]-s-indaceno[1,2-b:5,6-b’]dithiophene (Ossila, lot M2075A1), is spun at 1000 rpm for 20 s. While Y6, 2,2'-((2Z,2'Z)-((12,13-bis(2-ethylhexyl)-3,9-diundecyl-12,13-dihydro-[1,2,5]thiadiazolo[3,4-e]thieno[2",3’’:4’,5']thieno[2',3':4,5]pyrrolo[3,2-g]thieno [2',3':4,5]thieno[3,2-b]indole-2,10-diyl)bis(methanylylidene))bis(5,6-difluoro-3-oxo-2,3-dihydro-1H-indene-2,1-diylidene))dimalononitrile (Ossila, lot M2200A1) has a concentration of 12 mg/mL and is spun at 3000 rpm for 30 s. To finish the device, 10 nm of bathocuproine (BCP, > 99.5 %, Ossila) were thermally evaporated followed by the 100 nm thick silver electrode. The active area of all cells is 0.105 cm^2.

The concentration of the (6,5) PFO-BPy solution varied from 38-76 µg/mL for PTCDI-C8 devices to 70-139 µg/mL for the Y6 cells. The (6,5)/C_{60} and (6,5)/ITIC-2F are both fabricated from a 55-110 µg/mL solution.

6.4.2 Device Fabrication: (6,5):PM6:Y6 Ternary Solar Cell

The preparation procedure for the ternary stack with a (6,5) film underneath a PM6:Y6 layer, shown in Figure 6.3A, is identical to the one already described at least up to the (6,5) layer. The (6,5) PFO-BPy solution with a concentration of 37-74 µg/mL is spin cast 2, 4 or 6 times each round 55 µL achieving the different layer thicknesses.

Instead of an acceptor the donor/acceptor pair of PM6, poly[(2,6-(4,8-bis(5-(2-ethylhexyl-3-fluoro)thiophen-2-yl)-benzo[1,2-b:4,5-b′]dithiophene))-alt-(5,5-(1′,3′-di-2-thienyl-5′,7′-bis(2-ethylhexyl)benzo[1′,2′-c:4′,5′-c′]dithiophene-4,8-dione))], (Ossila, lot M2150A8) and Y6 are spin cast at 3000 rpm for 30 sec from a chloroform solution with a total concentration of 16 mg/mL resulting in a ≈ 150 nm thick film. The PM6:Y6 solution was mixed a few hours before use in a ratio of 1:1.2 and continuously stirred. For each batch of solar cells, the PM6:Y6 solution was freshly prepared leading to slight differences in the mixing ratios.

The ternary bulk heterojunction device consisted of the prepared (6,5) solution in toluene (73-145 µg/mL) and the PM6:Y6 (1:1.2) in chloroform all intermixed, as indicated in Figure 6.3A. In the ratios of 1:4, 1:2 and 2:3 the mixture was spin cast at 3000 rpm for 30 seconds directly on top of the PEDOT:PSS layer. These samples are named (6,5)C_7H_8 because of the direct use of (6,5) solution in toluene. On the other hand, (6,5)$CHCl_3$ was prepared with (6,5) SWCNTs transferred into chloroform to avoid solvent mixtures. Therefore 500 µL (6,5) solution in toluene (45-90 µg/mL) was heated up to evaporate the solvent and redisperse it afterwards in chloroform with the aid of tip sonication. This (6,5) chloroform solution was added to the PM6:Y6 (1:1.2) powders, stirred for minimum 2 hours and spun onto the PEDOT:PSS.

10-12 nm of Bathocuproine followed by the 100 nm thick silver electrode have finalized both device architectures.

6.5 References

[1] A. Graf, Y. Zakharko, S.P. Schiessl, C. Backes, M. Pfohl, B.S. Flavel, J. Zaumseil, *Carbon* **2016**, *105*, 593-599.
[2] J.T. Flach, J. Wang, M.S. Arnold, M.T. Zanni, *J Phys Chem Lett* **2020**, *11*, 6016-6024.
[3] L. Wieland, H. Li, C. Rust, J. Chen, B.S. Flavel, *Adv Energy Mater* **2020**, *11*, 2002880.
[4] Y. Joo, G.J. Brady, M.J. Shea, M.B. Oviedo, C. Kanimozhi, S.K. Schmitt, B.M. Wong, M.S. Arnold, P. Gopalan, *ACS Nano* **2015**, *9*, 10203-13.
[5] A.T. Mallajosyula, W. Nie, G. Gupta, J.L. Blackburn, S.K. Doorn, A.D. Mohite, *ACS Nano* **2016**, *10*, 10808-10815.
[6] X. Liu, X. Li, Y. Zou, H. Liu, L. Wang, J. Fang, C. Yang, *J Mater Chem A* **2019**, *7*, 3336-3343.
[7] X. He, C.C.S. Chan, J. Kim, H. Liu, C.J. Su, U.S. Jeng, H. Su, X. Lu, K.S. Wong, W.C.H. Choy, *Small Methods* **2022**, *6*, 2101475.
[8] L. Wieland, H. Li, X. Zhang, J. Chen, B.S. Flavel, *Small Science* **2022**, *3*, 2200079.
[9] M. Pfohl, K. Glaser, A. Graf, A. Mertens, D.D. Tune, T. Puerckhauer, A. Alam, L. Wei, Y. Chen, J. Zaumseil, A. Colsmann, R. Krupke, B.S. Flavel, *Adv Energy Mater* **2016**, *6*, 1600890.
[10] L. Lüer, S. Hoseinkhani, D. Polli, J. Crochet, T. Hertel, G. Lanzani, *Nat Phys* **2008**, *5*, 54-58.
[11] F. Wang, G. Dukovic, L.E. Brus, T.F. Heinz, *Science* **2005**, *308*, 838-41.
[12] R. Ihly, K.S. Mistry, A.J. Ferguson, T.T. Clikeman, B.W. Larson, O. Reid, O.V. Boltalina, S.H. Strauss, G. Rumbles, J.L. Blackburn, *Nat Chem* **2016**, *8*, 603-609.
[13] M.A. Green, E.D. Dunlop, G. Siefer, M. Yoshita, N. Kopidakis, K. Bothe, X.J. Hao, *Prog Photovoltaics* **2022**, *31*, 3-16.
[14] A. Classen, L. Einsiedler, T. Heumueller, A. Graf, M. Brohmann, F. Berger, S. Kahmann, M. Richter, G.J. Matt, K. Forberich, J. Zaumseil, C.J. Brabec, *Adv Energy Mater* **2018**, *8*, 1801913.
[15] M. Gong, T.A. Shastry, Y. Xie, M. Bernardi, D. Jasion, K.A. Luck, T.J. Marks, J.C. Grossman, S. Ren, M.C. Hersam, *Nano Lett* **2014**, *14*, 5308-14.
[16] M.J. Shea, M.S. Arnold, *Appl Phys Lett* **2013**, *102*, 243101.
[17] M. Zheng, B.A. Diner, *J Am Chem Soc* **2004**, *126*, 15490-4.
[18] L. Lüer, J. Crochet, T. Hertel, G. Cerullo, G. Lanzani, *ACS Nano* **2010**, *4*, 4265-4273.
[19] R.D. Mehlenbacher, T.J. McDonough, M. Grechko, M.Y. Wu, M.S. Arnold, M.T. Zanni, *Nat Commun* **2015**, *6*, 6732.
[20] A.M. Dowgiallo, K.S. Mistry, J.C. Johnson, J.L. Blackburn, *ACS Nano* **2014**, *8*, 8573-81.
[21] M. Pfohl, K. Glaser, J. Ludwig, D.D. Tune, S. Dehm, C. Kayser, A. Colsmann, R. Krupke, B.S. Flavel, *Adv Energy Mater* **2016**, *6*, 1501345.
[22] D.J. Bindl, M.S. Arnold, *J Phys Chem C* **2013**, *117*, 2390-2395.
[23] S.L. Guillot, K.S. Mistry, A.D. Avery, J. Richard, A.M. Dowgiallo, P.F. Ndione, J. van de Lagemaat, M.O. Reese, J.L. Blackburn, *Nanoscale* **2015**, *7*, 6556-66.
[24] M. Grechko, Y. Ye, R.D. Mehlenbacher, T.J. McDonough, M.Y. Wu, R.M. Jacobberger, M.S. Arnold, M.T. Zanni, *ACS Nano* **2014**, *8*, 5383-94.
[25] R.D. Mehlenbacher, J. Wang, N.M. Kearns, M.J. Shea, J.T. Flach, T.J. McDonough, M.Y. Wu, M.S. Arnold, M.T. Zanni, *J Phys Chem Lett* **2016**, *7*, 2024-2031.
[26] D.J. Bindl, M.J. Shea, M.S. Arnold, *Chem Phys* **2013**, *413*, 29-34.
[27] D.J. Bindl, M.Y. Wu, F.C. Prehn, M.S. Arnold, *Nano Lett* **2011**, *11*, 455-60.
[28] M.J. Shea, J.L. Wang, J.T. Flach, M.T. Zanni, M.S. Arnold, *APL Materials* **2018**, *6*, 056104.
[29] L. Wieland, C. Rust, H. Li, M. Jakoby, I. Howard, F. Li, J. Shi, J. Chen, B.S. Flavel, *Carbon* **2021**, *184*, 828-835.
[30] Y. Cai, Q. Li, G. Lu, H.S. Ryu, Y. Li, H. Jin, Z. Chen, Z. Tang, G. Lu, X. Hao, H.Y. Woo, C. Zhang, Y. Sun, *Nat Commun* **2022**, *13*, 2369.

[31] Y. Firdaus, V.M. Le Corre, S. Karuthedath, W. Liu, A. Markina, W. Huang, S. Chattopadhyay, M.M. Nahid, M.I. Nugraha, Y. Lin, A. Seitkhan, A. Basu, W. Zhang, I. McCulloch, H. Ade, J. Labram, F. Laquai, D. Andrienko, L.J.A. Koster, T.D. Anthopoulos, *Nat Commun* **2020**, *11*, 5220.
[32] Z. Zhang, L. Li, C. Xu, P. Jin, M. Huang, Y. Li, H. Wang, Y. Yi, C. Zhang, Y. Yang, W. Xu, Y. Lin, *Cell Rep Phys Sci* **2022**, *3*, 100895.
[33] J. Yuan, Y. Zhang, L. Zhou, G. Zhang, H.-L. Yip, T.-K. Lau, X. Lu, C. Zhu, H. Peng, P.A. Johnson, M. Leclerc, Y. Cao, J. Ulanski, Y. Li, Y. Zou, *Joule* **2019**, *3*, 1140-1151.
[34] O.V. Mikhnenko, P.W.M. Blom, T.-Q. Nguyen, *Energ Environ Sci* **2015**, *8*, 1867-1888.
[35] N. Tokmoldin, S.M. Hosseini, M. Raoufi, L. Phuong, O.J. Sandberg, H.L. Guan, Y.P. Zou, D. Neher, S. Shoaee, *J Mater Chem A* **2020**, *8*, 7854-7860.

- this page left intentionally blank -

- this page left intentionally blank -

7 Conclusion and Outlook

7.1 Conclusion

The performance values of SWCNT based solar cells are different for surfactant dispersed (6,5) in aqueous solution [1-3] or polymer-wrapped in toluene whereby the polymer sorted SWCNTs outperform those from aqueous separation.[4, 5] Whatever dispersant or solvent is used, the gentler shear-force mixing method enables higher efficiencies compared to sonication due to longer SWCNTs and therefore less quenching sites resulting in longer exciton lifetimes.[5, 6] For SWCNTs with a polymer shell, the exciton lifetime is enhanced due to the shielding of the nanotube from the surrounding environment.[7-9] In contrast, pristine SWCNTs are strongly coupled to each other leading to rapid downhill energy transfer to the smallest bandgap chirality in multichiral samples. Longer migration of the polymer-sorted CNTs, enabled by extended exciton lifetime, results in more excitons reaching the donor-acceptor interface and more efficient solar cells.[10-12] The majority of SWCNT solar cells are therefore fabricated with single chiral films of (6,5) and (7,5) mainly polymer-sorted because these are also the easiest to separate.

These SWCNT/C_{60} solar cells, especially bilayer architectures, suffer from the considerable distance every photogenerated exciton must travel to reach the interface. Rationally, thicker films should absorb more light and create more excitons resulting in higher efficiencies for SWCNT solar cells. However, most of these excitons will never reach the interface and be separated into charge carriers.[13] The optimum CNT film thickness is given by the exciton diffusion length which is defined as the average distance that an excited carrier will travel before recombining. In SWCNT bilayer cells the exciton diffusion length has been determined by ultrafast spectroscopy[11, 14] or photocurrent measurements to be 5-10 nm.[11, 15, 16] In this work, film thicknesses up to 18 nm obtained increasing solar cell performance for surfactant dispersed and shear-force mixed (6,5). Consequently, EQE increased as well with SWCNT film thickness until exciton diffusion length is reached and then fall abrupt.[5, 16-18]

Nevertheless, improving the light absorption is a key parameter for solar cells. If thicker films are not viable, the high absorbance coefficients of carbon nanotubes can be taken as advantage for light capture. The tailorable chirality dependent optical properties of SWCNTs led researchers to predictions of possible broadband light absorption for polychiral films to overcome the problem of narrow excitonic absorption peaks. This extension into the infrared would be favourable for

solar cells but in reality SWCNT mixtures instead of single chirality SWCNTs raise another problem. Energy transfer within the film usually occurs from the larger to the smaller bandgap CNTs[7, 11, 12] which typically results in a dark nonradiative state that cannot contribute to solar cell performance.[19]

The necessity of single chirality samples brings up the question which species would be ideal for photovoltaic and how can these CNTs be integrated into a solar cell. Recent advances in separation techniques, especially ATPE, make it is possible to isolate other single chiral SWCNT species in good semiconducting quality and significant amounts.[20-22] Larger diameter nanotubes are interesting because their S_{11} transition lies deeper in the IR region and they can encapsulate molecules like dyes in their cavity. Endohedral filling with the liquid phase filling[23] technique is simple and can be used for every SWCNT if they have open ends and the size of the filler molecule is smaller than the CNT diameter. Typically, SWCNT raw material is first filled followed by aqueous or polymer-sorting to gain individual filled chiralities for fabrication of solar cells.
While SWCNT/C_{60} solar cells only absorb in the infrared and roughly between 350 to 550 nm, they are missing the main visible part of the solar irradiation. Therefore, the idea is to encapsulate dye molecules such as squarylium that absorb in this region to complement the solar cell absorption. The energy transfer from dye to SWCNTs has been demonstrated to be fast, so the generated charges can contribute to the device current.[24, 25] Successful encapsulation of squarylium was accomplished for larger diameter CNTs in this work, aqueous sorting could than gain a variation of filled chiralities.[26] The incorporation of such dye filled SWCNTs is challenging because a minimum diameter of roughly 1.15 nm is required for the encapsulation[24] whereas the standard fullerene acceptor is limited to diameters of up to 0.95 nm in SWCNT/C_{60} solar cells.[3] Other smaller sized dye molecules with absorption in the visible are necessary or acceptors suitable for larger diameter nanotubes but their absorption should then not overlap with the dye.

Instead of optimizing the light capture of the SWCNT solar cells, already established broad band light absorbing solar cells can be combined with SWCNT/C_{60} to tandem solar cells for absorption extension into the infrared. For this purpose, a bifacial silicon solar cell is employed as top cell of a 4-probe tandem because it ensures that most of infrared light passes to the SWCNTs/fullerene cell underneath. The organic solar cells used for the tandem have S_{11} transitions that lie either on the edge or outside the absorption range of silicon to best complement to the absorption of silicon. A minimum diameter of ≈ 0.88 nm is necessary to ensure minimal overlap, additionally the upper

diameter limit is 0.95 nm[3] if C_{60} is used as acceptor. For larger diameter nanotubes, the energetic offset between the LUMO of the SWCNT and C_{60} is reduced leading to a smaller driving force that cannot overcome the exciton binding energy.[3, 15, 27] Given the current constraints of the fullerene acceptor and the amount of light eventually reaching a SWCNT/C_{60} cell, it was shown that (7,6) is currently the better choice compared to (10,3). On the other hand, there is a considerable window of opportunity in the AM1.5 solar spectrum for SWCNTs in the range 1500 – 1800 nm, where the S_{11} of larger diameter species like (14,6) is located,[21] but this will require the identification of new acceptors.

However, a large mismatch in current density from the SWCNT-based and silicon solar cells prohibit the realistic use of these two cells in a tandem architecture. Even if the AM1.5 spectrum is integrated over the residual IR region (1100 - 2500 nm), maximum ≈ 22.5 mA/cm^2 can be achieved which is roundabout half of the J_{SC} from a silicon solar cell device. Traditional approaches such as reducing the absorption of the window layer in the long wavelength range, improving passivation, increasing the internal reflectance at back interface, are more likely to lead to performance gains in this spectral region.

For the use of larger diameter nanotubes in SWCNT based solar cells, other acceptors as the standard fullerene or its derivates are required to achieve the appropriate LUMO offsets.

The non-fullerene acceptors ITIC-2F and Y6 are therefore tested in SWCNT/NFA solar cells due to their broad light absorption. Among the fabricated (6,5)/NFA solar cells, ITIC-2F has the best performance in terms of efficiency, while Y6 has the broadest spectral absorption and thus the highest J_{SC}. However, only fractions of the high energetic light from UV up to 600 nm is captured by those SWCNT/NFA devices. Endohedral filling of SWCNTs could complement such solar cells if a dye is encapsulated that absorbs in the UV and blue region like it was demonstrated for HINA. Alternatively, ternary structures with a third material absorbing in this region can optimize light capture and increase efficiency as shown for the PM6:Y6 donor-acceptor pair in combination with (6,5) SWCNTs as second donor. PM6 absorbs thereby light from 500 – 700 nm (max 610 nm),[28] Y6 from 600 – 1000 nm and (6,5) SWCNTs mainly in the IR.

Two different solar cell architectures were tested for the ternary architectures composed of PM6:Y6 and (6,5) SWCNTs as second donor are investigated. In the layered stack an EQE over 20 % was achieved with an 18 nm thick (6,5) film underneath the bulk PM6:Y6. The maximum SWCNT film thickness is as well limited by the short exciton diffusion length of carbon nanotubes to approximately 18 nm. Bulk heterojunctions can overcome this limitation but suffer from phase

separation by directly adding the (6,5) toluene solution into the PM6:Y6 in chloroform. The preparation in a single solvent resolved the morphology issue but the additional transfer step of the SWCNTs from toluene into chloroform makes it more difficult to gain high concentrated (6,5) SWCNT solutions and therefore significant EQE intensity at the S_{11} transition. Nevertheless, all prepared devices have shown absorption extension into the IR to some extent whereby the layered stack achieved the best EQE values for (6,5).

7.2 Outlook

Carbon nanotubes are a versatile material with multiple potential functions for photovoltaics. In principle, all elements of a solar cell, from the light sensitive component to carrier selective contacts, layers for passivation and transparent conducting films can be replaced by carbon nanotubes and their composites.

Bulk heterojunctions are promising architectures for SWCNT based solar cells if their bottle neck of high concentrated SWCNT is solved and larger amounts of carbon nanotubes can be incorporated into the solar cells without causing dramatic morphology changes. An alternative for morphology control could be the pre-formation of an aerogel and subsequent interpenetration of the acceptor. Ye at al.[29] demonstrated solar cells made of a SWCNT aerogel in combination with $PC_{71}BM$ as acceptor by the sacrificial matrix approach. The PCE and J_{SC} increased up to the optimum active layer thickness of 100 nm and achieved a maximum PCE of 1.7%. Limitation is here the sacrificial matrix approach based on the mixture of PMMA and s-SWCNTs because of the incomplete removal of PMMA on the donor acceptor interface.[16] The formation of an aerogel with chemical cross-linking of nanotubes avoids these contaminations.[30] However, an increase in exciton trap sites was observed after cross-linking. Setaro et al.[31] have shown that azidodichloro-triazine as cross-linker is capable of preserving the π-conjugation of the CNTs.

It is hard to envisage that the use of CNTs as light sensitive elements, at least under the constraints of current designs, will become an industrially attractive technology in the near future. It is possible to argue that CNTs will find their niche as hole transport and passivation layer in silicon solar cells or as transparent electrode due to their narrow absorption bands and the tailorable electronic property. Certainly, as a hole selective contact in silicon photovoltaics, devices are approaching performance values which are competitive with current industrial cells.[32, 33]

However, in infrared sensing it is difficult to argue why competing solar cell technologies such as perovskites, copper indium gallium selenide (CIGS), cadmium telluride (CdTe), and organic solar cells, which have achieved PCE values of 18–25%,[34] should be replaced by CNTs. There are still too many challenges that need to be addressed before organic CNT solar cells are able to compete with these systems. Primarily these are associated with improvements in the light absorption of the solar cells and the correspondingly low efficiency. It must become possible to use the entire range of s-SWCNTs (small and large diameter) and strategies to reduce excitonic trapping in mixtures of (n,m) species are required. The rapidly growing field of non-fullerene acceptors should in principle provide a solution to the first problem, but these remain expensive and to date have not been shown to enable the use of any chiral species not already accessible with C_{60}. For this reason, the use of thick single chiral films in the form of an aerogel in a bulk-heterojunction design is attractive to overcome the short exciton diffusion length in SWCNTs. Ideally the aerogel will have pore sizes similar to the exciton diffusion length and cross-links between the individual CNTs and/or acceptors should offer the best efficiency in terms of architectural considerations.

Besides aerogels, it will also be important to continue research on blended systems because of the high performance of the aforementioned thin film technologies. Certainly, these are built on established materials combinations, so they have a much higher probability of reaching competitive PCEs. Modifications to the side chains of PM6 or Y6 could make these molecules more compatible with the SWCNTs. In the future, new designed NFA or polymer donors could be able to directly disperse or even sort the carbon nanotubes making PFO-BPy as fourth component in the active layer redundant.

In truth, perhaps the most sensible way to utilise CNTs as a light sensitive element is to extend the light absorbed by other materials into the infrared rather than struggling to harvest broadband light with a narrow absorber.

7.3 References

[1] R.M. Jain, R. Howden, K. Tvrdy, S. Shimizu, A.J. Hilmer, T.P. McNicholas, K.K. Gleason, M.S. Strano, *Adv Mater* **2012**, *24*, 4436-4439.

[2] M. Pfohl, K. Glaser, J. Ludwig, D.D. Tune, S. Dehm, C. Kayser, A. Colsmann, R. Krupke, B.S. Flavel, *Adv Energy Mater* **2016**, *6*, 1501345.

[3] M. Pfohl, K. Glaser, A. Graf, A. Mertens, D.D. Tune, T. Puerckhauer, A. Alam, L. Wei, Y. Chen, J. Zaumseil, A. Colsmann, R. Krupke, B.S. Flavel, *Adv Energy Mater* **2016**, *6*, 1600890.

[4] A. Classen, L. Einsiedler, T. Heumueller, A. Graf, M. Brohmann, F. Berger, S. Kahmann, M. Richter, G.J. Matt, K. Forberich, J. Zaumseil, C.J. Brabec, *Adv Energy Mater* **2018**, *8*, 1801913.

[5] M.J. Shea, J.L. Wang, J.T. Flach, M.T. Zanni, M.S. Arnold, *APL Materials* **2018**, *6*, 056104.

[6] A. Graf, Y. Zakharko, S.P. Schiessl, C. Backes, M. Pfohl, B.S. Flavel, J. Zaumseil, *Carbon* **2016**, *105*, 593-599.

[7] D.H. Arias, D.B. Sulas-Kern, S.M. Hart, H.S. Kang, J. Hao, R. Ihly, J.C. Johnson, J.L. Blackburn, A.J. Ferguson, *Nanoscale* **2019**, *11*, 21196-21206.

[8] A.T. Mallajosyula, W. Nie, G. Gupta, J.L. Blackburn, S.K. Doorn, A.D. Mohite, *ACS Nano* **2016**, *10*, 10808-10815.

[9] N.F. Hartmann, R. Pramanik, A.M. Dowgiallo, R. Ihly, J.L. Blackburn, S.K. Doorn, *ACS Nano* **2016**, *10*, 11449-11458.

[10] M.S. Arnold, J.L. Blackburn, J.J. Crochet, S.K. Doorn, J.G. Duque, A. Mohite, H. Telg, *Phys Chem Chem Phys* **2013**, *15*, 14896-918.

[11] R.D. Mehlenbacher, J. Wang, N.M. Kearns, M.J. Shea, J.T. Flach, T.J. McDonough, M.Y. Wu, M.S. Arnold, M.T. Zanni, *J Phys Chem Lett* **2016**, *7*, 2024-2031.

[12] R.D. Mehlenbacher, M.Y. Wu, M. Grechko, J.E. Laaser, M.S. Arnold, M.T. Zanni, *Nano Lett* **2013**, *13*, 1495-501.

[13] L. Wieland, H. Li, C. Rust, J. Chen, B.S. Flavel, *Adv Energy Mater* **2020**, *11*, 2002880.

[14] M. Grechko, Y. Ye, R.D. Mehlenbacher, T.J. McDonough, M.Y. Wu, R.M. Jacobberger, M.S. Arnold, M.T. Zanni, *ACS Nano* **2014**, *8*, 5383-94.

[15] D.J. Bindl, M.Y. Wu, F.C. Prehn, M.S. Arnold, *Nano Lett* **2011**, *11*, 455-60.

[16] D.J. Bindl, M.J. Shea, M.S. Arnold, *Chem Phys* **2013**, *413*, 29-34.

[17] L. Wieland, C. Rust, H. Li, M. Jakoby, I. Howard, F. Li, J. Shi, J. Chen, B.S. Flavel, *Carbon* **2021**, *184*, 828-835.

[18] M.J. Shea, M.S. Arnold, *Appl Phys Lett* **2013**, *102*, 243101.

[19] J.T. Flach, J. Wang, M.S. Arnold, M.T. Zanni, *J Phys Chem Lett* **2020**, *11*, 6016-6024.

[20] J.A. Fagan, *Nanoscale Adv* **2019**, *1*, 3307-3324.

[21] H. Li, G. Gordeev, O. Garrity, N.A. Peyyety, P.B. Selvasundaram, S. Dehm, R. Krupke, S. Cambre, W. Wenseleers, S. Reich, M. Zheng, J.A. Fagan, B.S. Flavel, *ACS Nano* **2019**.

[22] H. Li, G. Gordeev, O. Garrity, S. Reich, B.S. Flavel, *ACS Nano* **2019**, *13*, 2567-2578.

[23] J. Campo, Y. Piao, S. Lam, C.M. Stafford, J.K. Streit, J.R. Simpson, A.R. Hight Walker, J.A. Fagan, *Nanoscale Horizons* **2016**, *1*, 317–324.

[24] S. van Bezouw, D.H. Arias, R. Ihly, S. Cambre, A.J. Ferguson, J. Campo, J.C. Johnson, J. Defillet, W. Wenseleers, J.L. Blackburn, *ACS Nano* **2018**, *12*, 6881-6894.

[25] K. Yanagi, K. Iakoubovskii, H. Matsui, H. Matsuzaki, H. Okamoto, Y. Miyata, Y. Maniwa, S. Kazaoui, N. Minami, H. Kataura, *J Am Chem Soc* **2007**, *129*, 4992-4997.

[26] S. Forel, H. Li, S. van Bezouw, J. Campo, L. Wieland, W. Wenseleers, B.S. Flavel, S. Cambre, *Nanoscale* **2022**, *14*, 8385-8397.

[27] J.L. Wang, S.R. Peurifoy, M.T. Bender, F. Ng, K.S. Choi, C. Nuckolls, M.S. Arnold, *J Phys Chem C* **2019**, *123*, 21395-21402.

[28] X. He, C.C.S. Chan, J. Kim, H. Liu, C.J. Su, U.S. Jeng, H. Su, X. Lu, K.S. Wong, W.C.H. Choy, *Small Methods* **2022**, *6*, 2101475.

[29] Y. Ye, D.J. Bindl, R.M. Jacobberger, M.Y. Wu, S.S. Roy, M.S. Arnold, *Small* **2014**, *10*, 3299.
[30] M. Schirowski, G. Abellan, E. Nuin, J. Pampel, C. Dolle, V. Wedler, T.P. Fellinger, E. Spiecker, F. Hauke, A. Hirsch, *J Am Chem Soc* **2018**, *140*, 3352-3360.
[31] A. Setaro, M. Adeli, M. Glaeske, D. Przyrembel, T. Bisswanger, G. Gordeev, F. Maschietto, A. Faghani, B. Paulus, M. Weinelt, R. Arenal, R. Haag, S. Reich, *Nat Commun* **2017**, *8*, 14281.
[32] J.H. Chen, L. Wan, H. Li, J. Yan, J.K. Ma, B. Sun, F. Li, B.S. Flavel, *Adv Funct Mater* **2020**, *30*, 2004476.
[33] G. Qing, J. Yan, H. Li, J. Chen, X. Yang, Y. Bai, X. Zhang, B. Chen, J. Guo, W. Duan, K. Han, F. Li, J. Wang, D. Song, S. Wang, B.S. Flavel, J. Chen, *Carbon* **2022**, *202*, 432-437.
[34] M.A. Green, E.D. Dunlop, G. Siefer, M. Yoshita, N. Kopidakis, K. Bothe, X.J. Hao, *Prog Photovoltaics* **2022**, *31*, 3-16.